frontiers | Research Topics

# Multicellularity: Views from cellular signaling and mechanics

**Edited by**
Hiroaki Hirata, Andrea Ravasio, Naotaka Nakazawa and Tsuyoshi Hirashima

**Published in**
Frontiers in Cell and Developmental Biology

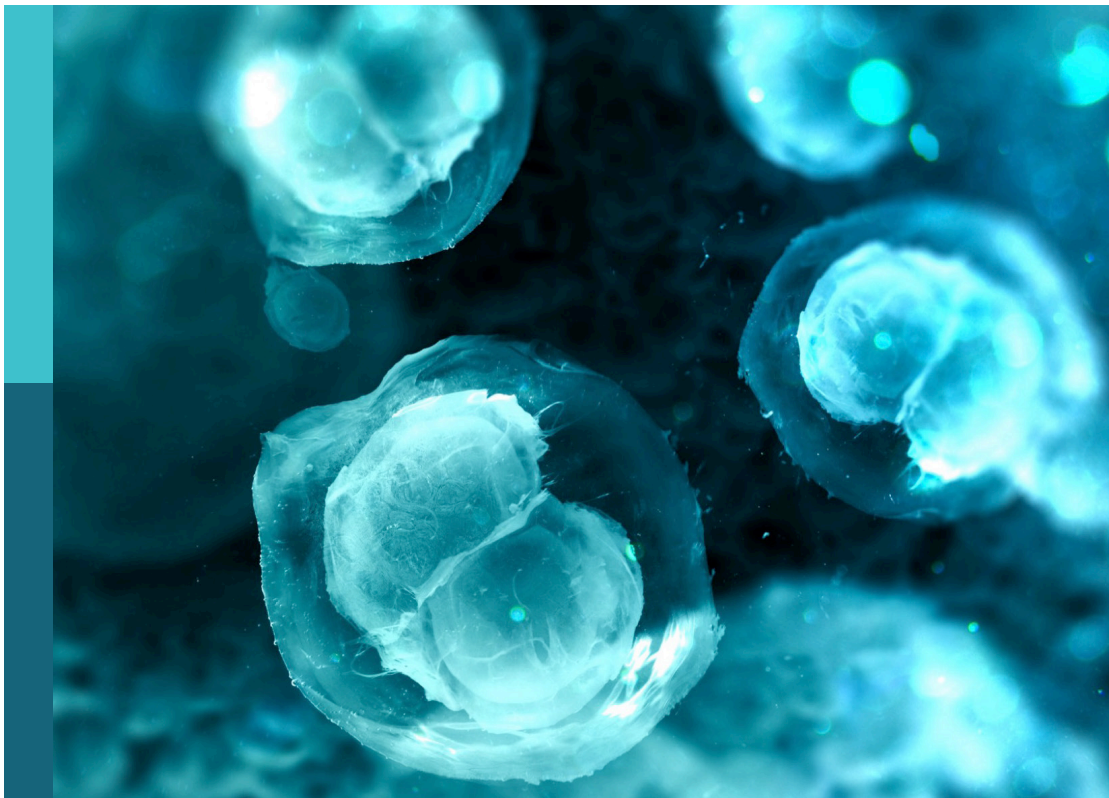

ISSN 1664-8714
ISBN 978-2-83252-026-0
DOI 10.3389/978-2-83252-026-0

## About Frontiers

Frontiers is more than just an open access publisher of scholarly articles: it is a pioneering approach to the world of academia, radically improving the way scholarly research is managed. The grand vision of Frontiers is a world where all people have an equal opportunity to seek, share and generate knowledge. Frontiers provides immediate and permanent online open access to all its publications, but this alone is not enough to realize our grand goals.

## Frontiers journal series

The Frontiers journal series is a multi-tier and interdisciplinary set of open-access, online journals, promising a paradigm shift from the current review, selection and dissemination processes in academic publishing. All Frontiers journals are driven by researchers for researchers; therefore, they constitute a service to the scholarly community. At the same time, the *Frontiers journal series* operates on a revolutionary invention, the tiered publishing system, initially addressing specific communities of scholars, and gradually climbing up to broader public understanding, thus serving the interests of the lay society, too.

## Dedication to quality

Each Frontiers article is a landmark of the highest quality, thanks to genuinely collaborative interactions between authors and review editors, who include some of the world's best academicians. Research must be certified by peers before entering a stream of knowledge that may eventually reach the public - and shape society; therefore, Frontiers only applies the most rigorous and unbiased reviews. Frontiers revolutionizes research publishing by freely delivering the most outstanding research, evaluated with no bias from both the academic and social point of view. By applying the most advanced information technologies, Frontiers is catapulting scholarly publishing into a new generation.

## What are Frontiers Research Topics?

Frontiers Research Topics are very popular trademarks of the *Frontiers journals series*: they are collections of at least ten articles, all centered on a particular subject. With their unique mix of varied contributions from Original Research to Review Articles, Frontiers Research Topics unify the most influential researchers, the latest key findings and historical advances in a hot research area.

Find out more on how to host your own Frontiers Research Topic or contribute to one as an author by contacting the Frontiers editorial office: frontiersin.org/about/contact

# Multicellularity: Views from cellular signaling and mechanics

**Topic editors**

Hiroaki Hirata — Kanazawa Institute of Technology, Japan
Andrea Ravasio — Pontifical Catholic University of Chile, Chile
Naotaka Nakazawa — Kindai University, Japan
Tsuyoshi Hirashima — National University of Singapore, Singapore

**Citation**

Hirata, H., Ravasio, A., Nakazawa, N., Hirashima, T., eds. (2023). *Multicellularity: Views from cellular signaling and mechanics*. Lausanne: Frontiers Media SA. doi: 10.3389/978-2-83252-026-0

# Table of contents

frontiers | Frontiers in Cell and Developmental Biology

TYPE Editorial
PUBLISHED 13 March 2023
DOI 10.3389/fcell.2023.1172921



OPEN ACCESS

EDITED AND REVIEWED BY
Claudia Tanja Mierke,
Leipzig University, Germany

*CORRESPONDENCE
Hiroaki Hirata,
hirata@neptune.kanazawa-it.ac.jp
Andrea Ravasio,
andrea.ravasio@uc.cl

SPECIALTY SECTION
This article was submitted to Cell Adhesion and Migration, a section of the journal Frontiers in Cell and Developmental Biology

RECEIVED 24 February 2023
ACCEPTED 07 March 2023
PUBLISHED 13 March 2023

CITATION
Hirata H, Nakazawa N, Hirashima T and Ravasio A (2023), Editorial: Multicellularity: Views from cellular signaling and mechanics.
*Front. Cell Dev. Biol.* 11:1172921.
doi: 10.3389/fcell.2023.1172921



# Editorial: Multicellularity: Views from cellular signaling and mechanics

Hiroaki Hirata[1]*, Naotaka Nakazawa[2], Tsuyoshi Hirashima[3] and Andrea Ravasio[4]*

[1]Department of Applied Bioscience, Kanazawa Institute of Technology, Hakusan, Japan, [2]Department of Energy and Materials, Faculty of Science and Engineering, Kindai University, Higashiosaka, Japan, [3]Mechanobiology Institute, National University of Singapore, Singapore, Singapore, [4]Institute for Biological and Medical Engineering, Schools of Engineering, Medicine and Biological Sciences, Pontificia Universidad Católica de Chile, Santiago, Chile

KEYWORDS

**cell-cell signaling, cell-cell communication, multicellular biomechanics, multicellular mechanobiology, morphogenesis, collective cell dynamics**

Editorial on the Research Topic
Multicellularity: Views from cellular signaling and mechanics

Appearance of multicellularity is a milestone for the evolution of life on our planet (Rose and Hammerschmidt, 2021). Multicellular organisms display emergent properties that cannot be predicted from simple cellular aggregation. Such properties stem from regulated mechanical interaction and dynamic communication between cells and between cells and their environment. Indeed, recent works have demonstrated that integration of mechano-chemical signaling is essential to specify cellular activity and maintain tissue homeostasis during key biological processes such as tissue morphogenesis, collective cell migration, cell differentiation and cell proliferation (Hannezo and Heisenberg, 2019). On the other hand, dysregulation of cell-cell communication and organization can cause fatal system failures and diseases, e.g., inappropriate execution of developmental processes and cancer transformation and progression (Northcott et al., 2018; Hannezo and Heisenberg, 2019).

To mechanistically understand how forms and functions of multicellular bodies arise, we need to know 1) mechanical and biological properties of individual constituent cells, and 2) how these properties are integrated into the whole system. Another to-be-emphasized aspect in multicellular systems is that mechanics and dynamics of individual cells are largely modulated by cues of the cell's environment, and local chemical and mechanical environments in the systems are, in turn, modified by cellular activities. Thus, for the understanding of multicellular systems, it is also requisite to unveil the mechanisms for reciprocal regulations between cells and environments. This Research Topic, with a series of nine articles from both experimental and theoretical approaches, highlights how mechanics-signaling integration in cells and their environments contributes to structures and functions of multicellular systems.

Development and maintenance of multicellular systems rely on adhesion of cells to their surrounding extracellular matrices and neighboring cells through tightly regulated interfacial protein complexes. Notably, the cell adhesion machineries suffer mechanical loads originated by biological activities and mechanics in both intracellular and extracellular spaces. Lim et al. comprehensively review molecular bases of "mechanotransduction" (i.e., transduction of mechanical stimuli into biochemical signals and vice versa) at cell-extracellular matrix

(ECM) and cell-cell adhesions, especially focusing on their impacts on the regulation of stem cell functions in their niche. Ravasio et al. propose a novel concept of "mechanoautophagy" by discussing potential synergies between mechanotransduction at cell adhesions complexes and autophagy, a regulated catabolic process used by cells to respond to a variety of cellular stresses, including those of mechanical nature.

Biswas et al. and Hirashima provide state-of-the-art reviews on integration of mechanical and biochemical signals as principles of multicellular tissue morphogenesis. Focusing on the process of egg formation in the ovarian follicle (folliculogenesis), Biswas et al. discuss how a range of crosstalks between local mechanical cues (e.g., ECM mechanics, luminal hydrostatic pressure, and cell-generated forces) and intracellular signaling (e.g., Hippo and Akt pathways) contribute to individual stages of follicle development. Furthermore, they summarize emerging experimental technologies employed for mechanobiological analyses in ovarian biology. On the other hand, Hirashima highlights importance of mechano-chemical feedback mechanisms for size regulation of epithelial tissues. Specifically, he discusses how the homeostasis of the epithelial tissue volume and the epithelial tube diameter is achieved by the control of cell division and cell rearrangement through the mutual feedback between cell-cell force communication and intracellular signal transduction.

The effect of ECM mechanics on the interaction between cell populations is revealed by Aparicio-Yuste et al. Epithelial cells infected with bacteria are known to be extruded from epithelial tissues through a mechanism called "cell competition", which involves competition between infected and surrounding uninfected cells. Using a combination of experimental and computational approaches, the authors show that a stiffer ECM promotes cell competition-mediated extrusion of infected cells by preferentially stimulating protrusive activities of uninfected cells.

Extensive efforts have long been made, from a wide range of experimental and theoretical approaches, to understand how body axes and patterns are developed in early embryos. In this Research Topic, three research groups develop new computational models to explore mechanical factors that contribute to body axis/pattern formation during embryonic development. Fujiwara et al. developed a simulation framework for a multicellular sphere based on vertex model, which is well-suitable for computational analysis of the body axis formation process. By incorporating parameters corresponding to cell-cell interfacial tension, without considering local control of cell division rate/orientation, they succeed to reproduce morphological and gene expression patterns observed during body axis elongation. Koyama et al. theoretically find that mismatches in viscous friction and cell area elasticity between two adjacent cell populations can lead to morphological changes similar to those observed in developing mouse embryos. Consistent with this finding, they experimentally confirm through AFM measurement that two contacting cell clusters during notochord elongation in mouse embryos exhibit varying cellular stiffness. Finally, Montenegro-Rojas et al. used early embryonic development of annual killifish as a model to computationally investigate the minimal mechanical requirements for *de-novo* formation of a cell aggregate. In this work, the authors developed a novel *in silico* framework that, combined with a bottom-up approach, allowed them to scan for those mechanical parameters (e.g., cell migration, modulation of cell-cell adhesion and of contact inhibition of locomotion and taxis mechanisms) necessary to maintain embryonic cells in dispersion on the surface of the yolk and thereafter aggregate at the embryo′s pole to initiate gastrulation.

The mechanism of multicellular pattern formation in embryos is addressed also using a gene expression analysis approach. Using undifferentiated cells and their nuclei dissociated from the early spider embryo, Akiyama-Oda et al. conducted single-cell and single-nucleus RNA sequencing and successfully reconstructed cell populations that correspond to the ectoderm, mesoderm and endoderm, as well as the cell patterning along the anterior-posterior axis in the ectoderm of the embryo. The transcriptome data resources provided in this study would be useful for further studies that aim at comprehensive identification of new patter-generating genes whose expression is spatially controlled.

The insights provided by the articles in this Research Topic contribute to a better understanding of mechano-chemical principles for emergence of multicellular functions and they highlight the importance of multidisciplinary investigation to unravel the intrinsic complexity of such systems. Indeed, while mono-disciplinary investigations explore the depth of the inner workings of living beings, combination of perspectives and technologies borrowed from different disciplines has provided the material and intellectual tools to navigate complexity found in multicellular organisms (Thomas et al., 2004; Grenci et al., 2019; Kim et al., 2020). On the same line, it is crucial to integrate approaches based on *in vivo* investigation, where physiological and pathological scenarios present themselves in their intricate completeness, with *in vitro* reductionist approaches where hypothesis testing can be based on simple assumptions and leverage from accurate control of experimental conditions as well as unparalleled precision and resolution. Finally, physical or statistical-based *in silico* approaches can be used to generate computational models and the same models can be further used to design informed investigations. Similarly, it seems natural to suggest that, due to the intrinsic complexity of the system, the plethora of approaches required, and the variety of results obtained, it will be increasingly necessary to adopt advanced statistical and computational methods such as Machine Learning and Artificial Intelligence to further advance the field. In conclusion, it is our shared opinion that the works presented here provide a substantial contribution to advancing our knowledge on how multicellular systems work in both physiological and pathological situations. Importantly, this may bring clues of novel strategies for engineering and medical application of multicellular systems, such as designable and efficient tissue engineering methods for regenerative medicine.

## Author contributions

All authors have made a substantial intellectual contribution to the editorial and approved it for publication.

## Funding

HH is supported by JSPS KAKENHI grants (20K12596 and 21H05127). NN is supported by JSPS KAKENHI grants (18K14819

and 21H05126). AR is supported by ANID SCIA/ACT192015, FONDECYT 1210872 and FONDEQUIP EMQ210101.

## Conflict of interest

The authors declare that the research was conducted in the absence of any commercial or financial relationships that could be construed as a potential conflict of interest.

## Publisher's note



## References

Grenci, G., Bertocchi, C., and Ravasio, A. (2019). Integrating microfabrication into biological investigations: The benefits of interdisciplinarity. *Micromachines* 10, 252. doi:10.3390/mi10040252

Hannezo, E., and Heisenberg, C. P. (2019). Mechanochemical feedback loops in development and disease. *Cell.* 178, 12–25. doi:10.1016/j.cell.2019.05.052

Kim, H., Jin, X., Glass, D. S., and Riedel-Kruse, I. H. (2020). Engineering and modeling of multicellular morphologies and patterns. *Curr. Opin. Genet. Dev.* 63, 95–102. doi:10.1016/j.gde.2020.05.039

Northcott, J. M., Dean, I. S., Mouw, J. K., and Weaver, V. M. (2018). Feeling stress: The mechanics of cancer progression and aggression. *Front. Cell. Dev. Biol.* 6, 17. doi:10.3389/fcell.2018.00017

Rose, C. J., and Hammerschmidt, K. (2021). What do we mean by multicellularity? The evolutionary transitions framework provides answers. *Front. Ecol. Evol.* 9, 730714. doi:10.3389/fevo.2021.730714

Thomas, J. D., Lee, T., and Suh, N. P. (2004). A function-based framework for understanding biological systems. *Annu. Rev. Biophys. Biomol. Struct.* 33, 75–93. doi:10.1146/annurev.biophys.33.110502.132654

frontiers in Cell and Developmental Biology

MINI REVIEW
published: 14 January 2022
doi: 10.3389/fcell.2021.820391

# Mechanical Feedback Control for Multicellular Tissue Size Maintenance: A Minireview

*Tsuyoshi Hirashima* [1,2,3]*†

[1]The Hakubi Center, Kyoto University, Kyoto, Japan, [2]Laboratory of Bioimaging and Cell Signaling, Graduate School of Biostudies, Kyoto University, Kyoto, Japan, [3]Japan Science and Technology Agency, PRESTO, Kawaguchi, Japan

All living tissues and organs have their respective sizes, critical to various biological functions, such as development, growth, and homeostasis. As tissues and organs generally converge to a certain size, intrinsic regulatory mechanisms may be involved in the maintenance of size regulation. In recent years, important findings regarding size regulation have been obtained from diverse disciplines at the molecular and cellular levels. Here, I briefly review the size regulation of biological tissues from the perspective of control systems. This minireview focuses on how feedback systems engage in tissue size maintenance through the mechanical interactions of constituent cell collectives through intracellular signaling. I introduce a general framework of a feedback control system for tissue size regulation, followed by two examples: maintenance of epithelial tissue volume and epithelial tube diameter. The examples deliver the idea of how cellular mechano-response works for maintaining tissue size.

**Keywords: epithelial tissues, control system, feedback regulation, mechano-response, tissue size maintenance**

OPEN ACCESS

***Edited by:***
*Takaaki Matsui, Nara Institute of Science and Technology, Japan*

***Reviewed by:***
*Eyal Schejter, Weizmann Institute of Science, Israel*
*Tatsuo Shibata, RIKEN, Japan*

***Correspondence:**
*Tsuyoshi Hirashima*
*hirashima.tsuyoshi2m@kyoto-u.ac.jp*

***ORCID:**
*Tsuyoshi Hirashima*
*orcid.org/0000-0001-7323-9627*

***Specialty section:***
*This article was submitted to Cell Adhesion and Migration, a section of the journal Frontiers in Cell and Developmental Biology*

***Received:*** *23 November 2021*
***Accepted:*** *27 December 2021*
***Published:*** *14 January 2022*

***Citation:***
*Hirashima T (2022) Mechanical Feedback Control for Multicellular Tissue Size Maintenance: A Minireview. Front. Cell Dev. Biol. 9:820391. doi: 10.3389/fcell.2021.820391*

## INTRODUCTION

The size of biological tissues and organs is a crucial variable closely related to various biological functions. Researchers have long been fascinated with biological size control since the pioneering essay by John Haldane, "On being the right size" in 1926 (Haldane, 1926). "How do organs know when they have reached the right size?" (Travis, 2013) is an old question that has remained unanswered till date. In recent years, extensive research has focused on understanding tissue size control as a system, in which the individual cells that make up the tissue interact with each other (Lander, 2011; Penzo-Mendez and Stanger, 2015; Boulan and Léopold, 2021). In this minireview, I describe how multicellular tissue size is regulated considering the control system in the context of mechanobiology, wherein the size is defined according to the dimension of interest as the target characteristic. In other words, size does not necessarily mean volume; it can correspond to the length or area in some cases. For example, when discussing the size of tubes, a typical structure of epithelial tissues, we often focus on their longitudinal or cross-sectional diameter, as discussed in a later section. The impact of the extracellular matrix on tissue size regulation has not been discussed, although it is critical in some cases.

## FEEDBACK CONTROL SYSTEM FOR TISSUE AND ORGAN SIZE

The issue of size regulation can be divided into two main classes: determination and maintenance of the right size. This section focuses on a control system that maintains the target value of the right size,

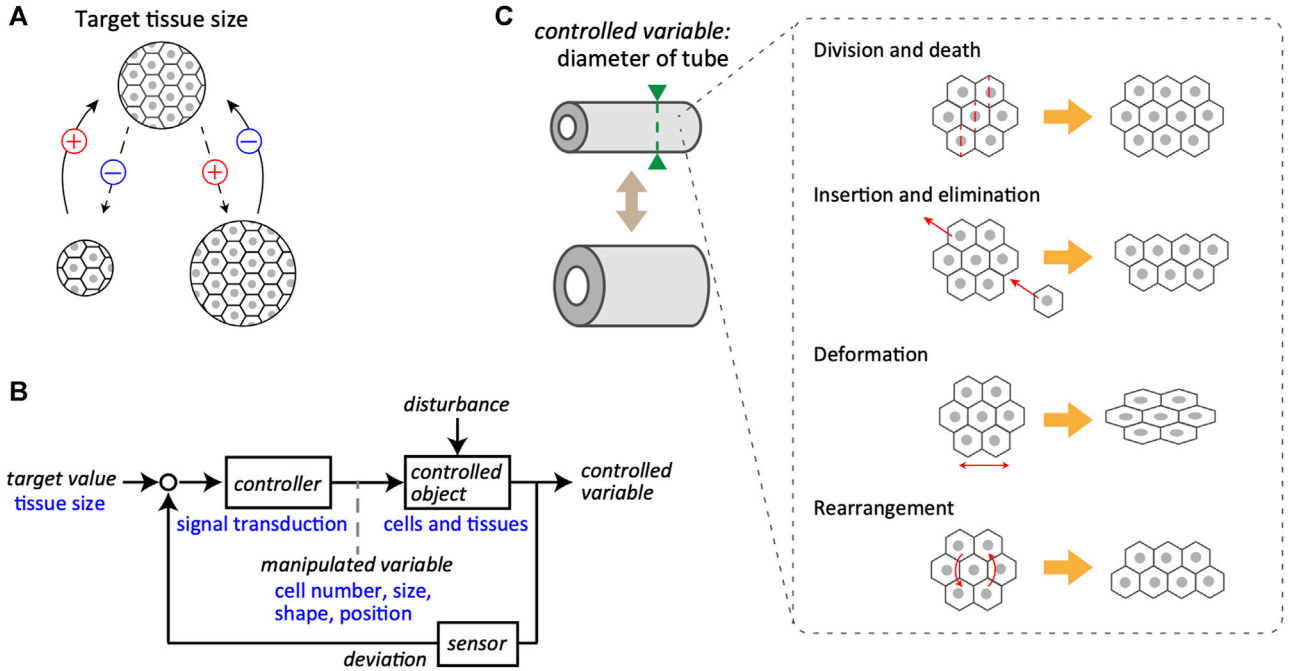


**FIGURE 1 |** Feedback control system in tissue size maintenance. **(A)** Schematics of the negative feedback loop for the maintenance of tissue size. A specific size of tissue, composed of cells, is set as the target value (top). Even if the tissue size may change during biological processes (bottom), it returns to the target value due to the negative feedback regulation. The plus and minus signs represent the notions of positive and negative change in the tissue size, respectively. **(B)** A block diagram of the control system for tissue size maintenance. General terms used in system engineering are indicated in black, whereas the corresponding examples of biological objects are in blue. Target value of tissue size is maintained by the closed loop mediated through controller, controlled object, and sensor. Note that the manipulated variable bridges from controller to controlled object. **(C)** Examples of manipulated variables for tube diameter as the controlled variable, including cell division and death, local cell insertion and elimination, cell deformation, and cell rearrangement.

provided that it has been determined *via* certain mechanisms. In most typical cases, the size of any living tissue does not diverge over time and is maintained at a specific value. This suggests the presence of a negative feedback loop, which is indispensable for the homeostasis and stabilization of the system, at the core of the regulatory mechanisms (**Figure 1A**). In other words, biological tissues are equipped with a system in which the difference between the current and target values is calculated, allowing the system to decrease and increase the size depending on the positive and negative differences, respectively.

Regarding the basic structure of the feedback control system that regulates tissue size, the system considered here is a closed-loop system for converging the size of tissues and organs to the target value (**Figure 1B**). Individual cells in the tissues receive information about the current size value through sensors and calculate the deviation from the target value. To reduce deviation, the cells yield manipulated variables, that is, output behaviors, such as the cell size, shape, and positions. This regulation proceeds through intracellular and intercellular signal transductions that act as the controller. When the manipulated quantity is supplemented to the controlled objects, such as cells and tissues, a controlled variable is updated. The controlled object is generally subjected to external disturbances along with the manipulated variables inside the system. A clear example of a disturbance is the partial resection of an organ. The mammalian liver can be considered an example of regenerative ability; in rats, it is known to recover its original size and function even after two-thirds of the liver is removed (Higgins, 1931; Taub, 2004). This suggests that certain organs possess mechanisms to robustly maintain their size against a large degree of disturbance and that the actual size is controlled by a coordinated coupling of each component in the feedback system, including target value, controller, controlled object, and sensor. The feedback loop is an essential control regulatory network for the size regulation of biological tissues, subjected to unpredictable disturbances.

In the following subsections, I provide brief descriptions of each component of the feedback control system concerning biological events.

## Target Value

The specific size of tissues is the target or desired value for the system and is determined by various factors, including genetic and physical constraints. In addition, tissue size varies according to life events, such as development, growth, and disease. For example, the number of pancreatic beta cells in pregnancy and obesity increases several times compared to that under normal conditions. This is because pancreatic beta cells, or insulin-producing cells, proliferate to compensate for increased insulin resistance, thereby preventing hyperglycemia

in diabetes (Zhou and Melton, 2018). There are also cases where the target size value increases locally in tissues because of endocrine or metabolic abnormalities, as in the case of the local gigantism of fingers and toes, also known as macrodactyly (Kalen et al., 1988).

## Controller

The controller is a core function that operates a system and corresponds to the device connecting the input and output, namely the signal transduction system of the cells. It receives information on tissue size as an input through chemical factors or mechanical forces caused by the tension between neighboring cells. In either case, the molecules and signaling pathways involved in regulating tissue size have been intensively investigated (Boulan et al., 2015). In particular, the Hippo signaling pathway has been well studied in this context (Yu et al., 2015; Panciera et al., 2017). In the downstream of the Hippo pathway, Yes-associated protein (YAP) and transcriptional co-activator with PDZ-binding motif (TAZ) regulate gene expressions with transcriptional factors TEADs, controlling the cell proliferation. Active YAP subcellular localization is more evident in the nucleus compared in the cytoplasm under higher cell densities, indicating the Hippo-YAP/TAZ signaling contributes to the tissue volume maintenance in response to mechanical tension within the cells and/or cell morphology (Dupont et al., 2011; Wada et al., 2011).

## Manipulated Variable

As the target value is related to tissue volume, the origins of the manipulated variables include various cellular behaviors related to the net change in volume, such as cell proliferation, hypertrophy, death, and atrophy. Epithelial-mesenchymal transition is also involved, as it corresponds to cell insertion and elimination in the tissue of interest. These cellular behaviors are directly linked to changes in tissue volume. However, if the target value is related to the cross-sectional diameter of the multicellular tube, the cellular behaviors as manipulated variables are more diverse (**Figure 1C**). For example, in proliferating monolayer epithelial tubes, the orientation of cell division is biased to the longitudinal axis, and the volume increase due to cell proliferation would be reflected mostly in the extension of the longitudinal axis but not of the circumferential axis of the tubes (Gillies and Cabernard, 2011; Tang et al., 2011; Tang et al., 2018). Cell deformation itself little affects the whole volume but directly affects the tube diameter owing to changes in the shape of constituent cells. Active cellular rearrangement at the supra-cellular scale is also critical in regulating tube diameter (Andrew and Ewald, 2010; Walck-Shannon and Hardin, 2014; Rauzi, 2020).

# EXAMPLES OF TISSUE AND ORGAN SIZE REGULATION

In this section, two examples of feedback control systems for tissue and organ size regulation are described. These systems employ a homeostatic system in which individual cells sense and respond to mechanical forces.

## Maintenance of Epithelial Tissue Volume by Controlling Cell Number

The first example is the size regulation of monolayer epithelial tissues by increasing or decreasing the number of cells as the manipulated variable in the system. Contact inhibition of cell proliferation, wherein the proliferative ability of cells decreases under high-density conditions, was reported half a century ago (Levine et al., 1965). In 2005, Shraiman proposed a mechanical feedback control system that regulates the proliferative ability of cells by sensing the mechanical force received by cells from their surroundings (Shraiman, 2005). The main points proposed are as follows. When cells strongly pull each other under low-density conditions, intracellular tension increases, and cell proliferation is accelerated. In contrast, when cells play a weak tug-of-war or push each other under high-density conditions, cell proliferation is suppressed. Further, cell death is induced in response to the high pressure occurring in overcrowded conditions. This theoretical study has been followed by additional theoretical and experimental studies (Hufnagel et al., 2007; Aegerter-Wilmsen et al., 2012; Eder et al., 2017), leading to a comprehensive picture of the system, in which tissue size is regulated by manipulating the number of cells through cellular sensing and response to the mechanical forces in living tissues. A series of studies have attracted attention for elucidating the signaling molecules involved as regulators of this system.

One of the critical signaling pathways for tissue homeostasis as the controller in this system could be triggered by a mechanosensitive ion channel. Mechanical forces activate the Piezo1 when exerted on cellular membranes, triggering intracellular signal transduction through converting the mechanical stimuli (Coste et al., 2010; Saotome et al., 2018; Lin et al., 2019). It has been demonstrated that Piezo1 works as the sensor to monitor the deviation of mechanical states in epithelial tissues for the tissue volume homeostasis using epithelial cultured cell lines and the zebrafish. When epithelial cells are at a high density, Piezo1 is activated in response to compressive force loading on the cells, followed by the activation of sphingosine 1-phosphate and Rho-kinase-dependent pulsatile myosin contraction, resulting in the cell extrusion (Eisenhoffer et al., 2012; Atieh et al., 2021). Interestingly, Piezo1 is also activated at a low cell density. In this case, cells sense the existing tension and respond by activating extracellular signal-regulated kinases (ERKs) *via* an increase in intracellular calcium ion concentration, eventually leading to cell proliferation (Gudipaty et al., 2017). In other words, Piezo1 uses different downstream signaling pathways depending on the degree of mechanical forces experienced by the cells. Knockdown of Piezo1 or inhibition of ERK activity prevented stretch-induced mitosis, indicating that each factor takes a key role as a sensor and a controller in the feedback system (Gudipaty et al., 2017). However, the molecular mechanisms underlying mechanical feedback systems are not uniquely determined and further elucidation of the signaling mechanism is needed.

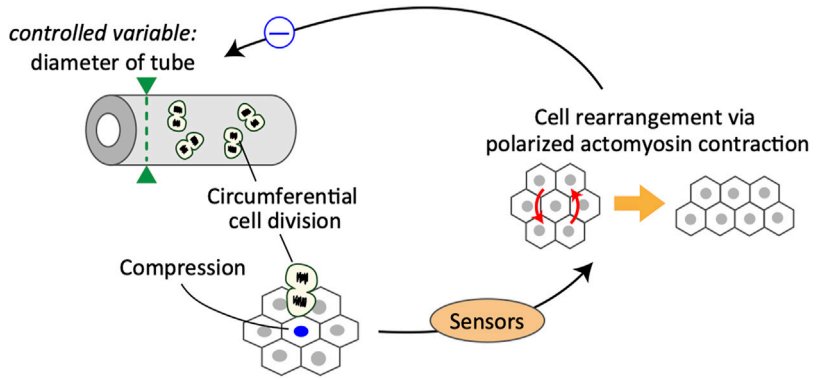


**FIGURE 2 |** Schematics of a control system for the maintenance of epididymal tubule diameter.

Recently, many efforts have been made to better understand how the mechanical and chemical changes in tissues are locally coordinated to eliminate cells for the homeostatic maintenance overall the epithelial tissues (Gudipaty and Rosenblatt, 2017; Ohsawa et al., 2018). Quantitative imaging approaches have revealed that the epithelial cells tend to be eliminated by compression-driven ERK inactivation (Moreno et al., 2019), and the extruding cells are governed through an interplay between actomyosin contractility and cell junctions (Lubkov and Bar-Sagi, 2014; Thomas et al., 2020). Moreover, the neighboring cell behaviors are also physically affected by the extruding cells through intercellular signal transmissions, such as calcium and ERK activation waves (Takeuchi et al., 2020; Gagliardi et al., 2021; Valon et al., 2021). These findings led to accelerating studies on mechanical cell competition – the mechanism for eliminating unfit cells for the tissue homeostasis (Brás-Pereira and Moreno, 2018; Matamoro-Vidal and Levayer, 2019).

## Maintenance of Epithelial Tube Diameter Through Cell Rearrangement

The second example is a mechanical feedback regulation to maintain tubule diameter, which is a physiologically important quantity of tissue structure. The epididymal tubule in the male reproductive tract is an experimental system that allows the examination of epithelial tube morphogenesis (Joseph et al., 2009; Murashima et al., 2015). During murine development, epithelial cells in the epididymal tubule divide in all directions on the tangential plane of the tubule (Xu et al., 2016; Hirashima and Adachi, 2019). As the cells divide longitudinally as well as along the circumferential axis of the tubule, the tubule diameter is expected to increase with time; however, the diameter of the epididymal tubules hardly changes throughout the morphogenetic process (Joseph et al., 2009; Hirashima, 2014). Feedback systems that have been poorly understood may be involved in controlling the deviation in the tube diameter from the target value.

The cellular dynamics of embryonic murine epididymal tubules under *ex vivo* culture conditions were examined using two-photon live-cell imaging. Live imaging analysis revealed that a group of cells adjacent to the dividing cells were more likely to cause cell rearrangement *via* actomyosin contraction in response to cell division along the tubule circumference (Hirashima and Adachi, 2019). Importantly, oriented cell division in the circumferential axis of tubules transmits mechanical signals through compressive forces, which would trigger polarized myosin activation to maintain the tube diameter (**Figure 2**). The obtained quantitative data were incorporated into a mathematical model of multicellular dynamics, and it was confirmed that the mechano-response system would maintain the diameter of developing tubes. Taken together, the analysis suggests that the polarized mechano-responsive cellular behavior at the supra-cellular scale maintains tube diameter at the whole-tissue scale (Hirashima and Adachi, 2019).

This is a typical example of a negative feedback control system, in which cells sense the increase in cell number along the circumferential axis of the tubules and the corresponding change in mechanical forces, eventually leading to active cell rearrangement for regulating the tube diameter (**Figure 2**). In this case, the controller in the system is partially composed of Rho-kinase-dependent acto-myosin contraction, and the manipulated variable is the cell position regulated by the cell rearrangement. One important but unclear aspect is the mechanism by which cells sense the size of a specific dimension. In the case of developing epididymal tubules, it is important to understand how epithelial cells acquire the information of specific orientation in sensing mechanical stimuli. One possible factor that provides information regarding the orientation of cells is planar cell polarity (PCP) proteins. PCP signaling activates Rho-associated kinase, an upstream kinase of non-muscle myosin (Nishimura et al., 2012; Guillot and Lecuit, 2013; Butler and Wallingford, 2017). Importantly, PCP proteins, such as Vang-like (VANGL) and tyrosine-protein kinase-like 7 (PTK7), are mainly localized on the apical junctions of tube cells circumferentially, and loss of PCP causes failure of cell arrangement, eventually leading to radial tube expansion in the epididymis (Xu et al., 2016; Hirashima and Adachi, 2019) and kidney (Karner et al., 2009; Kunimoto et al., 2017). Thus, PCP proteins likely serve as core regulators of the polarized mechano-response system. However,

the sensors involved and their ability to function in an integrated manner remain poorly understood and should be examined further in future studies.

Epididymal cells possess the ability to sense compressive forces, specifically along the circumferential axis of proliferative tubules. In response to compressive forces, cells undergo oriented cell rearrangement by generating actomyosin-based polarized contractile forces, which eventually suppress the increase in tube diameter due to circumferential cell division.

## CONCLUSIONS AND DISCUSSION

This review describes the mechanical feedback systems for multicellular tissue size maintenance. First, a general framework of the feedback loop underlying tissue size control has been introduced with a few physiological and pathological examples. As building blocks of tissues, cells seem to possess inherent size regulation systems as in collectives. Considering this, mapping each component in the feedback control system to biological events allows us to capture the phenomena from different views by simplifying the system. These have been presented using two examples of tissue size regulation, i.e., maintenance of epithelial tissue volume by controlling cell number and maintenance of epithelial tube diameter through cell rearrangement. Throughout this minireview, I have discussed the cellular responses to mechanical forces involving collective multicellular behaviors for organizing tissue size control. Although the multicellular mechanoresponse is not a sole regulatory mechanism, this would be a principle of cell-to-cell communication through cellular sensing of and responses to mechanical forces for tissue size homeostasis. These mechanoresponsive cellular behaviors likely play a pivotal role in the systemic regulation. The existence of feedback systems, where each component is well-coupled for the tissue size regulation, is a premise of this minireview, and biological outcomes caused by partial defects in the sensor or controller raised in the two examples support it. However, it remains unclear how the feedback components organize as a whole system for the tissue size control. Further efforts, especially to identify the molecules involved in sensing mechanical forces, are anticipated.

I expect that the polarized cellular mechano-response systems introduced in *Maintenance of the Epithelial Tube Diameter Through Cell Rearrangement* Section would serve as a fundamental mechanism for tissue morphogenesis during development and growth. Individual cells should have their polarity along each axis of tissue coordinate. Accordingly, molecular machineries responsible to the mechano-sensing would be localized at a subcellular scale according to the cell polarity, causing subsequent chemical signaling responding to the mechanical stimulus against the specific orientation. Maintaining the size along the specific axis in growing tissues links to another aspect of anisotropic tissue morphogenesis, which gives rise to diverse tissue shapes. Despite its importance, experimental studies are currently limited. Provided that constituent cells are loosely connected to each other under a low-density condition, the change in cell tension due to neighbor cell divisions would be negligible and the mechanical forces may not work as a signal to control the tube diameter. In that case, identifying what signals control the tube diameter is also demanded. I hope that future studies will fill the gap in understanding the polarized mechano-response system.

## AUTHOR CONTRIBUTIONS

The author confirms being the sole contributor of this work and has approved it for publication.

## FUNDING

This work was supported by the JST PRESTO grant JPMJPR1949 and by the JSPS KAKENHI grants 21H05290, 21H00426, and 21K18601.

## REFERENCES

Aegerter-Wilmsen, T., Heimlicher, M. B., Smith, A. C., de Reuille, P. B., Smith, R. S., Aegerter, C. M., et al. (2012). Integrating Force-Sensing and Signaling Pathways in a Model for the Regulation of wing Imaginal Disc Size. *Development* 125, e1. doi:10.1242/jcs.120758

Andrew, D. J., and Ewald, A. J. (2010). Morphogenesis of Epithelial Tubes: Insights into Tube Formation, Elongation, and Elaboration. *Develop. Biol.* 341, 34–55. doi:10.1016/j.ydbio.2009.09.024

Atieh, Y., Wyatt, T., Zaske, A. M., and Eisenhoffer, G. T. (2021). Pulsatile Contractions Promote Apoptotic Cell Extrusion in Epithelial Tissues. *Curr. Biol.* 31, 1129–1140. e4. doi:10.1016/j.cub.2020.12.005

Boulan, L., and Léopold, P. (2021). What Determines Organ Size during Development and Regeneration? *Development* 148. doi:10.1242/dev.196063

Boulan, L., Milán, M., and Léopold, P. (2015). The Systemic Control of Growth. *Cold Spring Harb. Perspect. Biol.* 7, a019117. doi:10.1101/cshperspect.a019117

Brás-Pereira, C., and Moreno, E. (2018). Mechanical Cell Competition. *Curr. Opin. Cel Biol.* 51, 15–21. doi:10.1016/j.ceb.2017.10.003

Butler, M. T., and Wallingford, J. B. (2017). Planar Cell Polarity in Development and Disease. *Nat. Rev. Mol. Cel Biol.* 18, 375–388. doi:10.1038/nrm.2017.11

Coste, B., Mathur, J., Schmidt, M., Earley, T. J., Ranade, S., Petrus, M. J., et al. (2010). Piezo1 and Piezo2 Are Essential Components of Distinct Mechanically Activated Cation Channels. *Science* 330, 55–60. doi:10.1126/science.1193270

Dupont, S., Morsut, L., Aragona, M., Enzo, E., Giulitti, S., Cordenonsi, M., et al. (2011). Role of YAP/TAZ in Mechanotransduction. *Nature* 474, 179–183. doi:10.1038/nature10137

Eder, D., Aegerter, C., and Basler, K. (2017). Forces Controlling Organ Growth and Size. *Mech. Develop.* 144, 53–61. doi:10.1016/j.mod.2016.11.005

Eisenhoffer, G. T., Loftus, P. D., Yoshigi, M., Otsuna, H., Chien, C.-B., Morcos, P. A., et al. (2012). Crowding Induces Live Cell Extrusion to Maintain Homeostatic Cell Numbers in Epithelia. *Nature* 484, 546–549. doi:10.1038/nature10999

Gagliardi, P. A., Dobrzyński, M., Jacques, M.-A., Dessauges, C., Ender, P., Blum, Y., et al. (2021). Collective ERK/Akt Activity Waves Orchestrate Epithelial Homeostasis by Driving Apoptosis-Induced Survival. *Develop. Cel* 56, 1712–1726. e6. doi:10.1016/j.devcel.2021.05.007

Gillies, T. E., and Cabernard, C. (2011). Cell Division Orientation in Animals. *Curr. Biol.* 21, R599–R609. doi:10.1016/j.cub.2011.06.055

Gudipaty, S. A., Lindblom, J., Loftus, P. D., Redd, M. J., Edes, K., Davey, C. F., et al. (2017). Mechanical Stretch Triggers Rapid Epithelial Cell Division through Piezo1. *Nature* 543, 118–121. doi:10.1038/nature21407

Gudipaty, S. A., and Rosenblatt, J. (2017). Epithelial Cell Extrusion: Pathways and Pathologies. *Semin. Cel Develop. Biol.* 67, 132–140. doi:10.1016/j.semcdb.2016.05.010

Guillot, C., and Lecuit, T. (2013). Mechanics of Epithelial Tissue Homeostasis and Morphogenesis. *Science* 340, 1185–1189. doi:10.1126/science.1235249

Haldane, J. B. S. (1926). On Being the Right Size. Available at: https://harpers.org/archive/1926/03/on-being-the-right-size/.

Higgins, G. M. (1931). Experimental Pathology of the Liver. I. Restoration of the Liver Following Partial Surgical Removal. *Arch. Pathol.* 12, 186–202.

Hinton, B., Murashima, A., and Xu, B. (2015). Understanding normal and Abnormal Development of the Wolffian/epididymal Duct by Using Transgenic Mice. *Asian J. Androl.* 17 (5), 749–755. doi:10.4103/1008-682X.155540

Hirashima, T., and Adachi, T. (2019). Polarized Cellular Mechanoresponse System for Maintaining Radial Size in Developing Epithelial Tubes. *Development* 146, dev181206. doi:10.1242/dev.181206

Hirashima, T. (2014). Pattern Formation of an Epithelial Tubule by Mechanical Instability during Epididymal Development. *Cel Rep.* 9, 866–873. doi:10.1016/j.celrep.2014.09.041

Hufnagel, L., Teleman, A. A., Rouault, H., Cohen, S. M., and Shraiman, B. I. (2007). On the Mechanism of wing Size Determination in Fly Development. *Proc. Natl. Acad. Sci.* 104, 3835–3840. doi:10.1073/pnas.0607134104

Joseph, A., Yao, H., and Hinton, B. T. (2009). Development and Morphogenesis of the Wolffian/epididymal Duct, More Twists and Turns. *Develop. Biol.* 325, 6–14. doi:10.1016/j.ydbio.2008.10.012

Kalen, V., Burwell, D. S., and Omer, G. E. (1988). Macrodactyly of the Hands and Feet. *J. Pediatr. Orthopaedics* 8, 311–315. doi:10.1097/01241398-198805000-00011

Karner, C. M., Chirumamilla, R., Aoki, S., Igarashi, P., Wallingford, J. B., and Carroll, T. J. (2009). Wnt9b Signaling Regulates Planar Cell Polarity and Kidney Tubule Morphogenesis. *Nat. Genet.* 41, 793–799. doi:10.1038/ng.400

Kunimoto, K., Bayly, R. D., Vladar, E. K., Vonderfecht, T., Gallagher, A.-R., and Axelrod, J. D. (2017). Disruption of Core Planar Cell Polarity Signaling Regulates Renal Tubule Morphogenesis but Is Not Cystogenic. *Curr. Biol.* 27, 3120–3131. doi:10.1016/j.cub.2017.09.011

Lander, A. D. (2011). Pattern, Growth, and Control. *Cell* 144, 955–969. doi:10.1016/j.cell.2011.03.009

Levine, E. M., Becker, Y., Boone, C. W., and Eagle, H. (1965). Contact Inhibition, Macromolecular Synthesis, and Polyribosomes in Cultured Human Diploid Fibroblasts. *Proc. Natl. Acad. Sci.* 53, 350–356. doi:10.1073/pnas.53.2.350

Lin, Y.-C., Guo, Y. R., Miyagi, A., Levring, J., MacKinnon, R., and Scheuring, S. (2019). Force-induced Conformational Changes in PIEZO1. *Nature* 573, 230–234. doi:10.1038/s41586-019-1499-2

Lubkov, V., and Bar-Sagi, D. (2014). E-Cadherin-Mediated Cell Coupling Is Required for Apoptotic Cell Extrusion. *Curr. Biol.* 24, 868–874. doi:10.1016/j.cub.2014.02.057

Matamoro-Vidal, A., and Levayer, R. (2019). Multiple Influences of Mechanical Forces on Cell Competition. *Curr. Biol.* 29, R762–R774. doi:10.1016/j.cub.2019.06.030

Moreno, E., Valon, L., Levillayer, F., and Levayer, R. (2019). Competition for Space Induces Cell Elimination through Compaction-Driven ERK Downregulation. *Curr. Biol.* 29, 23–34. doi:10.1016/j.cub.2018.11.007

Nishimura, T., Honda, H., and Takeichi, M. (2012). Planar Cell Polarity Links Axes of Spatial Dynamics in Neural-Tube Closure. *Cell* 149, 1084–1097. doi:10.1016/j.cell.2012.04.021

Ohsawa, S., Vaughen, J., and Igaki, T. (2018). Cell Extrusion: A Stress-Responsive Force for Good or Evil in Epithelial Homeostasis. *Develop. Cel* 44, 284–296. doi:10.1016/j.devcel.2018.01.009

Panciera, T., Azzolin, L., Cordenonsi, M., and Piccolo, S. (2017). Mechanobiology of YAP and TAZ in Physiology and Disease. *Nat. Rev. Mol. Cel Biol.* 18, 758–770. doi:10.1038/nrm.2017.87

Penzo-Méndez, A. I., and Stanger, B. Z. (2015). Organ-size Regulation in Mammals. *Cold Spring Harb. Perspect. Biol.* 7, a019240. doi:10.1101/cshperspect.a019240

Rauzi, M. (2020). Cell Intercalation in a Simple Epithelium. *Phil. Trans. R. Soc. B* 375, 20190552. doi:10.1098/rstb.2019.0552

Saotome, K., Murthy, S. E., Kefauver, J. M., Whitwam, T., Patapoutian, A., and Ward, A. B. (2018). Structure of the Mechanically Activated Ion Channel Piezo1. *Nature* 554, 481–486. doi:10.1038/nature25453

Shraiman, B. I. (2005). Mechanical Feedback as a Possible Regulator of Tissue Growth. *Proc. Natl. Acad. Sci.* 102, 3318–3323. doi:10.1073/pnas.0404782102

Takeuchi, Y., Narumi, R., Akiyama, R., Vitiello, E., Shirai, T., Tanimura, N., et al. (2020). Calcium Wave Promotes Cell Extrusion. *Curr. Biol.* 30, 670–681. e6. doi:10.1016/j.cub.2019.11.089

Tang, N., Marshall, W. F., McMahon, M., Metzger, R. J., and Martin, G. R. (2011). Control of Mitotic Spindle Angle by the RAS-Regulated ERK1/2 Pathway Determines Lung Tube Shape. *Science* 333, 342–345. doi:10.1126/science.1204831

Tang, Z., Hu, Y., Wang, Z., Jiang, K., Zhan, C., Marshall, W. F., et al. (2018). Mechanical Forces Program the Orientation of Cell Division during Airway Tube Morphogenesis. *Develop. Cel* 44, 313–325. e5. doi:10.1016/j.devcel.2017.12.013

Taub, R. (2004). Liver Regeneration: From Myth to Mechanism. *Nat. Rev. Mol. Cel Biol.* 5, 836–847. doi:10.1038/nrm1489

Thomas, M., Ladoux, B., and Toyama, Y. (2020). Desmosomal Junctions Govern Tissue Integrity and Actomyosin Contractility in Apoptotic Cell Extrusion. *Curr. Biol.* 30, 682–690. e5. doi:10.1016/j.cub.2020.01.002

Travis, J. (2013). Mysteries of Development. *Science* 340, 1156. doi:10.1126/science.340.6137.1156-a

Valon, L., Davidović, A., Levillayer, F., Villars, A., Chouly, M., Cerqueira-Campos, F., et al. (2021). Robustness of Epithelial Sealing Is an Emerging Property of Local ERK Feedback Driven by Cell Elimination. *Develop. Cel* 56, 1700–1711. e8. doi:10.1016/j.devcel.2021.05.006

Wada, K.-I., Itoga, K., Okano, T., Yonemura, S., and Sasaki, H. (2011). Hippo Pathway Regulation by Cell Morphology and Stress Fibers. *Development* 138, 3907–3914. doi:10.1242/dev.070987

Walck-Shannon, E., and Hardin, J. (2014). Cell Intercalation from Top to Bottom. *Nat. Rev. Mol. Cel Biol.* 15, 34–48. doi:10.1038/nrm3723

Xu, B., Washington, A. M., Domeniconi, R. F., Ferreira Souza, A. C., Lu, X., Sutherland, A., et al. (2016). Protein Tyrosine Kinase 7 Is Essential for Tubular Morphogenesis of the Wolffian Duct. *Develop. Biol.* 412, 219–233. doi:10.1016/j.ydbio.2016.02.029

Yu, F.-X., Zhao, B., and Guan, K.-L. (2015). Hippo Pathway in Organ Size Control, Tissue Homeostasis, and Cancer. *Cell* 163, 811–828. doi:10.1016/j.cell.2015.10.044

Zhou, Q., and Melton, D. A. (2018). Pancreas Regeneration. *Nature* 557, 351–358. doi:10.1038/s41586-018-0088-0

**Conflict of Interest:** The author declares that the research was conducted in the absence of any commercial or financial relationships that could be construed as a potential conflict of interest.

frontiers in Cell and Developmental Biology

HYPOTHESIS AND THEORY
published: 29 March 2022
doi: 10.3389/fcell.2022.864135

# Differential Cellular Stiffness Contributes to Tissue Elongation on an Expanding Surface

*Hiroshi Koyama*[1,2]*, *Makoto Suzuki*[2,3,4], *Naoko Yasue*[3], *Hiroshi Sasaki*[5], *Naoto Ueno*[2,3] and *Toshihiko Fujimori*[1,2]

[1]Division of Embryology, National Institute for Basic Biology (Div. Embryology, NIBB), Okazaki, Japan, [2]Department of Basic Biology, School of Life Science, SOKENDAI (The Graduate University for Advanced Studies), Hayama, Japan, [3]Division of Morphogenesis, National Institute for Basic Biology (Div. Morphogenesis, NIBB), Okazaki, Japan, [4]Amphibian Research Center, Graduate School of Integrated Sciences for Life, Hiroshima University (ARC, Hiroshima Univ.), Higashihiroshima, Japan, [5]Laboratory for Embryogenesis, Graduate School of Frontier Biosciences, Osaka University (FBS, Osaka Univ.), Suita, Japan

Pattern formation and morphogenesis of cell populations is essential for successful embryogenesis. Steinberg proposed the differential adhesion hypothesis, and differences in cell–cell adhesion and interfacial tension have proven to be critical for cell sorting. Standard theoretical models such as the vertex model consider not only cell–cell adhesion/tension but also area elasticity of apical cell surfaces and viscous friction forces. However, the potential contributions of the latter two parameters to pattern formation and morphogenesis remain to be determined. In this theoretical study, we analyzed the effect of both area elasticity and the coefficient of friction on pattern formation and morphogenesis. We assumed the presence of two cell populations, one population of which is surrounded by the other. Both populations were placed on the surface of a uniformly expanding environment analogous to growing embryos, in which friction forces are exerted between cell populations and their expanding environment. When the area elasticity or friction coefficient in the cell cluster was increased relative to that of the surrounding cell population, the cell cluster was elongated. In comparison with experimental observations, elongation of the notochord in mice is consistent with the hypothesis based on the difference in area elasticity but not the difference in friction coefficient. Because area elasticity is an index of cellular stiffness, we propose that differential cellular stiffness may contribute to tissue elongation within an expanding environment.

**Keywords: pattern formation, morphogenesis, tissue elongation, cellular stiffness, vertex model, theory, mouse notochord**

OPEN ACCESS

***Edited by:***
*Tsuyoshi Hirashima, Kyoto University, Japan*

***Reviewed by:***
*Marcel Hörning, University of Stuttgart, Germany*
*Makoto Sato, Kanazawa University, Japan*

***Correspondence:**
*Hiroshi Koyama*
*hkoyama@nibb.ac.jp*

***Specialty section:***
*This article was submitted to Cell Adhesion and Migration, a section of the journal Frontiers in Cell and Developmental Biology*

***Received:*** *28 January 2022*
***Accepted:*** *03 March 2022*
***Published:*** *29 March 2022*

***Citation:***
*Koyama H, Suzuki M, Yasue N, Sasaki H, Ueno N and Fujimori T (2022) Differential Cellular Stiffness Contributes to Tissue Elongation on an Expanding Surface. Front. Cell Dev. Biol. 10:864135. doi: 10.3389/fcell.2022.864135*

## 1 INTRODUCTION

Pattern formation and morphogenesis by cell populations includes cell sorting, intermixing of different cell types, etc. These patterns are observed in various embryos and tissues such as germ layers, oviduct, and cochlea (Yamanaka and Honda, 1990; Steinberg, 2007; Krieg et al., 2008; Togashi et al., 2011). A few hypotheses have been proposed to explain these phenomena, including the differential adhesion hypothesis by Steinberg (Steinberg, 1963) in 1963. According to these hypotheses, either differential cell–cell adhesion or cell–cell interfacial tensions are considered, and their strengths are assumed to differ among cell types. The roles of these mechanical parameters in tissue organization have been demonstrated by both

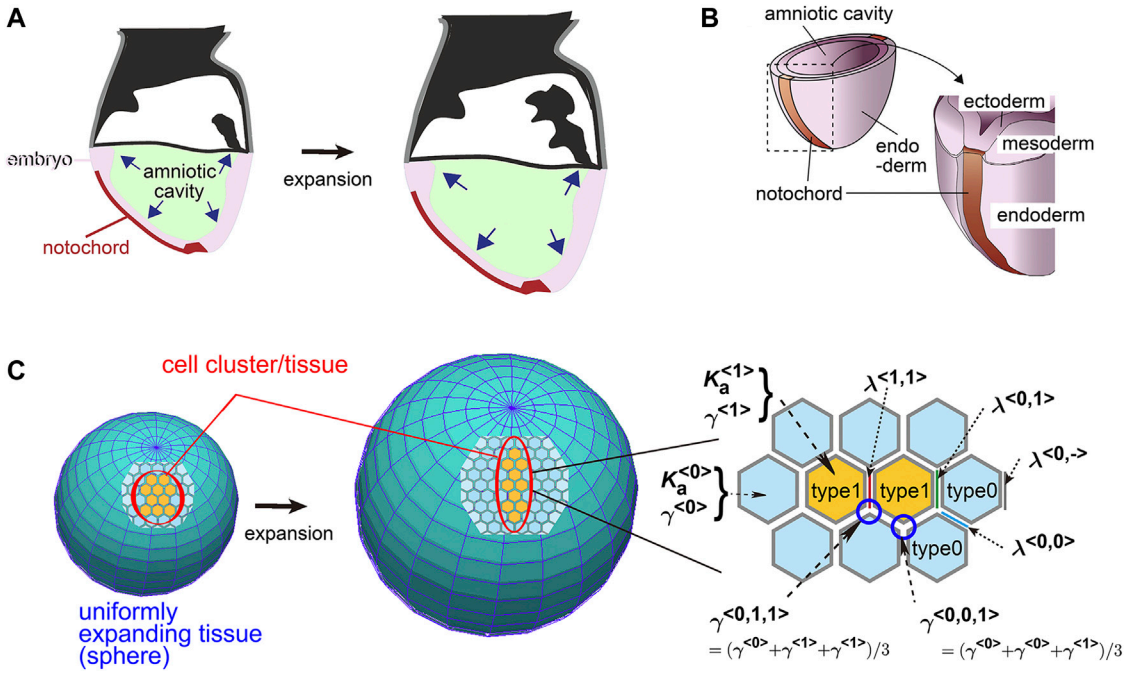


**FIGURE 1 |** Mouse notochord, uniformly expanding field, and vertex model. **(A)** Cross–sectional illustration of a mouse embryo is shown. The amniotic cavity pushes the embryo on the surface of which the notochord is located. **(B)** Three–dimensional illustration of a mouse embryo with the notochord, the cell layers, and the cavity is shown. **(C)** A theoretical framework of a uniformly expanding field and vertex model is described. In the left panel, on a uniformly expanding tissue (two spheres before and after expansion), a cell cluster (orange) with its surrounding cells (light blue) is located. In the right panel, the vertex model is described where the area elasticities, the friction coefficients, and the line tensions are shown. The type 1 cells, orange; the type 0 cells, light blue. The panels A and B are originated from our previous study with permission (Imuta et al., 2014).

theoretical and experimental studies (Duguay et al., 2003; Krieg et al., 2008; Manning et al., 2010).

There are cellular mechanical parameters other than cell–cell adhesion forces and cell–cell interfacial tensions as follows, but the roles of these parameters in tissue organization have not been investigated. Area elasticity of each cell and coefficient of viscous friction forces are generally considered as basic parameters in theoretical studies where the vertex model and the Cellular Potts model are often used as standard multicellular models (Zajac et al., 2003; Fletcher et al., 2014). These parameters are critical for describing cellular and tissue behaviors. Area elasticity denotes resistance against changes in apical cell surface area. For instance, when the apical cell surface is either stretched or compressed by external mechanical forces, the apical surface either increases or decreases, respectively, and the extent of the area change is determined by both the strength of the external forces and the area elasticity. Therefore, area elasticity can be considered as an index of cellular stiffness. Without this parameter, cells cannot maintain their apical surface area, and hence, this parameter is essential for theoretically describing epithelial cells. On the other hand, coefficient of viscous friction forces is derived from viscous friction forces exerted between cells and surrounding medium or tissues (Okuda et al., 2014); increased friction forces restrict both cell movement and deformation. The friction forces between cells and surrounding tissues are affected by cell–cell interactions, cell–extracellular matrix interactions mediated by focal adhesions, etc. (Smutny et al., 2017; Trepat and Sahai, 2018; Münster et al., 2019). A spatial difference in friction forces is involved in the positioning cell populations in fish embryogenesis (Smutny et al., 2017). However, the contributions of these two parameters to pattern formation and morphogenesis remain almost unknown.

In this study, to elucidate the contributions of the above two parameters (i.e., area elasticity and coefficient of friction forces), we focus on a following theoretical model which we previously developed for describing elongation of the mouse notochord. The notochord is located on a surface of the mouse embryo (**Figure 1A**). The embryo around this developmental stage (embryonic days 5.5–8.5) is cylindrical or spherical in shape, at the central region of which there are amniotic cavities. The cavities increase their volumes (**Figure 1A**), and pushes the surrounding cell layers that are composed of ectoderm, resulting in expansion of the ectodermal layer (**Figure 1B**). This expansion is subsequently transduced to the outer cell layers, namely the mesoderm, endoderm, and notochord (**Figure 1B**). The outermost layers in the mouse embryos are composed of the endoderm and notochord during the early stages of notochord formation (**Figure 1B**). Therefore, the endoderm and the notochord would experience friction forces from expanding inner cell layers or the basement membranes between those layers. Previously, we reported that, by experimentally inhibiting the increase in the cavity's volume,

elongation of the notochord was inhibited, indicating that the expansion of the cavities promotes the notochord elongation (Imuta et al., 2014). Subsequently, we reported that in theory, on a uniformly expanding surface (**Figure 1C**, an expanding sphere), a cell cluster is elongated (**Figure 1C, a** cell cluster in orange), whereas friction forces are considered between the cells and the expanding surface (Koyama and Fujimori, 2020). This kind of expanding surface or field is analogous to an expanding rubber balloon in that the rubber membrane expands due to an increase in the volume of enclosed air. Importantly, even if the expansion is uniform or isotropic and a cell cluster has no intrinsic activity for directional migration, the cell cluster is elongated (Koyama and Fujimori, 2020).

In the above theoretical work, we assumed an isolated cell cluster corresponding to the notochord. But in the real tissues, the mouse notochord is surrounded by endodermal cell populations, resulting in a continuous epithelial cell sheet on the growing embryo. In the presence of two different cell populations, we have not theoretically demonstrated whether a cell cluster of interest can elongate, and what kinds of differences in mechanical parameters between these two populations are critical for elongation.

In this study, we assumed a second cell population corresponding to the endoderm (**Figure 1C**, type 0) that surrounds a cell cluster of interest corresponding to the notochord (**Figure 1C**, type 1), and determined theoretically if the cell cluster can be elongated. Our model is based on a vertex model where area elasticity, friction coefficient, and cell–cell interfacial tensions were considered as well as a uniformly expanding field. We found that the cell cluster can elongate, when either the area elasticity or the friction coefficient in the cell cluster is higher than that in the surrounding cell population. Moreover, when comparing theoretical outcomes and experimental observations in the mouse notochord, the elongation of the mouse notochord is consistent with a difference in area elasticity, but not in friction coefficient.

# 2 THEORETICAL MODEL

## 2.1 Vertex Model

We adopted the simplest two-dimensional vertex model in which the mechanical potential energy ($U$) of a system is provided by line tensions of cell–cell interfaces and the area elasticity of each cell. A cell cluster of interest is defined as type 1 cells, and the surrounding cell populations as type 0 (**Figure 1C**). The potential energy is defined as follows (Koyama and Fujimori, 2020):

$$U = \sum_{<k,l>} \lambda L^{<k,l>} + \sum_{n} \frac{1}{2} K_{\mathrm{a}}^{<c>} \left( \frac{a_n}{a_{\mathrm{O}}} - 1 \right)^2 a_{\mathrm{O}} \tag{1}$$

where $\lambda$ and $L^{<k,l>}$ are the line tension and the length of the cell–cell interfaces between adjacent vertices $k$ and $l$ (**Figure 1C**), respectively. $\lambda$ can have different values according to two cells sharing the cell–cell interface $<k, l>$. For instance, $\lambda = \lambda^{<0,1>}$ for the case that the two cells are type 0 and type 1, and $\lambda = \lambda^{<1,1>}$ for the case that the two cells are both type 1s (**Figure 1C**). $a_n$ is the area of the $n$th cell. $a_{\mathrm{O}}$ and $K_{\mathrm{a}}^{<c>}$ are a preferred area of the cell and the coefficient of area elasticity of type $<c>$ cells, respectively (**Figure 1C**; $K_{\mathrm{a}}^{<0>}$ and $K_{\mathrm{a}}^{<1>}$). The preferred area is an apical surface area of a cell which is released from external forces; such cell is under a mechanically relaxed state. The coefficient of area elasticity functions to resist against changes in apical surface area from external forces. Therefore, this elasticity contributes to cellular stiffness. If the value of $K_{\mathrm{a}}^{<c>}$ is large, the cell tends to retain its apical surface area around $a_{\mathrm{O}}$. Because cellular stiffnesses are different among cell types *in vivo* (Zhou et al., 2009; Swift et al., 2013), $K_{\mathrm{a}}^{<c>}$ may be a cell type–specific property.

The force ($F_h$) exerted on an $h$th vertex is calculated as follows:

$$F_h = -\nabla U \tag{2}$$

where $\nabla$ is the nabla vector differential operator at each vertex. The motion of each vertex in polygonal cells is damped by friction forces and is described as follows:

$$V_h = F_h / \gamma_{\mathrm{V}} \tag{3}$$

where $V_h$ is the velocity of the $h$th vertex, and $\gamma_{\mathrm{V}}$ is the coefficient of the friction of a vertex. $\gamma_{\mathrm{V}}$ can have different values according to three cells sharing the vertex. For instance, $\gamma_{\mathrm{V}} = \gamma^{<0,0,1>}$ for the case that the three cells are type 0, type 0, and type 1, and $\gamma_{\mathrm{V}} = \gamma^{<0,1,1>}$ for the case that the three cells are type 0, type 1, and type 1 (**Figure 1C**). The friction coefficients for each cell type are defined as $\gamma^{<0>}$ and $\gamma^{<1>}$ for type 0 and type 1 cells, respectively. The coefficient for each vertex was defined as the mean of the coefficients for the three cells: e.g. $\gamma^{<0,0,1>} = (\gamma^{<0>} + \gamma^{<0>} + \gamma^{<1>})/3$ (**Figure 1C**). Okuda et al. (2014) also assumed differential coefficients of friction. The friction is exerted between the cells and their surrounding medium or tissues. In this study, we assumed that the friction from the expanding field as defined below is dominant to that from the medium.

## 2.2 A Uniformly Expanding Field

A uniformly expanding field is analogous to the surface of an expanding rubber balloon; the area of the surface increases uniformly regardless of location on the surface. In the case of mouse early embryos around embryonic day 7.5, the volume of the inner cavity (e.g., the amniotic cavity) is increased, and thus the surface of the embryo is expanding. Cell proliferation within the surface tissue also causes it to expand (Koyama and Fujimori, 2020). We adopted a simplifying assumption that a field expands in two dimensions. In this study, we placed a cell cluster on the expanding field with a surrounding cell population.

We previously defined the modeling of a uniformly expanding field (Koyama and Fujimori, 2020). Briefly, when we arbitrarily defined a point on the two-dimensional field as an origin, other points are assumed to move away from the origin with speeds proportional to the distances between the points and the origin: $V_{\mathrm{e}} \propto D_{\mathrm{e}}$, where $D_{\mathrm{e}}$ is the distance between the point and the origin, and $V_{\mathrm{e}}$ is the velocity. An object placed on this field also moves by $V_{\mathrm{e}}$ if there are no other forces. Consequently, the equation that describes the motion of each vertex is modified as follows:

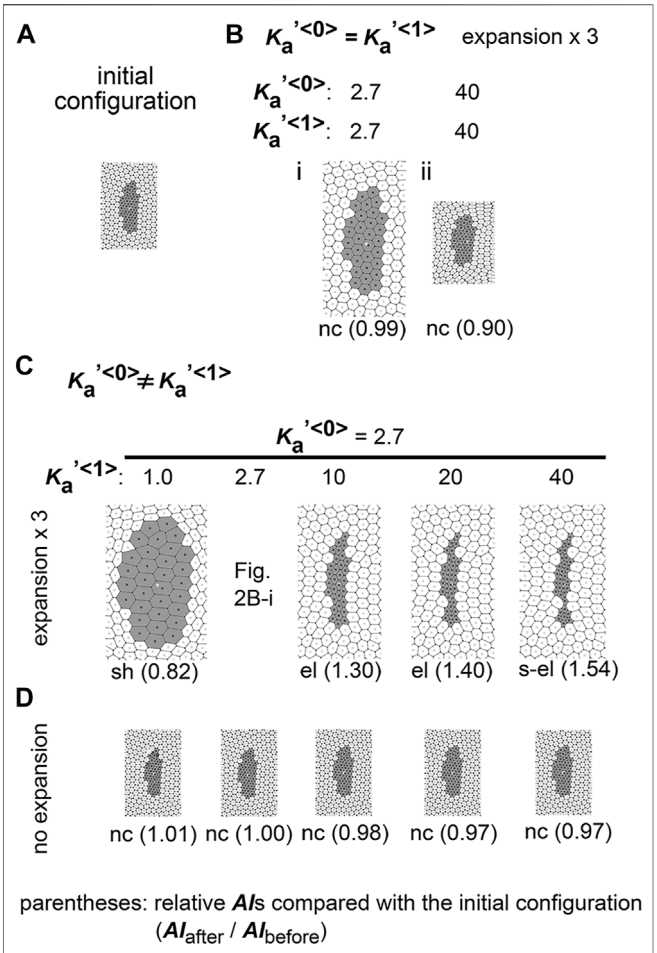


**FIGURE 2 |** Difference in area elasticity causes elongation of cell cluster on expanding field. **(A)** The initial configuration of simulation is shown. The gray and white cells are type 1 and type 0, respectively. The whole view of the configuration is provided in **Supplementary Figure S1**. **(B)** Simulation outcomes under the same value between $K_a'^{<0>}$ and $K_a'^{<1>}$ are shown. $K_a'^{<0>} = K_a'^{<1>} = 2.7$ in the left panel and $K_a'^{<0>} = K_a'^{<1>} = 40$ in the right panel. The fields were expanded by three times in area (expansion ×3). The scales of these images are the same each other. The relative *AI*s are shown with the morphological categories ["no change (nc)"]. **(C)** Simulation outcomes under different values between $K_a'^{<0>}$ and $K_a'^{<1>}$ are shown; $K_a'^{<0>} \neq K_a'^{<1>}$. $K_a'^{<0>}$ was fixed at 2.7. The fields were expanded by three times in area. The scales of these images are the same as those in B. The relative *AI*s are shown with the morphological categories ["elongation (el)", "strong elongation (s-el)", or "shrinkage (sh)"]. **(D)** Simulation outcomes under the same values of $K_a$ s as C are shown except that the fields were not expanded (no expansion). The scales of these images are the same as those in C. The relative *AI*s are shown with the morphological categories. Simulation results obtained using different area elasticity values are provided in **Supplementary Figure S2**.

$$V_h = F_h/\gamma_V + V_e \quad (4)$$

A similar formulation was previously proposed (Okuda et al., 2014). We can interpret this equation as follows: $V_h = F_h/\gamma_V + F_{e|h}/\gamma_V$, where $F_{e|h}$ is an apparent friction force provided by the expanding field. Under this assumption, we verified computationally and analytically that this expanding field does not yield any biased forces toward the cell cluster. Additionally, the expansion rate of the field was assumed to be temporally constant: $V_e = \varepsilon D_e$, where $\varepsilon$ is the expansion rate and is spatiotemporally constant. The parameters in our model were normalized by $\lambda^{<0,0>}$, $\sqrt{a_o}$, and $\gamma^{<0>}$, and their dimensionless parameters are represented with a prime, e.g., $K_a'^{<c>} = K_a^{<c>}\sqrt{a_o}/\lambda^{<0,0>}$, $\varepsilon' = \varepsilon\gamma^{<0>}\sqrt{a_o}/\lambda^{<0,0>}$.

# 3 RESULTS

## 3.1 Differential Area Elasticity Contributes to Cell Cluster Elongation

We previously reported that a cell cluster (i.e., type 1 cells in this study) elongates on a uniformly expanding field in the absence of surrounding cell populations (type 0 cells in this study). In real tissues, an epithelial cell cluster is not usually isolated but is instead surrounded by other cell populations. We theoretically searched for conditions under which the cell cluster can elongate even in the presence of surrounding cell populations.

First, we performed simulations using conditions under which type 1 and type 0 cells have the same parameter values, namely: $K_a^{<0>} = K_a^{<1>}$, $\gamma^{<0>} = \gamma^{<1>}$, and $\lambda^{<0,0>} = \lambda^{<1,1>} = \lambda^{<0,1>}$. An initial configuration for the cells is shown in **Figure 2A**. We set a slightly elongated initial configuration because we previously showed that this anisotropic configuration is a prerequisite for elongation (Koyama and Fujimori, 2020). In other words, we examined whether this initially elongated state will be enhanced on the expanding field and result in more elongated states. The field was expanded under a constant expansion rate ε, and when the field size increased by three times (**Figure 2B**, expansion × 3), we observed the shapes of the cell clusters. Note that, due to the continuously expanding field, the cell clusters are not expected to reach steady states as we previously reported (i.e., non-equilibrium system) (Koyama and Fujimori, 2020). The cell cluster was enlarged due to friction forces from the expanding field (**Figure 2B-i** *vs.* **Figure 2A**). An index of asymmetry/elongation (*AI*) of a cell cluster was defined as described in the Materials and Methods section. If a cell cluster (type 1) is circular, *AI* becomes 1.0. If a cell cluster is elongated, *AI* becomes larger than 1.0. To evaluate the change in *AI*s before and after the simulation, we calculated the *AI* relative to that of the initial configuration (i.e., relative $AI = AI_{after}/AI_{before}$). The relative *AI* value was 0.99 (**Figure 2B-i**), indicating that the elongation of the cell cluster was not enhanced. When the values of $K_a$ s were set to be different from **Figure 2B-i** under a constraint of $K_a^{<0>} = K_a^{<1>}$, the relative *AI* value was also ~1.0 (**Figure 2B-ii**), indicating that elongation of cell clusters is insensitive to the value of $K_a$.

Next, we assigned different area elasticity values between type 1 and type 0 cells: $K_a^{<0>} \neq K_a^{<1>}$ whereas $\gamma^{<0>} = \gamma^{<1>}$ and $\lambda^{<0,0>} = \lambda^{<1,1>} = \lambda^{<0,1>}$. If the area elasticity in type 1 cells was larger than that in type 0 cells (i.e., $K_a^{<1>} > K_a^{<0>}$), elongation of the cell cluster was enhanced and the relative *AI*s were higher (**Figure 2C**, $K_a'^{<1>} \geq 10$). In addition, if the area elasticity in the type 1 was smaller, the relative *AI* value of the cell cluster was

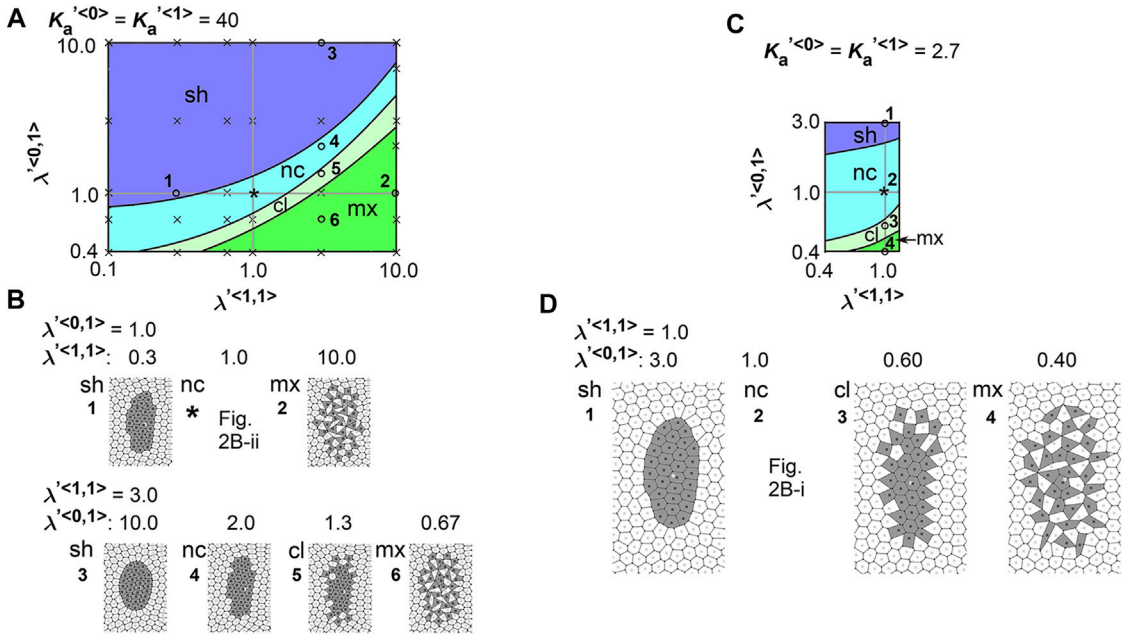


**FIGURE 3 |** Difference in cell–cell adhesion does not cause elongation of cell cluster on expanding field. Simulations were performed using various line tension values, whereas the area elasticity and coefficient of friction were assigned the same values between the two cell types: $\lambda^{<0,0>} \neq \lambda^{<1,1>} \neq \lambda^{<0,1>}$, whereas $K_a^{<0>} = K_a^{<1>}$ and $\gamma^{<0>} = \gamma^{<1>}$. The fields were expanded by three times in area. Phase diagrams and examples of simulation outcomes were shown under $K_a'^{<0>} = K_a'^{<1>} = 40$ **(A,B)** or under $K_a'^{<0>} = K_a'^{<1>} = 2.7$ **(C,D)**. The parameter values used for each condition in B and D are plotted on the diagrams (**A,C**), with the numbers corresponding to each condition (#1, #2, etc.). Simulation outcomes at the conditions with asterisks on the diagrams **(A,C)**, where $\lambda^{<0,0>} = \lambda^{<1,1>} = \lambda^{<0,1>}$, were previously shown in **Figure 2B-ii** and **Figure 2B-i**, respectively. Each phase in the diagrams is colored as follow: "sh", blue; "nc", light blue; "cl", light green; "mx", green. Black crosses in A, all simulation conditions tested.

decreased (**Figure 2C**, $K_a'^{<1>} = 1.0$). To examine whether the elongation depends on field expansion, we performed simulations without field expansion (i.e. expansion ×1) where the cells move to find a steady state under the given values of $K_a$ s. In **Figure 2D** where all simulations were performed under the same values of $K_a$ s as **Figure 2C**, the cell clusters were not elongated. In summary, under field expansion, if $K_a^{<0>} = K_a^{<1>}$, the relative *AI* is unchanged, and if $K_a^{<0>} \neq K_a^{<1>}$, the relative *AI* positively correlates to $K_a^{<1>}/K_a^{<0>}$. These results indicate that, in theory, different area elasticity values contribute to tissue elongation.

We classified the morphological patterns of cell clusters by the value of the relative *AI* as follows: strong elongation (s-el; $AI_{after}/AI_{before} > 1.5$), elongation (el; $AI_{after}/AI_{before} = 1.1–1.5$), no change (nc; $AI_{after}/AI_{before} = 0.9–1.1$), and shrinkage (sh; $AI_{after}/AI_{before} < 0.9$). In **Figures 2B–D**, these categories are written for each simulation outcome.

## 3.2 Differential Line Tension Between Cell–Cell Interfaces do Not Cause Cell Cluster Elongation

We tested whether the differential adhesion hypothesis can reproduce the elongation of a cell cluster: $\lambda^{<0,0>} \neq \lambda^{<1,1>} \neq \lambda^{<0,1>}$, whereas $K_a^{<0>} = K_a^{<1>}$ and $\gamma^{<0>} = \gamma^{<1>}$. According to this hypothesis, line tensions are derived from cortical tensions and cell–cell adhesion (Steinberg, 1963; Harris, 1976): cortical tension decreases the lengths of cell–cell interfaces, and adhesion increases the lengths, and thus, the effects of these two factors on the line tensions are opposite (i.e., [line tension] = [cortical tension]—[cell–cell adhesion]) (Maître et al., 2012 and references therein). For instance, smaller values of the line tensions can result from stronger cell–cell adhesion.

To comprehensively examine the effect of the line tensions, we performed multiple simulations under various values of the line tensions, and subsequently generated a phase diagram as follows. The parameter ranges tested in the simulations correspond to the vertical and horizontal axes in the phase diagram (**Figure 3A**, $\lambda^{<0,1>}$ and $\lambda^{<1,1>}$). For instance, a simulation condition where $\lambda'^{<1,1>} = \lambda'^{<0,1>} = 1.0 (= \lambda'^{<0,0>})$ is marked by an asterisk, whose simulation outcome corresponds to **Figure 2B-ii**. From this condition, if the value of $\lambda^{<1,1>}$ was solely changed (i.e., move leftward along the x–axis), we reached a simulation condition #1, whose simulation outcome is shown in **Figure 3B** (#1) where the pattern was classified as shrinkage ("sh"). On the other hand, under a larger value of $\lambda^{<1,1>}$ (#2), a pattern with intermixing ("mx") of the two cell populations was observed (**Figure 3B**, #2). Similarly, if the value of $\lambda^{<0,1>}$ was solely changed (i.e. move along the *y*–axis), various simulation outcomes were observed (**Figures 3A, B**, #3-#6). All simulation conditions are plotted on the diagram as black crosses (30–40 data points, see Materials and Methods). Then, all simulation outcomes were classified by the morphological categories defined in **Figure 2**. During

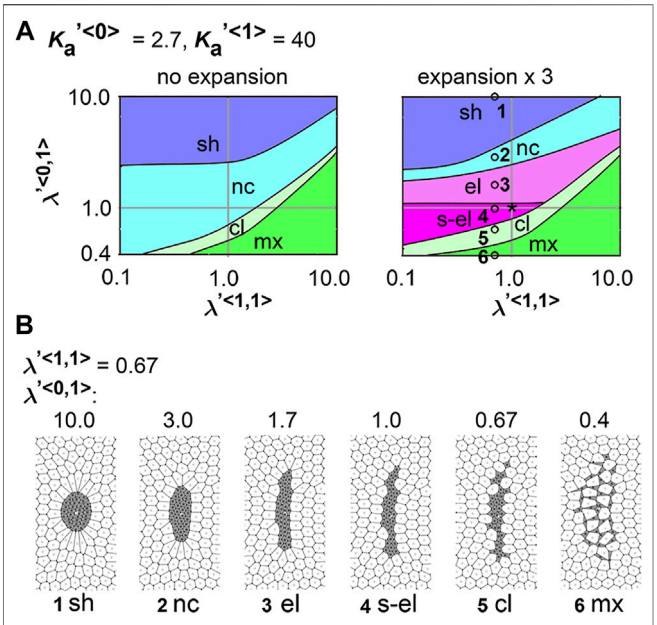


**FIGURE 4 |** Difference in cell–cell adhesion contributes to cell cluster elongation with differential area elasticity on expanding field. Simulations were performed under conditions with various values for line tension and area elasticity, whereas the coefficient of friction was assigned the same value for both cell types: $\lambda^{<0,0>} \neq \lambda^{<1,1>} \neq \lambda^{<0,1>}$ and $K_a^{<0>} \neq K_a^{<1>}$, whereas $\gamma^{<0>} = \gamma^{<1>}$. Phase diagrams in the absence and presence of the uniformly expanding field are shown under $K_a'^{<0>} = 2.7$ and $K_a'^{<1>} = 40$ [left and right panels in **(A)**, respectively]. In the panel on the right, the fields were expanded by three times in area. Examples of simulation outcomes are shown in **(B)**, where the parameter values used for each condition in B are plotted on the diagram [**(A)**, right panel], with the numbers corresponding to each condition (#1, #2, etc.). An asterisk on the diagram [**(A)**, right panel], where $\lambda^{<0,0>} = \lambda^{<1,1>} = \lambda^{<0,1>}$, corresponds to the condition in **Figure 2C** ($K_a'^{<1>} = 40$). Each phase in the diagrams is colored as follow: "s-el", magenta; "el", pink; "sh", blue; "nc", light blue; "cl", light green; "mx", green. Other simulation outcomes obtained with different values for the area elasticities are shown in **Supplementary Figure S3**. Simulation outcomes from a different initial configuration are shown in **Supplementary Figure S4**

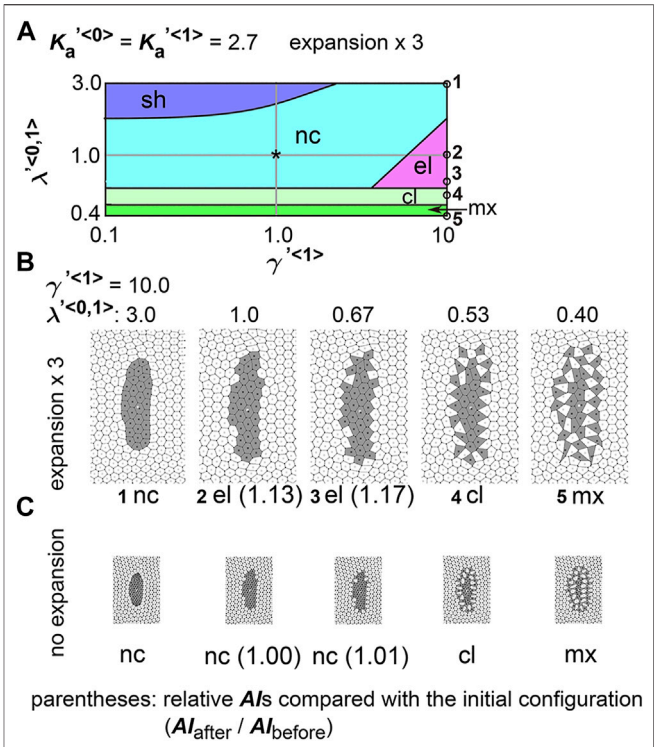


**FIGURE 5 |** Differences in coefficient of friction cause cell cluster elongation on an expanding field. Simulations were performed under conditions with various values of the coefficient of the friction, whereas values for the area elasticity were assigned to be equal for both two cell types: $\gamma^{<0>} \neq \gamma^{<1>}$, whereas $K_a^{<0>} = K_a^{<1>}$. The line tensions in the type 0 and type 1 cells were made equal in value, whereas the line tension between the type 0 and type 1 cells was different: $\lambda^{<0,0>} = \lambda^{<1,1>} \neq \lambda^{<0,1>}$. The fields were expanded by three times in area **(A,B)** or not expanded **(C)**. A phase diagram and examples of simulation outcomes were shown under $K_a'^{<0>} = K_a'^{<1>} = 2.7$. The parameter values used for each condition in B are plotted on the diagrams **(A)**, with numbers corresponding to each condition. A simulation outcome at the condition with an asterisk on the diagram **(A)** was previously shown in **Figure 2B-i**. Each phase in the diagrams is colored as follow: "el", pink; "sh", blue; "nc", light blue; "cl", light green; "mx", green. The parameter values except for the field expansion were set to be the same between B and C. The scales of the images in **(B,C)** are the same each other. Other simulation outcomes obtained with different area elasticity values are shown in **Supplementary Figure S5**.

classification, when more than two distinct cell clusters formed, the pattern was classified as either multi-cluster (cl; average cell number per cluster >1.5) or intermixed (mx; average cell number per cluster <1.5). Then, the phase diagram was divided into these morphological categories: e.g. a blue region for "sh", a light blue region for "nc". We could not find conditions under which cell cluster was elongated in **Figure 3A**.

We also performed a similar analysis under a different value of $K_a^{<c>}$ s and generated a phase diagram with some examples of the simulation outocomes (**Figures 3C, D**). A condition marked by an asterisk corresponds to **Figure 2B-i** where $\lambda'^{<0,0>} = \lambda'^{<1,1>} = \lambda'^{<0,1>}$ (= 1.0). The number of the simulation conditions used for generating the phase diagram is 30–40, but the data points are not depicted on the diagram. Similar to **Figure 3A**, we could not find conditions under which the cell cluster was elongated. Thus, the differential line tensions between cell–cell interfaces alone do not cause tissue elongation.

Here we interpret the above results. In the vertex models, if cell–cell adhesion is increased, the line tensions are decreased. In the phase diagrams, when $\lambda^{<1,1>}$ has a larger value (e.g., $\lambda'^{<1,1>} = 10.0$, and see along the x–axis), cell–cell adhesion between the type 1 and type 1 cells is decreased, and thus, the type 1 cells preferably adheres to the type 0 cells, resulting in intermixing patterns ("mx") or generation of multiple cell clusters ("cl"). For $\lambda^{<0,1>}$, decreased values of this parameter (e.g. $\lambda'^{<0,1>} = 0.4$, and see along the *y*–axis) mean increased adhesion between type 0 and type 1 cells, resulting in "mx" or "cl", whereas increased values (e.g., $\lambda'^{<0,1>} = 10.0$) prevent the cells from forming "mx" and "cl". Moreover, such increased values in $\lambda^{<0,1>}$ decrease in the line lengths of the cell–cell interfaces between the type 0 and type 1 cells, that leads to round-up of the type 1 cell cluster emerged as the "sh" pattern.

## 3.3 Optimal Line Tension Between Cell–Cell Interfaces are Necessary in Combination With Area Elasticity to Induce Cell Cluster Elongation

We analyzed the combinatorial effect of line tensions and area elasticity: $\lambda^{<0,0>} \neq \lambda^{<1,1>} \neq \lambda^{<0,1>}$ and $K_a^{<1>} > K_a^{<0>}$, whereas $\gamma^{<0>} = \gamma^{<1>}$. Similar to **Figure 3**, **Figure 4** shows the phase diagrams with the simulation outcomes with different line tension values for $\lambda^{<1,1>}$ and $\lambda^{<0,1>}$. In the left panel, the field was not expanded (i.e., expansion × 1), and thus, the cells move to find a steady state under the given values of $\lambda^{<1,1>}$ and $\lambda^{<0,1>}$. In the right panel, the field was expanded (expansion ×3). The same condition as that in **Figure 2C** ($K_a^{'<1>} = 40$) was plotted as an asterisk in **Figure 3A** (right panel, $\lambda^{'<1,1>} = \lambda^{'<0,1>} = 1.0$), where the simulation outcome was classified as "strong elongation (s-el)". In the phase diagrams, the regions of simulation conditions resulting in strong elongation ("s-el") or elongation ("el") are colored by magenta or pink. These regions were exclusively detected in the right panel but not the left panel, indicating that the elongation depended on field expansion. Moreover, in the right panel, if the value of $\lambda^{<0,1>}$ was solely changed (i.e., move along the *y*–axis), the cell cluster either showed no elongation ("nc" and "sh"), formation of multiple clusters ("cl"), or intermixing ("mx") [**Figure 4A**, right panel, and 4B, #1, #2, #5, and #6, *vs.* #3 ("el") and #4 ("s-el")]. These results indicate that, for the elongation induced by the differential area elasticity, optimal line tensions were required. Other outcomes under different conditions are shown in SI (**Supplementary Figures S3, S4**).

## 3.4 Differential Friction Coefficient Contributes to Cell Cluster Elongation

We determined whether the differential coefficient of the friction forces causes a cell cluster to elongate: $\gamma^{<0>} \neq \gamma^{<1>}$, whereas $\lambda^{<0,0>} = \lambda^{<1,1>} = \lambda^{<0,1>}$ and $K_a^{<0>} = K_a^{<1>}$. Similar to **Figures 3**, **4**, we generated a phase diagram except that the x–axis is $\gamma^{'<1>}$. The same condition as that in **Figure 2B-i** was plotted as an asterisk in **Figure 5A** where $\lambda^{'<0,1>} = 1.0 (= \lambda^{'<1,1>} = \lambda^{'<0,0>})$ and $\gamma^{'<1>} = 1.0 (= \gamma^{'<0>})$; the cell cluster was not elongated. From this condition, if the value of $\gamma^{'<1>}$ was solely increased (i.e., move rightward along the x–axis), we reached a simulation condition #2, whose simulation outcome is shown in **Figure 5B** (#2) where the pattern was classified as elongation ["el (1.13)"]. Moreover, **Figure 5C** showed simulation outcomes in the absence of field expansion, and the cell cluster was not elongated under the same values of $\gamma$ s as **Figure 5B** (#2). These results indicate that different values for the coefficient of friction contribute to tissue elongation, and this elongation depends on field expansion.

Next, we analyzed the combinatorial effect of line tensions and the coefficient of friction. In **Figure 5A**, under the same value of the coefficient of friction ($\gamma^{'<1>} = 10$), changes in the value of the line tension between the type 1 and type 0 cells (i.e., $\lambda^{<0,1>}$) resulted in patterns other than elongation ("el"), such as no elongation ("nc"), multiple clusters ("cl"), and intermixing ("mx") (**Figures 5A, B**, #1 ["nc"], #4 ["cl"], and #5 ["mx"] *vs.* #2 and #3 ["el"]). Thus, optimal line tensions were required for the elongation induced by varying coefficients of friction force. Moreover, in the absence of field expansion, elongation of the cell clusters was not induced, whereas the other patterns were observed (**Figure 5C**). Other outcomes under different conditions are shown in SI (**Supplementary Figure S5**).

## 3.5 Cell Behavior in Mouse Notochord Elongation

In real tissues, elongation of various tissues is usually explained by directionally active cell movement that results in convergent extension (Keller et al., 2000; Honda et al., 2008) where expanding fields are not considered. By contrast, we have shown experimentally that elongation of the mouse notochord depends on an increase in volume of the amniotic cavity (Imuta et al., 2014). From our theoretical analyses in **Figures 2**, **5**, we raised two hypotheses for field expansion–dependent tissue elongation: area elasticity–based one, and friction coefficient–based one. We determined whether the elongation of the mouse notochord is consistent with differences in area elasticity or differences in friction coefficient. According to our previous data in **Figure 2C** and **Figure 5B**-#2, the cell area in the cell cluster of interest appears to either be almost unchanged according to the area elasticity–based hypothesis or increased according to the friction–based hypothesis: the mean cell area is 1.4-fold of that in initial configuration under the area elasticity–based hypothesis, and is 5.2-fold under the friction–based hypothesis. Conversely, the cell area in the surrounding cell populations seems to increase according to both hypotheses: the mean cell area is 4.3-fold of that in initial configuration under the area elasticity–based hypothesis, and is 4.6-fold under the friction–based hypothesis.

We went on to measure the dynamics of the cell area both *in vivo* and in silico. *In vivo* cell areas were estimated from the densities of the cells in the notochord or the endoderm (**Figure 6A** and Materials and Methods). The apical cell area within the notochord was temporally unchanged, whereas that in the endoderm increased (**Figure 6B**). In the case of simulation data, we also estimated cell areas from the densities of the cells (**Figure 6C**). Under the area elasticity–based hypothesis, the cell area in the type 1 cell cluster was temporally unchanged, whereas that in the surrounding type 0 cell populations was increased (**Figure 6D**). Under the friction coefficient–based hypothesis, the cell areas in both the cell cluster and the surrounding cell populations were temporally increased (**Figure 6E**, a left panel, $K_a^{'<0>} = K_a^{'<1>} = 2.7$). In addition, if the area elasticities in both cell types were made larger under different friction coefficients, the increases in the cell areas were restricted for both cell types but the dynamic was equivalent between the two cell types (**Figure 6E**, a right panel, $K_a^{'<0>} = K_a^{'<1>} = 40$). Thus, the dynamics of the cell areas according to the area elasticity–based hypothesis are consistent with the *in vivo* dynamics but not for the friction–based hypothesis.

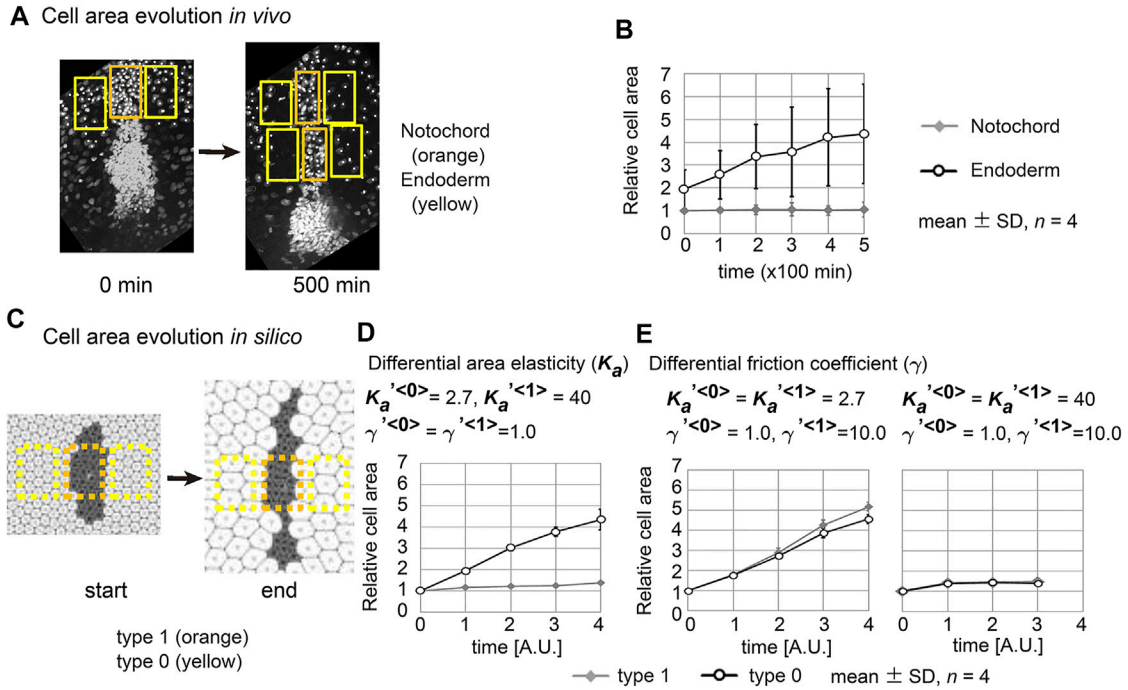


**FIGURE 6 |** Cell behaviors in mouse notochord and their comparison with two theories. **(A)** Confocal microscopic images at two time points in the mouse notochord and the surrounding endoderm are shown. Nuclei of the cells were visualized by histone 2B fused to EGFP. The orange and yellow rectangles are regions used for measuring cell areas within the notochord and endoderm, respectively. These microscopic images were obtained from our previous work (Imuta et al., 2014). **(B)** The cell areas in the notochord and endoderm are shown with their temporal evolutions. The mean cell area in the notochord at 0 min was defined as 1.0. Four embryos were analyzed ($n$ = 4). **(C)** Cell areas in simulations were measured. Simulation outcomes are indicated with orange and yellow rectangles that were used to measure cell areas in a similar manner to B. **(D)** Cell areas obtained with differential area elasticities, which were derived from the simulation outcomes in **Figure 2C** ($K_a^{'<1>}$ = 40), are shown. Four different initial configurations of the simulations ($n$ = 4) were applied. Parameter values for area elasticities and coefficients of friction are also indicated. **(E)** Cell areas obtained with differential friction coefficients, which were derived from the simulation outcomes in **Figure 5**; **Supplementary Figure S5**, are shown in a similar manner to **(D)**. The values from type 1 and type 0 cells are nearly identical in the right panel.

## 3.6 Differential Preferred Cell Area Contributes to Tissue Elongation in Field Expansion–independent Manner

Differentiation of cells may contribute to the differences in area elasticity as examined in the previous section. On the other hand, cell differentiation may directly change the preferred cell area $a_O$ defined in **Eq. 1**. As shown above, the cell areas were specifically increased in the surrounding cell populations (i.e., endodermal cell/type 0 cells). Such specific increase in the cell areas would be reproduced by increases in the preferred cell area. As an alternative to the differential area elasticity–based hypothesis, we investigated the influence of differential preferred cell area on not only the specific increase in the cell areas but also tissue elongation.

We assumed specific increases in the preferred cell areas in the type 0 cells where this parameter was set to temporally increase during simulations. In **Figure 7**, $a_O^{'<1>}$ and $a_O^{'<1>}$ denote $a_O^{'}$ in the type 1 and type 0 cells, respectively. The value of $a_O^{'<1>}$ was fixed at 1.0. In addition, the parameter normalization described in *A Uniformly Expanding Field* was performed using $\sqrt{a_o^{<1>}}$. The value of $a_O^{'<0>}$ was temporally changed from 1.0 at the start of simulations to 1.0, 2.0, or 4.0 at the end of simulations (**Figure 7**, start and end). The cell areas in the type 0 cells were specifically increased in the right panels (end = 4.0), regardless to the field expansion (expansion = "no" and "×3"). Furthermore, the type 1 cell cluster was elongated under the field expansion (expansion = "×3"). However, elongation of the type 1 cell cluster was also observed even without the field expansion (expansion = "no"). These results indicate that differential preferred cell areas cause tissue elongation, but the elongation does not depend on field expansion. Because the elongation of the mouse notochord depends on the field expansion (Imuta et al., 2014), this differential preferred cell area hypothesis is not consistent with the *in vivo* situations.

## 3.7 Experimental Measurement of Cellular Stiffness in Mouse Notochord Elongation

To further validate the area elasticity–based hypothesis in the mouse notochord, we measured cellular stiffness. To the best of our knowledge, no method for measuring area elasticity directly has been established to date. We used atomic force microscopy (AFM) that has been used to measure cellular stiffness (Young's modulus) (Addae-Mensah and Wikswo, 2008; Barriga et al., 2018; Kinoshita et al., 2020). The difference between area elasticity and

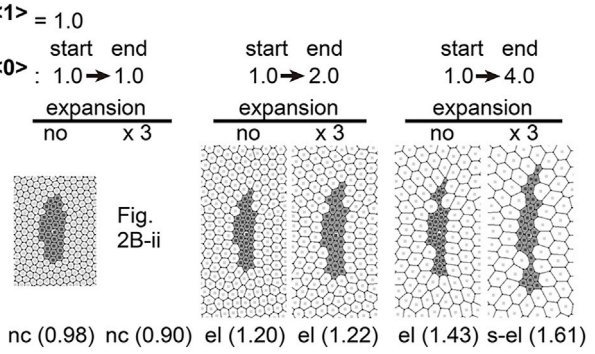


**FIGURE 7 |** Differences in preferred cell areas cause cell cluster elongation in a manner independent to field expansion. Simulations were performed under conditions with temporal changes in the preferred cell areas in the type 0 cells, whereas the values of other parameters were assigned to be equal for both two cell types: $a_O'^{<0>}$ = temporal increase, whereas $a_O'^{<1>} = const.$ (= 1.0), $\lambda'^{<0,0>} = \lambda'^{<1,1>} = \lambda'^{<0,1>}$ (= 1.0), $K_a'^{<0>} = K_a'^{<1>}$ (= 40), and $\gamma'^{<0>} = \gamma'^{<1>}$ (= 1.0). The values of $a_O'^{<0>}$ at the start and end of the simulations are shown (e.g., start [1.0] → end [4.0]). Two scenarios of the temporal changes were applied (end [2.0] and [4.0]), in addition to a scenario of temporally no change (end [1.0]). In the two scenarios, the values are linearly increased during the simulations [i.e., $a_O'^{<0>}(t) = ct + a_O'^{<1>}(0)$, where $t$ is time, and $c$ is const.]. The categories of the simulation outcomes are described with the relative *AI* values (parentheses).

the Young's modulus is discussed in the Discussion section. A mouse embryo is shown in **Figure 8A** where the nuclei in the notochord cells were labeled by green fluorescent proteins (GFP) and all the nuclei including the endodermal cells were labeled by other fluorescent proteins (mCherry) (**Figure 8A**). A mouse embryo was placed on an agarose gel (**Figure 8B**, light orange), and subsequently, a part of the embryo was overlaid by an additional agarose gel (**Figure 8B**, dark orange). The Young's modulus of the regions of the notochord or the surrounding endoderm was measured through indentation of the cantilever with a bead of diameter = 20 μm attached and subsequent acquisitions of force–indentation curves (**Figure 8C**; **Supplementary Figure S6**). A spatial map of the Young's modulus around the notochord and endoderm was obtained with interval = 20 μm (**Figure 8D**, "Measured regions"), where the colors for each data point reflect the values of the Young's modulus as defined by the color bar. In this embryonic stage, the widths of the notochord were 40–60 μm (**Figure 8A**) as described in Materials and Methods *Atomic Force Microscopy*. Therefore, the three columns adjacent to the midline were expected to be on the notochord (**Figure 8D**, NC) and the outer two columns for each side were on the endoderm (**Figure 8D**, Endo). Data points that did not yield a clear force–indentation curve were omitted from the data analysis (**Figure 8D**, white crosses). The mean values of the Young's moduli in four embryos were calculated (Materials and Method *Atomic Force Microscopy*), and the values are 0.51 [kPa] in the notochords and 0.40 [kPa] in the endoderms. **Figure 8E** is the comparison of the Young's moduli between the notochord and the endoderm, where the Young's moduli were normalized by the mean value in the endoderms. The Young's modulus of the notochord regions was larger than that of the endodermal regions. These results suggest that the Young's modulus of the notochord is higher than that of the endoderm. In addition, stiffnesses of various cells and tissues are 0.01–10 [kPa], and our measurement results are within this range (Davidson et al., 1999; Zhou et al., 2009).

## 4 DISCUSSION

In this study, we theoretically investigated the potential roles of area elasticities and coefficients of friction in tissue elongation on a uniformly expanding field. In the case that the area elasticities or coefficients of friction differed between the cell cluster and the surrounding cell populations, the cell cluster is elongated as summarized in **Table 1**. By contrast, differences in cell–cell adhesion based on the differential adhesion hypothesis cannot cause the cell cluster to elongate. On the other hand, the differences in the preferred cell areas lead to elongation even without field expansion. The two hypotheses based on the area elasticity and the friction coefficient lead to different cellular behaviors; the apical cell areas in the surrounding cell populations are increased in both hypotheses, whereas the areas in the cell cluster of interest are either almost unchanged according to the former hypothesis or increased according to the latter (**Table 1**). Therefore, the elongation of the mouse notochord may be explained by the area elasticity–based hypothesis, though we do not exclude the possibility that these hypotheses simultaneously contribute to the elongation.

Measurement of Young's modulus through AFM suggests that the notochord is stiffer than the endoderm. The Young's modulus of the notochord and endoderm differed by ~1.4 times, whereas the difference in the area elasticity in our simulations was up to 10 times. The Young's modulus differs from the area elasticity, although both are measures of cellular stiffness. During the AFM–based measurement, the direction of indentation is parallel to the apico–basal axis. On the other hand, the area elasticity is related to the change in apical cell area whose direction is perpendicular to the apico–basal axis. Nevertheless, the change in apical cell area and in the apico–basal height should be related under conserved cell volume; the increase of apical cell area should lead to the decrease in the apico–basal height, and vice versa. Although we do not have quantitative relationship between the Young's modulus and the area elasticity, we suppose that the Young's modulus reflects, at least partially, the area elasticity. In general, cell stiffness can differ by over an order of magnitude (Zhou et al., 2009; Swift et al., 2013). The notochord in chordates is believed to provide stiffness of their bodies (Hejnol and Lowe, 2014; Corallo et al., 2015), and the notochord in *Xenopus laevis* was experimentally shown to be several to several tens times stiffer than the endoderm (Zhou et al., 2009). In contrast to the Young's modulus and the area elasticity, both of which reflect mechanical properties of cells

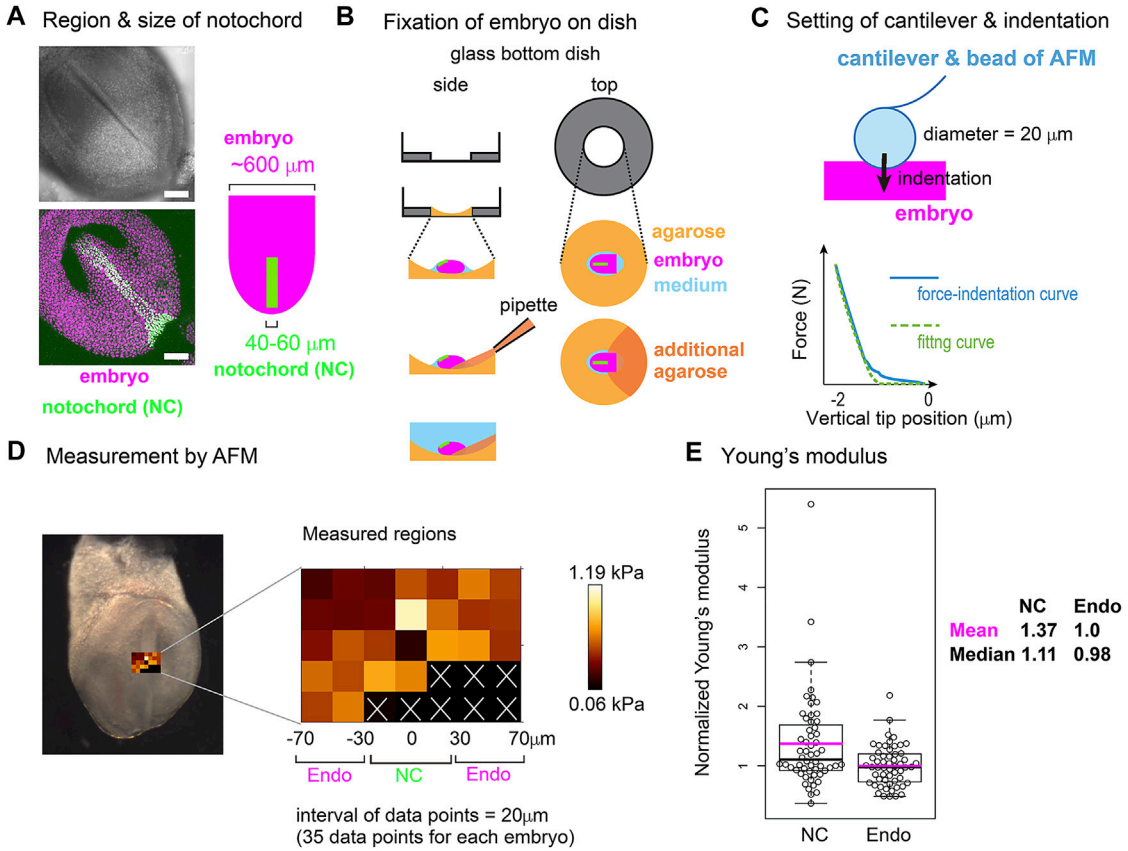


**FIGURE 8 |** Young's modulus measured using AFM in mouse notochord and endoderm. **(A)** Microscopic images of a mouse embryo are shown. Nuclei of the notochord cells were labeled with nuclear-EGFP (green), and nuclei of all embryonic cells including the endodermal cells as well as the notochord cells were labeled by histone 2B-mCherry (magenta). Upper panel, brightfield; bottom panel, a maximum intensity projection image constructed from confocal fluorescent images; left panel, illustration of an embryo and the notochord. Typical widths of the notochord and embryo are written. **(B)** Preparation procedure of embryo for AFM is illustrated. An embryo (magenta) is placed on an agarose gel (light orange) in a glass-bottom dish, and a part of the embryo is overlaid by an additional agarose gel (dark orange) before medium (blue) is added. Side and top views are shown. **(C)** AFM cantilever assembly and indentation. A bead of 20 μm diameter was attached to the cantilever as described in the Materials and Methods section. A force–indentation curve is schematically illustrated with a fitting curve which is used for calculating the Young's modulus. The x–axis is the depth of indentation. Examples of real force–indentation curves are shown in **Supplementary Figure S6**. **(D)** A spatial map of Young's modulus measured by AFM is shown. In the left panel, a brightfield microscopic image is provided where the regions subjected to the AFM measurement are also shown. In the middle panel, the Young's modulus for each region in the embryo is shown with a 20 μm spatial interval. In regions marked by white crosses, AFM measurements failed to be carried out. The regions of the notochord and endoderm were estimated by the width of the notochord. NC, notochord; Endo, endoderm. In the right panel, a color bar of Young's modulus is shown. **(E)** Young's moduli in the notochord and the endodermal regions are compared. The mean value in the endodermal regions was set at 1.0, and the relative values were plotted. Four embryos with several tens of data points were analyzed with total data points = 56 in both NC and Endo. Boxplots are shown where the boxes extend from the lower to upper quartiles and the whiskers indicate the 1.5–interquartile ranges. The *p*-value calculated using the Mann–Whitney–Wilcoxon test was 0.006. Magenta bars, mean; black bars, median; NC, notochord; Endo, endoderm. According to this boxplot, there are two or one outlier(s) located outside of the whiskers for NC and Endo. When these outliers are excluded, the statistic values become as follows: mean = 1.25 (NC), 0.98 (Endo), and median = 1.07 (NC), 0.98 (Endo), and *p*-value = 0.008. The mean values of the four individual embryos (#1–#4) are as follows (notochord, endoderm), #1 (0.37 [kPa], 0.22), #2 (0.48, 0.36), #3 (0.55, 0.47), and #4 (0.63, 0.53).

or tissues, the preferred cell area is not a parameter reflecting mechanical properties. Therefore, the Young's modulus is not related to the preferred cell area, and the differences in the Young's moduli between the two cell populations supports the differential area elasticity–based hypothesis.

The mechanism of tissue elongation on a uniformly expanding field was mathematically/analytically analyzed in our previous work where an isolated cell cluster was solely considered (i.e., type 1 cell) (Koyama and Fujimori, 2020). If a cell cluster is enlarged by external forces (i.e., $a_n$ becomes $>>a_O$) and then released from the forces in the absence of field expansion, the cell cluster decreases its area, and eventually reaches a natural state where each cell area becomes nearly $a_O$. Interestingly, during this process, the cell cluster transiently enhances its anisotropy, leading to the emergence of an elongated shape. Note that this anisotropy is finally diminished when the cell cluster reaches the steady state. On an expanding field, this enhancement of anisotropy is continued because the cell cluster is maintained under an enlarged state (i.e., $a_n>>a_O$), and thus, the cell cluster is continuously elongated. Furthermore, our analytical approach showed that this enhancement of anisotropy depends on both area elasticity

**TABLE 1 |** Summary of comparison of phenomena; *in vivo vs.* different models under uniformly expanding field.

| Phenomena | *In vivo* | Uniformly expanding field | | | |
|---|---|---|---|---|---|
| | ***Mouse notochord*** | ***Hypothesis A*** | ***Hypothesis B*** | ***Hypothesis C*** | ***Hypothesis D*** |
| | | **Differential cellular stiffness** | **Differential friction coefficient** | **Differential adhesion/ tension** | **Differential preferred cell area** |
| Elongation of cell cluster/tissue | +[a] | + | + | – | + |
| Relative increase in cell area (NC *vs.* END) | NC < END | NC < END | NC = END | Not determined | NC < END |
| Dependency of elongation on field expansion | Yes[a] | Yes | Yes | No elongation under field expansion | No |

*NC, notochord; END, endoderm.*
[a]*Imuta et al. (2014).*
*The elements consistent to the* in vivo *situations are shaded by gray.*

and increased cell area as shown in the eq. S16 of our previous work (Koyama and Fujimori, 2020).

On the other hand, our present study showed that differential area elasticity is effective for tissue elongation in the presence of surrounding cell populations. This seems to be consistent with our above analytical conclusion. Intuitively, if area elasticity in the surrounding cell populations (type 0) is significantly smaller than that in the cell cluster of interest (type 1), forces that the type 1 cells receive from the type 0 cells become negligible, leading to a situation equivalent to an isolated cell cluster. Imagine that, if a very stiff material is surrounded by very soft materials, the soft materials can have negligible influences to the behavior of the stiff material. We also showed that friction coefficient is effective for tissue elongation. According to **Eq. 4**, the apparent friction forces that a vertex receives from the expanding field is $F_{e|h} = \gamma_V V_e$, meaning that the force values are increased under larger friction coefficient $\gamma_V$. The apparent friction forces are effective for increasing cell areas; the increase results in the enhancement of anisotropy according to our previous analytical conclusion. In consistent with this, under the differential friction coefficients, the cell areas in type 1 become slightly larger than those in type 0 in our simulation (**Figure 6E**).

Mechanisms of tissue elongation have been experimentally and theoretically studied well (Keller et al., 2000; Honda et al., 2008). In these mechanisms, a cell cluster of interest is assumed to have an intrinsic activity of directional cell movement or anisotropic property of cell–cell interfaces (Zajac et al., 2000; Zajac et al., 2003; Honda et al., 2008), whereas any expanding field is not considered. Our present study shed light on a possible contribution of an expanding field to pattern formation, and consequently, the involvement of the area elasticity and the coefficient of the friction in tissue elongation was demonstrated. Expansion of a cavity and its role in morphogenesis has been discussed in both mouse and fish (Trinkaus, 1984; Tam and Behringer, 1997). Friction between fields and cells should exist in development of various multicellular systems including germ layers (Butler et al., 2009; Reig et al., 2017; Smutny et al., 2017), epidermis during pregnancy (Ichijo et al., 2017), and cells in contact with other cell layers such as smooth muscle layers or with external structures such as eggshells (Shyer et al., 2013; Koyama et al., 2016; Münster et al., 2019). Cell–extracellular matrix interaction is important for morphogenesis (Ryan et al., 2001; Goodwin et al., 2016) and would also be related to the friction forces. Further investigation is required to clarify what kind of real tissues our two hypotheses apply to.

# 5 MATERIALS AND METHODS

## 5.1 Mathematical Model and Analysis

The implementation of our mathematical model is essentially the same as that in our previous article. The surrounding cell populations have an outer boundary as shown in **Supplementary Figure S1**, and cropped views are shown in **Figures 2–5**, **7**. Total simulation time ($t' = t\lambda^{<0,0>}/(\gamma^{<0>}\sqrt{a_o})$) was fixed at 30 as a dimensionless time. Within this time period, ε was set so that the sizes of expanding fields become three times of the initial situations [i.e., $\exp(\varepsilon t) = 3$]. For the generation of all the phase diagrams, 30–40 simulation conditions were applied with some additional conditions for fine resolutions in specific regions as exemplified in **Figure 3A**. Simulations were performed using the Euler method.

The definition and measurement of the asymmetry/elongation index (*AI*) were reported previously (Koyama and Fujimori, 2020). The length of the longest axis of a cell cluster was measured as the maximum caliper. *AI* was defined as $AI = Feret/D_{circle}$, where *Feret* is the maximum caliper, and $D_{circle}$ is the diameter of a circle with the same area as the cell cluster. Thus, *AI* is 1.0 in a circle and is increased in an elongated shape. Simulation outcomes were converted to TIFF images, and the *Feret* and the area of a cell cluster were measured using ImageJ (*Feret* is prepared as a measurement option for ImageJ. https://imagej.nih.gov/ij/docs/menus/analyze.html#set).

The definition of the patterns in **Figures 2–5**, **7** is described in the main text. Briefly, when all type 1 cells formed a single cluster, the pattern was categorized as either "s-el", "el", "nc", or "sh", according to the ratio of *AI* after the simulation to *AI* before the simulation ($AI_{after}/AI_{before}$); when more than two separate clusters formed, the pattern was categorized into either "cl" or "mx".

## 5.2 Image Analysis for Estimating Cell Area

Cell areas in the mouse notochord and endoderm were estimated as follows. A rectangular region was defined on the notochord at 0 min (**Figure 6A**, left panel, 0 min, orange rectangle). Rectangular regions with the same width as the above were defined on the endodermal regions, which were also adjacent to the rectangle on the notochord (**Figure 6A**, 0 min, yellow rectangles). For images after time evolution (**Figure 6A**, 500 min), rectangular regions were defined on the notochord, whose widths may differ from that at 0 min. Rectangular regions set on the endodermal regions at 500 min have the same widths as at 0 min. Cell areas in these regions were defined as [the area of the rectangle/ the nuclear numbers]. Similar procedures were also carried out for simulation outcomes as shown in **Figure 6C** with orange and yellow rectangles.

## 5.3 Mouse Embryo

The notochord cells were identified by the expression of *Brachyury* (*T*). The *Brachyury*-expressing cells were labeled by nuclear enhanced green fluorescent protein (EGFP) as reported previously (Imuta et al., 2013) (Acc. No. CDB0604K; http://www2.clst.riken.jp/arg/mutant%20mice%20list.html). Briefly, knock-in mice expressing both Brachyury and nuclear EGFP from the endogenous *Brachyury* gene locus were used. All embryonic cells including the endodermal cells were labeled with mCherry-fused H2B (histone 2B proteins) expressed under the control of a ubiquitous promoter, *ROSA26*, as we reported previously (Abe et al., 2011). By mating these two mouse lines following a subsequent generation, we eventually obtained a mouse line that is both homozygous for *H2B-mCherry* and heterozygous for *Brachyury* with the nuclear *EGFP* gene. By mating males from this mouse line with ICR female mice (Japan SLC), embryos expressing both H2B-mCherry and nuclear EGFP were obtained with 50% probability.

## 5.4 Atomic Force Microscopy

Embryos described above were isolated on embryonic day 7.5. The embryos were placed in DMEM containing HEPES with 50% FBS on ice. The concentration of the agarose (BMA, SeaKem GTG, cat. 50,070) in **Figure 8B** is 1% melted in PBS. The embryos were placed on the agarose (**Figure 8B**, light orange), and the medium was almost removed. Finally, a small amount of 1% agarose was added to anchor the embryos (**Figure 8B**, dark orange). DMEM containing HEPES with 50% FBS was added on ice again. Thirty minutes before the AFM measurement, the above embryos were transferred to an incubator at 37°C, and the DMEM medium was replaced with PBS just before the AFM measurement. Four distinct embryos were subjected to AFM measurement, and for each embryo, several tens of measurement points were defined as described in **Figure 8D**. For each embryo, mean values of both the notochord and the endoderm were calculated, and the mean values of the four embryos are shown in the legend of **Figure 8E**. Calculation of the normalized Young's moduli in **Figure 8E** was performed for each embryo: all data points in one embryo were normalized by the mean value of the embryo's endoderm.

We could not identify the exact location of the notochord during AFM, because our AFM has a bright field microscope but not a good fluorescent one. Alternatively, we independently performed a fluorescent imaging using a confocal fluorescent microscope (Nikon A1, Japan) as shown in **Figure 8A**, and estimated the width of the notochord at 40–60 μm. Because the midline of the notochord was distinguishable in the bright field microscopy of the AFM (**Figure 8D**), we assumed that the notochords were located around the midline and 40–60 μm width.

AFM measurements were conducted as previously described (Kinoshita et al., 2020). In brief, a JPK Cellhesion 200 (Bruker) fitted with an x/y-motorized stage and mounted on a macro zoom microscope (Axio Zoom.V16, Zeiss) was used. Customized AFM probes (Novascan) were prepared by attaching borosilicate beads (**Figure 6C**, 20 μm diameter) to tipless rectangular silicon cantilevers (350 μm long, 32.5 μm wide, 1 μm thick; nominal spring constant 0.03 N/m, MikroMasch). Force–indentation curves (maximum indentation force: 3 nN, approach speed: 5 μm/s) were acquired every 20 μm apart in a bidirectional raster scan (**Figure 8D**), leading to that data points on the three columns adjacent to the midline were expected to be on the notochord. Cell elasticity (Young's modulus) values on the tissue surface were calculated based on the Hertz model and mapped onto brightfield images using the JPK data processing software (Bruker).

# DATA AVAILABILITY STATEMENT

The raw data supporting the conclusion of this article will be made available by the authors, without undue reservation.

# ETHICS STATEMENT

Animal care and experiments were conducted in accordance with National Institutes of Natural Sciences (NINS), the Guidelines of Animal Experimentation. The animal study was reviewed and approved by The Institutional Animal Care and Use Committee of NINS.

# AUTHOR CONTRIBUTIONS

HK designed the work; HK, HS, and TF contributed to the conception; HK designed models; HK developed computational algorithms; HK prepared embryos for AFM measurements; MS, NY, and NU designed and performed AFM experiments; HS provided mouse live imaging data; all authors wrote the manuscript; all authors contributed to the interpretation of the results.

## FUNDING

This work was supported by KAKENHI from the Japan Society for the Promotion of Science (JSPS) for TF (21H02494) and HK (17K15131), and the NINS program for cross-disciplinary science study for HK.

## SUPPLEMENTARY MATERIAL

The Supplementary Material for this article can be found online at: https://www.frontiersin.org/articles/10.3389/fcell.2022.864135/full#supplementary-material

## REFERENCES

Abe, T., Kiyonari, H., Shioi, G., Inoue, K.-I., Nakao, K., Aizawa, S., et al. (2011). Establishment of Conditional Reporter Mouse Lines at ROSA26 Locus for Live Cell Imaging. *Genesis* 49, 579–590. doi:10.1002/dvg.20753

Addae-Mensah, K. A., and Wikswo, J. P. (2008). Measurement Techniques for Cellular Biomechanics *In Vitro*. *Exp. Biol. Med. (Maywood)* 233, 792–809. doi:10.3181/0710-mr-278

Barriga, E. H., Franze, K., Charras, G., and Mayor, R. (2018). Tissue Stiffening Coordinates Morphogenesis by Triggering Collective Cell Migration *In Vivo*. *Nature* 554, 523–527. doi:10.1038/nature25742

Butler, L. C., Blanchard, G. B., Kabla, A. J., Lawrence, N. J., Welchman, D. P., Mahadevan, L., et al. (2009). Cell Shape Changes Indicate a Role for Extrinsic Tensile Forces in Drosophila Germ-Band Extension. *Nat. Cel Biol.* 11, 859–864. doi:10.1038/ncb1894

Corallo, D., Trapani, V., and Bonaldo, P. (2015). The Notochord: Structure and Functions. *Cell. Mol. Life Sci.* 72, 2989–3008. doi:10.1007/s00018-015-1897-z

Davidson, L. A., Oster, G. F., Keller, R. E., and Koehl, M. A. R. (1999). Measurements of Mechanical Properties of the Blastula Wall Reveal Which Hypothesized Mechanisms of Primary Invagination Are Physically Plausible in the Sea UrchinStrongylocentrotus Purpuratus. *Develop. Biol.* 209, 221–238. doi:10.1006/dbio.1999.9249

Duguay, D., Foty, R. A., and Steinberg, M. S. (2003). Cadherin-mediated Cell Adhesion and Tissue Segregation: Qualitative and Quantitative Determinants. *Develop. Biol.* 253, 309–323. doi:10.1016/s0012-1606(02)00016-7

Fletcher, A. G., Osterfield, M., Baker, R. E., and Shvartsman, S. Y. (2014). Vertex Models of Epithelial Morphogenesis. *Biophysical J.* 106, 2291–2304. doi:10.1016/j.bpj.2013.11.4498

Goodwin, K., Ellis, S. J., Lostchuck, E., Zulueta-coarasa, T., Fernandez-gonzalez, R., and Tanentzapf, G. (2016). Basal Cell-Extracellular Matrix Adhesion Regulates Force Transmission during Tissue Morphogenesis. *Develop. Cel* 39, 611–625. doi:10.1016/j.devcel.2016.11.003

Harris, A. K. (1976). Is Cell Sorting Caused by Differences in the Work of Intercellular Adhesion? A Critique of the Steinberg Hypothesis. *J. Theor. Biol.* 61, 267–285. doi:10.1016/0022-5193(76)90019-9

Hejnol, A., and Lowe, C. J. (2014). Animal Evolution: Stiff or Squishy Notochord Origins? *Curr. Biol.* 24, R1131–R1133. doi:10.1016/j.cub.2014.10.059

Honda, H., Nagai, T., and Tanemura, M. (2008). Two Different Mechanisms of Planar Cell Intercalation Leading to Tissue Elongation. *Dev. Dyn.* 237, 1826–1836. doi:10.1002/dvdy.21609

Ichijo, R., Kobayashi, H., Yoneda, S., Iizuka, Y., Kubo, H., Matsumura, S., et al. (2017). Tbx3-dependent Amplifying Stem Cell Progeny Drives Interfollicular Epidermal Expansion during Pregnancy and Regeneration. *Nat. Commun.* 8, 508. doi:10.1038/s41467-017-00433-7

Imuta, Y., Kiyonari, H., Jang, C.-W., Behringer, R. R., and Sasaki, H. (2013). Generation of Knock-In Mice that Express Nuclear Enhanced green Fluorescent Protein and Tamoxifen-Inducible Cre Recombinase in the Notochord fromFoxa2andTloci. *Genesis* 51, 210–218. doi:10.1002/dvg.22376

Imuta, Y., Koyama, H., Shi, D., Eiraku, M., Fujimori, T., and Sasaki, H. (2014). Mechanical Control of Notochord Morphogenesis by Extra-embryonic Tissues in Mouse Embryos. *Mech. Develop.* 132, 44–58. doi:10.1016/j.mod.2014.01.004

Keller, R., Davidson, L., Edlund, A., Elul, T., Ezin, M., Shook, D., et al. (2000). Mechanisms of Convergence and Extension by Cell Intercalation. *Phil. Trans. R. Soc. Lond. B* 355, 897–922. doi:10.1098/rstb.2000.0626

Kinoshita, N., Hashimoto, Y., Yasue, N., Suzuki, M., Cristea, I. M., and Ueno, N. (2020). Mechanical Stress Regulates Epithelial Tissue Integrity and Stiffness through the FGFR/Erk2 Signaling Pathway during Embryogenesis. *Cel Rep.* 30, 3875–3888. e3. doi:10.1016/j.celrep.2020.02.074

Koyama, H., and Fujimori, T. (2020). Isotropic Expansion of External Environment Induces Tissue Elongation and Collective Cell Alignment. *J. Theor. Biol.* 496, 110248. doi:10.1016/j.jtbi.2020.110248

Koyama, H., Shi, D., Suzuki, M., Ueno, N., Uemura, T., and Fujimori, T. (2016). Mechanical Regulation of Three-Dimensional Epithelial Fold Pattern Formation in the Mouse Oviduct. *Biophysical J.* 111, 650–665. doi:10.1016/j.bpj.2016.06.032

Krieg, M., Arboleda-Estudillo, Y., Puech, P.-H., Käfer, J., Graner, F., Müller, D. J., et al. (2008). Tensile Forces Govern Germ-Layer Organization in Zebrafish. *Nat. Cel Biol.* 10, 429–436. doi:10.1038/ncb1705

Maître, J.-L., Berthoumieux, H., Krens, S. F. G., Salbreux, G., Jülicher, F., Paluch, E., et al. (2012). Adhesion Functions in Cell Sorting by Mechanically Coupling the Cortices of Adhering Cells. *Science* 338, 253–256. doi:10.1126/science.1225399

Manning, M. L., Foty, R. A., Steinberg, M. S., and Schoetz, E.-M. (2010). Coaction of Intercellular Adhesion and Cortical Tension Specifies Tissue Surface Tension. *Proc. Natl. Acad. Sci. U.S.A.* 107, 12517–12522. doi:10.1073/pnas.1003743107

Münster, S., Jain, A., Mietke, A., Pavlopoulos, A., Grill, S. W., and Tomancak, P. (2019). Attachment of the Blastoderm to the Vitelline Envelope Affects Gastrulation of Insects. *Nature* 568, 395–399. doi:10.1038/s41586-019-1044-3

Okuda, S., Inoue, Y., Eiraku, M., Adachi, T., and Sasai, Y. (2014). Vertex Dynamics Simulations of Viscosity-dependent Deformation during Tissue Morphogenesis. *Biomech. Model. Mechanobiol.* 14, 413–425. doi:10.1007/s10237-014-0613-5

Reig, G., Cerda, M., Sepúlveda, N., Flores, D., Castañeda, V., Tada, M., et al. (2017). Extra-embryonic Tissue Spreading Directs Early Embryo Morphogenesis in Killifish. *Nat. Commun.* 8, 15431. doi:10.1038/ncomms15431

Ryan, P. L., Foty, R. A., Kohn, J., and Steinberg, M. S. (2001). Tissue Spreading on Implantable Substrates Is a Competitive Outcome of Cell-Cell vs. Cell-Substratum Adhesivity. *Proc. Natl. Acad. Sci. U.S.A.* 98, 4323–4327. doi:10.1073/pnas.071615398

Shyer, A. E., Tallinen, T., Nerurkar, N. L., Wei, Z., Gil, E. S., Kaplan, D. L., et al. (2013). Villification: How the Gut Gets its Villi. *Science* 342, 212–218. doi:10.1126/science.1238842

Smutny, M., Ákos, Z., Grigolon, S., Shamipour, S., Ruprecht, V., Čapek, D., et al. (2017). Friction Forces Position the Neural Anlage. *Nat. Cel Biol.* 19, 306–317. doi:10.1038/ncb3492

Steinberg, M. S. (2007). Differential Adhesion in Morphogenesis: a Modern View. *Curr. Opin. Genet. Develop.* 17, 281–286. doi:10.1016/j.gde.2007.05.002

Steinberg, M. S. (1963). Reconstruction of Tissues by Dissociated Cells. *Science* 141, 401–408. doi:10.1126/science.141.3579.401

Swift, J., Ivanovska, I. L., Buxboim, A., Harada, T., Dingal, P. C. D. P., Pinter, J., et al. (2013). Nuclear Lamin-A Scales with Tissue Stiffness and Enhances Matrix-Directed Differentiation. *Science* 341, 1240104. doi:10.1126/science.1240104

Tam, P. P. L., and Behringer, R. R. (1997). Mouse Gastrulation: The Formation of a Mammalian Body Plan. *Mech. Develop.* 68, 3–25. doi:10.1016/S0925-4773(97)00123-8

Togashi, H., Kominami, K., Waseda, M., Komura, H., Miyoshi, J., Takeichi, M., et al. (2011). Nectins Establish a Checkerboard-like Cellular Pattern in the Auditory Epithelium. *Science* 333, 1144–1147. doi:10.1126/science.1208467

Trepat, X., and Sahai, E. (2018). Mesoscale Physical Principles of Collective Cell Organization. *Nat. Phys* 14, 671–682. doi:10.1038/s41567-018-0194-9

Trinkaus, J. P. (1984). "Cells into Organs," in *The Forces that Shape the Embryo* (Englewood Cliffs: Prentice-Hall).

Yamanaka, H. I., and Honda, H. (1990). A Checkerboard Pattern Manifested by the Oviduct Epithelium of the Japanese Quail. *Int. J. Dev. Biol.* 34, 377–383.

Zajac, M., Jones, G. L., and Glazier, J. A. (2000). Model of Convergent Extension in Animal Morphogenesis. *Phys. Rev. Lett.* 85, 2022–2025. doi:10.1103/PhysRevLett.85.2022

Zajac, M., Jones, G. L., and Glazier, J. A. (2003). Simulating Convergent Extension by Way of Anisotropic Differential Adhesion. *J. Theor. Biol.* 222, 247–259. doi:10.1016/S0022-5193(03)00033-X

Zhou, J., Kim, H. Y., and Davidson, L. A. (2009). Actomyosin Stiffens the Vertebrate Embryo during Crucial Stages of Elongation and Neural Tube Closure. *Development* 136, 677–688. doi:10.1242/dev.026211

**Conflict of Interest:** The authors declare that the research was conducted in the absence of any commercial or financial relationships that could be construed as a potential conflict of interest.

**Publisher's Note:** All claims expressed in this article are solely those of the authors and do not necessarily represent those of their affiliated organizations, or those of the publisher, the editors and the reviewers. Any product that may be evaluated in this article, or claim that may be made by its manufacturer, is not guaranteed or endorsed by the publisher.

frontiers | Frontiers in Cell and Developmental Biology

MINI REVIEW
published: 01 June 2022
doi: 10.3389/fcell.2022.917662

# Mechanoautophagy: Synergies Between Autophagy and Cell Mechanotransduction at Adhesive Complexes

*Andrea Ravasio*[1]*, *Eugenia Morselli*[2] and *Cristina Bertocchi*[3]*

[1]Institute for Biological and Medical Engineering Schools of Engineering, Medicine and Biological Sciences, Pontificia Universidad Católica de Chile, Santiago, Chile, [2]Department of Basic Sciences, Faculty of Medicine and Sciences, Universidad San Sebastián, Santiago, Chile, [3]Laboratory for Molecular Mechanics of Cell Adhesion, Department of Physiology Pontificia Universidad Católica de Chile, Santiago, Chile

Cells are exposed and respond to various mechanical forces and physical cues stemming from their environment. This interaction has been seen to differentially regulate various cellular processes for maintenance of homeostasis, of which autophagy represents one of the major players. In addition, autophagy has been suggested to regulate mechanical functions of the cells including their interaction with the environment. In this minireview, we summarize the state of the art of the fascinating interplay between autophagy and the mechanotransduction machinery associated with cell adhesions, that we name "Mechanoautophagy"

**Keywords: mechanoautophagy, Extracellular Matrix, focal adhesion, cadherin mediated adhesion, Autophagy**

OPEN ACCESS

***Edited by:***
*Bojana Gligorijevic, Temple University, United States*

***Reviewed by:***
*Paolo Grumati, Telethon Institute of Genetics and Medicine (TIGEM), Italy*

***Correspondence:**
*Cristina Bertocchi*
*cbertocchi@bio.puc.cl*
*Andrea Ravasio*
*andrea.ravasio@uc.cl*

***Specialty section:***
*This article was submitted to Cell Adhesion and Migration, a section of the journal Frontiers in Cell and Developmental Biology*

***Received:*** *11 April 2022*
***Accepted:*** *13 May 2022*
***Published:*** *01 June 2022*

***Citation:***
*Ravasio A, Morselli E and Bertocchi C (2022) Mechanoautophagy: Synergies Between Autophagy and Cell Mechanotransduction at Adhesive Complexes. Front. Cell Dev. Biol. 10:917662. doi: 10.3389/fcell.2022.917662*

## 1 INTRODUCTION

How the mechanics of cellular environment influence biological properties is an emerging but yet poorly understood field of investigation. This is particularly true for macroautophagy (herein referred to as autophagy), a dynamic clearance process whereby cellular components, such as misfolded proteins, abnormal protein aggregates and damaged organelles, are sequestered and digested by lysosomes for degradation and recycling (Boya et al., 2013; Ortiz-Rodriguez and Arevalo, 2020; Aman et al., 2021; Hernández-Cáceres et al., 2021). At the molecular level, activation of the autophagic pathway begins with the dissociation of the ULK1/mTORC1 complex, where Unc-51 Like Autophagy Activating Kinase (ULK)1 initiates the recruitment of the autophagic machinery when freed from the inhibitory effect of the kinase mammalian target of rapamycin (mTORC)1 (Shang and Wang, 2011; Park et al., 2016). Downstream of inactivation of mTORC1-repressor function, there are around 20 autophagy-related proteins (collectively called ATGs) that initiate the process by recruiting the necessary machinery for phagophore formation (Geng et al., 2008), (Gómez-Sánchez et al., 2021). Following these initial steps, the phagophore elongates and closes into a double-membrane organelle, called autophagosome that matures into an autolysosome through fusion with lysosomes (Lőrincz and Juhász, 2020). This last step enables digestion of faulty cellular components, recycling of metabolic materials and rejuvenation of the cytosol. A mechanistic description of the whole process can be found in Hernandez et al., Frontiers 2021 (Hernández-Cáceres et al., 2021). In addition to be constantly needed as housekeeping process to maintain cellular homeostasis (Rabinowitz and White, 2010; Galluzzi et al., 2014; Kaur and Debnath, 2015), autophagy is essential during stress response, such as starvation, where, by degrading cytosolic material, autophagy provides nutrients and metabolites necessary for the cell to cope with stress and ensure its

survival (Rabinowitz and White, 2010; Das et al., 2012; Müller et al., 2015). Similar stress responses activating autophagy include oxidative stresses, DNA damage and pathogen infection (Filomeni et al., 2015; Eliopoulos et al., 2016; Ravanan et al., 2017; Evans et al., 2018). In addition to these biochemical stresses, we have recently proposed a possible mechanism for autophagy activation in response to mechanical stimuli through involvement of the mechanically activated mTORC2 and its well-known inhibitory effect over mTORC1 (Hernández-Cáceres et al., 2021; Ballesteros-Álvarez and Andersen, 2021).

Cells are exposed and respond to various mechanical forces and physical cues stemming from their micro- and macro-environment. These include properties of the extracellular matrix (e.g., composition, density, and stiffness), nano and micro-scale geometrical cues (e.g., topography, size, confinement, curvature) that can influence cortex and membrane tension, interaction with neighboring cells (e.g., cell crowding and migratory forces), and the large-scale tissue and organ dynamics (e.g., shear stress, fluid pressure, stretching and compression) (Ingber, 2008; Geiger and Bershadsky, 2002; Iskratsch et al., 2014; Sheetz and Yu, 2018). Mechanical forces are sensed by cells through various mechanosensors, such as adhesion complexes (e.g., adherens junction and focal adhesion), proteins sensing tension and curvature of the plasma membrane (e.g., BAR proteins) and of the cytoskeleton (e.g., filamin), and stretch activated ion channels (e.g., TRP and piezo) (Hernández-Cáceres et al., 2021; Sheetz and Yu, 2018). The mechanical input acting on these mechanosensors triggers cellular responses that may involve direct mechanical responses (largely through cytoskeletal and membrane dynamics) and signaling cascades that convert the mechanical stimulus into a biochemical response (i.e., mechanotransduction) leading to cytoskeletal reorganization, membrane and organelles trafficking, gene expression regulation and consequent modulation of various cellular functions (Iskratsch et al., 2014). Specifically, the interaction between cells and their physical environment regulates positively and negatively the autophagic process (Hernández-Cáceres et al., 2021; King et al., 2011; Dupont and Codogno, 2016; Claude-Taupin et al., 2021; Zhang et al., 2022). On the other hand, autophagic catabolism affects mechanical functions of the cells including their interaction with the environment (Hernández-Cáceres et al., 2021; King et al., 2011; Dupont and Codogno, 2016; Claude-Taupin et al., 2021). In this minireview, we aim to summarize the state of the art of the fascinating interplay between autophagy and the mechanotransduction machinery associated with adhesions that we named ¨Mechanoautophagy¨.

## 2 EXTRACELLULAR MATRIX AND AUTOPHAGY

The extracellular matrix (ECM) is a dynamic network with different macromolecular composition, structural architecture, and rheological properties that, through its constant remodeling by the cells, contributes to regulating tissue homeostasis (Vogel, 2018). It is indeed this continuous transformation of the ECM that eventually influences a wide array of biological functions (i.e., adhesion and cohesion, proliferation, differentiation, migration, etc) and cellular phenotypes, thus having a dramatic effect on intracellular signaling. This fundamental physiological role implies that the deregulation of such extracellular microniche could lead to diseases. Typically, aberrant ECM organization is observed in various pathological scenarios such as fibrosis and cancer, where ECM composition and rheological properties are altered as compared to the corresponding physiological tissue (Vogel, 2018; Lu et al., 2011).

Specific components associated with the ECM have been reported to play opposing roles on autophagy (Lock and Debnath, 2008; Neill et al., 2014; Schaefer and Dikic, 2021). Inhibitors of autophagy comprise laminin $\alpha$2, an ECM-associated protein, and two proteoglycans, lumican and perlecan. Laminin $\alpha$2 is the heavy chain of the laminin glycoprotein complex and it works as a connector between ECM and the cell membrane in skeletal muscles, Schwann cells, pericytes and astrocytes (Yurchenco et al., 2018). Laminin $\alpha$2 functions as an autophagy inhibitor, as indicated by the increase in autophagic flux in laminin $\alpha$2-deficient muscle cells and by recovery of the typical muscle morphology upon chemical inhibition of laminin $\alpha$2 in congenital muscular dystrophy models (Carmignac et al., 2011; Durbeej, 2015). Lumican has been reported to inhibit autophagy in pancreatic ductal adenocarcinoma through downregulation of AMP-activated protein kinase (AMPK) (Li et al., 2016). Finally, perlecan, as a whole molecule, has been seen to hinder autophagy through mTORC1 activation (Ning et al., 2015). On the other hand, several ECM-associated proteins such as collagen VI, kringle 5, endostatin, and various proteoglycans like decorin, endorepellin, biglycan function as activators of the autophagic process (Nguyen et al., 2007; Nguyen et al., 2009; Gubbiotti and Iozzo, 2015; Castagnaro et al., 2018). Collagen VI, similarly to the associated leucine-rich proteoglycan decorin, has pro-survival and autophagy instructive properties through inactivation of the Akt/mTOR/p70S6K pathway (Castagnaro et al., 2018), and through AMPK *via* the hepatocyte and the epithelial growth factors (HGF/Met and EGF, respectively). Together with decorin, another leucine-rich proteoglycan, biglycan, has been reported to evoke autophagy in macrophages *via* a novel CD44/Toll-like receptor 4 signaling cascade (Poluzzi et al., 2019). Interestingly, while the whole perlecan molecule has inhibitory functions, its c-terminus (AKA endorepellin) enhances autophagy through transcriptional upregulation of pro-autophagic genes such as PEG3, BECN1, and MAP1LC3A (Poluzzi et al., 2014). Kringle 5, the fifth kringle domain in human plasminogen, activates autophagy in a similar manner as endostatin, by enhancing BECN1 expression through β-catenin and Wnt-mediated signaling pathways (Nguyen et al., 2007).

While there are some evidences on how ECM can influence autophagy, little is known about the role of autophagy in regulating cell-ECM interactions. Interestingly, the term ¨secretory autophagy¨ has been coined to indicate the non-lytic autophagic pathway where autophagosomes, instead of fusing with a lysosome, fuse with the plasma membrane and

help excrete particulate substrates (Kimura et al., 2017; Ponpuak et al., 2015). The secretion of matrix components could possibly rely on such a mechanism, since deletion of ATG7 in mouse embryonic fibroblast cells produces a deficiency in the expression of collagen I, fibronectin, and periostin (Zhuo et al., 2013). Furthermore, the autophagic process can also influence conventional secretory pathways (i.e., constitutive and regulated secretion) by promoting the translocation of integral membrane proteins to the plasma membrane.

## 3 FOCAL ADHESIONS AND AUTOPHAGY

Mechanical and chemical signals from the extracellular matrix in normal and in pathological conditions are sensed by the integrin-mediated adhesions, also known as focal adhesions (Kanchanawong et al., 2010; Iskratsch et al., 2014). This supramolecular complex physically connects the ECM to the actin cytoskeleton through an intricate plaque of proteins (AKA adhesome network) organized in three distinct layers: a signaling layer composed of transmembrane integrins and adaptor proteins (e.g., paxillin), an intermediate force-transduction layer with mechanotransduction molecules (i.e., talin, vinculin) and signaling molecules (e.g., FAK, Src, PI3K), and, finally, an actin-regulatory layer with actin and actin linker proteins (e.g., filamin, α-actinin) (Kanchanawong et al., 2010; Xia et al., 2019). Mature focal adhesions are highly integrated with the cytoskeleton, as suggested by their presence at the anchor points of actin stress fibers. As such, they are instrumental in transmitting forces internally generated by the actomyosin network to the ECM, and vice versa (Burridge and Guilluy, 2016). Furthermore, focal adhesion assembly normally occurs in actin-rich regions, where clusters of integrins are delivered together by actin polymerization driven by actin retrograde flow (Oakes and Gardel, 2014). Interaction between integrin heterodimers ($\alpha$ and $\beta$) and ECM proteins initiates tension-induced conformational change in integrin cytoplasmic tails with consequent activation of the dimer and its engagement with talin and paxillin (Shattil et al., 2010). The increased tension prompts recruitment of proteins of the signaling layer (e.g., FAK, Src etc.) that, in turn, start the signaling cascade leading to actin polymerization and to the strengthening and growth of the adhesion (Iskratsch et al., 2014). Such a process of conversion of the extracellular mechanical stimuli into biochemical signals (mechanotransduction) is strongly related to several stress responses, including autophagy. One of the first pieces of evidence reporting the bidirectional connection between focal adhesion and autophagy comes from studies on hepatocytes' osmosensing (Dahl et al., 2003). In this model, integrins have been shown to mediate the activation of Src kinase when anchorage to the extracellular matrix and polarity of hepatocyte was preserved. This interaction triggers the activation of p38MAPK and Erk-1/Erk-2, promoting autophagy and proteolysis (Dahl et al., 2003). This study, was the first that suggested a relation between integrins signaling and autophagic proteolysis, which was then corroborated by more recent studies thatidentified additionaldownstream effectors of the integrin-dependent control of autophagy (Vlahakis and Debnath, 2017). In particular, simply providing detached cells with a laminin-rich ECM, re-establishing cell-ECM contact, abolishes autophagy; this effect is reversed when integrin $\beta$1 are blocked by using a specific antibody thus inhibiting the FAK and ILK (Integrin Linked Kinase) signaling cascade. Decrease of mechanical forces at the FA, due to detachment from ECM or changes in substrate rheology, leads to dissociation of FAK from integrin and FA (Martino et al., 2018). Soluble FAK can phosphorylate and activate mTORC2 and consequently initiate autophagy (Case et al., 2011). Furthermore, following cell detachment, integrin $\beta$1 and receptor tyrosine kinase c-Met are removed from the cell membrane and recruited to LC3 autophagic membranes (Barrow-McGee et al., 2016). The pool of internalized integrin $\beta$1 prompts the c-Met dependent phosphorylation and consecutive activation of ERK1/2, that allows for resistance to anoikis (a programmed cell death occurring upon cell detachment from the ECM (Barrow-McGee et al., 2016)). The activation of autophagy mediated by integrin detachment from ECM, could be thought as a failsafe mechanism to delay the onset of apoptosis and allow cell adaptation and survival (Lock and Debnath, 2008), (Vlahakis and Debnath, 2017), (Anlaş and Nelson, 2020). Unfortunately, this autophagy-mediated survival mechanism could also aid cancer onset and tumor progression (Buchheit et al., 2014).

On the other hand, it has been demonstrated that autophagy plays a crucial role in regulating focal adhesion dynamics. During cell migration, FAs undergo continuous assembling and disassembling cycles that depend on tension and phosphorylation, which is partially mediated by autophagy. For instance, autophagy targets integrin $\beta$1 during nutrient starvation (Vlahakis and Debnath, 2017) regulating FA dynamics and promoting their turnover (Sharifi et al., 2016). This occurs *via* different pathways involving LC3 and autophagy receptors that target specific FA components such as the selective autophagy cargo adaptor NBR1 that can bind to a variety of FA proteins (i.e., vinculin, FAK, paxillin, and zyxin), and recruits LC3-containing autophagosomes to FAs (Chang et al., 2017), (Kenific and Debnath, 2016). In addition, once phosphorylated by Src, paxillin is also targeted by LC3-containing-autophagosomes *via* its direct association with LC3. Finally, active Src can be targeted by the cargo adaptor, Cbl, which recruits autophagosomes to FA for Src degradation (Chang et al., 2017; Cecconi, 2012). An interesting venue of interplay between FAs and autophagy could also involve regulation of actin contractility and cytoskeletal dynamics. Autophagy can alter these processes by specifically degrading RhoA *via* the autophagic receptor p62/SQSTM1 (Bjørkøy et al., 2009).

## 4 CELL-CELL ADHESIONS AND AUTOPHAGY

Besides the adhesion between cells and ECM, integrity, homeostasis and dynamics of cells and tissues are regulated by physical interaction between neighboring cells. Despite the variety of adhesion complexes mediating adhesion and

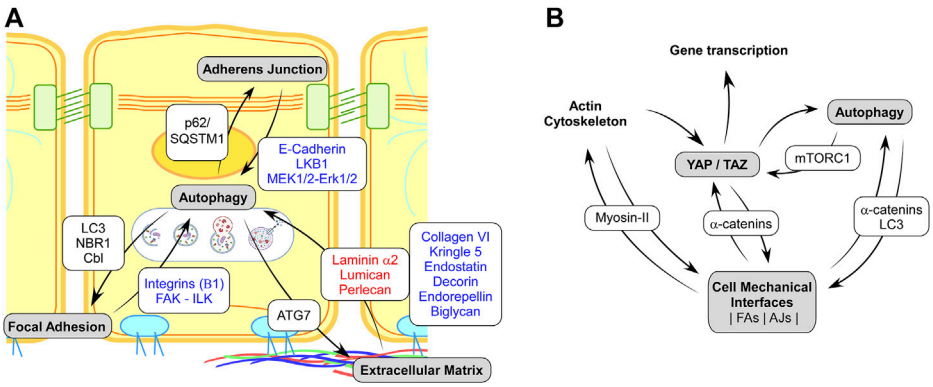


**FIGURE1 | (A)** Schematic representation of the known interplays between the mechanosensitive cell adhesions complexes and autophagy. Red and blue texts on white background indicate protein showing a negative or positive regulation of autophagy, respectively. Text in black on white background indicates proteins of the autophagy machinery targeting specific disassembly and recycling of Adherens Junction, Focal Adhesion, or Extracellular Matrix. **(B)**. Schematic representation of regulatory interaction involving cell mechanics, Autophagy and YAP/TAZ mechano-signaling. Black on white background text indicates the main proteins involved in the regulatory feedbacks.

communication between neighboring cells, in this minireview we will focus on adherens junctions (AJs) because of their role as mechanotransducers (Angulo-Urarte et al., 2020). AJs, also known as cadherin-mediated adhesion, mediate force transduction between cells by specialized transmembrane receptors (i.e., cadherins) that are connected to the cytoskeleton *via* a protein complex termed the cadhesome network (Zaidel-Bar, 2013). Superresolution microscopy experiments demonstrated that AJs share remarkable similarities with FAs, including a multilayered architecture (Kanchanawong et al., 2010; Bertocchi et al., 2017) with a signaling layer composed by cadherin, β-catenin, α-catenin, p120-catenin, a force transduction layer where vinculin, zyxin and VASP are and an actin regulatory layer with actin, α-actinin, and eplins (Bertocchi et al., 2017). Due to these similarities, one could expect that a comparable bidirectional control between autophagy and adhesions could be found. However, this is only partially true, and substantial investigations unveiling these interactions are still missing. It has been observed that autophagy-dependent survival was promoted in vascular smooth muscle cells following T-cadherin upregulation and activation of MEK1/2-Erk1/2 (Kyriakakis et al., 2017). Furthermore, it has been demonstrated that force application to E-cadherin adhesion, prompts autophagy through activation of Liver Kinase B1 (LKB1), which recruits AMPK at the site of the AJs (Bays et al., 2017). Similarly to what is observed for FAs, autophagy machinery also contributes to AJs turnover. In particular, it has been observed that in breast cancer, E-cadherin physically interacts with p62/SQSTM1 to mediate LC3 targeting and consequent delivery to LC3-containing autophagosomes (Damiano et al., 2020; Santarosa and Maestro, 2021). Additionally, LC3 has been found to directly interact with β-catenin to target its degradation (Petherick et al., 2013). Autophagy has been reported to degrade transcription factors SNAIL and SLUG, which control E-to N-cadherin switch during Epithelial to Mesenchymal Transition (EMT) process, *via* binding to the autophagy adaptor p62/SQSTM1 (Bertrand et al., 2015). This results in reduced migration and invasion of cancer cells (i.e. glioblastoma) and leads to reversing EMT. This EMT modulatory role of autophagy has been corroborated by the observation that its deficiency or suppression enhance cell migration, invasion, and proliferation, potentially due to the stabilization of transcription factor Twist1 by p62/SQSTM1 (Qiang and He, 2014). However additional sets of evidence support the opposing view that inhibition of autophagy (either chemically, or by silencing of core autophagy genes such as Beclin1 or ATG7) could foster the expression of epithelial markers, whereas its induction could lead to activation of SNAIL transcription factor and consequently EMT (Chen et al., 2019). Thus, lack of sufficient body of evidence leaves open to debate the effective role and actual importance of autophagy in maintaining tissue homeostasis and in regulating EMT.

## 5 YES-ASSOCIATED PROTEIN/ TRANSCRIPTIONAL CO-ACTIVATOR WITH PDZ-BINDING MOTIF MECHANICAL RESPONSE AND AUTOPHAGY

Yes-associated protein (YAP) and the transcriptional co-activator with PDZ-binding Motif (TAZ) are proto-oncogenes that can modulate gene expression in response to changes of the mechanical environment (Sudol, 1994; Low et al., 2014). Piccolo and co-workers have been the pioners in the study of YAP/TAZ mechanosensing mechanisms and demonstrated changes in localization of these two transcriptional activators, depending on mechanical forces. In particular, they have shown a differential translocation in and out of the nucleus (and consequent activation or inactivation), depending on extracellular matrix stiffness, cell density and cell geometry (Dupont et al., 2011). E-cadherin/catenin complex and integrins function as an upstream regulators of the Hippo

signaling pathway in signal transduction in mammalian cells (Kim et al., 2011; Kim and Gumbiner, 2015; Short, 2015; Block et al., 2020); it has been shown that in subconfluent epithelial cell cultures or when cells are seeded on a stiff ECM, YAP and TAZ remain in the nucleus where they promote cell proliferation, through their interaction with TEAD family of transcription factors (Aragona et al., 2013; Panciera et al., 2017). In high-cell density population, where contact between cells is preserved, or when cells are on a soft substrate, YAP and TAZ are not active and localize in the cytoplasm (Zhao et al., 2007). This is part of a self-defending mechanism that allows noncancerous cells to stop proliferating when they contact one another. Such contact inhibition appears deregulated in cancer cells, that bypass the command from cell adhesions and keep on proliferating (Pavel et al., 2018). In different cell types, it has been shown a contrasting effect on YAP/TAZ signaling in response to alteration of autophagy; some studies correlate defect of autophagy with inhibition of YAP/TAZ, failure in modulation of myosin-II gene expression and consecuent loss of F-actin stress fibers. In a feedback loop this loss of F-actin fibers leads to impairment in autophagosome formation by altering the amount of ATG16L1 puncta and by reduced co-localization with ATG9A-LC3 (Pavel et al., 2018). Low cell density induced YAP/TAZ activation in the nucleus, results in actin stress fibers formation and autophagosomes assembly. These results suggest a feedback loop between autophagy and Hyppo pathway.

On the other hand, other groups reported that autophagy alteration, by Beclin silencing or by cloroquine treatment, can induce expression of YAP in cancer cell lines (from lung, breast and colon) (Wang et al., 2019). These opposite responses in different cell types seems to be related to α-catenins levels (Pavel et al., 2021). Interestingly, α-catenins are common key signalling effectors between autophagy and Hyppo pathway; they are known to interact with LC3 and they can inhibit YAP/TAZ signaling. When α-catenins levels are low [i.e., in cancer cells from lung, breast, colon (Sun et al., 2014)], YAP/TAZ activity is increased upon autophagy inhibition, while, YAP/TAZ activity is reduced by autophagy when α-catenin levels are high (Pavel et al., 2021). Viceversa, inhibition of the Hyppo pathway, in response to the physical properties of the cell microenvironment (high cell density) (Pavel et al., 2018) reduces the efficiency of the autophagic flux (Totaro et al., 2019). At last, mTORC1 regulates YAP by mediating its autophagic degradation (Liang et al., 2014), further linking cellular nutrient status to YAP activity (Pocaterra et al., 2020), and strenghtening the hypothesis for crosstalk between the transcriptional coactivatorsYAP/TAZ and autophagy.

## 6 CONCLUSION

This minireview highlights a novel and exciting field of study, the Mechanoautophagy, that aims at understanding how autophagy regulates mechanotransduction machinery and mechanical processes of the cells regulate autophagy. While literature on this topic is in its infancy, this interplay plays an undoubtedly important role during cancer transformation where cancer cells manage to survive in a mechanical microenvironment that in normal conditions would lead to apoptotic clearance. For instance, cancer cells manage to survive in stiff and unstructured ECM, under growing pressure coming from cellular crowding where both cell-substrate and cell-cell adhesions are topologically misconfigured and subject to abnormal forces. Interestingly, escape from programmed cell death is a cancer hallmark that heavily rely on the aid of autophagy. Even more interesting, it has been reported that autophagy provides a mechanism to escape anoikis, i.e., a specific type of apoptosis that lead to clearance of adherence cells lacking proper connection to the ECM. Thus, autophagy is clearly involved in a large number of mechanically related cellular functions, which we only have started to appreciate. Additionally, while we have only discussed the role of mechanoautophagy in cancer transformation, there is a whole plethora of physio/pathological contexts where the study of mechanoautophagy is needed, such as development and/or obesity where the study of autophagy and mechanical forces *per se,* but not their synergy, has been considered. Thanks to technological innovations in creating biomimetic substrates, high temporal and special resolution microscopy as wells the adoption of interdisciplinary approaches, this new field of study could provide fundamental knowledge for a variety of medical conditions. We are thus convinced that better understanding of mechanoautophagy will open the possibility for novel therapeutic interventions targeting for mechanical pathways.

## AUTHOR CONTRIBUTIONS

All authors participated in the writing process. CB and AR conceptualized the minireview.

## FUNDING

AR and CB acknowledge the support of ANID PIA ACT192015, FONDECYT 1210872 and FONDEQUIP EMQ210101; EM by FONDECYT 1200499. CB and AR acknowledge seeds funds from the Pontificia Universidad Católica de Chile.

## REFERENCES

Aman, Y., Schmauck-Medina, T., Hansen, M., Morimoto, R. I., Simon, A. K., Bjedov, I., et al. (2021). Autophagy in Healthy Aging and Disease. *Nat. Aging* 1 (8), 634–650. doi:10.1038/s43587-021-00098-4

Angulo-Urarte, A., van der Wal, T., and Huveneers, S. (2020). Cell-cell Junctions as Sensors and Transducers of Mechanical Forces. *Biochimica Biophysica Acta (BBA) - Biomembr.* 1862 (9), 183316. doi:10.1016/J.BBAMEM.2020.183316

Anlaş, A. A., and Nelson, C. M. (2020). Soft Microenvironments Induce Chemoresistance by Increasing Autophagy Downstream of Integrin-Linked Kinase. *Cancer Res.* 80 (19), 4103–4113. doi:10.1158/0008-5472.CAN-19-4021

Aragona, M., Panciera, T., Manfrin, A., Giulitti, S., Michielin, F., Elvassore, N., et al. (2013). A Mechanical Checkpoint Controls Multicellular Growth through YAP/TAZ Regulation by Actin-Processing Factors. *Cell* 154 (5), 1047–1059. doi:10.1016/j.cell.2013.07.042

Ballesteros-Álvarez, J., and Andersen, J. K. (2021). mTORC2: The Other mTOR in Autophagy Regulation. *Aging Cell* 20 (8), 13421. doi:10.1111/ACEL.13431

Barrow-McGee, R., Kishi, N., Joffre, C., Ménard, L., Hervieu, A., Bakhouche, B. A., et al. (2016). Beta 1-Integrin-C-Met Cooperation Reveals an Inside-In Survival Signalling on Autophagy-Related Endomembranes. *Nat. Commun.* 7 (Jun), 11942. doi:10.1038/NCOMMS11942

Bays, J. L., Campbell, H. K., Heidema, C., Sebbagh, M., and Demali, K. A. (2017). Linking E-Cadherin Mechanotransduction to Cell Metabolism through Force-Mediated Activation of AMPK. *Nat. Cell Biol.* 19 (6), 724–731. doi:10.1038/NCB3537

Bertocchi, C., Wang, Y., Ravasio, A., Hara, Y., Wu, Y., Sailov, T., et al. (2017). Nanoscale Architecture of Cadherin-Based Cell Adhesions. *Nat. Cell Biol.* 19 (1), 28–37. doi:10.1038/ncb3456

Bertrand, M., Petit, V., Jain, A., Amsellem, R., Johansen, T., Larue, L., et al. (2015). SQSTM1/p62 Regulates the Expression of Junctional Proteins through Epithelial-Mesenchymal Transition Factors. *Cell Cycle* 14 (3), 364–374. doi:10.4161/15384101.2014.987619

Bjørkøy, G., Lamark, T., Pankiv, S., Øvervatn, A., Brech, A., and Johansen, T. (2009). *Chapter 12 Monitoring Autophagic Degradation of p62/SQSTM1*, 181–197.

Block, M. R., Brunner, M., Ziegelmeyer, T., Lallemand, D., Pezet, M., Chevalier, G., et al. (2020). The Mechano-Sensitive Response of β1 Integrin Promotes SRC-Positive Late Endosome Recycling and Activation of Yes-Associated Protein. *J. Biol. Chem.* 295 (39), 13474–13487. Sep. 2020. doi:10.1074/jbc.RA120.013503

Boya, P., Reggiori, F., and Codogno, P. (2013). Emerging Regulation and Functions of Autophagy. *Nat. Cell Biol.* 15 (7), 713–720. doi:10.1038/ncb2788

Buchheit, C. L., Weigel, K. J., and Schafer, Z. T. (2014). Cancer Cell Survival during Detachment from the ECM: Multiple Barriers to Tumour Progression. *Nat. Rev. Cancer* 14 (9), 632–641. doi:10.1038/nrc3789

Burridge, K., and Guilluy, C. (2016). Focal Adhesions, Stress Fibers and Mechanical Tension. *Exp. Cell Res.* 343 (1), 14–20. doi:10.1016/j.yexcr.2015.10.029

Carmignac, V., Svensson, M., Körner, Z., Elowsson, L., Matsumura, C., Gawlik, K. I., et al. (2011). Autophagy Is Increased in Laminin α2 Chain-Deficient Muscle and its Inhibition Improves Muscle Morphology in a Mouse Model of MDC1A. *Hum. Mol. Genet.* 20 (24), 4891–4902. doi:10.1093/hmg/ddr427

Case, N., Thomas, J., Sen, B., Styner, M., Xie, Z., Galior, K., et al. (2011). Mechanical Regulation of Glycogen Synthase Kinase 3β (GSK3β) in Mesenchymal Stem Cells Is Dependent on Akt Protein Serine 473 Phosphorylation via mTORC2 Protein. *J. Biol. Chem.* 286 (45), 39450–39456. doi:10.1074/jbc.M111.265330

Castagnaro, S., Chrisam, M., Cescon, M., Braghetta, P., Grumati, P., and Bonaldo, P. (2018). Extracellular Collagen VI Has Prosurvival and Autophagy Instructive Properties in Mouse Fibroblasts. *Front. Physiol.* 9 (AUG), 1129. doi:10.3389/FPHYS.2018.01129/BIBTEX

Cecconi, F. (2012). c-Cbl Targets Active Src for Autophagy. *Nat. Cell Biol.* 14 (1), 48–49. doi:10.1038/ncb2413

Chang, C.-H., Bijian, K., Qiu, D., Su, J., Saad, A., Dahabieh, M. S., et al. (2017). Endosomal Sorting and C-Cbl Targeting of Paxillin to Autophagosomes Regulate Cell-Matrix Adhesion Turnover in Human Breast Cancer Cells. *Oncotarget* 8 (19), 31199–31214. doi:10.18632/oncotarget.16105

Chen, H.-T., Liu, H., Mao, M.-J., Tan, Y., Mo, X.-Q., Meng, X.-J., et al. (2019). Crosstalk between Autophagy and Epithelial-Mesenchymal Transition and its Application in Cancer Therapy. *Mol. Cancer* 18 (1), 101. doi:10.1186/S12943-019-1030-2

Claude-Taupin, A., Codogno, P., and Dupont, N. (2021). Links between Autophagy and Tissue Mechanics. *J. Cell Sci.* 134 (17). Sep. 2021. doi:10.1242/JCS.258589

Dahl, S. v., Schliess, F., Reissmann, R., Görg, B., Weiergräber, O., Kocalkova, M., et al. (2003). Involvement of Integrins in Osmosensing and Signaling toward Autophagic Proteolysis in Rat Liver. *J. Biol. Chem.* 278 (29), 27088–27095. doi:10.1074/JBC.M210699200

Damiano, V., Spessotto, P., Vanin, G., Perin, T., Maestro, R., and Santarosa, M. (2020). The Autophagy Machinery Contributes to E-Cadherin Turnover in Breast Cancer. *Front. Cell Dev. Biol.* 8 (Jun), 545–2020. doi:10.3389/FCELL.2020.00545/FULL

Das, G., Shravage, B. V., and Baehrecke, E. H. (2012). Regulation and Function of Autophagy during Cell Survival and Cell Death. *Cold Spring Harb. Perspect. Biol.* 4, a008813. doi:10.1101/cshperspect.a008813

Dupont, N., and Codogno, P. (2016). Autophagy Transduces Physical Constraints into Biological Responses. *Int. J. Biochem. Cell Biol.* 79, 419–426. doi:10.1016/J.BIOCEL.2016.08.021

Dupont, S., Morsut, L., Aragona, M., Enzo, E., Giulitti, S., Cordenonsi, M., et al. (2011). Role of YAP/TAZ in Mechanotransduction. *Nature* 474 (7350), 179–183. doi:10.1038/nature10137

Durbeej, M. (2015). Laminin-α2 Chain-Deficient Congenital Muscular. *Dystrophy* 2015, 31–60. doi:10.1016/bs.ctm.2015.05.002"

Eliopoulos, A. G., Havaki, S., and Gorgoulis, V. G. (2016). DNA Damage Response and Autophagy: A Meaningful Partnership. *Front. Genet.* 7 (NOV), 204. doi:10.3389/fgene.2016.00204

Evans, R. J., Sundaramurthy, V., and Frickel, E.-M. (2018). The Interplay of Host Autophagy and Eukaryotic Pathogens. *Front. Cell Dev. Biol.* 6 (SEP), 118. doi:10.3389/fcell.2018.00118

Filomeni, G., De Zio, D., and Cecconi, F. (2015). Oxidative Stress and Autophagy: the Clash between Damage and Metabolic Needs. *Cell Death Differ.* 22 (3), 377–388. doi:10.1038/CDD.2014.150

Galluzzi, L., Pietrocola, F., Levine, B., and Kroemer, G. (2014). Metabolic Control of Autophagy. *Cell* 159 (6), 1263–1276. doi:10.1016/J.CELL.2014.11.006

Geiger, B., and Bershadsky, A. (2002). Exploring the Neighborhood: Adhesion-Coupled Cell Mechanosensors. *Cell* 110 (2), 139–142. doi:10.1016/S0092-8674(02)00831-0

Geng, J., Baba, M., Nair, U., and Klionsky, D. J. (2008). Quantitative Analysis of Autophagy-Related Protein Stoichiometry by Fluorescence Microscopy. *J. Cell Biol.* 182 (1), 129–140. doi:10.1083/jcb.200711112

Gómez-Sánchez, R., Tooze, S. A., and Reggiori, F. (2021). Membrane Supply and Remodeling during Autophagosome Biogenesis. *Curr. Opin. Cell Biol.* 71, 112–119. doi:10.1016/j.ceb.2021.02.001

Gubbiotti, M. A., and Iozzo, R. V. (2015). Proteoglycans Regulate Autophagy via Outside-In Signaling: an Emerging New Concept. *Matrix Biol.* 48, 6–13. doi:10.1016/j.matbio.2015.10.002

Hernández-Cáceres, M. P., Munoz, L., Pradenas, J. M., Pena, F., Lagos, P., Aceiton, P., et al. (2021). Mechanobiology of Autophagy: The Unexplored Side of Cancer. *Front. Oncol.* 11, 421. doi:10.3389/FONC.2021.632956/BIBTEX

Ingber, D. E. (2008). Tensegrity-based Mechanosensing from Macro to Micro. *Prog. Biophysics Mol. Biol.* 97 (2–3), 163–179. Jun. 2008. doi:10.1016/j.pbiomolbio.2008.02.005

Iskratsch, T., Wolfenson, H., and Sheetz, M. P. (2014). Appreciating Force and Shape - the Rise of Mechanotransduction in Cell Biology. *Nat. Rev. Mol. Cell Biol.* 15 (12), 825–833. doi:10.1038/NRM3903

Kanchanawong, P., Shtengel, G., Pasapera, A. M., Ramko, E. B., Davidson, M. W., Hess, H. F., et al. (2010). Nanoscale Architecture of Integrin-Based Cell Adhesions. *Nature* 468 (7323), 580–584. doi:10.1038/nature09621

Kaur, J., and Debnath, J. (2015). Autophagy at the Crossroads of Catabolism and Anabolism. *Nat. Rev. Mol. Cell Biol.* 16 (8), 461–472. doi:10.1038/nrm4024

Kenific, C. M., and Debnath, J. (2016). NBR1-dependent Selective Autophagy Is Required for Efficient Cell-Matrix Adhesion Site Disassembly. *Autophagy* 12 (10), 1958–1959. doi:10.1080/15548627.2016.1212789

Kim, N.-G., and Gumbiner, B. M. (2015). Adhesion to Fibronectin Regulates Hippo Signaling via the FAK-Src-Pi3k Pathway. *J. Cell Biol.* 210 (3), 503–515. doi:10.1083/JCB.201501025

Kim, N.-G., Koh, E., Chen, X., and Gumbiner, B. M. (2011). E-cadherin Mediates Contact Inhibition of Proliferation through Hippo Signaling-Pathway Components. *Proc. Natl. Acad. Sci. U.S.A.* 108 (29), 11930–11935. doi:10.1073/pnas.1103345108

Kimura, T., Jia, J., Claude-Taupin, A., Kumar, S., Choi, S. W., Gu, Y., et al. (2017). Cellular and Molecular Mechanism for Secretory Autophagy. *Autophagy* 13 (6), 1084–1085. doi:10.1080/15548627.2017.1307486

King, J. S., Veltman, D. M., and Insall, R. H. (2011). The Induction of Autophagy by Mechanical Stress. *Autophagy* 7 (12), 1490–1499. doi:10.4161/AUTO.7.12.17924

Kyriakakis, E., Frismantiene, A., Dasen, B., Pfaff, D., Rivero, O., Lesch, K.-P., et al. (2017). T-cadherin Promotes Autophagy and Survival in Vascular Smooth Muscle Cells through MEK1/2/Erk1/2 axis Activation. *Cell. Signal.* 35, 163–175. doi:10.1016/J.CELLSIG.2017.04.004

Li, X., Roife, D., Kang, Y., Dai, B., Pratt, M., and Fleming, J. B. (2016). Extracellular Lumican Augments Cytotoxicity of Chemotherapy in Pancreatic Ductal Adenocarcinoma Cells via Autophagy Inhibition. *Oncogene* 35 (37), 4881–4890. doi:10.1038/ONC.2016.20

Liang, N., Zhang, C., Dill, P., Panasyuk, G., Pion, D., Koka, V., et al. (2014). Regulation of YAP by mTOR and Autophagy Reveals a Therapeutic Target of Tuberous Sclerosis Complex. *J. Exp. Med.* 211 (11), 2249–2263. doi:10.1084/JEM.20140341

Lock, R., and Debnath, J. (2008). Extracellular Matrix Regulation of Autophagy. *Curr. Opin. Cell Biol.* 20 (5), 583–588. doi:10.1016/j.ceb.2008.05.002

Lőrincz, P., and Juhász, G. (2020). Autophagosome-Lysosome Fusion. *J. Mol. Biol.* 432 (8), 2462–2482. Apr. 2020. doi:10.1016/J.JMB.2019.10.028

Low, B. C., Pan, C. Q., Shivashankar, G. V., Bershadsky, A., Sudol, M., and Sheetz, M. (2014). YAP/TAZ as Mechanosensors and Mechanotransducers in Regulating Organ Size and Tumor Growth. *FEBS Lett.* 588 (16), 2663–2670. doi:10.1016/j.febslet.2014.04.012

Lu, P., Takai, K., Weaver, V. M., and Werb, Z. (2011). Extracellular Matrix Degradation and Remodeling in Development and Disease. *Cold Spring Harb. Perspect. Biol.* 3 (12), a005058. doi:10.1101/cshperspect.a005058

Martino, F., Perestrelo, A. R., Vinarský, V., Pagliari, S., and Forte, G. (2018). Cellular Mechanotransduction: From Tension to Function. *Front. Physiol.* 9 (JUL), 824. doi:10.3389/FPHYS.2018.00824

Sheetz, M., and Yu, H. (2018). *The Cell as a Machine*.

Müller, M., Schmidt, O., Angelova, M., Faserl, K., Weys, S., Kremser, L., et al. (2015). The Coordinated Action of the MVB Pathway and Autophagy Ensures Cell Survival during Starvation. *Elife* 4, e07736. doi:10.7554/ELIFE.07736

Neill, T., Schaefer, L., and Iozzo, R. V. (2014). Instructive Roles of Extracellular Matrix on Autophagy. *Am. J. Pathology* 184 (8), 2146–2153. doi:10.1016/J.AJPATH.2014.05.010

Nguyen, T. M. B., Subramanian, I. V., Kelekar, A., and Ramakrishnan, S. (2007). Kringle 5 of Human Plasminogen, an Angiogenesis Inhibitor, Induces Both Autophagy and Apoptotic Death in Endothelial Cells. *Blood* 109 (11), 4793–4802. doi:10.1182/blood-2006-11-059352

Nguyen, T. M. B., Subramanian, I. V., Xiao, X., Ghosh, G., Nguyen, P., Kelekar, A., et al. (2009). Endostatin Induces Autophagy in Endothelial Cells by Modulating Beclin 1 and β-catenin Levels. *J. Cell. Mol. Med.* 13 (9b), 3687–3698. doi:10.1111/j.1582-4934.2009.00722.x

Ning, L., Xu, Z., Furuya, N., Nonaka, R., Yamada, Y., and Arikawa-Hirasawa, E. (2015). Perlecan Inhibits Autophagy to Maintain Muscle Homeostasis in Mouse Soleus Muscle. *Matrix Biol.* 48, 26–35. doi:10.1016/j.matbio.2015.08.002

Oakes, P. W., and Gardel, M. L. (2014). Stressing the Limits of Focal Adhesion Mechanosensitivity. *Curr. Opin. Cell Biol.* 30, 68–73. doi:10.1016/j.ceb.2014.06.003

Ortiz-Rodriguez, A., and Arevalo, M.-A. (2020). The Contribution of Astrocyte Autophagy to Systemic Metabolism. *Int. J. Mol. Sci.* 21 (7), 2479. doi:10.3390/IJMS21072479

Panciera, T., Azzolin, L., Cordenonsi, M., and Piccolo, S. (2017). Mechanobiology of YAP and TAZ in Physiology and Disease. *Nat. Rev. Mol. Cell Biol.* 18 (12), 758–770. doi:10.1038/nrm.2017.87

Park, J.-M., Jung, C. H., Seo, M., Otto, N. M., Grunwald, D., Kim, K. H., et al. (2016). The ULK1 Complex Mediates MTORC1 Signaling to the Autophagy Initiation Machinery via Binding and Phosphorylating ATG14. *Autophagy* 12 (3), 547–564. doi:10.1080/15548627.2016.1140293

Pavel, M., Renna, M., Park, S. J., Menzies, F. M., Ricketts, T., Füllgrabe, J., et al. (2018). Contact Inhibition Controls Cell Survival and Proliferation via YAP/TAZ-autophagy axis. *Nat. Commun.* 9 (1), 1–18. doi:10.1038/s41467-018-05388-x

Pavel, M., Park, S. J., Frake, R. A., Son, S. M., Manni, M. M., Bento, C. F., et al. (2021). α-Catenin Levels Determine Direction of YAP/TAZ Response to Autophagy Perturbation. *Nat. Commun.* 12 (1), 1703. doi:10.1038/s41467-021-21882-1

Petherick, K. J., Williams, A. C., Lane, J. D., Ordóñez-Morán, P., Huelsken, J., Collard, T. J., et al. (2013). Autolysosomal β-catenin Degradation Regulates Wnt-Autophagy-P62 Crosstalk. *EMBO J.* 32 (13), 1903–1916. doi:10.1038/EMBOJ.2013.123

Pocaterra, A., Romani, P., and Dupont, S. (2020). YAP/TAZ Functions and Their Regulation at a Glance. *J. Cell Sci.* 133 (2), 425. doi:10.1242/JCS.230425

Poluzzi, C., Casulli, J., Goyal, A., Mercer, T. J., Neill, T., and Iozzo, R. V. (2014). Endorepellin Evokes Autophagy in Endothelial Cells. *J. Biol. Chem.* 289 (23), 16114–16128. Jun. 2014. doi:10.1074/JBC.M114.556530

Poluzzi, C., Nastase, M.-V., Zeng-Brouwers, J., Roedig, H., Hsieh, L. T.-H., Michaelis, J. B., et al. (2019). Biglycan Evokes Autophagy in Macrophages via a Novel CD44/Toll-like Receptor 4 Signaling axis in Ischemia/reperfusion Injury. *Kidney Int.* 95 (3), 540–562. Mar. 2019. doi:10.1016/j.kint.2018.10.037

Ponpuak, M., Mandell, M. A., Kimura, T., Chauhan, S., Cleyrat, C., and Deretic, V. (2015). Secretory Autophagy. *Curr. Opin. Cell Biol.* 35, 106–116. doi:10.1016/j.ceb.2015.04.016

Qiang, L., and He, Y.-Y. (2014). Autophagy Deficiency Stabilizes TWIST1 to Promote Epithelial-Mesenchymal Transition. *Autophagy* 10 (10), 1864–1865. doi:10.4161/auto.32171

Rabinowitz, J. D., and White, E. (2010). Autophagy and Metabolism. *Science* 330, 1344–1348. doi:10.1126/science.1193497

Ravanan, P., Srikumar, I. F., and Talwar, P. (2017). Autophagy: The Spotlight for Cellular Stress Responses. *Life Sci.* 188, 53–67. doi:10.1016/j.lfs.2017.08.029

Santarosa, M., and Maestro, R. (2021). The Autophagic Route of E-Cadherin and Cell Adhesion Molecules in Cancer Progression. *Cancers* 13 (24), 6328. doi:10.3390/CANCERS13246328

Schaefer, L., and Dikic, I. (2021). Autophagy: Instructions from the Extracellular Matrix. *Matrix Biol.* 100-101, 1–8. Jun. 2021. doi:10.1016/j.matbio.2021.06.002

Shang, L., and Wang, X. (2011). AMPK and mTOR Coordinate the Regulation of Ulk1 and Mammalian Autophagy Initiation. *Autophagy* 7 (8), 924–926. doi:10.4161/auto.7.8.15860

Sharifi, M. N., Mowers, E. E., Drake, L. E., Collier, C., Chen, H., Zamora, M., et al. (2016). Autophagy Promotes Focal Adhesion Disassembly and Cell Motility of Metastatic Tumor Cells through the Direct Interaction of Paxillin with LC3. *Cell Rep.* 15 (8), 1660–1672. doi:10.1016/J.CELREP.2016.04.065

Shattil, S. J., Kim, C., and Ginsberg, M. H. (2010). The Final Steps of Integrin Activation: the End Game. *Nat. Rev. Mol. Cell Biol.* 11 (4), 288–300. doi:10.1038/nrm2871

Short, B. (2015). Integrin Signaling Tranquilizes Hippo. *J. Cell Biol.* 210 (3), 364. doi:10.1083/JCB.2103ITI3

Sudol, M. (1994). Yes-associated Protein (YAP65) Is a Proline-Rich Phosphoprotein that Binds to the SH3 Domain of the Yes Proto-Oncogene Product. *Oncogene* 9 (8), 2145–2152. https://pubmed.ncbi.nlm.nih.gov/8035999/.

Sun, Y., Zhang, J., and Ma, L. (2014). α-Catenin. *Cell Cycle* 13 (15), 2334–2339. doi:10.4161/cc.29765

Totaro, A., Zhuang, Q., Panciera, T., Battilana, G., Azzolin, L., Brumana, G., et al. (2019). Cell Phenotypic Plasticity Requires Autophagic Flux Driven by YAP/TAZ Mechanotransduction. *Proc. Natl. Acad. Sci. U.S.A.* 116 (36), 17848–17857. doi:10.1073/pnas.1908228116

Vlahakis, A., and Debnath, J. (2017). The Interconnections between Autophagy and Integrin-Mediated Cell Adhesion. *J. Mol. Biol.* 429 (4), 515–530. doi:10.1016/J.JMB.2016.11.027

Vogel, V. (2018). Unraveling the Mechanobiology of Extracellular Matrix. *Annu. Rev. Physiol.* 80 (1), 353–387. doi:10.1146/annurev-physiol-021317-121312

Wang, P., Gong, Y., Guo, T., Li, M., Fang, L., Yin, S., et al. (2019). Activation of Aurora A Kinase Increases YAP Stability via Blockage of Autophagy. *Cell Death Dis.* 10 (6), 432. doi:10.1038/s41419-019-1664-4

Xia, S., Yim, E. K. F., and Kanchanawong, P. (2019). Molecular Organization of Integrin-Based Adhesion Complexes in Mouse Embryonic Stem Cells. *ACS Biomater. Sci. Eng.* 5 (8), 3828–3842. doi:10.1021/acsbiomaterials.8b01124

Yurchenco, P. D., McKee, K. K., Reinhard, J. R., and Rüegg, M. A. (2018). Laminin-deficient Muscular Dystrophy: Molecular Pathogenesis and Structural Repair Strategies. *Matrix Biol.* 71-72 (72), 174–187. doi:10.1016/j.matbio.2017.11.009

Zaidel-Bar, R. (2013). Cadherin Adhesome at a Glance. *J. Cell Sci.* 126 (2), 373–378. Jan. 2013. doi:10.1242/JCS.111559

Zhang, J.-m., Wang, Z.-g., He, Z.-y., Qin, L., Wang, J., Zhu, W.-t., et al. (2022). Cyclic Mechanical Strain with High-Tensile Triggers Autophagy in Growth Plate Chondrocytes. *J. Orthop. Surg. Res.* 17117 (1), 1–13. Mar. 2022. doi:10.1186/S13018-022-03081-W

Zhao, B., Wei, X., Li, W., Udan, R. S., Yang, Q., Kim, J., et al. (2007). Inactivation of YAP Oncoprotein by the Hippo Pathway Is Involved in Cell Contact Inhibition and Tissue Growth Control. *Genes Dev.* 21 (21), 2747–2761. Nov. 2007. doi:10.1101/GAD.1602907

Zhuo, C., Ji, Y., Chen, Z., Kitazato, K., Xiang, Y., Zhong, M., et al. (2013). Proteomics Analysis of Autophagy-Deficient Atg7−/− MEFs Reveals a Close Relationship between F-Actin and Autophagy. *Biochem. Biophysical Res. Commun.* 437 (3), 482–488. doi:10.1016/j.bbrc.2013.06.111

**Conflict of Interest:** The authors declare that the research was conducted in the absence of any commercial or financial relationships that could be construed as a potential conflict of interest.

**Publisher's Note:** All claims expressed in this article are solely those of the authors and do not necessarily represent those of their affiliated organizations, or those of the publisher, the editors and the reviewers. Any product that may be evaluated in this article, or claim that may be made by its manufacturer, is not guaranteed or endorsed by the publisher.

frontiers | Frontiers in Cell and Developmental Biology

ORIGINAL RESEARCH
published: 22 June 2022
doi: 10.3389/fcell.2022.912318

# A Stiff Extracellular Matrix Favors the Mechanical Cell Competition that Leads to Extrusion of Bacterially-Infected Epithelial Cells

*Raúl Aparicio-Yuste*[1,2], *Marie Muenkel*[2], *Andrew G. Clark*[3,4], *María J. Gómez-Benito*[1]* and *Effie E. Bastounis*[2]*

[1]Department of Mechanical Engineering, Multiscale in Mechanical and Biological Engineering (M2BE), Instituto de Investigación en Ingeniería de Aragón (I3A), University of Zaragoza, Zaragoza, Spain, [2]Interfaculty Institute of Microbiology and Infection Medicine, Cluster of Excellence "Controlling Microbes to Fight Infections" (CMFI, EXC 2124), University of Tübingen, Tübingen, Germany, [3]Institute of Cell Biology and Immunology/Stuttgart Research Center Systems Biology, University of Stuttgart, Stuttgart, Germany, [4]Center for Personalized Medicine, University of Tübingen, Tübingen, Germany

OPEN ACCESS

**Edited by:**
Tsuyoshi Hirashima,
Kyoto University, Japan

**Reviewed by:**
Takumi Kawaue,
Kyoto University, Japan
Tamal Das,
Max Planck Institute for Intelligent Systems, Germany

***Correspondence:**
María J. Gómez-Benito
gomezmj@unizar.es
Effie E. Bastounis
effie.bastounis@uni-tuebingen.de

**Specialty section:**
This article was submitted to Cell Adhesion and Migration, a section of the journal Frontiers in Cell and Developmental Biology

**Received:** 05 April 2022
**Accepted:** 31 May 2022
**Published:** 22 June 2022

**Citation:**
Aparicio-Yuste R, Muenkel M, Clark AG, Gómez-Benito MJ and Bastounis EE (2022) A Stiff Extracellular Matrix Favors the Mechanical Cell Competition that Leads to Extrusion of Bacterially-Infected Epithelial Cells. Front. Cell Dev. Biol. 10:912318. doi: 10.3389/fcell.2022.912318

Cell competition refers to the mechanism whereby less fit cells ("losers") are sensed and eliminated by more fit neighboring cells ("winners") and arises during many processes including intracellular bacterial infection. Extracellular matrix (ECM) stiffness can regulate important cellular functions, such as motility, by modulating the physical forces that cells transduce and could thus modulate the output of cellular competitions. Herein, we employ a computational model to investigate the previously overlooked role of ECM stiffness in modulating the forceful extrusion of infected "loser" cells by uninfected "winner" cells. We find that increasing ECM stiffness promotes the collective squeezing and subsequent extrusion of infected cells due to differential cell displacements and cellular force generation. Moreover, we discover that an increase in the ratio of uninfected to infected cell stiffness as well as a smaller infection focus size, independently promote squeezing of infected cells, and this phenomenon is more prominent on stiffer compared to softer matrices. Our experimental findings validate the computational predictions by demonstrating increased collective cell extrusion on stiff matrices and glass as opposed to softer matrices, which is associated with decreased bacterial spread in the basal cell monolayer *in vitro*. Collectively, our results suggest that ECM stiffness plays a major role in modulating the competition between infected and uninfected cells, with stiffer matrices promoting this battle through differential modulation of cell mechanics between the two cell populations.

**Keywords: finite element analysis, cell competition, cell mechanics, traction and monolayer stresses, infection, *Listeria monocytogenes*, epithelial cells, cell extrusion**

## 1 INTRODUCTION

Cell competition refers to the process whereby less fit cells, often denoted "losers", are sensed and eliminated by more fit neighboring cells, accordingly referred to as "winners" (Gradeci et al., 2021). This competition between losers and winners is essential for tissue homeostasis but it also emerges during tissue development and can play a role in various pathologies including tumor development

(Meyer et al., 2014; Moreno et al., 2019). Although the chemical signals driving the battle between two different cell populations are relatively more explored, an increasing number of studies showcases that mechanical signals such as differential sensitivity to compression during cell crowding are also crucial in driving such interactions (Gradeci et al., 2019; Matamoro-Vidal and Levayer, 2019; Moreno et al., 2019; Bastounis et al., 2021b).

We recently showed that a mechanical competition during late infection drives the collective onslaught and elimination of infected cells out of the epithelial monolayer (Bastounis et al., 2021b). When epithelial cells in monolayer get exposed to low dosage of *Listeria monocytogenes* (*L.m.*), a food-borne facultative intracellular bacterial pathogen, some sparse cells in the monolayer get infected. Within several hours *L.m.* has the ability to replicate intracellularly and spread intercellularly to larger domains containing hundreds of cells. However, at later times post-infection (~16 h post-infection, hpi), we discovered that surrounding uninfected cells ("winners") responding to innate immune signals, migrate actively and in a coordinated fashion towards the infection focus, squeezing the infected cells and eventually forcing their massive extrusion (mounding) out of the monolayer (~24 hpi). Infected cells ultimately die, possibly due to their forceful separation out of their basement membrane, thus suggesting that the "infection mounding" process is a beneficial for the host process in that it obstructs infection dissemination through the cell monolayer. Interestingly, this competition that leads to infected cell elimination is mechanical in nature, and depends on: 1) a decrease in contractility (i.e., traction stresses exerted by the cells on their matrix) of infected as opposed to uninfected neighbors; 2) a lowering in the passive stiffness of infected as opposed to uninfected neighbors, and 3) the presence of cell-cell adhesions since lack of those completely stalls mound formation. Thus, it appears that cell-matrix and cell-cell force transduction as well as cellular stiffness are crucial determinants in driving the mechanical competition that emerges during infection (Bastounis et al., 2022).

Studies conducted over the last decades have underlined the importance of extracellular matrix (ECM) stiffness in regulating important cellular functions such as cell motility, by modulating the cellular traction forces, the intercellular forces and/or the bulk stiffness of cells (Solon et al., 2007; Califano and Reinhart-King, 2010; Borau et al., 2011; Bastounis et al., 2019; Doss et al., 2020). In many different cell types, as ECM stiffness increases, cellular traction force generation also increases, and this effect is particularly prominent in single cells and to a lesser degree in cellular monolayers (Lampi et al., 2016; Zhao et al., 2018; Bastounis et al., 2019). Given that ECM stiffness increases in certain pathologies including fibrotic diseases, cancer and inflammatory bowel diseases (IBD) (Lampi and Reinhart-King, 2018; Onfroy-Roy et al., 2020), it remains still an open question whether varying ECM stiffness would promote or limit infected cell extrusion and, if so, what would be the physical and molecular mechanisms involved. Interestingly, Gradeci et al., showed that changes in the ratio of winner-to-loser cell stiffness altered the kinetics of cell competition between wild-type MDCK cells and cells depleted for the polarity protein scribble, although ECM stiffness was not addressed in this study (Gradeci et al., 2021). Another study on competition between wild-type cells and oncogenically-transformed ones did show that increasing ECM stiffness attenuates extrusion of transformed cells by tuning the dynamic localization of filamin, an important F-actin crosslinking protein (Pothapragada et al., 2022). Thus, it remains unclear whether there are generalizable mechanisms that could predict how ECM stiffness impacts cell behavior and thus the outcome of a cell competition, and whether those would apply to epithelial cells that are infected with intracellular bacterial pathogens, which can replicate intracellularly and also dynamically spread from cell to cell.

To explore such questions, studies often rely on *in vitro* experiments. Such experiments have provided great insight into how intracellular bacteria efficiently spread through epithelial cells in monolayer and on the physical cellular processes that bacteria often hijack to promote their dissemination (Lamason et al., 2016; Faralla et al., 2018). However, *in silico* cellular models and simulations can complement *in vitro* experiments and even facilitate the design of future *in vitro* experiments (Brodland, 2015; Gradeci et al., 2021). Such models present several advantages such as that they are controllable, time-efficient, and cost-effective. Moreover, one can tweak one parameter at a time, thus making it easier to reach causal conclusions. Nevertheless, they do need *in vitro* and *in vivo* models to be properly validated and calibrated. Most infection computational models have focused on the dynamics of bacterial spread in colonies considering contact forces, bacterial growth or the interaction between bacteria and biomaterials (Delarue et al., 2016). Others have focused on the dynamics of intracellular bacterial spread, with the bacteria modeled as particles within two-dimensional (2-D) rigid host cells (Ortega et al., 2019). Recently, we developed a computational, three-dimensional (3-D) finite element model (FEM) to explore the physical mechanisms that drive the squeezing and extrusion of bacterially infected cells during their competition with surrounding uninfected cells (Bastounis et al., 2021b). This simplified model not only validated our experimental results but also predicted that cell-cell adhesions between infected cells and immediate surrounders are necessary for mound formation, a result that we then confirmed experimentally.

Herein, we introduce an extension to our infection computational model with the aim to investigate the previously overlooked role of ECM stiffness in potentially modulating the forceful extrusion of infected cells by uninfected surrounders (Bastounis et al., 2021b). The parameters of our model are selected based on our experimental observations. We find that increasing ECM stiffness promotes the collective squeezing and subsequent extrusion of infected cells due to differential cellular displacements and cellular force generation. Moreover, we discover that an increase in the ratio of uninfected to infected cell stiffness as well as a smaller infection focus size, both promote squeezing of infected cells, and this phenomenon is more prominent on stiffer as opposed to softer matrices. Our experimental findings validate the computational predictions by demonstrating increased collective cell extrusion on stiff

matrices and glass as opposed to softer matrices, accompanied by decreased bacterial spread in the basal cell monolayer *in vitro*. Collectively, our results suggest that ECM stiffness plays a major role in modulating the competition between "winner" uninfected cells and "loser" infected cells with stiffer matrices promoting this battle through differential modulation of cell mechanics between the two cell populations.

# 2 MATERIALS AND METHODS

## 2.1 *In vitro* Experiments

### 2.1.1 Cell Culture

Epithelial cells type II MDCK cells and type II MDCK cells that express E-cadherin-RFP were a generous gift of the Nelson lab, Stanford University (Perez et al., 2008). MDCK cells were cultured in high glucose DMEM medium (Thermofisher; 10741574) containing 4.5 g/L glucose and supplemented with 10% fetal bovine serum (Thermofisher, 10270106), further referred to as DMEM. They were kept at a temperature of 37°C with 5% $CO_2$.

### 2.1.2 Bacterial Infections and Fixation of Samples for Imaging Mound Volumes

Infection of MDCK cells with *L.m.* was performed as described previously (Bastounis et al., 2021a) using *L.m.* strain JAT607 (Species: *L.m.* 1043S, Genotype/Description: ActAp::mTagRFP) (Ortega et al., 2017). JAT607 *L.m.* express mtagRFP under the control of the ActA promoter which makes them fluoresce only few hours (approximately 4 h) after host cell internalization. The infection assays were performed as follows. Three days prior to infection frozen glycerol stocks of JAT607 were streaked on BHI agar plates containing 7.5 μg/ml chloramphenicol and 0.2 mg/ml streptomycin and incubated at 37°C for approximately 1 day until colonies formed. 16 h prior to infection a 2 ml BHI solution supplemented with 7.5 μg/ml chloramphenicol and 0.2 mg/ml streptomycin was inoculated with JAT607 bacteria from the BHI agar plates and incubated for approximately 16 h in the dark, without shaking at room temperature (RT). The optical density ($OD_{600}$) of the overnight culture was then measured (approximately 0.4), the bacterial cultures were centrifuged at 2000 g for 5 min at RT and re-suspended in 2 ml PBS. 0.5 ml of this bacterial suspension was added to 24 ml DMEM medium. MDCK cells were washed once with PBS and 1 ml of the bacterial-containing DMEM solution was added to each well, so that the resulting multiplicity of infection (MOI) was approximately ~ 250 bacteria/cell. After 30 min incubation at 37°C with 5% $CO_2$ the bacterial-containing medium was exchanged with DMEM containing 5 μg/ml Hoechst (Fisher, 11534886) to stain the host cell nuclei. After 10 min incubation under the previous conditions MDCK cells were washed with PBS three times and DMEM containing 20 μg/ml gentamycin (Fisher, 15820243) was added. 24 h post-infection MDCK cells were washed once again with PBS after which 4% methanol free paraformaldehyde (Thermofisher, 28906) in PBS was added in each well for 10 min. Samples were then washed once in PBS and stored in PBS at 4°C until microscopy imaging was performed.

### 2.1.3 Mound Volume Calculations, Infection Focus Area and Total Bacterial Fluorescence

Volumes of infected extruded cell domains were calculated using custom MATLAB scripts as previously explained in detail (Bastounis et al., 2021a). Briefly, images of Hoechst-stained MDCK nuclei and of the bacterial fluorescence in and around a given infection focus were taken using a z-spacing of 0.2 μm. For imaging, we used a Zeiss AxioObserver SD Spinning Disk microscope, equipped with an Axiocam 503 mono CCD camera and a Plan-Apochromat 40x/1.4 Oil DIC objective. For imaging the Hoechst-stained host cell nuclei, we used the blue channel (excitation laser 405 nm, emission filter 450/50 nm) and for the mtagRFP-expressing bacteria, we used the red channel: (excitation laser 561 nm, emission filter 600/50 nm). Nuclei located at the basal cell monolayer were disregarded, and only z-stacks of nuclei of cells extruded from that monolayer were considered. We calculated the area occupied by cells in each z-stack slice individually and then determined the total volume of the extruded area using this information. As a proxy of space occupied by cells, we used the signal of the nuclei and applied an alpha shape for area calculations (MATLAB (MathWorks) function alphaShape). First, the individual z-stack images were flatfield and background corrected and then a multi-threshold (between 5 and 3 thresholds per image) was applied to create a binary mask of the nuclei. The area occupied by cells in each z-stack was then multiplied by the height between z-stack slices, in order to determine the volume of the entire extruded domain. The codes used are written in Matlab (Mathworks) and can be found at https://github.com/ebastoun/Infection_mound_volume. For calculating the size of infection foci, we used epifluorescence imaging, and specifically an inverted Nikon Eclipse Ti2 with an EMCCD camera (Andor Technologies) and a 40 × 0.60 NA Plan Fluor air objective. The system was controlled by the MicroManager software. To characterize the efficiency of *L.m.* spread from cell-to-cell through the MDCK cell monolayer, we measured the size of infection foci as previously described (Ortega et al., 2019). The codes used are written in Matlab (Mathworks) and can be found at https://github.com/Fabianjr90/Listeria_focus_shape_analysis.

### 2.1.4 Fabrication of Polyacrylamide Hydrogels

Polyacrylamide hydrogels were prepared on glass bottom 24-well plates (MatTek, P24G-1.5-13-F) as previously described in (Bastounis et al., 2021a). Briefly, glass coverslips were pretreated with 0.5 M NaOH for 30 min at RT, rinsed with water and then incubated for 5 min at RT with 2% APTS ((3-Aminopropyl)triethoxysilane, Sigma, A3648-100ML) in 95% EtOH. After a rinsing step with water, the coverslips were incubated for another 30 min with 0.5% Glutaraldehyde (Sigma, G6257-100ML), rinsed again with water and finally dried at RT. Polyacrylamide hydrogels were built in two layers to achieve a sufficiently thin layer of fluorescent beads on the surface. 3 kPa hydrogels were prepared by mixing 5% acrylamide (Sigma, A4058-100ML) and 0.1% bis-acrylamide (Fisher, 10193523). 35 kPa hydrogels were prepared by mixing 8% acrylamide and 0.26% bis-acrylamide. Polymerization was

initiated by addition of 0.06% ammonium persulfate and 0.43% TEMED. The first layer was created by adding 3.6 μL of the acrylamide mix on the glass coverslip and covering it with a 12 mm round cover glass which was gently pressed on top to create a flat surface. During the polymerization of the first layer, an additional 0.03% of 0.2 μm fluorescent beads (Thermofisher, F8810) was added to the second layer solution. 2.4 μL of the second layer solution were then added on top of the first layer after removing the glass coverslip. A 12 mm round cover glass was again placed on top to generate a flat polyacrylamide layer containing tracer beads. After polymerization and removal of the round cover glass the gels maintained in 50 mM Hepes, pH 7.5 were UV sterilized for 1 h. Gels were then activated by addition of 200 μL of 0.5% w/v heterobifunctional cross-linker Sulfo-SANPAH (Fisher; 10474005) in 1% dimethyl sulfoxide (DMSO, Sigma, D2650-5X10ML) in 50 mM HEPES, pH 7.5, and exposure to UV light ($\lambda$ = 302 nm) for 10 min. The Sulfo-SANPAH was then removed, and the gels were washed with 50 mM HEPES, pH 7.5. Gels were incubated overnight with 200 μL of 0.25 mg/ml rat tail collagen (Thermofisher, A1048301) and the following day washed once with 50 mM HEPES, pH 7.5 and stored in the same buffer.

### 2.1.5 Traction Force Microscopy (TFM)

TFM was performed as previously described (Lamason et al., 2016; Bastounis et al., 2021a). More specifically, polyacrylamide hydrogels were equilibrated for 30 min at 37°C with cell media prior to cell seeding. Subsequently, $4 \times 10^5$ MDCK cells were seeded on the hydrogels. 24 h post-seeding, cells were stained with 5 μg/ml Hoechst stain (Fisher, 11534886) for 10 min. Cells were washed once in PBS, and 1 ml of Leibovitz's L-15 Medium, without phenol red (Fisher, 21083027) and supplemented with 10% fetal bovine serum was added in each well. The multi-well plate was then transferred to the microscope stage for initiation of time-lapse acquisition. For imaging we used an inverted Nikon Eclipse Ti2-E with a Prime BSI sCMOS camera (Teledyne Photometrics) using a ×40 CFI Super Plan Fluor ADM ELWD objective with a NA 0.60 and the NIS-Elements Microscope Imaging Software (Nikon Metrology). Multi-channel images of the phase contrast image of cells, the nuclei fluorescence and the tracer beads' fluorescence were taken every 10 min. After approximately 8 h of imaging, the acquisition was stopped and 10% SDS was added to the wells to detach the cells from their matrix. Reference images of the beads in the undisturbed hydrogel surface were acquired. We used a particle image velocimetry-like technique to compare the image of the tracer beads at each instance of time with the reference image to determine the beads' displacements in MATLAB (MathWorks) (Gui and Wereley, 2002). We used interrogation windows of 48 × 24 pixels (window size × overlap). Calculations of the two-dimensional traction stresses that MDCK cells in monolayer exert on the hydrogel are described elsewhere (Bastounis et al., 2014; Lamason et al., 2016) and were performed also in MATLAB. For calculation of the number of nuclei in each recording the images of Hoechst-stained nuclei were used and the Fiji (ImageJ) plugin Trackmate was used for segmentation of cell nuclei and tracking. Output data from Trackmate were exported as xml files and read in Matlab to calculate cell speed based on nuclear motion (Hayer et al., 2016).

### 2.1.6 Monolayer Stress Microscopy (MSM)

Traction stresses were retrieved from the TFM measurements described above. We assumed perfect cell-substrate adhesions and complete confluence of the monolayer. We neglected the components of the traction forces perpendicular to the plane of the monolayer. We considered the traction forces exerted by the cells on their substrate are equal to the forces applied by the substrate on the cells but pointing in the opposite direction (third Newton's law). We also assumed that the monolayer displayed a uniform and constant thickness, which was much smaller than the dimensions of the monolayer. Thus, this methodology is only valid at the early stages of intercellular bacterial spread, just before mounding occurs (approximately 16 h post-infection). The domain was discretized with a finite element mesh (element size 28.352 μm) and monolayer stresses (that is inter- and intra-cellular stresses) were computed under the hypothesis of plane stress [for more details of the methodology see Tambe et al. (2011); Aparicio-Yuste et al. (2022)]. We initially considered that the stiffness of both uninfected surrounders and infected cells is the same ($R_E = 1$) but also ran MSM for the case where infected cells are four-fold softer than uninfected surrounders ($R_E = 4$) and confirmed that qualitatively the tangential monolayer stresses did not look significantly different. Custom-written scripts are publicly available at https://github.com/ebastoun/Monolayer-Stress-Microscopy.

## 2.2 *In silico* Experiments

We built an *in silico* model of the epithelial monolayer considering both infected and uninfected surrounder cells as well as cell-cell and cell-ECM adhesion contacts. The monolayer resided on either a 3 kPa, 10 kPa, 20 or 35 kPa ECM or on a 2 GPa glass coverslip.

### 2.2.1 The Geometry and Material Properties of our Model

Although the ECM microstructural composition and mechanical properties are highly complex and vary at different length scales (Sun, 2021), for simplicity we assumed that the matrix where cells reside is a continuum medium and as such an average value of its mechanical properties was chosen. We also assumed that the matrix is an elastic isotropic material, as proposed previously (Kandemir et al., 2018). Epithelial cells were simulated in this work as individual components. Although the cell monolayer structure and functions arise from individual entities or cells, we assumed that cells in the monolayer act as a collective since every given cell interacts with its neighbors through cell-cell junctions. Cells were simulated as regular hexagonal prisms despite the more diverse topology they show in a monolayer. This hexagonal pattern is the most frequent polygon type in cell monolayers since it maximizes the space filled by cells in a tissue (Lecuit and Lenne, 2007). Each individual cell was divided into three domains: the contractile, the adhesive and the expanding/protrusive (Bastounis et al., 2021b). This enabled us to simplify the cell architecture and allowed us to simulate computationally cell dynamic changes,

such as cellular deformations, cell-ECM traction adhesions and cell protrusions. Additionally, both active and passive cell behaviors were considered in our model. The passive was simulated so to account for the stiffness arising from the cellular cytoskeleton (e.g., the microtubules or intermediate filament network), whereas the active accounted for the actomyosin contractile apparatus and actin polymerization (Moreo et al., 2008; Borau et al., 2011).

### 2.2.2 Cell-ECM and Cell-Cell Mechanical Interactions Considered

The mechanical interactions of cells with their ECM and between each other were taken into account in our model through cell-ECM contact and cell-cell interactions, respectively. Cell-cell interactions were considered through a continuum approach, assuming perfect adhesions through a linear elastic thin element that transmits the loads between cells. Thus, cells were able to sense forces from their neighbors and interact with them. Cell-ECM adhesions were simulated by a cohesive contact interaction between two surfaces, the given cell and the ECM. The higher the stiffness of the contact, the more difficult the relative displacement between the two surfaces. Furthermore, we worked under the assumption of perfect cell-ECM adhesions, meaning that all the force is transmitted from the cell to the ECM and vice versa.

### 2.2.3 Assumed Mechanotransduction Scheme Used by Non-infected Cells to Detect Infection

To better examine the impact of infection on the collective squeezing that leads to extrusion of infected epithelial cells, we simulated a cellular cycle where certain cells (e.g., infected) are allowed to experience different degrees of protrusion or strength of adhesion to their ECM. In settings not involving infection (uninfected case), all cells presented the same mechanical behavior. To simulate infection, cells infected with bacteria were assumed to have distinct mechanical properties as compared to neighboring uninfected cells (infected case). More specifically and based on previous experimental findings, infected cells were considered softer and with decreased active stiffness as compared to neighboring uninfected cells (Bastounis et al., 2021b).

For simplicity, bacterial infection was considered fixed, that is, bacteria did not spread or replicate intracellularly during the simulation period. For both infected and uninfected monolayers, we analyzed the cellular behavior over the course of this cellular cycle and according to a mechanotransduction scheme. Briefly, all cells were first exposed to a round of contraction in order to sense and bear loads from their neighboring cells and their ECM. This contraction resulted in cell-ECM displacements and allowed the cells to move with respect to their ECM. If the cell-ECM displacements were large when cells contract, we assumed new cell-ECM adhesions would form, followed by a new cycle of contraction. Once new adhesions were formed, cellular protrusion would occur only if the given cell exhibited asymmetry in its tensional distribution (in the direction of the stress gradient). This means that the cell actively responded to the non-symmetrical distribution of the stresses by protruding. In our simulations, this occurred only during infection and was observed only in uninfected cells close to the infection focus. These cells exhibited tensional asymmetry and thus protruded towards the direction of minimum stress, which lied at the edge of the infection focus.

To summarize, we simulated and examined the 3D dynamics of a cell monolayer residing on a flat ECM of a given stiffness in two particular cases: uninfected and infected condition. We considered that in the uninfected case, all cells in the monolayer exhibited similar mechanical properties and interactions with their ECM. However, under conditions involving infection, cell-ECM traction adhesions of infected cells were weakened compared to uninfected surrounder cells, and new strong traction adhesions were formed along surrounding uninfected cells (where the cells sense there was a large relative displacement with respect to the ECM). In turn, the uninfected cells protruded towards the infection focus due to their tensional asymmetry.

### 2.2.4 Implementation

The mechanical interactions of infected cells with surrounding uninfected cells in a monolayer were analyzed with a three-dimensional, finite element model using the commercial software ABAQUS CAE 6.14 (Dassault systèmes Simulia Corporation). The general model is described elsewhere (Bastounis et al., 2021b). Based on this model, we built here a FEM of infected and uninfected cell monolayers taking into account additional considerations as outlined below. Regarding the geometry, we assumed two main entities: the ECM and the cells. The parameters characterizing the cells and ECM domains are summarized (**Table 1**) and were chosen based on previous *in vitro* studies (O'Dea and King, 2012; Schmedt et al., 2012; Escribano et al., 2019). Overall, 217 individual cells and their junctions coexisted, collectively forming a hexagonal monolayer. This hexagonal pattern of the monolayer was selected to avoid artifacts arising from asymmetries.

Our model is composed by four main domains: uninfected cells ($\Omega_{uninf}$), infected cells ($\Omega_{\mathrm{inf}}$), cell-cell junctions ($\Omega_{junction}$) and ECM ($\Omega_{ECM}$). Concerning material properties, cells and ECM were assumed to behave as linear elastic materials (Escribano et al., 2018); as we were not interested in long-term effects, we just simulated a short period of time (one contraction-protrusion cycle). The Young's modulus (measure of stiffness) of uninfected surrounder cells was considered of the order of 1,000 Pa, while that of infected cells of 250 Pa, as previously measured by Atomic Force Microscopy (AFM) experiments (Bastounis et al., 2021b). Cell-cell junctions were assumed to have a Young's modulus of 1,000 Pa, and this value was selected so that the continuity of the mechanical properties of the monolayer is preserved. To interrogate the role of ECM stiffness on infected cell squeezing, we considered different ECM stiffnesses in our simulations, namely: soft, stiff and glass matrices with elastic moduli of 3 kPa, 10 kPa, 20 kPa, 35 kPa, and 2 GPa, respectively, values corresponding to the polyacrylamide hydrogels we built for our *in vitro* experiments and the glass coverslips commonly used. The Poisson's ratios were set to 0.48 (Moreo et al., 2008) and 0.45 (Alvarez-González

**TABLE 1 |** Summary of the features of the computational model.

| Domain | Geometry | Dimensions ($\mu m$) | Mechanical properties |
|---|---|---|---|
| ECM | Rectangular prism | 220 × 220 × 20 (LxWxH) | $E$ = 3, 10, 20, 35 kPa and 2 GPa (glass); $\nu$ = 0.45 |
| Cell | Hexagonal prism | Hexagon side length = 7; Height = 7 | $E$ = 1 kPa (uninfected cells); $\nu$ = 0.48 |
| Cell-cell junction | Thin sheet | 7 × 0.01 × 7 (LxWxH) | $E$ = 1 kPa; $\nu$ = 0 |

**TABLE 2 |** Mechanical parameters in our computational model.

| | Uninfected | | Infected | |
|---|---|---|---|---|
| | $E$ (Pa) | $\nu$ (–) | $E$ (Pa) | $\nu$ (–) |
| Passive | 500 | 0.48 | 125 | 0.48 |
| Active | 500 | 0 | 125 | 0 |
| Cell | 1,000 | — | 250 | — |

et al., 2017) for cells and ECM, respectively, since both are nearly incompressible. We modeled the cells' active and passive behavior through two different meshes in the model with shared nodes. This strategy allowed us to separate active protrusion and contraction from passive contractility.

In order to simulate cell contraction and expansion/protrusion, we followed the analogy of the thermoelastic expansion equations governing volumetric changes in both contraction and expansions processes (Vujošević and Lubarda, 2002; Hervás-Raluy et al., 2019; Nieto et al., 2020). We assumed the contractile part of the cell was exposed to a negative volumetric change, decreasing its volume. On the contrary, the protruding part of the cell was subjected to a positive volumetric change, increasing its volume. According to our experimental observations, minimal change in cell height was observed during contraction, remarking the importance of cell contraction in the plane of the monolayer. Therefore, we assumed non-isotropic contraction, i.e., the contraction occurred just in the plane of the monolayer to avoid changes in cell height. In such manner, we generated area changes in the plane of the monolayer, but not in the normal direction, thus the Poisson's coefficient of the active part was set to zero and the same was applied to cell-cell junctions (**Table 1** and **Table 2**).

Cell-cell interactions were simulated in ABAQUS through a contact interaction, where the normal direction of the contact behaved as a "hard" contact and the tangential direction acted as a frictionless surface. However, we used surface-to-surface contacts to model cell-ECM adhesions under the assumption of perfect cell-ECM adhesions. The domain of the cell referred to as adhesion site was attached to the ECM surface via a cohesive contact. The strength of the traction adhesions (active cellular adhesion sites that transmit traction forces to the ECM) was determined by the stiffness of the matrix **K** and its stiffness coefficients ($K_x$, $K_y$, $K_z$), where $K_x$ and $K_y$ are the two shear traction adhesions in the plane of the ECM and $K_z$ the normal traction adhesion to the plane of the ECM. The higher the stiffness coefficients $K_i$, the stronger the traction adhesion between the cell and the ECM is and the lower the $K_i$, the weaker the traction adhesion is. By tuning these parameters, we differentiated three types of cell-ECM contacts. The first type of contact described the formation of new adhesions at the edge of the infection focus on the side of the surrounding uninfected cells, with the stiffness coefficients ($K_x$, $K_y$, $K_z$) = (10, 10, 10) kPa. These high values created a strong cell-ECM contact which is one of the mechanisms that uninfected cells use to fight against infected cells, by squeezing them and eventually eliciting their extrusion. The second type of contact is a general cell-ECM contact whose stiffness coefficients were set to (0,0,0.1) kPa. This condition represented a general cell-ECM attachment, meaning that cells could move in the plane but they could not be separated from the ECM. The third contact concerned infected cells which present weaker cell-ECM traction adhesions and therefore, we assumed their stiffness coefficients were (0,0,0.001) kPa. This distinction between infected and uninfected traction adhesion coefficients was not considered in our previous model (Bastounis et al., 2021b).

The ECM was meshed with standard linear hexahedral solid elements, whose mesh density was higher at the center of the upper surface. Both cell-cell junctions, regions of the cell referred to as protrusion and adhesion, were meshed with linear hexahedral solid elements in order to obtain coincident nodes and regular connectivity. The cell contraction part was meshed with linear triangular prisms to keep the continuity of the mesh. Additionally, to account for the passive and active behavior of the cell, we used two superimposed meshes to which we associated the mechanical properties of the active and passive part of the cell (**Table 2**). The model resulted in 93.948 nodes and 148.239 elements. As boundary conditions, we assumed all displacements were prevented at the bottom surface of the ECM. In addition, the displacements of all the cells that were at the edge of the monolayer were restricted. These conditions were consistent with our experimental setup. Furthermore, our *in vitro* experiments were performed by choosing the field of view to be near the center of the well on which the cellular monolayer was formed, thus edge effects should be negligible.

To provide novel insight into the role of ECM stiffness in promoting infected cell squeezing, we run simulations using our computational model. First, we tested the impact of ECM stiffness in mound formation by assigning distinct values of ECM stiffness. We considered matrices that are soft, stiff and infinitely stiff (i.e., glass) with an elastic modulus of 3 kPa, 10 kPa, 20 kPa, 35 kPa and 2 GPa, respectively. Second, we investigated how infection spread affects mounding by considering different size infection foci comprised by varying number of infected cells on both soft and stiff

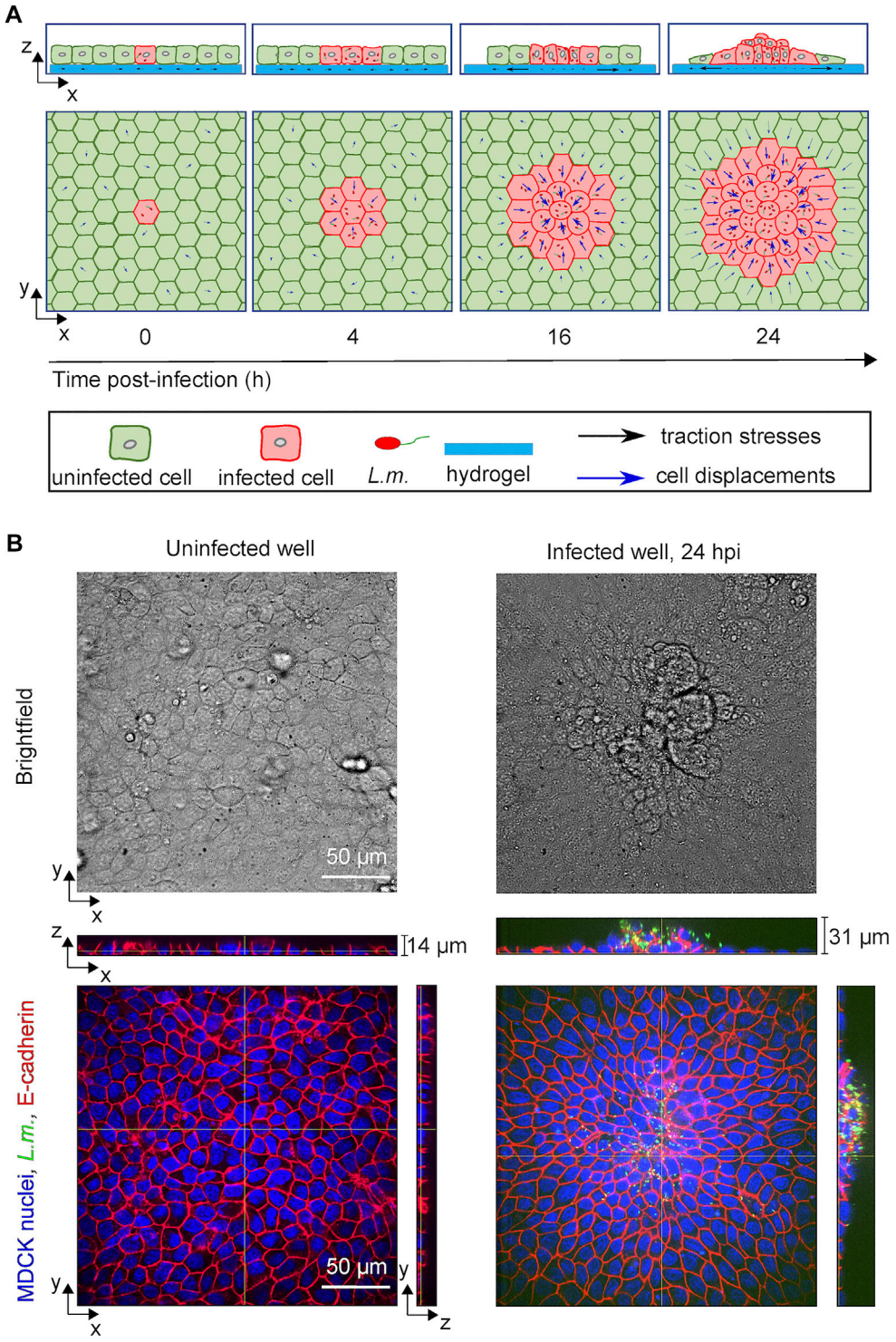


**FIGURE 1 |** *L.m.*-infected epithelial cells in monolayer get collectively extruded at late infection. **(A)** Schematic illustration showing the time course of *in vitro* infection of host epithelial cells with *L.m.* so that infection mounds emerge at late infection (24 hpi). Initially a single cell gets infected by *L.m.* (0 hpi), but as time proceeds bacteria replicate and spread to neighboring cells (4 hpi). Uninfected surrounder cells (green) start actively migrating towards the infection focus comprised by several infected cells (red), while softer and less contractile infected cells get squeezed (16 hpi) and eventually extruded (24 hpi) out of the cellular monolayer. **(B)** Representative brightfield image (top row) and orthogonal views (bottom row) of *L.m.* fluorescence in green, E-cadherin in red and MDCK nuclei in blue for cells originating from an uninfected well (left column) and from a *L.m.*-infected well with the field of view shown focused around and infection focus at 24 hpi (right column).

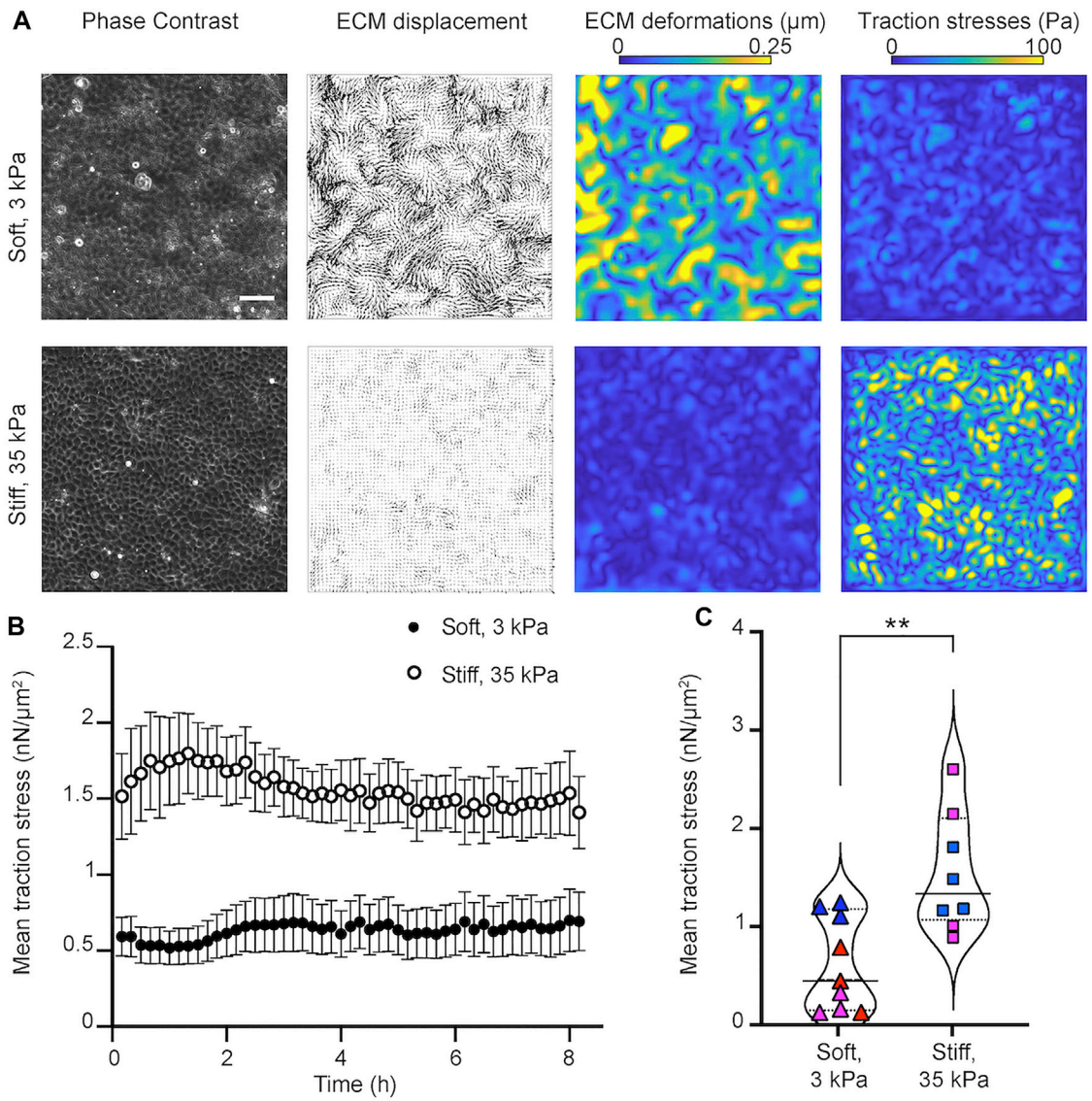


**FIGURE 2 |** Epithelial cells in monolayer exert higher traction stresses when residing on stiff as opposed to softer matrices. **(A)** Traction force microscopy performed on MDCK cells residing on soft, 3 kPa (upper row) and stiff, 35 kPa (bottom row) hydrogels. Columns of a representative time instance show: phase contrast image of cells, displacements imparted by the cells on the hydrogel (vectors), corresponding deformations (colormap shows magnitude, μm) and traction stresses exerted by cells (colormap shows magnitude, Pa). Scale bar is 50 μm. **(B)** Plot of the mean traction stress magnitude (*y*-axis) versus time (*x*-axis). Mean ± SEM are shown for $N = 8$ and $N = 9$ TFM recordings performed on stiff 35 kPa and soft 3 kPa gels, respectively. **(C)** Violin plots of the mean traction stress magnitude for all recordings and time points shown in panel **(B)**. Symbols show the time average of the mean traction stress for each recording. Same color points correspond to recordings performed the same day on different wells. Solid line indicates the mean and dotted the STD of all time averages. **: $p < 0.001$, Wilcoxon Ran Sum test.

matrices. Lastly, we examined how the ratio of uninfected to infected cell passive and active stiffness affects mound formation when ECM stiffness varies. We ran several cases within the same range of the ratio of uninfected to infected cell stiffness ($R_E$), which we defined as:

$$R_E = \frac{E_{uninf}}{E_{\text{inf}}} \tag{1}$$

where $E_{uninf}$ the Young's modulus of uninfected cells and $E_{\text{inf}}$ the Young's modulus of infected cells.

# 3 RESULTS

## 3.1 Epithelial Cells Exert Higher Traction Stresses When Residing on Stiff as Compared to Soft Matrices

We have shown that during late infection of epithelial cells with *L.m.* ( > 16 hpi) a mechanical competition takes place leading to squeezing of softer and less contractile infected cells by stiffer and more contractile uninfected surrounder cells, which actively

migrate with high speeds towards the infection focus (Bastounis et al., 2021b) (**Figure 1A**). As a result of this mechanical battle, infected cells are extruded out of the basal monolayer and pile up forming large 3D "mounds" whose height typically exceeds 30 μm, which is at least three-fold higher than the typical height of cells in non-infected cell monolayers (**Figure 1B**). Given that it is well known that cell mechanics are modulated by ECM stiffness, we hypothesized that ECM stiffness will impact cellular stiffness and traction force generation and that these, in turn, would impact formation of infection mounds. To assess whether ECM stiffness affects the traction stress-generating ability of cells and whether the magnitude of traction stresses is modulated based on ECM stiffness, we cultured Madin-Darby Canine Kidney (MDCK) epithelial cells as confluent monolayers on hydrogels of varying stiffness. We chose this cell line because it forms polarized and homogeneous monolayers in tissue culture and have broadly been used in studies examining *L.m.* infection (Ortega et al., 2019; Bastounis et al., 2021b). Cells were placed on collagen-I coated soft polyacrylamide hydrogels of 3 kPa or stiff hydrogels of 35 kPa. These values were chosen based on previous studies reporting that the elasticity of intestinal ECM broadly ranges from 1 to 68 kPa (Onfroy-Roy et al., 2020). Hydrogels were embedded with tracer beads such that, as cells in the monolayer pull on the hydrogels via their focal adhesions and on each other via cell-cell adhesions, tracer bead movement can be monitored via time-lapse microscopy. Using the fluorescence images of the beads we inferred the deformations that cells imparted on the gels and the traction stresses they exerted on to it through Traction Force Microscopy (TFM) (**Figure 2A** and **Supplementary Movie S1**). 3 kPa is the lowest stiffness we examined since as reported, MDCK on low stiffness gels ( < 3 kPa) do not form monolayers but rather aggregate-like structures (Balcioglu et al., 2020). 35 kPa gels are considered as our stiffest condition, since this was found to be the highest stiffness on which the cells can still deform the gels at enough resolution to be measured accurately with TFM (data not shown).

By seeding MDCK cells at a concentration of $4 \times 10^5$ cells per well, on wells from a 24-well plate, we found that MDCK were able to form confluent monolayers with similar number of cells on soft 3 kPa and stiff 35 kPa gels 24 h post-seeding (**Supplementary Figure S1A**). Moreover, at these high cell confluence conditions, the speed of migration of cells was minimal (~ 0.08 μm/min) and similar on soft and stiff hydrogels (**Supplementary Figure S1B**). Nevertheless, MDCK residing on stiff 35 kPa gels generated significantly higher traction stresses but imparted reduced deformations as opposed to the softer 3 kPa gels where deformations were higher but traction stresses were overall lower. As expected, the average traction stresses generated by cells pertaining in a field of view were significantly higher for cells residing on stiff as compared to softer matrices (**Figures 2B,C**). Therefore, we conclude that under conditions that do not involve infection and where epithelial cells form a highly confluent monolayer, that is, at steady state, cells exert higher traction forces on stiff 35 kPa hydrogels as opposed to softer 3 kPa ones.

## 3.2 Considerations and Assumptions of the Infection Computational Model That Accounts for the ECM Stiffness

Our experimental results demonstrate that epithelial cells in monolayer exert higher traction stresses when residing on stiff as opposed to softer matrices. Given this finding, we wondered whether ECM stiffness would similarly impact cell produced traction stresses if we were to use and further develop our model to run *in silico* infection experiments (Bastounis et al., 2021b). Using this model, in turn, we could examine how cellular traction stresses vary as a function of ECM stiffness also when a focus of infected cells is present within the monolayer.

Our computational model relies on certain simplifications, namely, the cells are considered as linear elastic hexagonal prisms and are divided in three domains: the contractile, the adhesive and the expanding/protrusive (**Figure 3A**). We model cell-cell junctions as linear elastic elements in contact to each other (**Figure 3B**), and cell-ECM traction adhesions (i.e., focal areas at the ventral side of cells where traction stresses are exerted onto the underlying matrix) as surface-to-surface contacts (**Figure 3C**). The strength of the traction adhesions is characterized by the matrix parameter **K**, which links cellular traction stresses to cell and matrix displacements in all three different directions. Given our previous study, we also take into account that uninfected surrounding cells exert higher traction stresses as compared to nearby infected cells (**Figure 3C**). In the case of infection, for simplicity we assume that bacteria cannot replicate intracellularly or spread from cell to cell, so cells are either infected (red) or not (green) and their total number is fixed. In our *in silico* 3D monolayer the mechanical parameters of cells are based on previous experimental measurements (Bastounis et al., 2021b), and ECM stiffness is chosen so that it matches our experimental results and *in vitro* measurements (**Figure 3D**). The simulations were run using a finite element method (FEM) approach which allowed us to analyze the cell displacements and stresses in the whole considered geometry and according to the mechanotransduction mechanism depicted in **Figure 3E**.

## 3.3 *In silico* Model Predicts That Increased ECM Stiffness Promotes Mounding by Enhancing Cell Displacements and the Traction Stresses That are Generated by Nearby Uninfected Cells

Through our *in silico* model, we examined first whether cells on soft 3 kPa ECM as compared to stiff 35 kPa ECM would impart increased ECM displacements and exert reduced traction stresses *in silico* similar to what we previously determined *in vitro* (**Figure 2**). Not only were we able to validate our computational model but given the time efficiency of running *in silico* experiments, we sought to predict how would cells behave on ECM of intermediate stiffness (namely 10 and 20 kPa) and on stiff (~2 GPa) glass typically used for *in vitro* experiments

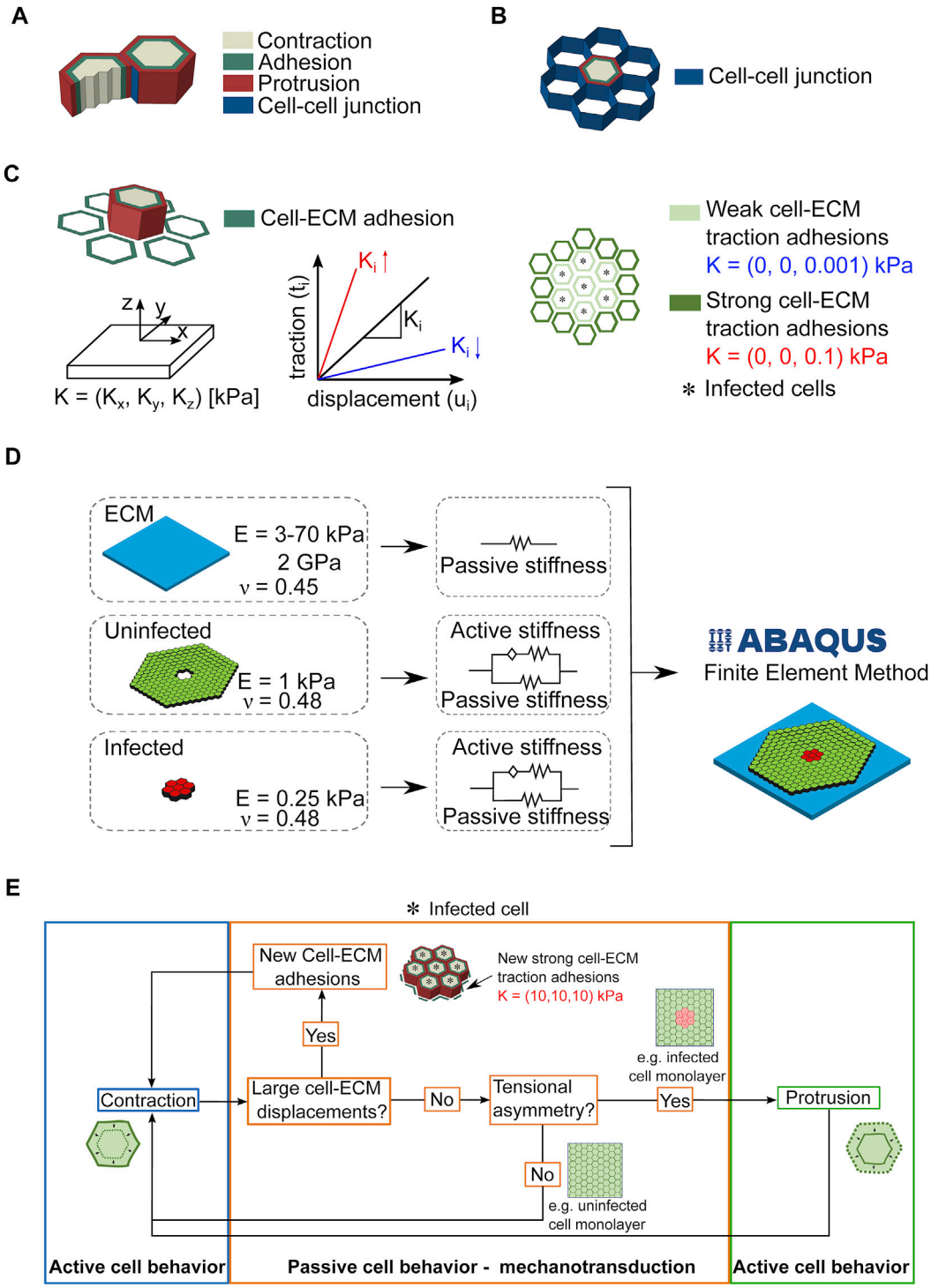


**FIGURE 3 |** Considerations and assumptions of the infection computational model. **(A,B)**. Sketch showing that cells are approximated in the computational model as hexagonal prisms that form cell-cell junctions with six neighboring cells and are partitioned in three domains: contractile, adhesive and protrusive **(A)**. Cell-cell junctions are modeled as linear thin elastic elements **(B)**. **(C)** Left schematic illustration shows how the cell produced traction stresses exerted to the ECM are modeled through surface-to-surface contacts between the cell and its ECM. The strength of the traction adhesions is characterized by **K** through its stiffness coefficients ($K_x$, $K_y$, $K_z$), with z being the normal direction to the surface, and x and y the directions in the plane of the surface. The higher (lower) the value of $K_i$ (for i equal to x, y or z), the stronger (weaker) the traction adhesions shown in red (blue). Right schematic illustrates an *in silico* infection focus with infected cells denoted by an asterisk. In our model, unlike surrounding uninfected cells, infected cells form very weak traction adhesions with the ECM. **(D)** Sketch depicting the domains of the Finite Element Model (FEM) used to compute cellular displacements and traction stresses exerted by cells on their ECM over time and during bacterial infection. The mechanical properties characterizing the domains are also shown. **(E)** Diagram illustrating the cell mechanotransduction mechanism that drives cell kinematics and dynamics in the cell computational model.

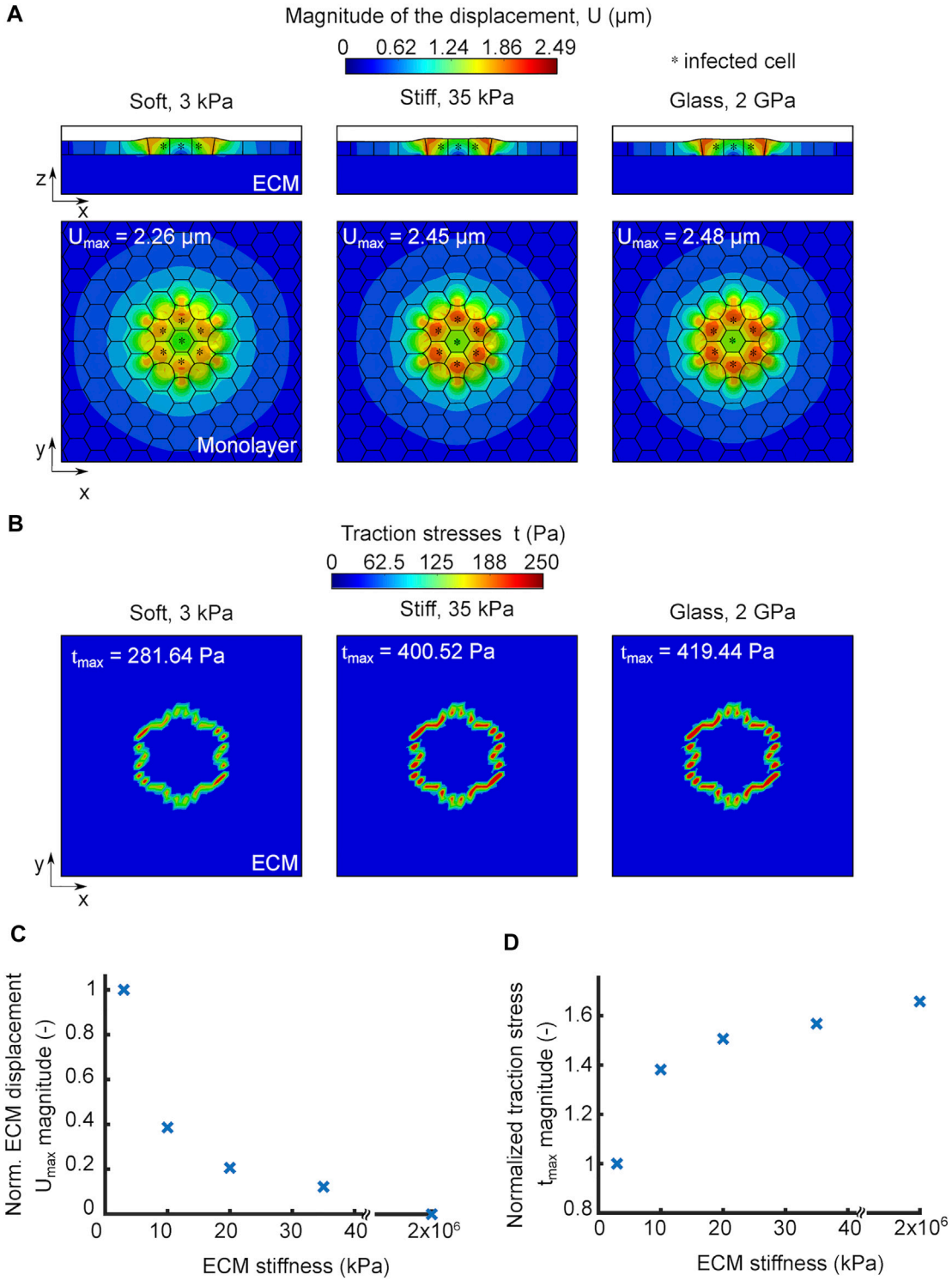


**FIGURE 4 |** *In silico* model predicts that increased ECM stiffness promotes infected cell squeezing by enhancing cell displacements and traction stresses of nearby uninfected cells. **(A)** Orthogonal view maps of the magnitude of cellular displacements U (μm) of *in silico* infected cells residing on soft 3 kPa gel (left), stiff 35 kPa gel (middle) and 2 GPa glass substrate (right). Top (x–y) and side (x–z) views are shown in all three cases, and infected cells are denoted by an asterisk. An infection focus comprised by 7 cells is considered. The maximum cell displacement is indicated. **(B)** Orthogonal view maps of traction stresses exerted onto the ECM by the cells shown in panel A which have been exposed to *in silico* infection and reside on soft, stiff and glass matrices. The maximum traction stress is indicated. **(C)** Plot showing magnitude of maximum cell displacement ($U_{max}$, *y*-axis) versus ECM stiffness (*x*-axis) for *in silico* cells in an infected monolayer. $U_{max}$ values are normalized relative to $U_{max}$ for cells residing on soft 3 kPa ECM. **(D)** Plot showing the magnitude of maximum traction stress ($t_{max}$, *y*-axis) versus ECM stiffness (*x*-axis) for *in silico* cells in an infected monolayer. $t_{max}$ values are normalized relative to $t_{max}$ for cells residing on soft 3 kPa ECM. For C-D the infection focus consists of $N = 7$ infected cells.

(**Supplementary Figures S2A,B**). We found that ECM displacements imparted by cells decreased following an exponential decay with increasing matrix stiffness. On the contrary, traction stresses increased monotonically reaching an asymptotic value at higher ECM stiffness.

We used our *in silico* model, to examine whether ECM stiffness would play a role in infection impacting the traction stress generating capacity of uninfected surrounder cells and, in turn, their mechanical competition with infected cells. We simulated infection by considering a cell monolayer residing on an ECM of a given stiffness and comprised by an infection focus containing just seven infected cells. We considered three different cases where the only parameter we varied was the ECM stiffness. Similar to our TFM experiments, we simulated infection in three different conditions, that is, with cells residing on 3 kPa ECM (soft), on 35 kPa ECM (stiff) or on a 2 GPa glass coverslip (glass), and let the simulations run for the same amount of time (one contraction-protrusion cycle). We noticed that cells in monolayers residing on a stiff matrix or glass exhibited larger cellular displacements compared to those residing on a soft matrix (**Figure 4A**). The maximum displacements observed in the simulations were 2.26, 2.45 and 2.48 μm for cells residing on soft matrix, stiff matrix and glass, respectively. Therefore, we can conclude that *in silico* cells within and near infection foci undergo larger displacements (directly related to squeezing of infected cells and subsequent mounding) when residing on stiff as opposed to softer ECM.

We previously showed that the ability of uninfected surrounders to produce strong traction stresses as they migrate towards the infected cells is key in squeezing the latter and eventually eliciting their extrusion. We thus wondered whether the more pronounced cellular displacements observed on stiff ECMs are driven by the increased traction stress generating capacity of uninfected, surrounding cells. To test that, we computed the traction stresses that cells exert on all three scenarios presented in **Figure 4A** and found the magnitude of traction stresses was higher for cells residing on stiffer matrices and predominantly high for surrounding, uninfected cells just at the edge of the focus since those are the ones that form protrusions in our model due to their tensional asymmetry (**Figure 4B**). The maximum traction stresses exerted by cells on the substrate were 281.64, 400.52 and 419.44 Pa for the soft, stiff and glass matrices, respectively. It is interesting that a 10-fold difference in ECM stiffness, when one compares cells residing on soft 3 kPa to stiff 35 kPa matrices, results in 42% increase in traction stresses, while a five order of magnitude increase in ECM stiffness, when comparing cells residing on 35 kPa hydrogels to 2 GPa glass, results in only 5% increase in the traction stress magnitude, suggesting that this mechanosensing mechanism is highly non-linear. Consistent with this, the change in maximum cellular displacements when comparing soft to stiff ECM is larger than when comparing stiff ECM to glass. When we ran simulations to examine the modulation of ECM displacements and traction stresses in a range of ECM stiffnesses for *in silico* cells during infection, we found the same trend as for non-infected cells (**Supplementary Figures S2A,B** and **Figures 4C,D**). The only difference between infected versus non-infected monolayers is that the extent to which traction forces increased with increasing ECM stiffness was larger during infection, likely because cells in this case are able to undergo protrusion due to development of stress asymmetries. Altogether, we conclude that increasing ECM stiffness gives rise to stronger cell-ECM traction stresses and enhanced cellular displacements, which is expected to increase infected cell squeezing and subsequent extrusion.

## 3.4 A Smaller Infection Focus or a Larger Difference in Stiffness of Uninfected Surrounders Relative to Infected Cells (Mounders) Increases the Squeezing of Infected Cells

Previous studies on endothelial cells infected with *L.m.* suggest that intercellular bacterial spread is enhanced when cells reside on softer ECM where enlarged infection foci are observed as compared to a stiffer ECM (Bastounis et al., 2018). To examine how the size of infection foci might impact cellular displacements and infected cell squeezing, we considered in our simulations two scenarios: 1) an infection focus comprised of just seven infected cells (small) and 2) a larger infection focus comprised of 19 infected cells (large). We also considered that these foci can be present on soft, stiff or glass ECM and run our simulations to compute the resulting cellular displacements (**Figure 5A**). We found that, independent of ECM stiffness, smaller infection foci result in cells undergoing larger cellular displacements and therefore, infected cell squeezing as compared to larger infection foci (**Figure 5B**). However, the percentage of reduction in maximum cell displacement when comparing small to large infection foci is more pronounced on stiffer as opposed to softer matrices, although the difference is subtle (**Figure 5C**).

An additional mechanical property that could change when host cells reside on soft versus stiff ECM is their passive stiffness arising from the organization of their cytoskeleton. Previous AFM measurements we conducted showed that, when residing on soft 3 kPa gels, infected cells at the edge of mounds exhibit a mean stiffness of 350 Pa while uninfected surrounding cells are 1,000 Pa stiff (Bastounis et al., 2021b). We also showed that changes in the ratio of uninfected to infected cell stiffness between the two populations are sufficient to lead to infected cell extrusion. Here we sought to determine whether and how changes in the ratio of uninfected to infected cell stiffness influence infected cell squeezing depending on ECM stiffness. To that end, we considered three distinct values of stiffness for uninfected surrounder cells, namely, 500, 1,000 and 2,000 Pa (left, center and right plot in **Figure 5D**). For each of these fixed values we ranged the stiffness of infected cells so that $R_E$ (the ratio of uninfected to infected cell stiffness) ranges from 1 to 16. In addition, as in previous *in silico* experiments, we considered three different degrees of ECM stiffness, namely, soft, stiff and glass. We found that, irrespective of the stiffness of surrounder cells, the larger the value of $R_E$, the higher the cellular displacements and thus infected cell squeezing. However, once $R_E$ becomes higher than approximately 5, a slightly asymptotic behavior emerges, and the displacements stop increasing monotonically as if they

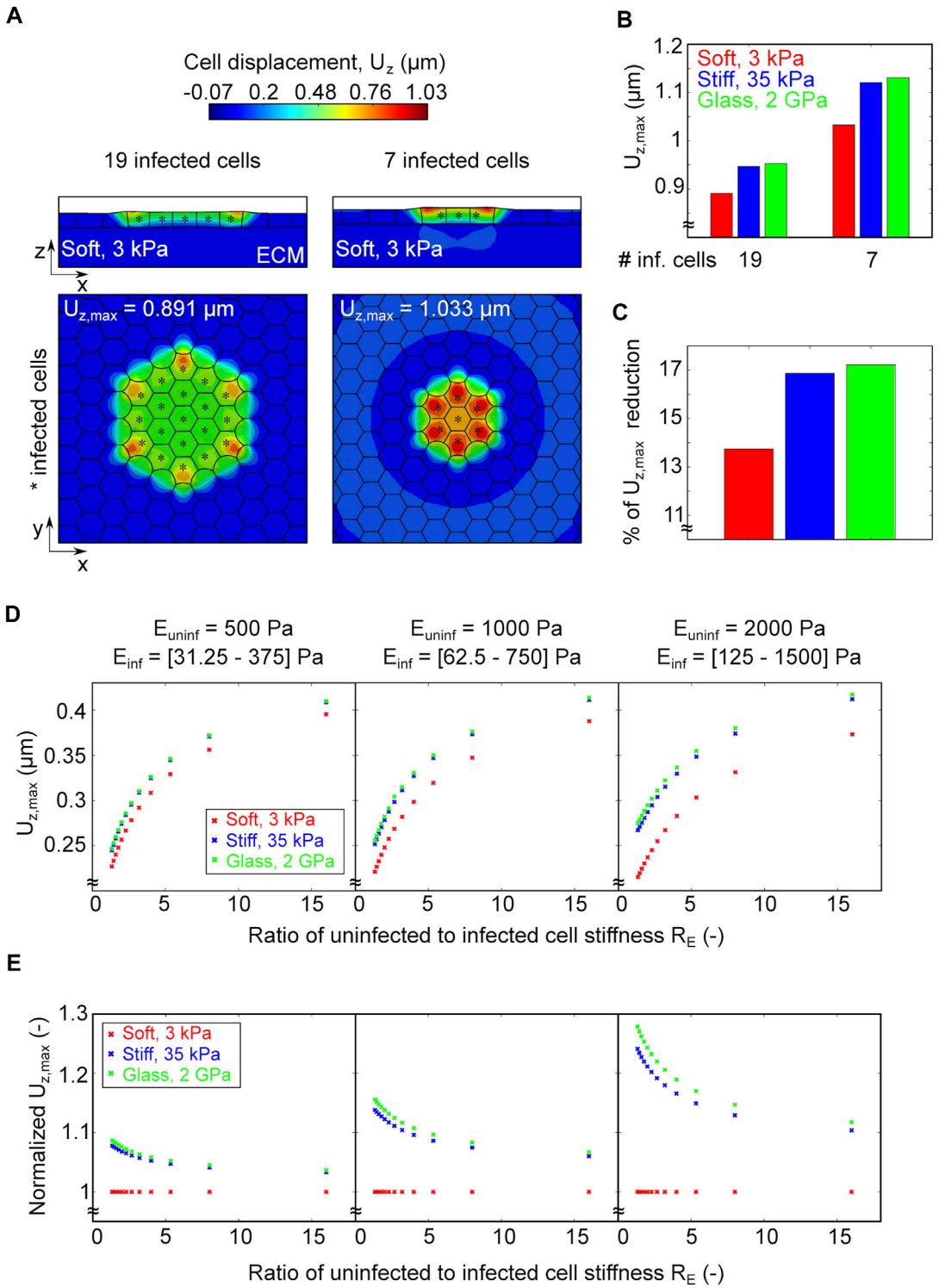


**FIGURE 5 |** A smaller infection focus or a larger difference in the ratio of uninfected to infected cell stiffness increase infected cell squeezing. **(A)** Ortoghonal view maps of the magnitude of cellular displacements in the vertical axis $U_z$ (μm) of *in silico* infected cells residing on a soft 3 kPa gel. On the left panel the focus is comprised by 19 infected cells denoted by asterisk, whereas on the right by 7. Top (x–y) and side (x–z) views are shown in both cases. **(B)** Barplot of the maximum vertical displacement $U_{z,max}$ of cells residing on soft (red), stiff (blue) and glass (green) matrices in the case of a focus comprised by 19 or 7 infected cells. **(C)** Barplot of the relative decrease in $U_{z,max}$ when comparing foci comprised of 7 relative to 19 infected cells for each of the varying stiffness matrices indicated in the panels above. **(D)** Plots of the maximum vertical displacement $U_{z,max}$ (μm, vertical axis) versus the ratio of uninfected to infected cell stiffness ($R_E$, horizontal axis) for *in silico* infection foci comprised of 7 infected cells and cells reside on soft 3 kPa (red), stiff 35 kPa (blue) and 2 GPa glass (green) matrix. In the simulations we assumed that the stiffness of the uninfected surrounder cells was fixed and equal to 500 Pa (left), or 1,000 Pa (middle), or 2,000 Pa (right), while infected cells could experience a range of stiffness shown below the plots ($R_E$ = 1–16). **(E)** Same as panel D but *y*-axis shows $U_{z,max}$ normalized to $U_{z,max}$ exhibited by cells on a soft 3 kPa matrix.

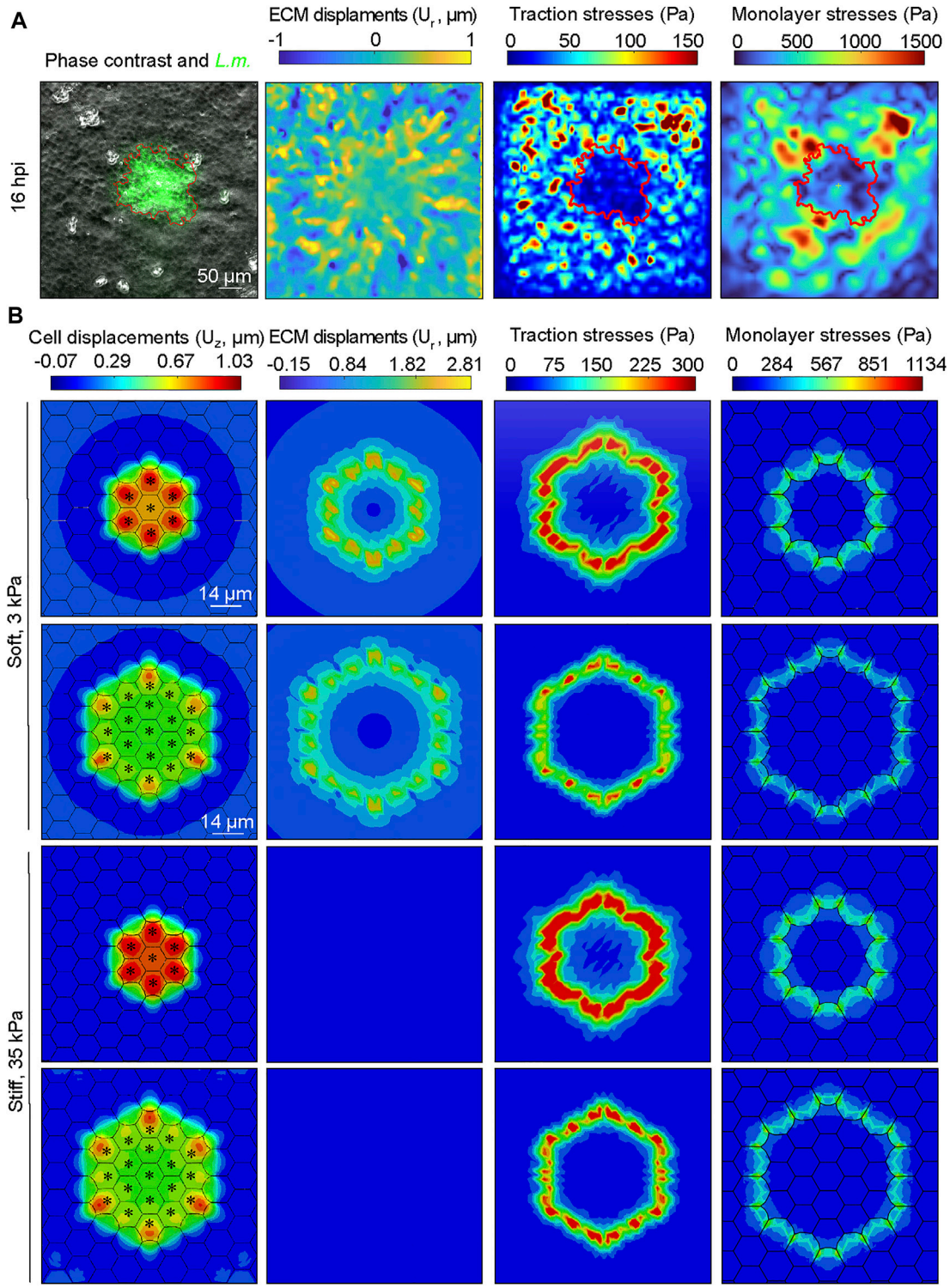


**FIGURE 6 |** Monolayer stresses are concentrated at the interface between infected and surrounding uninfected cells both experimentally and in our computational model. **(A)** Exemplary image of MDCK cells residing on a soft 3 kPa hydrogel and infected with *L.m.* Time point shown refers to 16 h. p.i. Field of view imaged is centered around an infection focus. Columns show from left to right: phase contrast image overlayed with *L.m.* fluorescence (green), radial ECM displacements ($U_r$: positive values indicate displacements pointing away from the focus center, μm), magnitude of traction stresses exerted by cells on the ECM (Pa), and magnitude of maximum monolayer tangential stresses (Pa). Red contour line indicates the area covered by infected cells (infection focus). **(B)** Same as panel A but the images depict the corresponding results of the infection computational simulations, with the exception of the first column which shows the configuration of the monolayer, the cell vertical displacements (μm) and where infected cells are denoted by an asterisk. First (second) row refers to a small (large) focus consisting of $N = 7$ ($N = 19$) infected cells residing on a soft 3 kPa ECM. Third (fourth) row refers to a small (large) focus consisting of $N = 7$ ($N = 19$) infected cells and cells reside on a stiff 35 kPa ECM.

had reached some plateau (**Figure 5E**). Moreover, we discovered that, irrespective of the stiffness of surrounder cells, for any given $R_E$ the maximum cell displacements are lower for cells residing on soft matrices, while the displacements for cells residing on stiff matrix or glass are approximately the same, with those exhibited on glass being slightly higher than on stiff 35 kPa ECM. Interestingly, we found that the higher the absolute value of stiffness of uninfected surrounder cells, the stronger the difference in cellular displacements that cells undergo depending on ECM stiffness (**Figures 5D,E**). That is, for a given $R_E$, if the stiffness of uninfected surrounders is larger (e.g., 2000 versus 500 Pa) then the effect of increased ECM stiffness in enhancing cellular displacements and therefore infected cell squeezing will be more prominent (**Figure 5E**). Altogether, these results suggest that a smaller infection focus and/or large differences in stiffness between surrounders and mounders, both promote large cell displacements and enhance infected cell squeezing. In addition, both these effects will be stronger if the ECM stiffness is increased, although for larger ECM stiffness the increase in cellular displacements stops being monotonic reaching asymptotic values which indicate a saturation in the cell mechanical sensitivity to its surrounding environment.

## 3.5 Monolayer Stresses are Concentrated at the Interface Between Infected and Surrounding Uninfected Cells Both Experimentally and in Our Computational Model

Our simulations indicate that increasing the ratio of uninfected to infected cell stiffness between uninfected and infected cells enhances cellular displacements and squeezing of infected cells pertaining in the focus. This suggests that inter- and intra-cellular stresses at the interface between the two cell populations might play a critical role in promoting mounding. To test this, we first calculated the radial ECM displacements imparted by cells, the traction stresses they exert and the cell-cell stresses *in vitro* in an actual infection experiment focusing our attention on a single growing *L.m.* infection focus. We used TFM and Monolayer Stress Microscopy (MSM) to measure traction stresses as well as intra- and inter-cellular stresses (referred from here on as monolayer stresses) of cells residing on a soft 3 kPa hydrogel, prior to infected cell extrusion (**Figure 6A** and **Supplementary Figure S3A**). As previously shown, we noticed that the radial deformations $U_r$ of surrounders just at the edge of the mound were large, indicative of them grabbing the ECM and pulling it away from the mound as they move directionally towards it. This traction stress orientation is not consistent with extrusion generated by a "purse-string" but is consistent with lamellipodial protrusion and directed cell migration (Kocgozlu et al., 2016). Thus, mounds are not caused by contraction of infected cells but rather by active crawling of uninfected surrounders that migrate toward the focus, squeezing and extruding the infected cells. Infected cells exerted reduced traction stresses compared to uninfected surrounders cells, consistent with previous findings (Bastounis et al., 2021b). Maximum monolayer tangential stresses were also lower for infected cells compared to uninfected surrounders (**Figure 6A**, fourth column). Interestingly, the maximum monolayer tangential stresses were localized at the edge of the infection focus, exactly where uninfected surrounder cells forcefully and actively moved towards the infection focus while pulling the ECM away from it, to eventually squeeze and extrude infected cells (**Figure 6A**, fourth column).

We then sought to examine whether similar behavior would be observed in our *in silico* model and used this opportunity as a means to validate our model but also to examine how monolayer stresses would be modulated *in silico* under conditions of varying ECM stiffness and focus size (**Figure 6B** and **Supplementary Figure S3B**). Consistent with the *in vitro* observations, radial ECM displacements were positive for the surrounder uninfected cells proximal to the infection focus and much larger for cells residing on soft as opposed to stiffer ECM, (**Figure 6B**, see second column). Moreover, both cellular traction stresses and monolayer tangential stresses exhibited the same tendency as in the *in vitro* experiment, including a high concentration of monolayer stresses at the interface of infected and non-infected cells (**Figure 6B**, see third and fourth columns). The range of values was within the same order of magnitude as that of the *in vitro* experiment, which validates our model despite the large variability in experimental observations. When inspecting the stress maps at the interface between infected and surrounding uninfected cells for cells residing on soft 3 kPa ECM, we found that both traction and monolayer stresses are increased to a higher extent around small as compared to large infection foci ($t_{max}$ increases 13%, and $\sigma_{max}$ increases 6%). We then wondered how stresses would be modulated at small as compared to large infection foci, for cells residing on stiff 35 kPa ECM. We discovered the same trend as when cells reside on soft ECM, with the exception that the relative differences in the magnitude of the maximum traction stress and monolayer stress were higher when comparing small versus large infection foci for cells residing on 35 kPa ECM ($t_{max}$ increases 21%, and $\sigma_{max}$ increases 8%). Altogether, these findings reveal that at least *in silico* both traction stresses and monolayer stresses are increased for uninfected surrounder cells proximal to the infection focus when the focus size is smaller as opposed to larger, and that this effect is stronger for cells residing on stiff 35 kPa as compared to soft 3 kPa ECM.

## 3.6 *In vitro* Experiments Validate *In silico* Predictions Showing That Infected Cell Extrusion is Enhanced When Epithelial Cells Reside on Stiff as Opposed to Softer Matrices

Our *in silico* infection experiments suggest that cells residing on stiffer matrices will undergo more prominent infected cell squeezing and subsequent extrusion as opposed to cells residing on softer matrices. To test whether the predictions of our computational model are correct, we seeded MDCK cells in monolayer on soft 3 kPa hydrogels, or stiff 35 kPa hydrogels, or on glass coverslips and infected them with low dosage of *L.m.* At 24 hpi samples were fixed and confocal microscopy imaging was

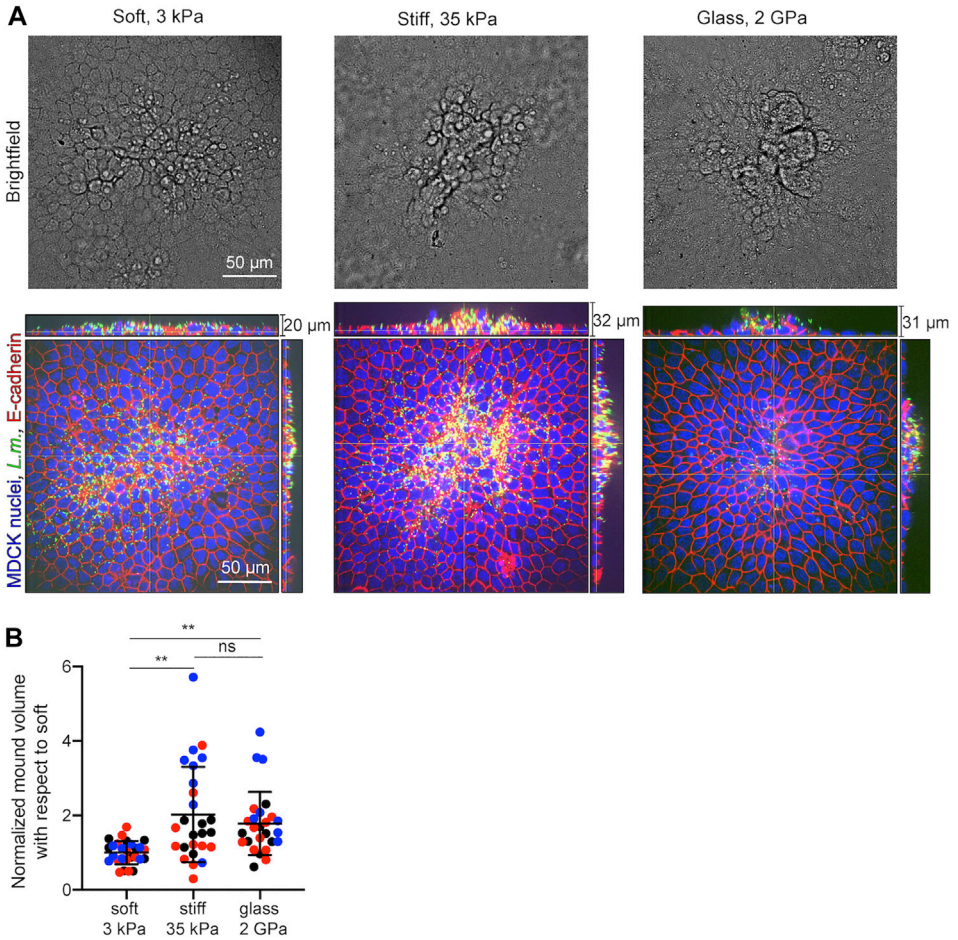


**FIGURE 7 |** *In vitro* infection experiments validate the computational finding of increased infection mounding when cells reside on stiffer matrices. **(A)** Representative brightfield image (top row) and orthogonal views (bottom row) of *L.m.* fluorescence in green, E-cadherin in red and MDCK nuclei in blue for cells originated from a *L.m.*-infected well with the field of view shown focused around and infection focus at 24 hpi. MDCK cells resided on soft 3 kPa hydrogels (left), or stiff 35 kPa hydrogels (middle), or on glass coverslips (right). **(B)** Barplots of relative *L.m.*-infection mound volume at 24 hpi for MDCK cells residing on soft 3 kPa hydrogels, on stiff 35 kPa hydrogels, or on glass. For each of $N = 3$ independent experiments (shown in different color), values have been normalized relative to the mean mound volume of cells residing on a soft 3 kPa matrix and each circle corresponds to a distinct mound (N = 26 or 27 mound volumes quantified for each condition). (mean ± SD, Wilcoxon Rank Sum test: **: $p < 0.01$, ns: non-significant).

performed to obtain z-stacks around infection foci. Although infected cell squeezing and extrusion were observed under all conditions, they were much more prominent for cells residing on stiff 35 kPa hydrogels or glass coverslips as opposed to soft 3 kPa hydrogels (**Figures 7A,B**). Moreover, especially on glass coverslips, surrounding uninfected cells appeared much more polarized as compared to the other two conditions (**Figure 7A**). When we quantified the volume of extruded cell domains relative to that which infected cells exhibit on a soft 3 kPa matrix using alpha shapes (Bastounis et al., 2021a), we found it to be 2-fold increased for cells residing on stiff 35 kPa matrices and 1.78-fold for cells residing on glass. Therefore, we can conclude that both computationally and experimentally a stiffer ECM promotes infection mounding and also that above a certain stiffness threshold an asymptotic behavior is reached and further increase in stiffness does not lead to further increase in mounding. Moreover, increased mounding observed for cells residing on stiffer ECM and glass was associated to decreased bacterial load (as evidence by the integral of the bacterial fluorescence) and decreased area of the infection focus (**Supplementary Figure S4**), reinforcing that infection mounding may limit bacterial spread across the basal cell monolayer as previously suggested (Bastounis et al., 2021b).

## 4 DISCUSSION

The stiffness of the extracellular matrix (ECM) on which cells reside is a crucial determinant in modulating a variety of cellular functions such as cell motility, proliferation, and differentiation (Lo et al., 2000; Engler et al., 2006; LaValley et al., 2017). Here we showed that ECM stiffness also modulates the outcome of the cell competition that arises during intracellular bacterial infection of epithelial cells in monolayer and leads to the collective onslaught

via extrusion of infected cells. Both our *in silico* model and the *in vitro* experiments show that increased ECM stiffness promotes the collective extrusion of infected cells as compared to a softer ECM. Through our *in silico* model, we found that the larger the difference in the ratio of stiffness between infected and uninfected surrounder cells, the larger will be the displacements that cells undergo and that lead to squeezing of infected cells and their subsequent extrusion. Moreover, through our computational model, we discovered that this effect is more prominent for cells residing on stiffer as opposed to softer ECM. Although *in vitro* experiments measuring cellular displacements, traction stresses or stiffness of infected versus non-infected cells and how those vary overtime as the infection focus grows on varying stiffness ECM were not conducted (we solely examined traction stress dynamics for infected cells at 3 kPa ECM *in vitro*), they could be the focus of future studies. Nevertheless, our *in vitro* measurements that reveal increased mounding for cells residing on stiff as opposed to softer ECM concern the computational predictions. Previous studies not involving infection have explored the role of physical cues in modulating the outcome of a mechanical cell competition (Matamoro-Vidal and Levayer, 2019; Gradeci et al., 2021). Consistent with our results, Gradeci et al. through a computational approach, showed that the higher stiffness of winner as opposed to loser cells during crowding leads to the compression of losers and an increase in their local density which is a prerequisite for their subsequent elimination (Gradeci et al., 2021). This study also showed that decreasing the ratio of stiffness of winner to loser cells will delay the kinetics of the ongoing competition rather than the final outcome. It is plausible to speculate that infection mounding could also occur for cells residing on soft matrices to the same extent as on stiff, if one was to inspect mounds at a later time point post-infection ( > 24 hpi). However, unlike the case of cell competition between wild-type and transformed cells where, only two cell populations are present, in the case of infection the landscape is more complex with some cells remaining uninfected, some being infected with few bacteria and others in the center of the focus being filled with bacteria. Moreover, it remains to be explored if delayed mounding means that bacteria can spread more at the basal cell monolayer (since cells are not extruded to the same extent) and thus, the number of infected cells still adhering to the substratum will increase faster than in the case when those are rapidly extruded, as occurs on a stiffer ECM.

Quite some studies have highlighted the importance of the relative difference in cell stiffness, adhesion strength, contractility and/or motility between two cell populations in regulating the outcome of a mechanical cell competition (Levayer et al., 2015; Matamoro-Vidal and Levayer, 2019). At the same time, it is well established that in many cell types, bulk cell stiffness and traction force generation tend to increase with increased ECM stiffness, as supported by our computational and experimental data for MDCK (Wells, 2008; Han et al., 2012). However, to our knowledge very few studies so far have explicitly tried to address the role of ECM stiffness in regulating any type of cell competition. Pothapragada et al. recently found that stiffening of the ECM attenuates extrusion of oncogenically transformed MDCK cells driven by their wild-type neighbors, which is the opposite of what we find in the case of infection (Pothapragada et al., 2022). In this study, however, which involves only two cell populations, cellular biomechanics were not characterized and the reasoning behind the enhanced elimination observed on soft ECM was the dynamic localization of the actin crosslinking protein filamin. On soft ECM filamin was found to localize at cell-cell contacts between transformed and non-transformed cells and that was necessary for driving the extrusion of the former. On stiffer ECM, instead, filamin localized perinuclearly. It is also worth noting that Pothapragada and colleagues documented a low number of extruded cells, which is distinct from the massive extrusion of infected cells we observe *in vitro*. It is likely that the mechanical mechanism driving extrusion in this case is different which could be due to the distinct biological process studied. Moreover, the authors of this study documented a bimodal extrusion pattern where extrusion counts were similar up to ECM stiffness of 11 kPa and then dropped to 50% less on ECMs 23 kPa or higher. On the contrary, we found significantly less infected cell extrusion when comparing soft 3 kPa ECM to stiff 35 kPa ECM, however the difference between stiff 35 kPa ECM and non-physiologically stiff glass coverslips is minimal, suggesting that, above a certain value, mechanical competition arising during infection becomes insensitive to stiffness and that saturation is reached above a stiffness around 35 kPa.

Our computational model suggests that ECM stiffness modulates the relative cell stiffness between infected and non-infected cells and that by itself it is sufficient to enhance infected cell squeezing on stiffer ECM. Moreover, the model predicts that a larger focus size will limit squeezing of infected cells as compared to a smaller focus size. These results raise the question of whether decreased infected cell squeezing observed on soft ECM is due to: 1) *L.m.* spreading more efficiently when cells reside on soft ECM; 2) the fact that the relative difference in stiffness of winners to losers is not as high as on a stiff ECM; or 3) both. Previous studies on endothelial cells showed that, when host cells resided on soft ECM, *L.m.* spread was favored, likely because of the decreased monolayer tension favoring the formation of bacterial protrusions and engulfment from the donor to the recipient cell (Bastounis et al., 2018). Thus, it is plausible that *L.m.* may also spread more efficiently between epithelial cells residing on soft as opposed to stiff ECM, leading to decreased ability of surrounders to squeeze infected cells since the infection focus becomes larger. This is consistent with the increased focus size we measure at 24 hpi. However, the increased relative stiffness difference between infected and non-infected cells could also play a role in promoting infected cell squeezing on stiffer ECM. Future studies could measure explicitly infected or not cell stiffness depending on ECM stiffness through atomic force microscopy (Buxboim et al., 2010; Bastounis et al., 2021b). Moreover, our computational model considers a fixed number of infected cells in each simulation, a simplification since *in vitro* the number of infected cells changes due to *L.m.* replicating and spreading intercellularly over time. Future studies could focus on incorporating the bacterial dynamics into the current computational model. Finally, it is worth mentioning that in our model we simulate one mechanotransduction cycle due to convergence issues arising while solving the relevant equations governing the dynamics of cell movement otherwise. *In vitro*, though, cells constantly sense and transmit forces from the microenvironment, thus going through multiple such cycles.

Despite this limitation, the protrusion of uninfected surrounding cells is sufficient to allow us to inspect how infected cell squeezing and formation of mounds will be governed by the physical cues that cells display depending on their ECM stiffness. Finally, an additional limitation of the model is that the size and frequency of cell-cell and cell-ECM adhesions are considered constant regardless of the stiffness of the ECM on which cells reside. However, it was recently shown that cells can adapt their focal adhesion size and number based on ECM stiffness (Cao et al., 2017; Yeh et al., 2017). A more elaborate, future version of the computational model could account for changes in cell-cell and cell-ECM adhesion size as well as frequency. However, prior *in vitro* experiments will be necessary to investigate whether those change in a differential manner for uninfected surrounders versus infected cells.

Our discovery underscores the importance of ECM stiffness in regulating the cellular mechanical competition that arises during infection and leads to elimination of bacterially-infected cells. Intriguingly, in the small intestine, where food-borne infections like the one triggered by *L.m.* take place, ECM stiffness can increase significantly from typical values of few kPa in healthy conditions to several tenths of kPa in pathological states (*e.g.*, fibrosis) (Stewart et al., 2018; Onfroy-Roy et al., 2020). Studying further the dynamics of biochemical and (extra)-cellular physical signals during infection including using more elaborate computational models and live-cell biosensors will further reveal how those signals spatiotemporally crosstalk in health and during infection. This, in turn, will be critical to enhance our understanding of how healthy cells eliminate unfit ones during infection but also during other (patho)physiological processes involving cell competition.

## DATA AVAILABILITY STATEMENT

Data collected and computer codes are available on request to the corresponding authors, and also available for public download as indicated in the methods section. MSM codes can be downloaded here: https://github.com/ebastoun/Monolayer-Stress-Microscopy. The codes for calculating volume of extruded cell domains (mounds) can be downloaded here: https://github.com/ebastoun/Infection_mound_volume.

## AUTHOR CONTRIBUTIONS

Conceptualization, EB and MG-B; Methodology, EB and MG-B; Software, EB, MG-B, RA-Y, and MM; Investigation, EB, MG-B, RA-Y, and MM; Writing—Original Draft, EB, MG-B, RA-Y; Writing—Review and Editing, EB, MG-B, RA-Y, MM, and AC; Resources, EB, MG-B, and AC; Supervision, EB, MG-B.

## FUNDING

This work was supported by the Deutsche Forschungsgemeinschaft (DFG, German Research Foundation) under Germany's Excellence Strategy—EXC2124—390838134 (EB and MM), the European Research council [ICoMICS Adg grant agreement: 1,01018587, (RA-Y and MG-B)], the Spanish Ministry of Universities [grant FPU 20/05274 (RA-Y)] and Grant PID2021-124271OB-I00 founded by MCIN/AEI/10.13039/501100011033 (RA-Y and MG-B) and ERDF A way of making Europe (RA-Y and MG-B).

## ACKNOWLEDGMENTS

We are grateful to Julie A. Theriot for her insight, scientific discussions and sharing her resources. We thank José M. García-Aznar for the scientific discussion on the computational model. We also thank Libera Lo Presti for discussions and for revising the manuscript and rest of the materials. We acknowledge that part of our MSM codes are based on the original code (plane stress problem) written by Siva Srinivas Kolukula and we hence used some functions from his code.

## SUPPLEMENTARY MATERIAL

The Supplementary Material for this article can be found online at: https://www.frontiersin.org/articles/10.3389/fcell.2022.912318/full#supplementary-material

## REFERENCES

Álvarez-González, B., Zhang, S., Gómez-González, M., Meili, R., Firtel, R. A., Lasheras, J. C., et al. (2017). Two-layer Elastographic 3-d Traction Force Microscopy. *Sci. Rep.* 7, 39315. doi:10.1038/srep39315

Aparicio-Yuste, R., Gómez-Benito, M. J., Reuss, A., Blacker, G., Tal, M. C., and Bastounis, E. (2022). *Borrelia Burgdorferi* Induces Changes in the Physical Forces and Immunity Signaling Pathways of Endothelial Cells Early but Not Late during *In Vitro* Infection. Available at SSRN: https://ssrn.com/abstract=4024544.

Balcioglu, H. E., Balasubramaniam, L., Stirbat, T. V., Doss, B. L., Fardin, M.-A., Mège, R.-M., et al. (2020). A Subtle Relationship between Substrate Stiffness and Collective Migration of Cell Clusters. *Soft Matter* 16, 1825–1839. doi:10.1039/C9SM01893J

Bastounis, E. E., Ortega, F. E., Serrano, R., and Theriot, J. A. (2018). A Multi-Well Format Polyacrylamide-Based Assay for Studying the Effect of Extracellular Matrix Stiffness on the Bacterial Infection of Adherent Cells. *JoVE* e57361. doi:10.3791/57361

Bastounis, E. E., Radhakrishnan, P., Prinz, C. K., and Theriot, J. A. (2022). Mechanical Forces Govern Interactions of Host Cells with Intracellular Bacterial Pathogens. *Microbiol. Mol. Biol. Rev.* 0, e00094–20. doi:10.1128/mmbr.00094-20

Bastounis, E. E., Radhakrishnan, P., Prinz, C. K., and Theriot, J. A. (2021a). Volume Measurement and Biophysical Characterization of Mounds in Epithelial Monolayers after Intracellular Bacterial Infection. *Star. Protoc.* 2, 100551. doi:10.1016/j.xpro.2021.100551

Bastounis, E. E., Serrano-Alcalde, F., Radhakrishnan, P., Engström, P., Gómez-Benito, M. J., Oswald, M. S., et al. (2021b). Mechanical Competition Triggered by Innate Immune Signaling Drives the Collective Extrusion of Bacterially Infected Epithelial Cells. *Dev. Cell* 56, 443–460. e11. doi:10.1016/j.devcel.2021.01.012

Bastounis, E. E., Yeh, Y.-T., and Theriot, J. A. (2019). Subendothelial Stiffness Alters Endothelial Cell Traction Force Generation while Exerting a Minimal Effect on the Transcriptome. *Sci. Rep.* 9, 18209. doi:10.1038/s41598-019-54336-2

Bastounis, E., Meili, R., Álvarez-González, B., Francois, J., del Álamo, J. C., Firtel, R. A., et al. (2014). Both contractile Axial and Lateral Traction Force Dynamics Drive Amoeboid Cell Motility. *J. cell Biol.* 204, 1045–1061. doi:10.1083/jcb.201307106

Borau, C., Kamm, R. D., and García-Aznar, J. M. (2011). Mechano-sensing and Cell Migration: a 3d Model Approach. *Phys. Biol.* 8, 066008. doi:10.1088/1478-3975/8/6/066008

Brodland, G. W. (2015). How Computational Models Can Help Unlock Biological Systems. *Seminars Cell & Dev. Biol.* 47-48, 62–73. doi:10.1016/j.semcdb.2015.07.001

Buxboim, A., Rajagopal, K., Brown, A. E. X., and Discher, D. E. (2010). How Deeply Cells Feel: Methods for Thin Gels. *J. Phys. Condens. Matter* 22, 194116. doi:10.1088/0953-8984/22/19/194116

Califano, J. P., and Reinhart-King, C. A. (2010). Substrate Stiffness and Cell Area Predict Cellular Traction Stresses in Single Cells and Cells in Contact. *Cel. Mol. Bioeng.* 3, 68–75. doi:10.1007/s12195-010-0102-6

Cao, X., Ban, E., Baker, B. M., Lin, Y., Burdick, J. A., Chen, C. S., et al. (2017). Multiscale Model Predicts Increasing Focal Adhesion Size with Decreasing Stiffness in Fibrous Matrices. *Proc. Natl. Acad. Sci. U.S.A.* 114, E4549–E4555. doi:10.1073/pnas.1620486114

Delarue, M., Hartung, J., Schreck, C., Gniewek, P., Hu, L., Herminghaus, S., et al. (2016). Self-driven Jamming in Growing Microbial Populations. *Nat. Phys.* 12, 762–766. doi:10.1038/nphys3741

Doss, B. L., Pan, M., Gupta, M., Grenci, G., Mège, R.-M., Lim, C. T., et al. (2020). Cell Response to Substrate Rigidity Is Regulated by Active and Passive Cytoskeletal Stress. *Proc. Natl. Acad. Sci. U.S.A.* 117, 12817–12825. doi:10.1073/pnas.1917555117

Engler, A. J., Sen, S., Sweeney, H. L., and Discher, D. E. (2006). Matrix Elasticity Directs Stem Cell Lineage Specification. *Cell* 126, 677–689. doi:10.1016/j.cell.2006.06.044

Escribano, J., Chen, M. B., Moeendarbary, E., Cao, X., Shenoy, V., Garcia-Aznar, J. M., et al. (2019). Balance of Mechanical Forces Drives Endothelial Gap Formation and May Facilitate Cancer and Immune-Cell Extravasation. *PLoS Comput. Biol.* 15, e1006395–21. doi:10.1371/journal.pcbi.1006395

Escribano, J., Sunyer, R., Sánchez, M. T., Trepat, X., Roca-Cusachs, P., and García-Aznar, J. M. (2018). A Hybrid Computational Model for Collective Cell Durotaxis. *Biomech. Model Mechanobiol.* 17, 1037–1052. doi:10.1007/s10237-018-1010-2

Faralla, C., Bastounis, E. E., Ortega, F. E., Light, S. H., Rizzuto, G., Gao, L., et al. (2018). *Listeria Monocytogenes* Inlp Interacts with Afadin and Facilitates Basement Membrane Crossing. *PLoS Pathog.* 14, e1007094–26. doi:10.1371/journal.ppat.1007094

Gradeci, D., Bove, A., Vallardi, G., Lowe, A. R., Banerjee, S., and Charras, G. (2019). Cell-scale Biophysical Determinants of Cell Competition in Epithelia. *bioRxiv*. doi:10.1101/729731

Gradeci, D., Bove, A., Vallardi, G., Lowe, A. R., Banerjee, S., and Charras, G. (2021). Cell-scale Biophysical Determinants of Cell Competition in Epithelia. *eLife Sci.* 10, e61011. doi:10.7554/eLife.61011

Gui, L., and Wereley, S. T. (2002). A Correlation-Based Continuous Window-Shift Technique to Reduce the Peak-Locking Effect in Digital PIV Image Evaluation. *Exp. Fluids* 32, 506–517. doi:10.1007/s00348-001-0396-1

Han, S. J., Bielawski, K. S., Ting, L. H., Rodriguez, M. L., and Sniadecki, N. J. (2012). Decoupling Substrate Stiffness, Spread Area, and Micropost Density: A Close Spatial Relationship between Traction Forces and Focal Adhesions. *Biophysical J.* 103, 640–648. doi:10.1016/j.bpj.2012.07.023

Hayer, A., Shao, L., Chung, M., Joubert, L.-M., Yang, H. W., Tsai, F.-C., et al. (2016). Engulfed Cadherin Fingers Are Polarized Junctional Structures between Collectively Migrating Endothelial Cells. *Nat. Cell Biol.* 18, 1311–1323. doi:10.1038/ncb3438

Hervás-Raluy, S., García-Aznar, J. M., and Gómez-Benito, M. J. (2019). Modelling Actin Polymerization: the Effect on Confined Cell Migration. *Biomech. Model Mechanobiol.* 18, 1177–1187. doi:10.1007/s10237-019-01136-2

Kandemir, N., Vollmer, W., Jakubovics, N. S., and Chen, J. (2018). Mechanical Interactions between Bacteria and Hydrogels. *Sci. Rep.* 8, 10893. doi:10.1038/s41598-018-29269-x

Kocgozlu, L., Saw, T. B., Le, A. P., Yow, I., Shagirov, M., Wong, E., et al. (2016). Epithelial Cell Packing Induces Distinct Modes of Cell Extrusions. *Curr. Biol.* 26, 2942–2950. doi:10.1016/j.cub.2016.08.057

Lamason, R. L., Bastounis, E., Kafai, N. M., Serrano, R., del Álamo, J. C., Theriot, J. A., et al. (2016). Rickettsia Sca4 Reduces Vinculin-Mediated Intercellular Tension to Promote Spread. *Cell* 167, 670–683. e10. doi:10.1016/j.cell.2016.09.023

Lampi, M. C., Faber, C. J., Huynh, J., Bordeleau, F., Zanotelli, M. R., and Reinhart-King, C. A. (2016). Simvastatin Ameliorates Matrix Stiffness-Mediated Endothelial Monolayer Disruption. *PLOS ONE* 11, e0147033–20. doi:10.1371/journal.pone.0147033

Lampi, M. C., and Reinhart-King, C. A. (2018). Targeting Extracellular Matrix Stiffness to Attenuate Disease: From Molecular Mechanisms to Clinical Trials. *Sci. Transl. Med.* 10, eaao0475. doi:10.1126/scitranslmed.aao0475

LaValley, D. J., Zanotelli, M. R., Bordeleau, F., Wang, W., Schwager, S. C., and Reinhart-King, C. A. (2017). Matrix Stiffness Enhances VEGFR-2 Internalization, Signaling, and Proliferation in Endothelial Cells. *Converg. Sci. Phys. Oncol.* 3, 044001. doi:10.1088/2057-1739/aa9263

Lecuit, T., and Lenne, P.-F. (2007). Cell Surface Mechanics and the Control of Cell Shape, Tissue Patterns and Morphogenesis. *Nat. Rev. Mol. Cell Biol.* 8, 633–644. doi:10.1038/nrm2222

Levayer, R., Hauert, B., and Moreno, E. (2015). Cell Mixing Induced by *Myc* Is Required for Competitive Tissue Invasion and Destruction. *Nature* 524, 476–480. doi:10.1038/nature14684

Lo, C.-M., Wang, H.-B., Dembo, M., and Wang, Y.-l. (2000). Cell Movement Is Guided by the Rigidity of the Substrate. *Biophysical J.* 79, 144–152. doi:10.1016/S0006-3495(00)76279-5

Matamoro-Vidal, A., and Levayer, R. (2019). Multiple Influences of Mechanical Forces on Cell Competition. *Curr. Biol.* 29, R762–R774. doi:10.1016/j.cub.2019.06.030

Meyer, S. N., Amoyel, M., Bergantiños, C., de la Cova, C., Schertel, C., Basler, K., et al. (2014). An Ancient Defense System Eliminates Unfit Cells from Developing Tissues during Cell Competition. *Science* 346, 1258236. doi:10.1126/science.1258236

Moreno, E., Valon, L., Levillayer, F., and Levayer, R. (2019). Competition for Space Induces Cell Elimination through Compaction-Driven ERK Downregulation. *Curr. Biol.* 29, 23–34. e8. doi:10.1016/j.cub.2018.11.007

Moreo, P., García-Aznar, J. M., and Doblaré, M. (2008). Modeling Mechanosensing and its Effect on the Migration and Proliferation of Adherent Cells. *Acta Biomater.* 4, 613–621. doi:10.1016/j.actbio.2007.10.014

Nieto, A., Escribano, J., Spill, F., Garcia-Aznar, J. M., and Gomez-Benito, M. J. (2020). Finite Element Simulation of the Structural Integrity of Endothelial Cell Monolayers: A Step for Tumor Cell Extravasation. *Eng. Fract. Mech.* 224, 106718. doi:10.1016/j.engfracmech.2019.106718

O'Dea, R. D., and King, J. R. (2012). Continuum Limits of Pattern Formation in Hexagonal-Cell Monolayers. *J. Math. Biol.* 64, 579–610. doi:10.1007/s00285-011-0427-3

Onfroy-Roy, L., Hamel, D., Foncy, J., Malaquin, L., and Ferrand, A. (2020). Extracellular Matrix Mechanical Properties and Regulation of the Intestinal Stem Cells: When Mechanics Control Fate. *Cells* 9, 2629. doi:10.3390/cells9122629

Ortega, F. E., Koslover, E. F., and Theriot, J. A. (2019). *Listeria Monocytogenes* Cell-To-Cell Spread in Epithelia Is Heterogeneous and Dominated by Rare Pioneer Bacteria. *eLife* 8, e40032. doi:10.7554/eLife.40032.001

Ortega, F. E., Rengarajan, M., Chavez, N., Radhakrishnan, P., Gloerich, M., Bianchini, J., et al. (2017). Adhesion to the Host Cell Surface Is Sufficient to mediateListeria Monocytogenesentry into Epithelial Cells. *MBoC* 28, 2945–2957. doi:10.1091/mbc.e16-12-0851

Perez, T. D., Tamada, M., Sheetz, M. P., and Nelson, W. J. (2008). Immediate-early Signaling Induced by E-Cadherin Engagement and Adhesion. *J. Biol. Chem.* 283, 5014–5022. doi:10.1074/jbc.M705209200

Pothapragada, S. P., Gupta, P., Mukherjee, S., Das, T., and Das, T. (2022). Matrix Mechanics Regulates Epithelial Defence against Cancer by Tuning Dynamic Localization of Filamin. *Nat. Commun.* 13, 218. doi:10.1038/s41467-021-27896-z

Schmedt, T., Chen, Y., Nguyen, T. T., Li, S., Bonanno, J. A., and Jurkunas, U. V. (2012). Telomerase Immortalization of Human Corneal Endothelial Cells Yields Functional Hexagonal Monolayers. *PLOS ONE* 7, e51427–11. doi:10.1371/journal.pone.0051427

Solon, J., Levental, I., Sengupta, K., Georges, P. C., and Janmey, P. A. (2007). Fibroblast Adaptation and Stiffness Matching to Soft Elastic Substrates. *Biophysical J.* 93, 4453–4461. doi:10.1529/biophysj.106.101386

Stewart, D. C., Berrie, D., Li, J., Liu, X., Rickerson, C., Mkoji, D., et al. (2018). Quantitative Assessment of Intestinal Stiffness and Associations with Fibrosis in Human Inflammatory Bowel Disease. *PLOS ONE* 13, e0200377–16. doi:10.1371/journal.pone.0200377

Sun, B. (2021). The Mechanics of Fibrillar Collagen Extracellular Matrix. *Cell Rep. Phys. Sci.* 2, 100515. doi:10.1016/j.xcrp.2021.100515

Tambe, D. T., Corey Hardin, C., Angelini, T. E., Rajendran, K., Park, C. Y., Serra-Picamal, X., et al. (2011). Collective Cell Guidance by Cooperative Intercellular Forces. *Nat. Mater* 10, 469–475. doi:10.1038/nmat3025

Vujosevic, L., and Lubarda, V. A. (2002). Finite-strain Thermoelasticity Based on Multiplicative Decomposition of Deformation Gradient. *Theor. Appl. Mech. (Belgr)* 379, 379–399. doi:10.2298/TAM0229379V

Wells, R. G. (2008). The Role of Matrix Stiffness in Regulating Cell Behavior. *Hepatology* 47, 1394–1400. doi:10.1002/hep.22193

Yeh, Y.-C., Ling, J.-Y., Chen, W.-C., Lin, H.-H., and Tang, M.-J. (2017). Mechanotransduction of Matrix Stiffness in Regulation of Focal Adhesion Size and Number: Reciprocal Regulation of Caveolin-1 and β1 Integrin. *Sci. Rep.* 7, 2045–2322. doi:10.1038/s41598-017-14932-6

Zhao, T., Zhang, Y., Wei, Q., Shi, X., Zhao, P., Chen, L.-Q., et al. (2018). Active Cell-Matrix Coupling Regulates Cellular Force Landscapes of Cohesive Epithelial Monolayers. *npj Comput. Mater* 4, 10. doi:10.1038/s41524-018-0069-8

**Conflict of Interest:** The authors declare that the research was conducted in the absence of any commercial or financial relationships that could be construed as a potential conflict of interest.

**Publisher's Note:** All claims expressed in this article are solely those of the authors and do not necessarily represent those of their affiliated organizations, or those of the publisher, the editors and the reviewers. Any product that may be evaluated in this article, or claim that may be made by its manufacturer, is not guaranteed or endorsed by the publisher.

frontiers | Frontiers in Cell and Developmental Biology

ORIGINAL RESEARCH
published: 22 July 2022
doi: 10.3389/fcell.2022.933220

# Reconstruction of the Global Polarity of an Early Spider Embryo by Single-Cell and Single-Nucleus Transcriptome Analysis

*Yasuko Akiyama-Oda*[1,2,3]*, *Takanori Akaiwa*[1,4] *and Hiroki Oda*[1,4]

[1]JT Biohistory Research Hall, Takatsuki, Japan, [2]PRESTO, Japan Science and Technology Agency, Kawaguchi, Japan, [3]Department of Microbiology and Infection Control, Faculty of Medicine, Osaka Medical and Pharmaceutical University, Takatsuki, Japan, [4]Department of Biological Science, Graduate School of Science, Osaka University, Toyonaka, Japan

Patterning along an axis of polarity is a fundamental step in the development of a multicellular animal embryo. In the cellular field of an early spider embryo, Hedgehog signaling operates to specify a "fuzzy" French-flag-like pattern along the primary axis, which is related to the future anterior–posterior (A–P) axis. However, details regarding the generation and development of a diversity of cell states based on the embryo polarity are not known. To address this issue, we applied single-cell RNA sequencing to the early spider embryo consisting of approximately 2,000 cells. Our results confirmed that this technique successfully detected 3 cell populations corresponding to the germ layers and some transient cell states. We showed that the data from dissociated cells had sufficient information for reconstruction of a correct global A–P polarity of the presumptive ectoderm, without clear segregation of specific cell states. This outcome is explained by the varied but differentially overlapping expression of Hedgehog-signal target genes and newly identified marker genes. We also showed that the data resources generated by the transcriptome analysis are applicable to a genome-wide search for genes whose expression is spatially regulated, based on the detection of pattern similarity. Furthermore, we performed single-nucleus RNA sequencing, which was more powerful in detecting emerging cell states. The single-cell and single-nucleus transcriptome techniques will help investigate the pattern-forming processes in the spider model system in an unbiased, comprehensive manner. We provided web-based resources of these transcriptome datasets for future studies of pattern formation and cell differentiation.

**Keywords: spider, arthropod, pattern formation, transcriptome, single-nuclei RNA-seq (snRNA-seq), single-cell RNA-seq (scRNA-seq), embryo, axis formation**

OPEN ACCESS

***Edited by:***
*Yoshiko Takahashi, Kyoto University, Japan*

***Reviewed by:***
*Siegfried Roth, University of Cologne, Germany*
*Prashant Sharma, University of Wisconsin-Madison, United States*

***Correspondence:**
*Yasuko Akiyama-Oda*
*yasuko@brh.co.jp*

***Specialty section:***
*This article was submitted to Morphogenesis and Patterning, a section of the journal Frontiers in Cell and Developmental Biology*

***Received:*** *03 May 2022*
***Accepted:*** *22 June 2022*
***Published:*** *22 July 2022*

***Citation:***
*Akiyama-Oda Y, Akaiwa T and Oda H (2022) Reconstruction of the Global Polarity of an Early Spider Embryo by Single-Cell and Single-Nucleus Transcriptome Analysis. Front. Cell Dev. Biol. 10:933220. doi: 10.3389/fcell.2022.933220*

## INTRODUCTION

In the cellular field of a developing tissue or embryo, a reproducible complex pattern of gene expression forms through dynamic gene regulations and cell–cell interactions. Formation of spatial periodic stripe patterns in the *Drosophila* blastoderm embryo has long stood as a simple, excellent model system to study and understand pattern-forming processes and the underlying mechanisms in multicellular animals (Bate and Arias, 1993). However, most of the patterning process in this *Drosophila* system occurs in a syncytial environment, allowing transcription factors and cytoplasmic

components to diffuse over a long range (Driever and Nüsslein-Volhard, 1988a). This peculiar situation may limit applicability and generalization of our knowledge from the *Drosophila* patterning system.

The spider *Parasteatoda tepidariorum*, which together with *Drosophila* belongs to the phylum Arthropoda, has emerged as a model organism to study pattern-forming processes and the underlying mechanisms in a cellular field (Hilbrant et al., 2012; Oda and Akiyama-Oda, 2020). In this spider embryo, a segmented germ band with conserved stripes of gene expression forms like *Drosophila*; however, the cellular and molecular processes leading to these similar outcomes are highly different. In the early *Parasteatoda* embryo, cellularization is achieved by the stage when the number of the cleavage nuclei increases to sixteen (Kanayama et al., 2010), and the A-P and dorsal-ventral (D-V) axes and periodic segmental stripes are specified by cell–cell interactions mediated by signaling pathways (Akiyama-Oda and Oda, 2003, Akiyama-Oda and Oda, 2006, Akiyama-Oda and Oda, 2010, Akiyama-Oda and Oda, 2020; McGregor et al., 2008; Kanayama et al., 2011; Schönauer et al., 2016; Setton and Sharma, 2021). The Hedgehog (Hh) signaling pathway regulates the formation of global polarity along the primary axis: an axis of radial symmetry that emerges during the formation of a disc-shaped epithelial cell sheet called the germ disc. The roles of Hh signaling pathway in the early *Parasteatoda* embryo are similar to those of maternal transcription factor morphogens, such as Bicoid, in the early *Drosophila* embryo (Driever and Nüsslein-Volhard, 1988b; Briscoe and Small, 2015). Hh signaling plays key roles in a variety of tissue patterning events in bilaterians, including D-V patterning in the vertebrate neural tube (Dessaud et al., 2008; Ribes and Briscoe, 2009; Placzek and Briscoe, 2018), digit patterning in the vertebrate appendage primordia (Tickle and Towers, 2017; Zhu and Mackem, 2017), and the generation of repetitive ridges in the mammalian palate (Economou et al., 2012). In these patterning tissue fields, Hh signaling network, owing to its positive and negative feedback loops (Briscoe and Thérond, 2013; Kong et al., 2019), dynamically controls the expression of genes in respective cells. However, these fields are located inside an embryo or organ and organized by dynamic cell populations, in which the position of individual cells is not easily followable. In contrast, the early *Parasteatoda* embryo, like the *Drosophila* blastoderm embryo, provides a simple, easily observable cellular field (but not syncytial), in which periodic stripe formation progresses (Hemmi et al., 2018) by the mechanisms mediated by Hh and other signaling pathways (McGregor et al., 2008; Kanayama et al., 2011; Schönauer et al., 2016; Akiyama-Oda and Oda, 2020; Setton and Sharma, 2021).

The *Parasteatoda* late stage-5 germ disc (**Figure 1A**) is a large field of single-layered epithelial cell sheet that consists of approximately 2,000 morphologically uniform, undifferentiated cells (Akiyama-Oda and Oda, 2020). This field has global polarities reflecting the future A-P axis of the embryo but has not gained spatially periodic patterns of gene expression. The center of the germ disc, also referred to as the embryonic pole, corresponds to the future posterior pole, whereas the peripheral region of the germ disc corresponds to the future anterior. Most of the area of the germ disc develops into the surface ectoderm maintaining its continuity. The other germ layers, the endoderm and mesoderm, develop from cells internalized at and near the center of the germ disc and the rim of the germ disc (Yamazaki et al., 2005; Oda et al., 2007). A previous study using the combination of RNA interference (RNAi) and RNA sequencing (RNA-seq) identified many genes expressed in concentric circle patterns on the germ disc under the control of Hh signaling (Akiyama-Oda and Oda, 2020). Expression of genes positively regulated by Hh signaling is detected in the peripheral region of the germ disc, and expression of those negatively regulated is detected in the central region. Some genes that require both positive and negative regulations are expressed in the intermediate region. These situations remind us of the French flag model (Wolpert, 1969; Briscoe and Small, 2015); however, the boundaries of individual gene expression domains are obscure or fuzzy, and expression of some genes is sparse or dynamic on the static germ disc. Following the germ-disc stage, the cellular field undergoes a planar remodeling to transform into a germ band, in which an increasing number of stripes arise through dynamic regulation of wave-like expression of genes (Kanayama et al., 2011; Schönauer et al., 2016; Hemmi et al., 2018; Akiyama-Oda and Oda, 2020). To date, several genes expressed in specific regions of the germ disc that play roles for specific steps in *Parasteatoda* segmentation have been identified. These genes include an *orthodenticle* homolog *Pt-otd*, an *odd-paired* homolog *Pt-opa*, a *distal-less* homolog *Pt-dll,* and a *muscle segment homeobox* (*msh*) homolog *Pt-msx1* (Pechmann et al., 2009, Pechmann et al., 2011; Kanayama et al., 2011; Akiyama-Oda and Oda, 2016, Akiyama-Oda and Oda, 2020). The roles for some of these in segmentation were unpredictable based on our knowledge from the *Drosophila* model system. For example, in *Drosophila*, *msh* functions under the specification of several muscle cells and neuroectodermal cells (Lord et al., 1995; Isshiki et al., 1997), whereas in *Parasteatoda*, *Pt-msx1* is essential for generating gene expression dynamics involved in segmentation. These previous findings strongly suggest the need for a genome-wide, unbiased approach that can capture spatially regulated gene expression to investigate the pattern-forming processes in the new spider model system.

To this end, the present study tested the applicability of single-cell RNA-seq (Jaitin et al., 2014; Macosko et al., 2015) to the *Parasteatoda* embryo at the late germ-disc stage. We showed that this technique worked effectively using only twenty or less embryos for each experiment. Analyses of quantitative datasets obtained from dissociated cells successfully separated 3 cell populations corresponding to the presumptive ectoderm, mesoderm, and endoderm and reconstructed a global A-P polarity in the ectodermal cell population. We also performed single-nucleus RNA-seq (Grindberg et al., 2013; Habib et al., 2016), which produced similar results to those of single-cell RNA-seq, but with higher sensitivity to dynamic cell states emerging from the center of the germ disc. The resulting resources enabled us to conduct a genome-wide search *in silico* for genes whose expression is spatially regulated in the germ disc. The single-cell and single-nucleus transcriptome techniques will help investigate

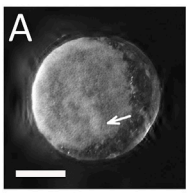


C

| | Cells (Nuclei) | Ave. Mols /Cell (Nucleus) | Ave. Genes /Cell (Nucleus) | Total Genes | Ave. Mols /gene |
|---|---|---|---|---|---|
| 1st Cell | 505 | 16,953 | 3,319 | 17,770 | 482 |
| 2nd Cell | 3,621 | 14,519 | 3,094 | 16,871 | 3,116 |
| 2nd Nucleus | 4,720 | 5,509 | 2,549 | 20,281 | 1,282 |

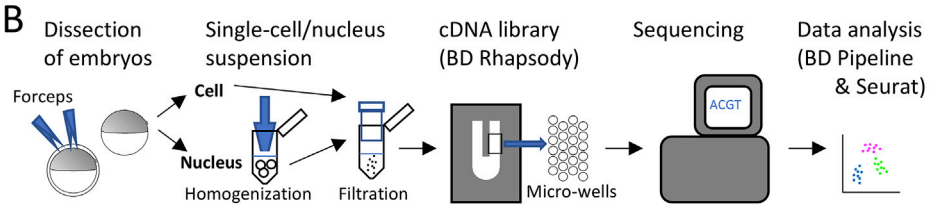


**FIGURE 1 |** Single-cell and single-nucleus transcriptomics of the early spider embryo. **(A)** An embryo at late germ-disc stage (late stage 5). The germ disc is observed as the white sheet. The arrow indicates the cumulus. Scale Bar = 200 µm. **(B)** Diagram showing single-cell and single-nucleus experimental procedure. **(C)** Metrics summary after filtering out low-quality cells (nuclei). Numbers of cells and nuclei examined in the first single-cell, the second single-cell, and the single-nucleus analyses, average of detected molecules per cell (nucleus), average of detected genes per cell (nucleus), total numbers of detected genes, and average of detected molecules per gene.

the pattern-forming processes in the spider model system in an unbiased, comprehensive manner.

## MATERIALS AND METHODS

### Spider

Animal experiments were conducted according to the protocol reviewed and approved by the Institutional Animal Care and Use Committee of JT Biohistory Research Hall (No. 2020-1). We used laboratory stocks of the spider *Parasteatoda tepidariorum* (syn. *Achaearanea tepidariorum*), which were maintained at 25°C with a 16 h light/8 h dark cycle. Developmental stages have been described previously (Akiyama-Oda and Oda, 2003, Akiyama-Oda and Oda, 2010). We monitored the development of the eggs and determined the beginning of stage 5, when internalization of the cumulus mesenchymal (CM) cells is completed. The image of the spider embryo shown in **Figure 1A** was captured using a zoom microscope Zeiss Axio Zoom.V16 equipped with a digital camera Zeiss Axiocam506 (Carl Zeiss). Z-series images (5 µm × 56) were processed using an ImageJ plugin (Extended Depth of Field).

### Isolation of Single Cell and Single Nucleus

The spider embryos were dechorionated using 100% commercial bleach, rinsed with distilled water, and transferred into CGBS-CMF [Chan and Gehring buffered saline (Chan and Gehring, 1971), Ca and Mg-free: 55 mM NaCl, 40 mM KCl, 10 mM Tricine, pH6.95]–0.01% (for cell) or 0.5% (for nucleus) BSA (Nacalai tesque, 01278-44) solution. In this solution, vitelline membrane was manually removed with forceps. To obtain dissociated cells, the devitellinized sample was filtered through a 40-µm cell strainer (pluriStrainer-Mini, 43-10040-40) and collected in a DNA LoBind Tube (Eppendorf 022431021). For preparation of nuclei, the devitellinized sample was centrifuged in a 1.5-ml tube and suspended in 400 µL homogenization buffer (McLaughlin et al., 2021) [250 mM Sucrose, 10 mM Tris (pH 8.0), 25 mM KCl, 5 mM $MgCl_2$, 0.1% Triton-X100, 0.1 mM DTT, 100 u/mL RNase Inhibitor (SUPERaseIn RNase Inhibitor: Invitrogen, AM2694), Protease Inhibitor at 1:100 dilution (Nacalai tesque, 25955-11)], where the sample was homogenized with a loose plastic pestle (fisher scientific, 12-141-368) by 40 strokes. Next, the sample was centrifuged and resuspended with CGBS-CMF-0.5% BSA-100 u/mL RNase Inhibitor solution, followed by filtration through a 40-µm cell strainer. The centrifugation and resuspension steps (without the filtration step) were repeated twice. Four volumes of CellCover (Anacyte Laboratories, 800-050) were added to the cell and nucleus samples, which were then stored at 4°C. To proceed to the library construction step, stored samples were centrifuged and resuspended with the CGBS-CMF-0.025% Tween 20 (first single-cell library), CGBS-CMF-0.01% BSA (second single-cell library), or CGBS-CMF-0.01% BSA-100 u/mL RNase Inhibitor (single-nucleus library) solution. In these solutions, the samples were loaded onto BD Rhapsody cartridges (BD Biosciences).

For the first single-cell transcriptome library construction, we used ten late stage-5 eggs (approximately 8 h from the beginning of stage 5) derived from an egg sac. For the second single-cell and single-nucleus transcriptome library construction, we used 20 eggs each derived from another egg sac. To prepare the nuclei sample, eggs were dechorionated at the end of stage 5/the start of stage 6 (9–10 h from the beginning of stage 5), and for the second single-cell sample, eggs were dechorionated 1 h 20 min later, when preparation of the nuclei sample was completed.

### Construction of Libraries and RNA Sequencing

Single-cell RNA-seq libraries were constructed using a BD Rhapsody Targeted mRNA and AbSeq Amplification kit (BD

Biosiences, 633774) or a BD Rhapsody WTA Amplification kit (BD Biosiences, 633801) according to the manufacturer's instructions. To construct the single-nucleus RNA-seq library, a BD Rhapsody WTA Amplification kit was used with some modifications: RNase Inhibitor (SUPERaseIn RNase Inhibitor) was added at 100 u/mL to the sample buffer supplied in the kit, which was used for the bead wash steps, Proteinase K was added at 0.5 mg/ml to the Lysis buffer, and the lysis step was prolonged from 2 min to 5 min. Sequencing was performed using the HiSeqX Sequencing system (Illumina) with 150 paired-end reads, and 8 bp index reads were also performed for the second single-cell and single-nucleus libraries.

## Sequence Alignment and Count Matrix Generation

RNA-seq reads were processed using the BD Rhapsody WTA analysis pipeline on the Seven Bridges Genomics cloud platform (Tzani et al., 2021) with the default parameters. The R1 reads, possessing information of the cell barcode and the adjusted unique molecular index (UMI), were used to identify cells and molecules. The R2 reads, which were second strand cDNA sequences, were aligned using the STAR index created by STAR-2.5.2b (Dobin et al., 2013) against the *Parasteatoda tepidariorum* genome (Schwager et al., 2017), GCF_000365465.2_Ptep_2.0 (all libraries) and GCF_000365465.3_Ptep_3.0 (second single-cell and single-nucleus libraries). To count both exonic and intronic reads, an annotation file (a gtf file) accompanied with GCF_000365465.3_Ptep_3.0 was modified and used to align the second single-cell and the single-nucleus libraries. Integrating cellular and molecular information obtained from R1 reads and results of the alignment of R2 reads, a cell/nuc and gene count matrix for each sample was generated (GSE201705). Count metrics are summarized in **Supplementary Tables S1, S7**.

## Preprocessing and Clustering

Using the Seurat package (v.4.0.3) (Satija et al., 2015), the generated count matrices were filtered based on both the number of unique genes and the total number of RNA molecules or the total number of RNA molecules to exclude low-complex cells/nuclei and potential doublets; the thresholds were as follows: cells having 2,000 to 4,800 genes and having less than 30,000 molecules for the first single-cell library, 6,866 to 27,465 molecules (50%–200% of the mode) for the second single-cell library, and 2,667 to 10,670 molecules (50%–200% of the mode) for the single-nucleus library. Metrics of these quality-filtered counts are shown in **Figure 1C**. Log-normalization, identification of variable features, scaling, principal component (PC) analysis, dimensionality reduction, cell clustering, and detection of cluster marker genes were performed on these counts according to instructions of the Seurat package. In the clustering analysis, we tried multiple parameter settings to confirm that the cell populations were similarly detected. In the clustering analyses using the single-cell datasets, putative ectodermal cells were constantly separated into two large populations with various parameter settings; differentially expressed genes (DEGs) (**Supplementary Tables S2, S8**) were identified between the two ectodermal populations that were detected using the following parameters: 50 PCs and resolution 0.5 for the first single-cell analysis and 20 PCs and resolution 0.1 for the second single-cell analysis. These parameter values were optimized in each case, so that smaller subclusters were not generated within the ectodermal populations. The identified DEGs were excluded from the downstream analyses. The clustering output was visualized using a uniform manifold approximation and projection (UMAP) plot embedded in the Seurat package. UMAP plots showing expression of all identified genes can be viewed in a web database at https://www.brh2.jp and have been deposited, including the DEGs, in the Figshare repository (doi:10.6084/m9.figshare.c.5963571).

## Production of Composite Images of Two or Three UMAP Plots

UMAP plots generated in gray-black colors using Seurat were converted into gray-scale images using the ImageJ (FIJI) software (version 2.3.0/1.53f). Next, they were transformed into negative images and overlayed to produce composites in RGB colors using the ImageMagick convert and combine function.

## Identification of Cell Cycle Genes

*Parasteatoda* cell-cycle genes were searched using amino-acid sequences of *Drosophila* cell-cycle genes (https://github.com/hbc/tinyatlas/blob/master/cell_cycle/Drosophila_melanogaster.csv) as queries for tblastn searches against *Parasteatoda* genes, and nucleotide sequences of *Parasteatoda* top-hit genes were then used reciprocally for blastx searches against *Drosophila* genes. *Parasteatoda* putative orthologs of the *Drosophila* cell-cycle genes are listed in **Supplementary Table S3**.

## Construction of Dendrogram and Heatmap

We prepared three matrices of normalized counts from the first single-cell transcriptomes using 1) 411 cells belonging to clusters 2–5 (presumptive ectodermal cells), and the *Pt-hh* gene and 48 Hh-signaling target genes expressed in specific regions of the germ disc (total of 49 genes) (Akiyama-Oda and Oda, 2020); 2) 140 cells belonging to clusters 0–2 (presumptive endodermal, mesodermal, and peripheral ectodermal cells), and cluster 0 and cluster 1 markers and 20 peripheral genes that were selected from the above 49 genes (total of 137 genes); 3) 93 cells belonging to clusters 1 and 2 (presumptive mesodermal and peripheral ectodermal cells), and above 20 genes and markers of cluster 1 (total of 77 genes). Using R functions, Euclidian distances between cells were calculated and hierarchical clustering of cells was performed with the ward2 method. The results were visualized in dendrograms with the heatmap showing normalized counts.

## Identification of CM-Cell Markers

The expression of LOC107451717 (*Pt-Ets4*) (Pechmann et al., 2017) was used to identify a putative CM cell (#614005), and genes that showed specific expression at this cell were searched based on the following criteria: genes with normalized

count >2 in the cell #614005 and genes whose expression was detected at < 20 cells.

## Image Similarity Search With Open CV Template Matching

A UMAP plot of LOC107444265 (*Pt-noggin-D*) (Akiyama-Oda and Oda, 2020) was used to identify genes specifically expressed at the cumulus. The area of the plot including *Pt-noggin-D*-positive and negative cells (**Figure 6B'**) was used as a template to search the corresponding areas of plots of all other genes for similar images. The background color of UMAP plots was set same as the color of the nonexpressing cells, and searches were performed using the python Open CV template matching module with the normalized correlation coefficient (CCOEFF_NORMED) method.

## cDNA Cloning

Full-length or partial cDNAs were obtained from our laboratory stocks of EST clones or were isolated using PCR. The resulting cDNAs were used to synthesize probes. The cDNA clones and the PCR primers used are listed in **Supplementary Table S10**.

## *In Situ* Hybridization and Image Acquisition

Whole mount *in situ* hybridization (WISH) and fluorescence *in situ* hybridization (FISH) were performed as described previously (Akiyama-Oda and Oda, 2003, Akiyama-Oda and Oda, 2016). Digoxigenin (DIG)-labeled probes were used for the alkaline-phosphatase chromogenic staining of WISH. Signals were amplified with a combination of anti-DIG-POD (used at 1: 1000 dilution, Roche 11 207 733 910), dinitrophenyl (DNP)-tyramide (1:100 dilution, TSA plus DNP system, PerkinElmer), and anti-DNP-AP (1:100 dilution, Vector MB-3100) and were visualized with NBT/BCIP. In FISH, DIG and DNP probes were used in combination with anti-DIG-POD (used at 1: 1000 dilution, Roche 11 207 733 910) and anti-DNP-HRP (used at 1:200 dilution, PerkinElmer FP1129) and 5-(and-6)-carboxyfluorescein and DyLight680 tyramides. Samples were counterstained with DAPI (Sigma-Aldrich) to visualize DNA.

Stained embryos were mounted on glass slides with spacers. WISH samples were observed using a stereomicroscope SZX12 (Olympus) equipped with a color 3CCD camera C7780-10 (Hamamatsu Photonics). FISH samples were observed using a TCS SPE confocal system (Leica). Images were processed using Imaris version 7.6.5 (Bitplane) and Adobe Photoshop CC 2020 and 2021 software.

# RESULTS AND DISCUSSION

## Single-Cell Transcriptome and Clustering of Cells

In the first single-cell RNA-seq experiment, we first utilized dissociated cells from ten late germ-disc stage embryos (late stage 5) (**Figure 1A**). We constructed a single-cell cDNA library using the BD Rhapsody microwell-based platform, followed by sequencing on the Illumina platform and data processing using the BD Rhapsody WTA analysis pipeline (**Supplementary Table S1**) and the Seurat package v.4.0.3 (**Figure 1B**). Transcriptome data obtained from 505 single cells were used for subsequent analysis. On average, 16,953 molecules/cell transcribed from 3,319 genes/cell were detected with a total of 17,770 genes counted once or more in these 505 cells (**Figure 1C**).

Clustering analysis of these cells revealed 4 cell clusters (**Supplementary Figure S1A**). Expression of known markers indicated that two of the four clusters comprise germ-disc epithelial cells (presumptive ectoderm), with the other two comprising mesodermal and endodermal clusters (**Supplementary Figure S1B**) (Yamazaki et al., 2005; Akiyama-Oda and Oda, 2010). The two ectodermal clusters differed in the number of unique genes and molecules detected per cell (**Supplementary Figure S1A**) but similarly exhibited polarized expression of selected A-P marker genes (Akiyama-Oda and Oda, 2020) on the UMAP plot (**Supplementary Figure S1B**) (we will mention the polarization in detail below). To investigate the cause of the separation of two ectodermal cell populations, we identified 445 DEGs between the two ectodermal clusters (**Supplementary Table S2**). Expression of most of these DEGs was detected rather ubiquitously and at high levels (9,373 molecules/gene for the DEGs, in contrast to 482 molecules/gene for all counted genes on average, **Figure 1C**), although the expression levels were different between the two clusters (**Supplementary Figure S1C**, **Supplementary Table S2**). Biased levels of expression between the two clusters were not observed for cell-cycle genes except LOC107436263 (**Supplementary Table S3**, **Supplementary Figure S1D**). This indicated that differences in expression levels of highly expressed genes (the 445 DEGs), but not the cell-cycle states, were the main cause of the cluster separation.

Re-clustering analysis following the exclusion of the 445 DEGs grouped cells into three populations, which corresponded to the presumptive endoderm, mesoderm, and ectoderm (**Figures 2A,B**). The first two populations (clusters 0 and 1, **Figure 2A**) were confirmed by expression of known markers, *At_eW_012_A08* (endoderm) (Akiyama-Oda and Oda, 2010) and *Pt-twist* (*Pt-twi*; mesoderm) (Yamazaki et al., 2005) (**Figure 2B**). New marker genes identified for these clusters were consistently expressed in the endoderm and mesoderm (**Supplementary Table S4**, **Supplementary Figure S2**). The endodermal markers identified by this single-cell transcriptome analysis of late stage 5 embryos largely overlapped genes identified by comparative transcriptome analyses using stage-3 and stage-5 embryos depleted of activity of a novel gata-family gene in another study (Iwasaki-Yokozawa et al., 2022). The two separate studies revealed a consistent endodermal gene set.

The presumptive ectodermal cells were subgrouped into four clusters (clusters 2-5, **Figure 2A**) without clear segregation of specific cell states and without clear differences in distributions of the numbers of molecules and genes per cell (**Supplementary Figure S1E**). Comparison of the expression patterns of selected A-P marker genes (Akiyama-Oda and Oda, 2020) visualized on

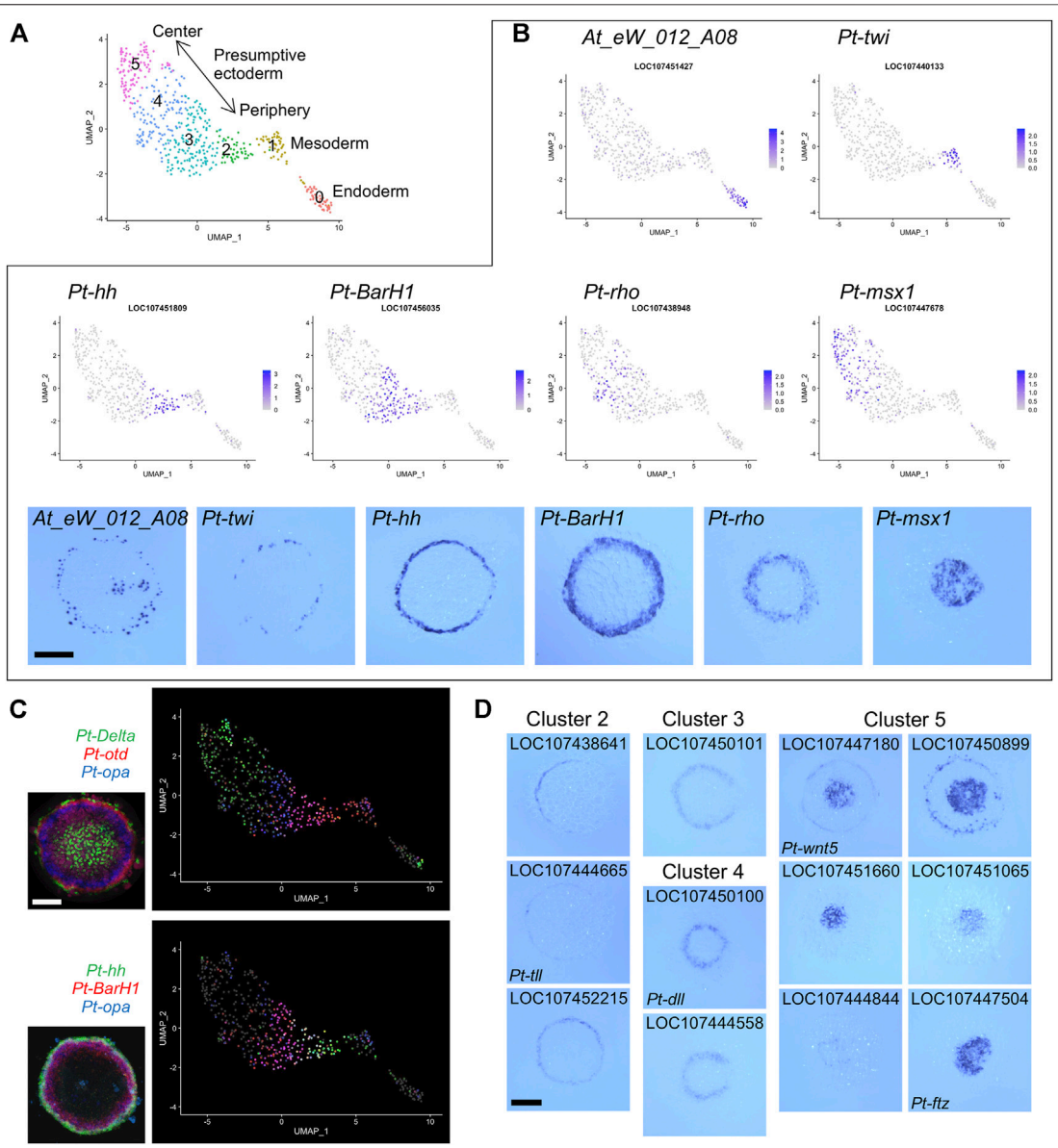


**FIGURE 2 |** Detection of germ layers and the ectodermal polarity using single-cell transcriptomics. **(A)** Clustering analysis of the germ-disc stage embryonic cells. The UMAP plot of 505 cells shows presumptive endodermal (cluster 0), mesodermal (cluster 1), and ectodermal (clusters 2–5) clusters. The arrow shows the reconstructed orientation of the germ disc. The clustering was performed using 48 PCs with a resolution parameter of 1.0. **(B)** Visualization of the expression of germ-layer marker genes and A-P marker genes on the UMAP plot with the color code of the normalized expression levels and in the germ disc at late stage 5 using WISH. *At_eW_012_A08*, endoderm; *Pt-twi* (*twist*), mesoderm; *Pt-hh* (*hedgehog*), peripheral region; *Pt-BarH1*, broad peripheral region; *Pt-rho* (*rhomboid*), intermediate region; *Pt-msx1*, central region. **(C)** Visualization of the expression of three genes on the UMAP plot and in the late germ disc using multicolor FISH. *Pt-Delta* (green), *Pt-otd* (*orthodenticle*, red), and *Pt-opa* (*odd-paired*, blue); *Pt-hh* (green), *Pt-BarH1* (red), and *Pt-opa* (blue). The FISH images are from (Akiyama-Oda and Oda, 2020) (CCBY4.0). **(D)** Expression of marker genes identified for clusters 2–5 in the late germ disc. Scale Bars = 200 μm.

the UMAP plot and detected on the germ disc using WISH indicated that the spatial order of the four clusters on the UMAP plot was correlated with the peripheral-to-central spatial order on the germ disc (**Figure 2B**). This correlation was further supported by multicolor visualization of expression of multiple A-P marker genes on the UMAP plot and the germ disc (**Figure 2C**). A similar correlation was observed even in a smaller spatial range of the UMAP plot and the germ disc (**Figure 2C**, bottom).

Next, we listed possible marker genes for each cluster (**Supplementary Table S4**). The lists of cluster 2 and cluster 3 markers included more than ten genes that had been identified as positive targets of Hh signaling in the previous study and are expressed in the peripheral region of the germ disc. Conversely, the list of cluster 5 markers included six genes that had been identified as negative targets of Hh signaling and are expressed in the central region. The cluster 4 markers included eight genes that

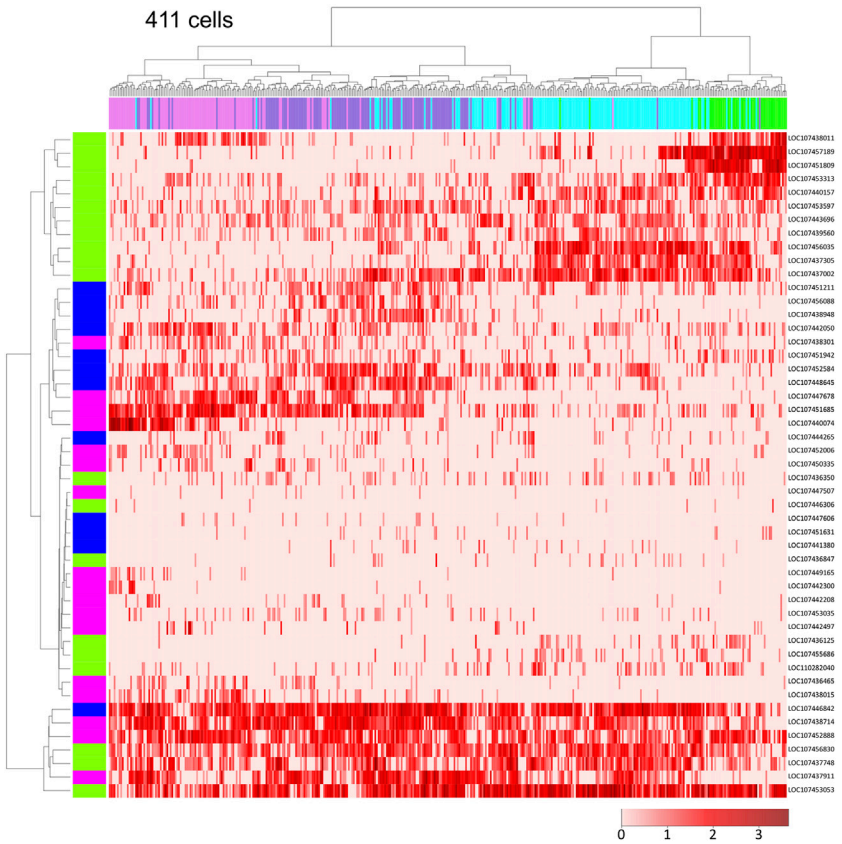


**FIGURE 3 |** Single-cell transcriptome data showing global polarization of presumptive ectodermal cells. Dendrograms of 411 presumptive ectodermal cells (top) and *Pt-hh* and 48 genes regulated by Hh signaling (left) were constructed by hierarchical clustering of the normalized expression level of each gene in each cell. The bar on the top displays the cluster of the cells shown in **Figure 2A**: green, cluster 2; light blue, cluster 3; purple, cluster 4; magenta, cluster 5. The bar on the left shows the expression domain of genes in the germ disc revealed by WISH: green, peripheral region; blue, intermediate region; pink, central region. The heatmap shows the normalized expression levels of genes in the cells (The color code in the bottom right).

had been shown to require negative regulation or both positive and negative regulations by Hh signaling and are expressed in the broad central or intermediate region. Some of the possible marker genes were cloned to show their specific expression in predicted regions of the germ disc (**Figure 2D**). These results suggested that single-cell transcriptome analysis, even when using a small number of early spider embryos, achieves sufficient resolution for separating 3 cell populations corresponding to the germ layers and successfully reconstructs the peripheral-to-central polarity (i.e., the future A-P polarity) in the ectodermal cell population.

## Global A-P Polarity of the Germ Disc

Next, we focused on the ectodermal cell population to investigate the diversity of cell states in detail. Using single-cell RNA-seq data on *Pt-hh* and 48 genes that are expressed in a specific region of the germ disc under the control of Hh signaling (Akiyama-Oda and Oda, 2020), we performed hierarchical clustering analysis of the 411 germ-disc cells belonging to the clusters 2-5. This analysis showed that the cells were roughly grouped in accordance with the clusters; however, cells from the neighboring clusters were not clearly separated but intermingled in the dendrogram (**Figure 3**). It was also shown that individual cell states were highly varied, but not completely different, exhibiting overlapping combinations of expressed genes. These results may represent the nature of the Hh signaling patterning system, which is able to produce a "fuzzy" French-flag-like pattern in a large cellular field. This nature of the Hh signaling patterning system revealed in the *Parasteatoda* embryo sharply contrasts with that of the maternal morphogen system in the *Drosphila* embryo, in which sharp boundaries of gap gene expression domains are established (Jaeger, 2011).

## Reconstruction of Mesodermal Cell Internalization From the Periphery of the Germ Disc

To investigate the separation of the germ layers, we focused on the mesodermal cell population, which internalizes from the periphery of the germ disc (Oda et al., 2007). This cell internalization starts at late stage 5, following the internalization of endodermal cells. We examined the transcript profiles of 140 cells belonging to the clusters 0–2 (**Figure 2A**), possibly corresponding to the presumptive endodermal and mesodermal cell populations and cells at the

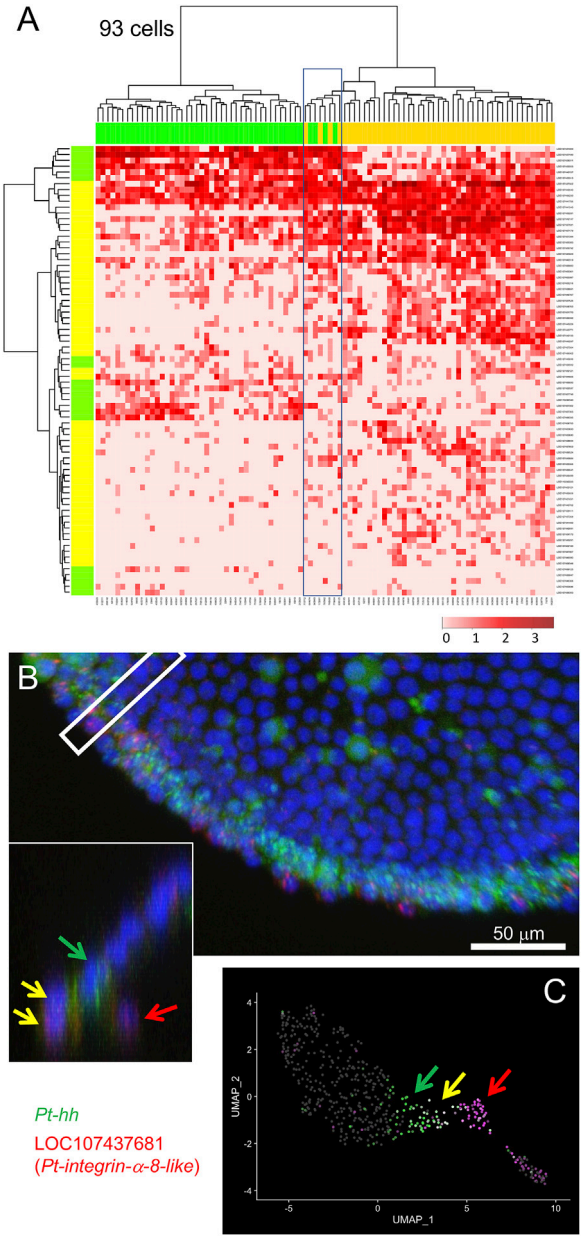


**FIGURE 4 |** Specification of mesodermal cells at the peripheral region. **(A)** Dendrograms of 93 presumptive peripheral ectodermal and mesodermal cells (top) and 77 peripheral and mesodermal marker genes (left) were constructed by hierarchical clustering of the normalized expression level. The bar on the top displays the cluster of the cells shown in **Figure 2A**: yellow, cluster 1 (mesoderm); green, cluster 2 (peripheral ectoderm). The bar on the left shows the group of genes: yellow, mesodermal markers; green, peripheral markers which are the same genes shown in green in **Figure 3**. The heatmap shows the normalized expression levels (color code in the bottom right). Boxed cells show relatively high-level expression of both mesodermal and peripheral markers. **(B)** Detection of *Pt-hh* (green) and LOC107437681 (*Pt-integrin alpha-8-like*, red) transcripts using FISH at the peripheral region of the germ disc at late stage 5. The cross section of the boxed region is shown in the inset. Scale Bar = 50 µm. **(C)** Expression of the two genes visualized on the UMAP plot. In B and C, green arrows show *Pt-hh*-positive cells, red arrows show LOC107437681-positive cells, and yellow allows show double-positive cells.

peripheral region of the germ disc, respectively, using 137 marker genes recognized in previous and ongoing studies. Hierarchical clustering analysis clearly separated the endodermal cells (cluster 0) from the mesodermal and ectodermal cells (clusters 1 and 2) with restricted expression of the cluster 0 markers (**Supplementary Figure S3**). Some of the cluster 1 markers were expressed at relatively high levels in both the mesodermal and endodermal cells. However, we did not detect cells that were in an intermediate state of the endoderm and mesoderm or the endoderm and ectoderm (**Supplementary Figures. S2, S3**). This result provided substantial evidence to suggest that "endodermal" cells were already in distinct cell states at late stage 5.

Following exclusion of the endodermal cells, we examined the remaining 93 cells, possibly including mesodermal cells and cells at the peripheral region of the germ disc, using 77 selected marker genes. Hierarchical clustering analysis revealed the presence of two large cell populations in accordance with clusters 1 and 2, but with a small cell subpopulation displaying intermediate states (**Figure 4A**). To confirm whether cells displaying such intermediate states were present in the late stage-5 embryo, expression of a mesodermal (LOC107437681, *Pt-integrin alpha-8-like*) and a peripheral (LOC107451809, *Pt-hh*) gene was examined using FISH. As a result, cells that expressed both genes were observed at the edge of the germ disc (**Figure 4B**, yellow arrows), with adjacent cells on the germ-disc side expressing only the peripheral gene (**Figure 4B**, the green arrow) and nearby internal cells expressing only the mesodermal gene (**Figure 4B**, the red arrow). These observations suggested the possibility that the double-positive cells at the edge of the germ disc might be in an intermediate state undergoing commitment toward the mesodermal fate. The corresponding intermediate cell state was recognized in the UMAP plot (**Figure 4C**). These examples of data from single-cell RNA-seq analysis highlight the potential of this technique to follow cell state transitions in the developing spider embryo.

## Search for CM Cell Markers

The D-V axis of the spider embryo is specified by symmetry-breaking migration of clustered cells sending Dpp signals from the center of the germ disc following internalization (Akiyama-Oda and Oda, 2003, Akiyama-Oda and Oda, 2006, Akiyama-Oda and Oda, 2010). These cells are referred to as the CM cells. Known markers for this cell type include *Pt-dpp* (LOC107442925), *Pt-fascin (singed)* (At_eW_022_P10, LOC107440147), and *Pt-ets4* (LOC107451717) (Pechmann et al., 2017) (**Figure 5A**). To examine the comprehensiveness and practical use of our single-cell transcriptome data, we searched for additional CM-cell marker genes. Highly specific expression of *Pt-ets4* at the CM cells allowed us to identify a single cell #614005 demonstrating this cell type. This cell was grouped together with many other cells assigned to the presumptive endoderm (**Figure 5B**), strongly suggesting that the CM cells are part of the endoderm, not the mesoderm. Next, we listed up genes showing high levels of expression in the cell #614005 but no expression in most other cells (**Figure 5C**; **Supplementary Table S5**). The top-ranked gene in the list was *Pt-ets4* itself. Eight genes following

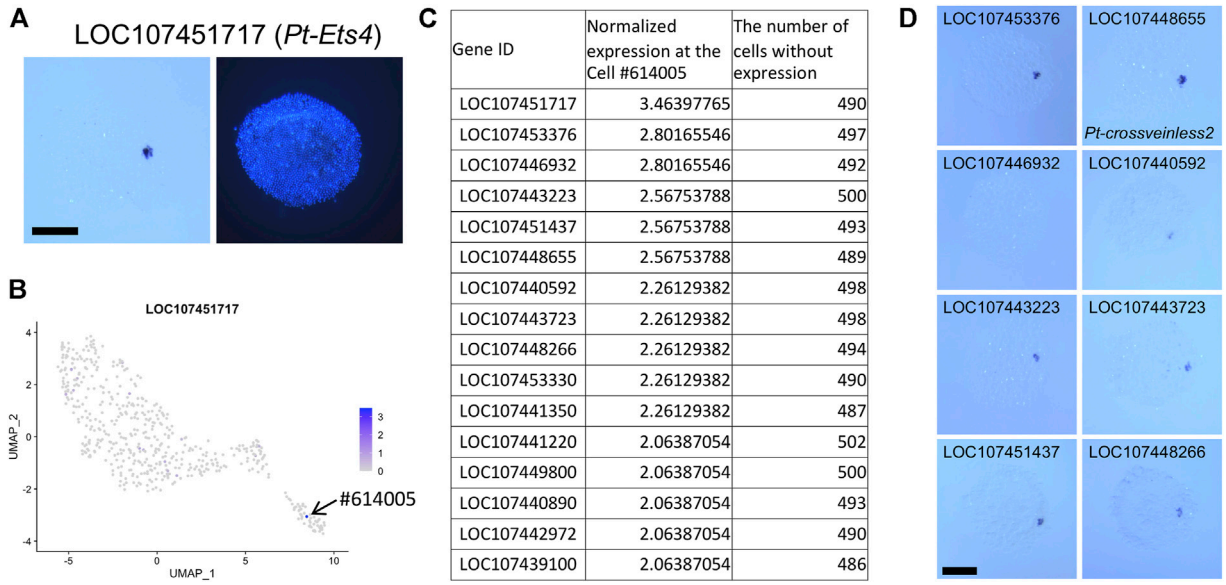


| Gene ID | Normalized expression at the Cell #614005 | The number of cells without expression |
|---|---|---|
| LOC107451717 | 3.46397765 | 490 |
| LOC107453376 | 2.80165546 | 497 |
| LOC107446932 | 2.80165546 | 492 |
| LOC107443223 | 2.56753788 | 500 |
| LOC107451437 | 2.56753788 | 493 |
| LOC107448655 | 2.56753788 | 489 |
| LOC107440592 | 2.26129382 | 498 |
| LOC107443723 | 2.26129382 | 498 |
| LOC107448266 | 2.26129382 | 494 |
| LOC107453330 | 2.26129382 | 490 |
| LOC107441350 | 2.26129382 | 487 |
| LOC107441220 | 2.06387054 | 502 |
| LOC107449800 | 2.06387054 | 500 |
| LOC107440890 | 2.06387054 | 493 |
| LOC107442972 | 2.06387054 | 490 |
| LOC107439100 | 2.06387054 | 486 |

**FIGURE 5 |** Identification of CM cell transcriptome. **(A)** Expression of LOC107451717 (*Pt-Ets4*) in a germ disc at late stage 5. The signal is detected at the CM cells. The right panel shows DAPI staining of the same embryo. **(B)** Expression of LOC107451717 visualized on the UMAP plot. Strong expression is detected specifically at the cell #614005 in the endodermal cluster. **(C)** The list of genes that show specific expression in the cell #614005. The normalized expression level in the cell #614005 and the number of cells (out of 505 cells) with no expression of the gene are shown. **(D)** Detection of transcripts of the top 9 genes (except LOC107451717) in the list. Signals are detected at the CM cells. Scale Bars = 200 μm.

*Pt-ets4* in the list were confirmed to be specifically expressed in the CM cells using WISH staining (**Figure 5D**). These results indicated that single-cell transcriptome data provide comprehensive resources that help to detect specific cell populations, even a small one, and marker genes for such cell types.

## Search for Genes With Similar Expression Pattern by Template Matching

We further attempted a gene search based on expression pattern similarity using the Open CV template matching module, which was applied to the UMAP plots displaying expression of individual genes. We focused on the region called the cumulus (Akiyama-Oda and Oda, 2003, Akiyama-Oda and Oda, 2006). Expression of several known genes, including LOC107444265 (*Pt-noggin-D*) (**Figure 6A**) and LOC107448880 (*Pt-gata1/gataC*) (Akiyama-Oda and Oda, 2010, Akiyama-Oda and Oda, 2020), is induced at the cumulus in response to the signals from the CM cells. As a simple example, we chose a rectangular region on the UMAP plot where several presumptive ectodermal (germ-disc) cells expressing high levels of *Pt-noggin-D* expression, which presumably correspond to the cumulus, are included together with several nonresponding cells (**Figure 6B,B'**). Using the rectangular region, we performed the template matching search against the corresponding regions of the UMAP plot images for all genes. Ten genes that were hit with highest similarity scores were listed, which included *Pt-noggin-D* itself and *Pt-gata1* (**Figure 6C**; **Supplementary Table S6**). The top 6 genes, except the fifth gene LOC107455782, whose expression was rather ubiquitous in the UMAP plot, were confirmed to show highly specific expression to the cumulus cells (**Figure 6D**). Application of a template matching tool to single-cell RNA-seq datasets provides a way to genome-widely identify genes whose expression is spatially regulated.

## Application of Single-Nucleus RNA-Seq for the Spider Embryo

Single-nucleus RNA-seq can be used to access mRNA (de novo transcripts or pre-mRNA) in nuclei. This technique is sometimes substituted for the single-cell RNA-seq technique, especially in cases where dissociation and collection of cells are difficult and target tissues are composed of divergent cell types (Grindberg et al., 2013; Habib et al., 2016; Zeng et al., 2016; Hu et al., 2017). We simultaneously applied single-cell and single-nucleus RNA-seq to the *Parasteatoda* germ-disc stage embryo to compare the performance of the two transcriptome techniques. In this second analysis, nuclei were extracted from 20 sibling embryos, and cells were subsequently dissociated from the same number of sibling embryos. Since the nuclei extraction took approximately 1 h 20 min to complete, the developmental stage for the nuclei sample was correspondingly earlier than those for the cell sample. When comparing the sampling timing of the cell samples between the first and second analyses, samples used for the second analysis were a little older (1–2 h) than those used for the first analysis. During the course of data analysis, the reference genome assembly of *Parasteatoda* was updated (Ptep_3.0). Therefore, we aligned RNA-seq reads against both the version-2 and version-3 genomes and also against the version-

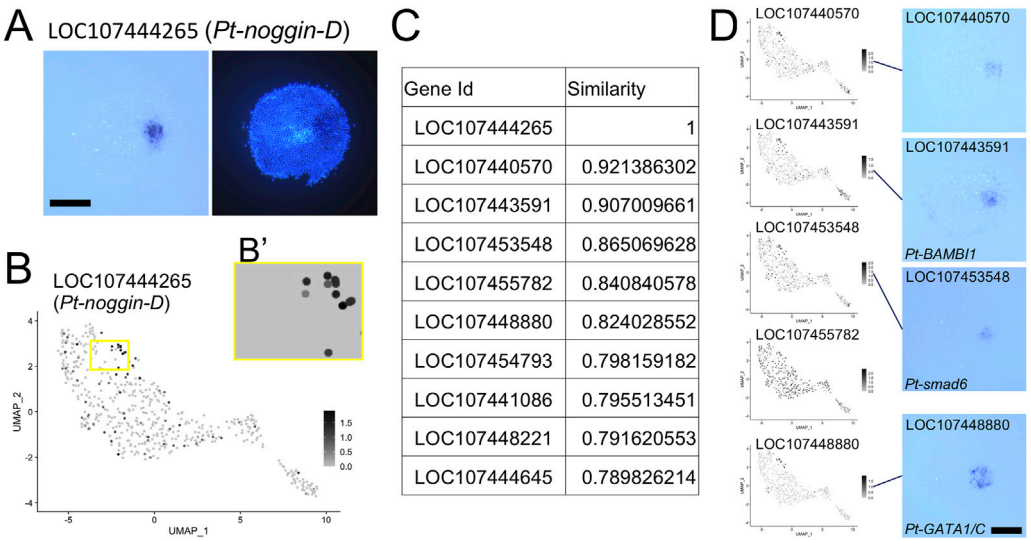


| Gene Id | Similarity |
|---|---|
| LOC107444265 | 1 |
| LOC107440570 | 0.921386302 |
| LOC107443591 | 0.907009661 |
| LOC107453548 | 0.865069628 |
| LOC107455782 | 0.840840578 |
| LOC107448880 | 0.824028552 |
| LOC107454793 | 0.798159182 |
| LOC107441086 | 0.795513451 |
| LOC107448221 | 0.791620553 |
| LOC107444645 | 0.789826214 |

**FIGURE 6 |** Identification of the cumulus on the UMAP plot. **(A)** Expression of LOC107444265 (*Pt-noggin-D*) in a germ disc at late stage 5. The signal is detected at the cumulus. The right panel shows DAPI staining of the same embryo. **(B)** Expression of LOC107444265 visualized on the UMAP plot. The region boxed in yellow was used as a template in the Open CV similarity search after the background color was changed to the color of cells without expression as in **(B')**. **(C)** The list of genes with highest similarity scores in the similarity search. **(D)** Expression of the top 6 genes except LOC107444265 visualized on the UMAP plot and detected using WISH. *In situ* hybridization of LOC107455782 was not performed. Scale Bars = 200 μm.

3 genome whose annotation was modified to count both intronic and exonic reads. As summarized in **Supplementary Table S7**, alignment against the version-3 genome resulted in detection of a slightly higher number of molecules than that against the version-2 genome in both single-cell and single-nucleus experiments. An increased number of molecules were detected when using the modified version-3 genome to analyze single-nucleus data. We used single-cell data aligned to the version-3 genome and single-nucleus data aligned to the modified version-3 genome for downstream analysis.

We followed similar procedures as the first single-cell data analysis (**Figure 1B**). After filtering out low-quality cells (**Figure 1C**), we performed a clustering analysis. In the single-cell analysis, germ-disc epithelial cells (presumptive ectodermal cells) with polarized expression of A-P marker genes were separated into two large clusters similar to the first single-cell analysis (**Supplementary Figures S1, S4A**), although this time the two clusters did not differ in the numbers of genes and molecules detected per cell. The situation of the single-nucleus analysis result was distinct; in the UMAP plot, presumptive ectodermal cells were distributed in one large mass with mesodermal cells, and the first split of ectodermal subclusters was detected between the peripheral cells and others (**Supplementary Figure S4B**).

The following analyses were performed with data that excluded 85 genes identified as DEGs of the two ectodermal clusters in this single-cell analysis (**Supplementary Table S8**), which showed ubiquitous and high levels of expression. The clustering analysis using this dataset showed similar results as in the first single-cell analysis (**Supplementary Figure S5**; **Figure 2**). We detected three germ layers and the A-P polarization of germ-disc cells in the single-nucleus as well as the single-cell analysis. The CM cells and a cluster for the cumulus cells were also detected. However, there was one uncharacterized cluster in the single-cell analysis (cluster 5 in **Supplementary Figure S5A**) and one cluster consisting of nuclei with relatively low numbers of genes and molecules in the single-nucleus analysis (cluster 7 in **Supplementary Figure S5B**). These indicated that the single-nucleus and single-cell RNA-seq analyses produced mostly consistent results, but one difference between the two methods was found: single-cell RNA-seq, unlike single-nucleus RNA-seq, was affected by the expression levels of a set of genes expressed ubiquitously and at high levels.

## Identification of Dynamic Cell States by Single-Nucleus Transcriptome

Next, to compare the capabilities of detecting and separating dynamic cell states in the single-cell and single-nucleus transcriptome analyses, we tested higher resolution parameters. As shown in **Supplementary Figure S5**, the clustering analysis at a low-resolution parameter identified four clusters of ectodermal cells corresponding to peripheral-to-central (future anterior-to-posterior) series of regions of the germ disc both in the single-cell (clusters 3, 0, 1, 2 in **Supplementary Figure S5A**) and single-nucleus analysis (clusters 3, 2, 1, 0 in **Supplementary Figure S5B**). Using higher resolution parameters, more clusters were identified (**Figure 7A**). Here, we focused on two types of dynamic gene expression that are known to occur in the central region of the germ disc. One of the two originates from the progressive activation of Delta-Notch signaling from around the center of the germ disc, which leads to the formation of a salt-and-pepper pattern of gene expression that reflects the specification

of the caudal mesodermal and caudal ectodermal cell fates (Oda et al., 2007). The other is initiation of oscillatory gene expression that contributes to the formation of segmental stripes in the posterior ectoderm (Akiyama-Oda and Oda, 2020). In the single-cell analysis using a high-resolution parameter, the central cluster (cluster 2 in **Supplementary Figure S5A**) was split into two subclusters (clusters 2 and 12 in **Figure 7A**), while in the single-nucleus analysis, cluster 0 in **Supplementary Figure S5B** was split into three subclusters (clusters 2, 6, and 9 in **Figure 7B**). Both the cluster 2s were comparable to each other, representing cell states in the wide central region similar to those detected with the low-resolution parameters. Cluster 12 in the single-cell analysis was comparable to cluster 6 in the single-nucleus analysis. Both clusters were characterized by expression of *Pt-Delta* and two other genes (LOC107440074, LOC107442300; **Supplementary Table S9**; **Supplementary Figure S6**), representing the cell state specified as the caudal mesoderm. The additional cluster 9 in the single-nucleus analysis was characterized by expression of *Pt-aslH*, *Pt-krü1*, and other genes (LOC107447499, LOC107450670), which were faintly detected in cells around the center of the germ disc at late stage 5 (38 h AEL) and strongly detected in a broader area at early stage 6 (41 h AEL) (**Figure 7C**). The expression of these genes was developed to exhibit a dynamic pattern which varied depending on the gene in the opisthosomal region (53 h AEL). The location of the cluster 9 on the UMAP plot in the single-nucleus analysis was in accordance with the reconstructed global polarity in the ectodermal cell population, with the emerging caudal mesodermal cell population (cluster 6) being separated. Moreover, differential ranges of the expression regions of the cluster 9-specific genes were recognized on the UMAP plot (**Figure 7D**), possibly capturing ordered transcriptional activations in the posterior terminal cell population. In contrast to the single-nucleus analysis, the single-cell analysis did not detect the corresponding posterior terminal cell population as a separate subcluster even when parameters for the dimension and resolution were raised. Nevertheless, cell states characterized by expression of the four genes (*Pt-aslH*, *Pt-krü1*, LOC107447499, and LOC107450670) were found in a limited area in the posterior terminal cell population on the UMAP plot, but the polarity reconstruction was imperfect (**Supplementary Figure S7**). Considering that the sampling timing for the single-cell transcriptome was a little later than that for the single-nucleus transcriptome, the poorer resolution of the single-cell transcriptome was likely due to lower sensitivity to the emerging cell states. Collectively, these results suggested that single-nucleus RNA-seq is more powerful than single-cell RNA-seq in detecting dynamic cell states in early spider embryos.

## Future Applications of Single-Cell and Single-Nucleus Transcriptome Techniques in the Spider Model System

In this study, we showed that the singe-cell/nucleus transcriptome techniques are applicable to examination of patterning of early spider embryos. Our results indicate that these techniques exhibit different features. Owing to a higher sensitivity, the single-nucleus RNA-seq enables detection of dynamic cell states. On the other hand, because the single-cell RNA-seq can detect mRNA molecules in the cytoplasm, data obtained with this technique are suitable for quantitative comparison with gene expression data obtained by FISH and can be used to spatial reconstruction of gene expression.

There are many merits of using singe-cell/nucleus transcriptome techniques for studying the patterning processes in *Parasteatoda*. Most previous studies using this spider model system have relied on molecular and genetic knowledge accumulated in the well-studied model organisms, such as *Drosophila*. Application of these techniques, however, allows us to focus our research on components of the *Parasteatoda* genome in an unbiased way. The fact that the gene expression patterns in the early spider embryo are reconstructed to a large extent by the single-nucleus transcriptome indicates that genome-wide discovery of genes whose expression is spatially regulated is possible without laborious staining of embryos. Moreover, if such gene discovery is combined with functional gene screening (e.g., parental and embryonic RNAi), as done in some previous studies (Oda et al., 2007; Akiyama-Oda and Oda, 2010, Akiyama-Oda and Oda, 2020; Kanayama et al., 2011; Pechman et al., 2017), we would be able to identify key genes necessary for specific steps in the patterning processes.

When the sequenced genome is available for a species, a popular method to find genes of interest is to search for sequences using sequence similarity detection tools, such as BLAST. Given that the gene expression patterns are reconstructed, an alternative can be to search patterns using image similarity detection tools, such as template matching. However, we will require a web-based application to facilitate this type of gene searches.

In this work, our analyses were focused on the late stage 5 of *Parasteatoda* embryonic development. An issue that should be addressed is to what extent the gene expression patterns can be reconstructed by single-cell/nucleus transcriptome analyses when using older embryos, in which more complicated patterns of gene expression have been developed. If pattern reconstruction is achieved in a broad range of developmental stages, we might be able to analyze time-series samples to obtain clues about genetic components that contribute to driving pattern-forming processes.

# CONCLUSION

This work has demonstrated that single-cell and single-nucleus RNA-seq analyses are applicable to the germ-disc stage embryo in *Parasteatoda*. Both techniques worked effectively using only twenty or fewer embryos as the starting material for each experiment. UMAP clustering reveals separation of the three germ layers and a reconstruction of the global polarity in the presumptive ectodermal cell population. Additionally, we showed that the data resources generated by the transcriptome analyses help to conduct a genome-wide search for genes whose expression is spatially regulated,

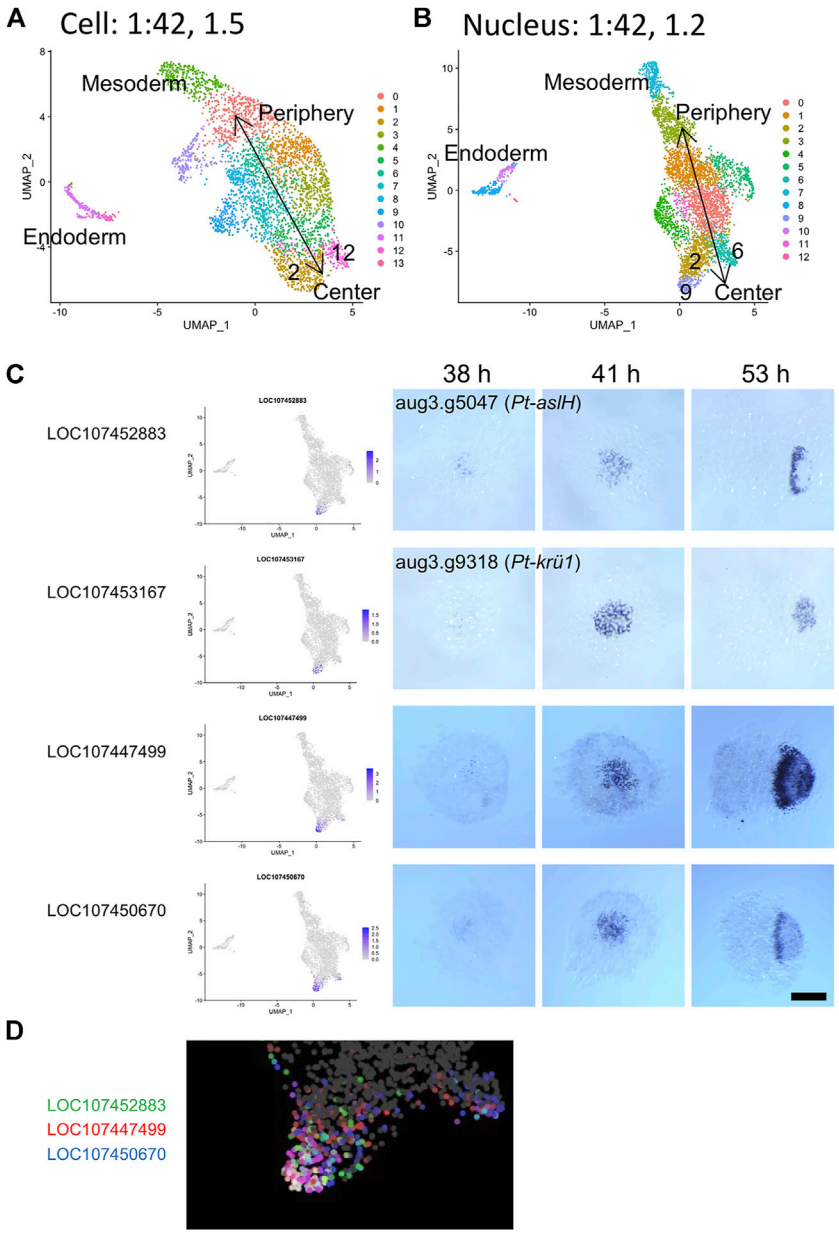


**FIGURE 7 |** Detection of a dynamically emerging cell state using single-nucleus transcriptomics. **(A,B)** The UMAP plots of 3,621 cells **(A)** and 4,720 nuclei **(B)**, showing clusters generated from the second single-cell **(A)** and the single-nucleus **(B)** transcriptome data. The clustering was performed using 42 PCs and with resolution parameters of 1.5 **(A)** and 1.2 **(B)**. Annotations of the germ layers and the reconstructed orientation of the germ disc are indicated. **(C)** Expression of cluster 9 marker genes identified in the single-nucleus transcriptome analysis. The expression is visualized on the UMAP plot (left) and is detected using WISH. The stained embryos are at late germ-disc stage (38 h, late stage 5), the start of germ-disc to germ-band transition stage (41 h, early stage 6), and early germ-band stage (53 h, stage 7). Embryos shown in the right panels (53 h) are oriented anterior to the left. Scale Bar = 200 μm. The images of embryos stained for *Pt-aslH* and *Pt-krü1* transcripts are from Akiyama-Oda and Oda (2020) (CCBY4.0). **(D)** Expression of three cluster 9 marker genes visualized in three colors on the UMAP plot. The cluster 9 region is enlarged.

based on the detection of pattern similarity. We also showed that single-nucleus transcriptome analysis is more powerful than single-cell transcriptome analysis in detecting dynamic cell states in developing spider embryos. We propose that future applications of these transcriptome techniques to *Parasteatoda* embryos at broader developmental stages may help to study the pattern formation in a simple cellular field, which cannot be accessible by the *Drosophila* blastoderm embryo.

## DATA AVAILABILITY STATEMENT

The datasets presented in this study can be found in online repositories. The names of the repository/repositories and accession number(s) can be found at: GEO accession GSE201705.

## ETHICS STATEMENT

The animal study was reviewed and approved by JT Biohistory Research Hall (No. 2020-1).

## AUTHOR CONTRIBUTIONS

YA and HO conceived the project. YA performed the experiments and data analysis. TA and HO designed the method of the similarity search. YA designed the image visualization with image magic, and TA arranged the laboratory database with help from YA and HO. YA wrote the manuscript with support from HO.

## FUNDING

This work was supported by JST PRESTO (JPMJPR2041), JSPS Kakenhi (20K06676), and JT Biohistory Research Hall.

## ACKNOWLEDGMENTS

The authors would like to thank Dr. S. Iwasaki-Yokozawa for *Pt-Ets4* and LOC107439896 probes, Ms. A. Noda for technical assistance, Prof. K. Sano, Prof. T. Nakano, and Prof. Y. Takahashi for encouragement and discussion, and the members of JT Biohistory Research Hall and the members of the PRESTO Multicellular System project for discussion.

## SUPPLEMENTARY MATERIAL

The Supplementary Material for this article can be found online at: https://www.frontiersin.org/articles/10.3389/fcell.2022.933220/full#supplementary-material

## REFERENCES

Akiyama-Oda, Y., and Oda, H. (2006). Axis Specification in the Spider Embryo: dppis Required for Radial-To-Axial Symmetry Transformation Andsogfor Ventral Patterning. *Development* 133, 2347–2357. doi:10.1242/dev.02400

Akiyama-Oda, Y., and Oda, H. (2010). Cell Migration that Orients the Dorsoventral axis Is Coordinated with Anteroposterior Patterning Mediated by Hedgehog Signaling in the Early Spider Embryo. *Development* 137, 1263–1273. doi:10.1242/dev.045625

Akiyama-Oda, Y., and Oda, H. (2003). Early Patterning of the Spider Embryo: a Cluster of Mesenchymal Cells at the Cumulus Produces Dpp Signals Received by Germ Disc Epithelial Cells. *Development* 130, 1735–1747. doi:10.1242/dev.00390

Akiyama-Oda, Y., and Oda, H. (2020). Hedgehog Signaling Controls Segmentation Dynamics and Diversity via *Msx1* in a Spider Embryo. *Sci. Adv.* 6, eaba7261. doi:10.1126/sciadv.aba7261

Akiyama-Oda, Y., and Oda, H. (2016). Multi-color FISH Facilitates Analysis of Cell-type Diversification and Developmental Gene Regulation in theParasteatodaspider Embryo. *Dev. Growth Differ.* 58, 215–224. doi:10.1111/dgd.12263

Bate, M., and Arias, A. M. (1993). *The Development of* Drosophila melanogaster. New York: Cold Spring Harbor Laboratory Press.

Briscoe, J., and Small, S. (2015). Morphogen Rules: Design Principles of Gradient-Mediated Embryo Patterning. *Development* 142, 3996–4009. doi:10.1242/dev.129452

Briscoe, J., and Thérond, P. P. (2013). The Mechanisms of Hedgehog Signalling and its Roles in Development and Disease. *Nat. Rev. Mol. Cell. Biol.* 14, 416–429. doi:10.1038/nrm3598

Chan, L.-N., and Gehring, W. (1971). Determination of Blastoderm Cells in *Drosophila melanogaster*. *Proc. Natl. Acad. Sci. U.S.A.* 68, 2217–2221. doi:10.1073/pnas.68.9.2217

Dessaud, E., McMahon, A. P., and Briscoe, J. (2008). Pattern Formation in the Vertebrate Neural Tube: a Sonic Hedgehog Morphogen-Regulated Transcriptional Network. *Development* 135, 2489–2503. doi:10.1242/dev.009324

Dobin, A., Davis, C. A., Schlesinger, F., Drenkow, J., Zaleski, C., Jha, S., et al. (2013). STAR: Ultrafast Universal RNA-Seq Aligner. *Bioinformatics* 29, 15–21. doi:10.1093/bioinformatics/bts635

Driever, W., and Nüsslein-Volhard, C. (1988a). A Gradient of Bicoid Protein in Drosophila Embryos. *Cell.* 54, 83–93. doi:10.1016/0092-8674(88)90182-1

Driever, W., and Nüsslein-Volhard, C. (1988b). The Bicoid Protein Determines Position in the Drosophila Embryo in a Concentration-dependent Manner. *Cell.* 54, 95–104. doi:10.1016/0092-8674(88)90183-3

Economou, A. D., Ohazama, A., Porntaveetus, T., Sharpe, P. T., Kondo, S., Basson, M. A., et al. (2012). Periodic Stripe Formation by a Turing Mechanism Operating at Growth Zones in the Mammalian Palate. *Nat. Genet.* 44, 348–351. doi:10.1038/ng.1090

Grindberg, R. V., Yee-Greenbaum, J. L., McConnell, M. J., Novotny, M., O'Shaughnessy, A. L., Lambert, G. M., et al. (2013). RNA-Sequencing from Single Nuclei. *Proc. Natl. Acad. Sci. U.S.A.* 110, 19802–19807. doi:10.1073/pnas.1319700110

Habib, N., Li, Y., Heidenreich, M., Swiech, L., Avraham-Davidi, I., Trombetta, J. J., et al. (2016). Div-Seq: Single-Nucleus RNA-Seq Reveals Dynamics of Rare Adult Newborn Neurons. *Science* 353, 925–928. doi:10.1126/science.aad7038

Hemmi, N., Akiyama-Oda, Y., Fujimoto, K., and Oda, H. (2018). A Quantitative Study of the Diversity of Stripe-Forming Processes in an Arthropod Cell-Based Field Undergoing axis Formation and Growth. *Dev. Biol.* 437, 84–104. doi:10.1016/j.ydbio.2018.03.001

Hilbrant, M., Damen, W. G. M., and McGregor, A. P. (2012). Evolutionary Crossroads in Developmental Biology: the Spider Parasteatoda Tepidariorum. *Development* 139, 2655–2662. doi:10.1242/dev.078204

Hu, P., Fabyanic, E., Kwon, D. Y., Tang, S., Zhou, Z., and Wu, H. (2017). Dissecting Cell-type Composition and Activity-dependent Transcriptional State in Mammalian Brains by Massively Parallel Single-Nucleus RNA-Seq. *Mol. Cell.* 68, 1006–1015. e7. doi:10.1016/j.molcel.2017.11.017

Isshiki, T., Takeichi, M., and Nose, A. (1997). The Role of the Msh Homeobox Gene during Drosophila Neurogenesis: Implication for the Dorsoventral Specification of the Neuroectodermfication of the Neuroectoderm. *Development* 124, 3099–3109. doi:10.1242/dev.124.16.3099

Iwasaki-Yokozawa, S., Nanjo, R., Akiyama-Oda, Y., and Oda, H. (2022). Lineage-specific, Fast-Evolving GATA-like Gene Regulates Zygotic Gene Activation to Promote Endoderm Specification and Pattern Formation in the Theridiidae Spider. *bioRxiv* 6, 495620. doi:10.1101/2022.06.10.495620

Jaeger, J. (2011). The Gap Gene Network. *Cell. Mol. Life Sci.* 68, 243–274. doi:10.1007/s00018-010-0536-y

Jaitin, D. A., Kenigsberg, E., Keren-Shaul, H., Elefant, N., Paul, F., Zaretsky, I., et al. (2014). Massively Parallel Single-Cell RNA-Seq for Marker-free Decomposition of Tissues into Cell Types. *Science* 343, 776–779. doi:10.1126/science.1247651

Kanayama, M., Akiyama-Oda, Y., Nishimura, O., Tarui, H., Agata, K., and Oda, H. (2011). Travelling and Splitting of a Wave of Hedgehog Expression Involved in Spider-Head Segmentation. *Nat. Commun.* 2, 500. doi:10.1038/ncomms1510

Kanayama, M., Akiyama-Oda, Y., and Oda, H. (2010). Early Embryonic Development in the Spider Achaearanea Tepidariorum: Microinjection Verifies that Cellularization Is Complete before the Blastoderm Stage. *Arthropod Struct. Dev.* 39, 436–445. doi:10.1016/j.asd.2010.05.009

Kong, J. H., Siebold, C., and Rohatgi, R. (2019). Biochemical Mechanisms of Vertebrate Hedgehog Signaling. *Development* 146, dev166892. doi:10.1242/dev.166892

Lord, P. C. W., Lin, M.-H., Hales, K. H., and Storti, R. V. (1995). Normal Expression and the Effects of Ectopic Expression of the Drosophila Muscle Segment Homeobox (Msh) Gene Suggest a Role in Differentiation and Patterning of Embryonic Muscles. *Dev. Biol.* 171, 627–640. doi:10.1006/dbio.1995.1310

Macosko, E. Z., Basu, A., Satija, R., Nemesh, J., Shekhar, K., Goldman, M., et al. (2015). Highly Parallel Genome-wide Expression Profiling of Individual Cells Using Nanoliter Droplets. *Cell.* 161, 1202–1214. doi:10.1016/j.cell.2015.05.002

McGregor, A. P., Pechmann, M., Schwager, E. E., Feitosa, N. M., Kruck, S., Aranda, M., et al. (2008). Wnt8 Is Required for Growth-Zone Establishment and Development of Opisthosomal Segments in a Spider. *Curr. Biol.* 18, 1619–1623. doi:10.1016/j.cub.2008.08.045

McLaughlin, C. N., Brbić, M., Xie, Q., Li, T., Horns, F., Kolluru, S. S., et al. (2021). Single-cell Transcriptomes of Developing and Adult Olfactory Receptor Neurons in Drosophila. *eLife* 10, e63856. doi:10.7554/eLife.63856

Oda, H., and Akiyama-Oda, Y. (2020). The Common House Spider Parasteatoda Tepidariorum. *EvoDevo* 11, 6. doi:10.1186/s13227-020-00152-z

Oda, H., Nishimura, O., Hirao, Y., Tarui, H., Agata, K., and Akiyama-Oda, Y. (2007). Progressive Activation of Delta-Notch Signaling from Around the Blastopore Is Required to Set up a Functional Caudal Lobe in the spiderAchaearanea Tepidariorum. *Development* 134, 2195–2205. doi:10.1242/dev.004598

Pechmann, M., Benton, M. A., Kenny, N. J., Posnien, N., and Roth, S. (2017). A Novel Role for Ets4 in axis Specification and Cell Migration in the Spider Parasteatoda Tepidariorum. *eLife* 6, e27590. doi:10.7554/eLife.27590

Pechmann, M., Khadjeh, S., Turetzek, N., McGregor, A. P., Damen, W. G. M., and Prpic, N.-M. (2011). Novel Function of Distal-Less as a Gap Gene during Spider Segmentation. *PLoS Genet.* 7, e1002342. doi:10.1371/journal.pgen.1002342

Pechmann, M., McGregor, A. P., Schwager, E. E., Feitosa, N. M., and Damen, W. G. M. (2009). Dynamic Gene Expression Is Required for Anterior Regionalization in a Spider. *Proc. Natl. Acad. Sci. U.S.A.* 106, 1468–1472. doi:10.1073/pnas.0811150106

Placzek, M., and Briscoe, J. (2018). Sonic Hedgehog in Vertebrate Neural Tube Development. *Int. J. Dev. Biol.* 62, 225–234. doi:10.1387/ijdb.170293jb

Ribes, V., and Briscoe, J. (2009). Establishing and Interpreting Graded Sonic Hedgehog Signaling during Vertebrate Neural Tube Patterning: The Role of Negative Feedback. *Cold Spring Harb. Perspect. Biol.* 1, a002014. doi:10.1101/cshperspect.a002014

Satija, R., Farrell, J. A., Gennert, D., Schier, A. F., and Regev, A. (2015). Spatial Reconstruction of Single-Cell Gene Expression Data. *Nat. Biotechnol.* 33, 495–502. doi:10.1038/nbt.3192

Schönauer, A., Paese, C. L. B., Hilbrant, M., Leite, D. J., Schwager, E. E., Feitosa, N. M., et al. (2016). The Wnt and Delta-Notch Signalling Pathways Interact to Direct Pair-Rule Gene Expression via *Caudal* during Segment Addition in the Spider *Parasteatoda Tepidariorum*. *Development* 143, 2455–2463. doi:10.1242/dev.131656

Schwager, E. E., Sharma, P. P., Clarke, T., Leite, D. J., Wierschin, T., Pechmann, M., et al. (2017). The House Spider Genome Reveals an Ancient Whole-Genome Duplication during Arachnid Evolution. *BMC Biol.* 15, 62. doi:10.1186/s12915-017-0399-x

Setton, E. V. W., and Sharma, P. P. (2021). A Conserved Role for Arrow in Posterior axis Patterning across Arthropoda. *Dev. Biol.* 475, 91–105. doi:10.1016/j.ydbio.2021.02.006

Tickle, C., and Towers, M. (2017). Sonic Hedgehog Signaling in Limb Development. *Front. Cell. Dev. Biol.* 5, 14. doi:10.3389/fcell.2017.00014

Tzani, I., Herrmann, N., Carillo, S., Spargo, C. A., Hagan, R., Barron, N., et al. (2021). Tracing Production Instability in a Clonally Derived CHO Cell Line Using Single-cell Transcriptomics. *Biotech Bioeng.* 118, 2016–2030. doi:10.1002/bit.27715

Wolpert, L. (1969). Positional Information and the Spatial Pattern of Cellular Differentiation. *J. Theor. Biol.* 25, 1–47. doi:10.1016/S0022-5193(69)80016-0

Yamazaki, K., Akiyama-Oda, Y., and Oda, H. (2005). Expression Patterns of a Twist-Related Gene in Embryos of the Spider Achaearanea Tepidariorum Reveal Divergent Aspects of Mesoderm Development in the Fly and Spider. *Zoological Sci.* 22, 177–185. doi:10.2108/zsj.22.177

Zeng, W., Jiang, S., Kong, X., El-Ali, N., Ball, A. R., Ma, C. I.-H., et al. (2016). Single-nucleus RNA-Seq of Differentiating Human Myoblasts Reveals the Extent of Fate Heterogeneity. *Nucleic Acids Res.* 44, e158. doi:10.1093/nar/gkw739

Zhu, J., and Mackem, S. (2017). John Saunders' ZPA, Sonic Hedgehog and Digit Identity - How Does it Really All Work? *Dev. Biol.* 429, 391–400. doi:10.1016/j.ydbio.2017.02.001

**Conflict of Interest:** The authors declare that the research was conducted in the absence of any commercial or financial relationships that could be construed as a potential conflict of interest.

**Publisher's Note:** All claims expressed in this article are solely those of the authors and do not necessarily represent those of their affiliated organizations, or those of the publisher, the editors, and the reviewers. Any product that may be evaluated in this article, or claim that may be made by its manufacturer, is not guaranteed or endorsed by the publisher.

frontiers | Frontiers in Cell and Developmental Biology

TYPE Original Research
PUBLISHED 12 August 2022
DOI 10.3389/fcell.2022.932814



OPEN ACCESS

EDITED BY
Tsuyoshi Hirashima,
National University of Singapore,
Singapore

REVIEWED BY
Adrian Neagu,
Victor Babes University of Medicine and Pharmacy, Romania
Simon Kaspar Schnyder,
The University of Tokyo, Japan

*CORRESPONDENCE
Motohiro Fujiwara,
motohiro.fujiwara@brh.co.jp
Hiroki Oda,
hoda@brh.co.jp

SPECIALTY SECTION
This article was submitted to Cell Adhesion and Migration, a section of the journal Frontiers in Cell and Developmental Biology

RECEIVED 30 April 2022
ACCEPTED 08 July 2022
PUBLISHED 12 August 2022

CITATION
Fujiwara M, Akiyama-Oda Y and Oda H (2022), Virtual spherical-shaped multicellular platform for simulating the morphogenetic processes of spider-like body axis formation.
*Front. Cell Dev. Biol.* 10:932814.
doi: 10.3389/fcell.2022.932814



# Virtual spherical-shaped multicellular platform for simulating the morphogenetic processes of spider-like body axis formation

Motohiro Fujiwara[1]*, Yasuko Akiyama-Oda[1,2,3] and Hiroki Oda[1,4]*

[1]Laboratory of Evolutionary Cell and Developmental Biology, JT Biohistory Research Hall, Takatsuki, Japan, [2]PRESTO, Japan Science and Technology Agency (JST), Kawaguchi, Japan, [3]Department of Microbiology and Infection Control, Faculty of Medicine, Osaka Medical and Pharmaceutical University, Takatsuki, Japan, [4]Department of Biological Science, Graduate School of Science, Osaka University, Toyonaka, Japan

Remodeling of multicellular architecture is a critical developmental process for shaping the axis of a bilaterally symmetric animal body and involves coordinated cell–cell interactions and cell rearrangement. In arthropods, the early embryonic process that leads to the segmented body axis varies at the cellular and molecular levels depending on the species. Developmental studies using insect and spider model species have provided specific examples of these diversified mechanisms that regulate axis formation and segmentation in arthropod embryos. However, there are few theoretical models for how diversity in the early embryonic process occurred during evolution, in part because of a limited computational infrastructure. We developed a virtual spherical-shaped multicellular platform to reproduce body axis-forming processes. Each virtual cell behaves according to the cell vertex model, with the computational program organized in a hierarchical order from cells and tissues to whole embryos. Using an initial set of two different mechanical states for cell differentiation and global directional signals that are linked to the planar polarity of each cell, the virtual cell assembly exhibited morphogenetic processes similar to those observed in spider embryos. We found that the development of an elongating body axis is achieved through implementation of an interactive cell polarity parameter associated with edge tension at the cell–cell adhesion interface, with no local control of the cell division rate and direction. We also showed that modifying the settings can cause variation in morphogenetic processes. This platform also can embed a gene network that generates waves of gene expression in a virtual dynamic multicellular field. This study provides a computational platform for testing the development and evolution of animal body patterns.

KEYWORDS

**embryogenesis, body plan, arthropod, body axis formation, cell vertex model, mathematical modeling**

# 1 Introduction

Multicellular animals comprise more than 20 phyla, each with a different basic body plan (Brusca and Brusca, 2003; Valentine, 2004; Willmore, 2012). Body plan formation is achieved through cell proliferation and differentiation, cell movement and rearrangement, and cell–cell interaction and communication, which are controlled by the genome and cell mechanics (Forgacs and Newman, 2005). Genome information is inheritable but changeable over generations, with the body-forming process being able to diversify without disrupting the traits of the phylum (Richardson, 1995; Galis et al., 2002; Raff, 2012). How these modifications of the body-forming processes can occur during organism evolution is a fundamental question required for understanding the source of animal diversity.

Early embryonic development in animals in the phylum Arthropoda is characterized by body axis formation and segmentation (Scholtz and Wolff, 2013). Cellular and molecular studies of a wide range of species, including the fruit fly *Drosophila melanogaster* (Irvine and Wieschaus, 1994), the red flour beetle *Tribolium castaneum* (Benton et al., 2013; Benton, 2018), the amphipod crustacean *Parhyale hawaiensis* (Sun and Patel, 2019), and the common house spider *Parasteatoda tepidariorum* (Oda and Akiyama-Oda, 2020), have revealed that the processes and mechanisms of body axis formation and segmentation vary substantially depending on the species despite conserved gene expression patterns during mid-embryogenesis (Liu and Kaufman, 2005; Peel et al., 2005; Sachs et al., 2015; Oda et al., 2020). The variation in early development among arthropods might be linked to the diversity in size, shape, composition, and other properties of the egg, which reproductive strategies associated with environmental adaptation (Scholtz and Wolff, 2013). Hence, species richness in phylum Arthropoda implies high flexibility and evolvability of its developmental systems (Stansbury and Moczek, 2013; Thomas et al., 2020). However, this evolutionary diversity is not easily testable in real organisms; therefore, mathematical modeling of arthropod embryos and simulation of their development contribute to investigating how early developmental processes are diversified. In many cases, tissue morphogenesis dynamics are accompanied by the development of gene expression patterns (Irvine and Wieschaus, 1994; Akiyama-Oda and Oda, 2010). Spatially periodic stripe formation associated with body-axis segmentation in arthropod and vertebrate embryos provides representative examples of these types of patterning processes in dynamic cellular fields. Studies of these examples have highlighted waves of gene expression that behave in various modes to generate periodic stripe patterns (Sarrazin et al., 2012; Hubaud and Pourquié, 2014; Akiyama-Oda and Oda, 2020). Because segmentation in the *Drosophila* blastoderm embryo occurs mostly in a syncytial environment, this popular model system only provides limited information about the relationship between pattern formation and tissue field dynamics. In contrast, similar to many other arthropod embryos, body axis formation and segmentation in the spider embryo occurs in the cellular field (Figure 1A; Kanayama et al., 2010; Hemmi et al., 2018; Akiyama-Oda and Oda, 2020).

An increasing number of mathematical modeling studies have simulated the dynamics of multicellular assemblies (Goriely, 2017), with many using cell vertex models in which each vertex follows motion equations based on cell mechanics (Honda, 1983; Farhadifar et al., 2007; Fletcher et al., 2014). Indeed, two-dimensional cell vertex models have effectively simulated the growth and morphogenesis of *Drosophila* epithelial tissues (Aliee et al., 2012; Kong et al., 2017). These models assume that the cortical actomyosin network and adherens junctions are localized at the apicolateral portions of cell–cell contacts (Fletcher et al., 2014). These adhesions play a major mechanical role in regulating cell size, shape, and behavior (Lecuit and Lenne, 2007; Paluch and Heisenberg, 2009). Actomyosin activity generates cortical tension on individual cells in a tissue, while adhesions resist tension and transform it into tissue-level tension (Heer and Martin, 2017). Cortical tension anisotropy is associated with planar cell polarity in epithelial tissues (Bertet et al., 2004; Keller, 2006). This tension can function as part of the mechanism of cell–cell intercalation to orient the movement of cell populations (Bertet et al., 2004; Blankenship et al., 2006), and differential tensions at the cell–cell interface can lead to local cell sorting (Landsberg et al., 2009).

The use of cell vertex models has been extended to three-dimensional (3D) tissue shaping (Honda et al., 2008; Alt et al., 2017; Okuda et al., 2018), which considers both the volume and 3D shape of individual cells. These developments in cell vertex models may complicate the handling parameters and increase the burden on calculations, which limits the number of cells which can be considered. Spider embryos undergoing segmentation along the emerging body axis are comprised of more than 3,000 cells (Akiyama-Oda and Oda, 2020), each of which has dynamic states of gene expression and dynamic interactions with surrounding cells. The simplicity of the modeling design is, therefore, key to reproducing the function of the animal embryo for morphogenesis and pattern formation.

Here, we propose a cell vertex model with a spherical surface in which a multicellular system deforms spatiotemporally based on cell dynamics. We attempted to model an arthropod-like whole embryo by mimicking the common house spider (*P. tepidariorum*) embryo. The proposed model helps us to understand the diversity of the body axis-forming processes. We also showed an expansion of

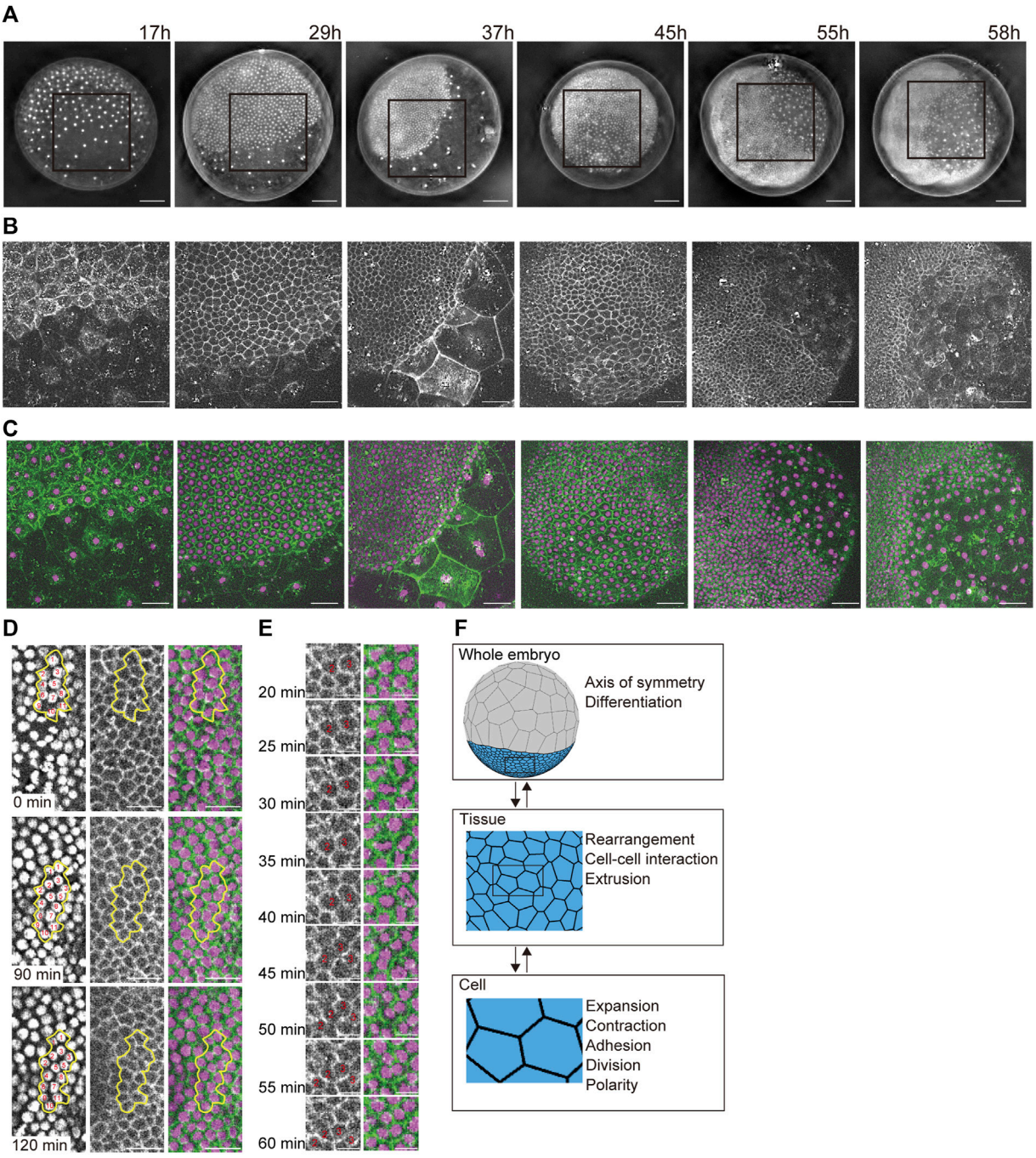


FIGURE 1
Developing multicellular architecture of the *P. tepidariorum* embryo. **(A–C)** Extended depth-of-field images of whole embryos at different developmental stages in which DNA [**(A,C)** in magenta] and F-actin [**(B,C)** in green] are labeled with vital fluorescent dyes. Time after egg laying (AEL) is indicated. For each embryo, the region boxed in **(A)** is magnified in **(B,C)**. **(D,E)** Time-lapse images of mediolaterally oriented cell intercalations and variously oriented cell divisions in the future thoracic region of the ectoderm in a live embryo labeled for DNA and F-actin. In **(D)**, individual cells grouped together outlined with yellow lines are numbered to aid tracking. In **(E)**, cell divisions are highlighted at higher temporal resolution. See Supplementary Movie S2 for details. Scale bars = 100 μm in **(A)**, 50 μm in **(B,C)**, 25 μm in **(D)**, and 10 μm in **(E)**. **(F)** Schematics of three hierarchical layers in our mathematical modeling of a spider embryo-like multicellular assembly and the phenomena/properties assigned to each layer. See Supplementary Movie S1 for details.

the vertex model by introducing gene expression patterning based on molecular networks.

# 2 Materials and methods

## 2.1 Structural framework of the virtual spider-like embryo

We modeled a spider-like embryo as a yolk-containing elastic ball with a surface occupied by a single layer of packed epithelial cells. We assumed that the shape of each epithelial cell was represented by the two-dimensional shape of its apical surface, which was expressed as a polygon. Epithelial tissue was modeled as a collective polygon defined by connections of vertices. The positions of vertices are the main dynamic variables in the cell vertex model (Honda, 1983). To model the embryo, we used object-oriented computer programming (C++) to construct the vertex, cell, and tissue using a hierarchical relationship. The coordinates of each vertex $i$ denote $\overrightarrow{r_i} = (x_i, y_i, z_i)$ with respect to the center of the spherical embryo. Based on the assumption that the tissue contraction force is balanced with the repulsive force derived from the egg contents, we introduced a restoring force with a spring that constrained the vertices to the surface of the sphere:

$$\frac{d\overrightarrow{r_i}}{dt} = \vec{F}_{constraint} = -k_i\left(R_i - R_{0i}\right)\frac{\overrightarrow{r_i}}{\left|\overrightarrow{r_i}\right|}. \quad \text{(Eq. 1)}$$

The constraint force to the spherical surface $\vec{F}_{constraint}$ is exerted on vertex $i$, while the length of sphere $R_i = |\overrightarrow{r_i}|$ approaches the preferred length of $R_{0i}$ ($R_{0i}$ = 270 μm radius for the spider *P. tepidariorum* embryo). The parameter $k_i$ = 30 for all vertices.

## 2.2 Formulating the cell dynamics

The cell vertex model is useful for simulating the mechanical deformation of cells in tissues based on the forces acting on each cell, where the cell configurations are described as polygons whose vertices form cell junctions when subjected to mechanical forces (Farhadifar et al., 2007; Fletcher et al., 2014). Cells change their shape based on force balance. The model is represented by ordinary differential equations of the position vector of each vertex:

$$\frac{d\overrightarrow{r_i}}{dt} = \vec{F}_{area\ elasticity} + \vec{F}_{adhesion} + \vec{F}_{contraction} = -\frac{dE}{d\overrightarrow{r_i}}, \quad \text{(Eq.2)}$$

$$E = \sum_n \frac{1}{2}\alpha_n\left(A_n - A_{0n}\right)^2 + \sum_{i,j}\beta_{ij}(t)L_{ij} + \sum_n \frac{1}{2}\gamma_n\left(P_n - P_{0n}\right)^2. \quad \text{(Eq. 3)}$$

The area elasticity $\vec{F}_{area\ elasticity}$ is exerted on vertex $i$ by the cell face $n$, to which vertex $i$ belongs, while the area of cell $A_n$ approaches the preferred area of $A_0$. The tension at the cell–cell adhesion interface $\vec{F}_{adhesion}$ is exerted on vertex $i$ by the connecting edges between vertices $i$ and $j$, where the cell adhesion increases as the edge length between vertices $i$ and $j$ ($L_{ij}$) increases depending on the cell adhesion parameter $\beta_{ij}(t)$. The magnitude of cell adhesion parameter $\beta_{ij}(t)$ changes over time, owing to implementation of interactive cell polarity directions of cells facing each cell edge, described in a later paragraph (Eq. 7 in Section 2.3). The cell contraction $\vec{F}_{contraction}$ is exerted on vertex $i$ by the perimeter of cell $P_n$, while $\vec{F}_{contraction}$ increases to minimize the difference between the perimeter $P_n$ and the preferred perimeter $P_{0n}$. Taken together, the following defines the differential changes in the position of each vertex, including the constraint force:

$$\frac{d\overrightarrow{r_i}}{dt} = \vec{F}_{constraint} + \vec{F}_{area\ elasticity} + \vec{F}_{adhesion} + \vec{F}_{contraction}. \quad \text{(Eq. 4)}$$

We integrated the cell vertex model numerically using the Euler method and confirmed that the results were not greatly influenced by the choice of the temporal discretization size $dt$.

## 2.3 Cell differentiation and cell polarity

We set two conditions in the virtual embryo, which were intended to mimic the contraction (germ disc formation) and the embryo elongation (germ band formation) phases. The multicell was grouped into two cell types that reflected cell differentiation: embryonic and abembryonic for germ disc formation or embryonic and extraembryonic for germ band formation, where cell mechanical parameters were set to be different depending on each cell type.

For the embryo elongation phase (germ band formation), planar cell polarity in an embryonic cell $n$ denotes a time-development vector $\vec{g}_n(t)$ ($n$ = 1 … N, where N is the number of embryonic cells). We assume that the change in the polarity direction of cell $n$ is calculated by the difference between the polarity vectors of its neighboring cells $m$ ($m$ = 1, … , $M_n$) and its own polarity vector as follows:

$$\Delta\vec{g}_n = \frac{\sum_{m=1}^{M_n}\left(\vec{g}_m - \vec{g}_n\right)}{M_n}. \quad \text{(Eq. 5)}$$

Then, the cell polarity in the next time step direction $\vec{g}_n(t+1)$ is determined by adding the difference of the cell polarity to the current cell polarity $\vec{g}_n(t)$:

$$\vec{g}_n(t+1) = \vec{g}_n(t) + k_{fd}\Delta\vec{g}_n. \quad \text{(Eq. 6)}$$

The magnitude of $k_{fd}$ represents the feedback strength. The direction of cell polarity is in parallel with the plane determined by the cell vertices, the position of which is kept close to the surface of the sphere owing to the spring term in

the motion equation (Eq. 4). In the virtual embryo with a large number of cells (approximately 3,000 or more), the cell and its neighboring cells are aligned in nearly an identical plane close to the spherical surface. This situation makes the collective vector, calculated from the main and surrounding cells in Eq. 5, stay nearly tangential to the spherical surface over time. The cell adhesion parameters of each cell edge underwent time-dependent changes according to the cell polarity direction. We adopted a similar scheme for coupling the cell adhesion and the cell polarity to that described in a previous study (Sato et al., 2015):

$$\beta_{ij}(t) = \frac{\beta_{0ij}}{2}\left(1 + G\cos\left(\theta_{\vec{g}_n} - \theta_{ij}\right)\right) + \frac{\beta_{0ij}}{2}\left(1 + G\cos\left(\theta_{\vec{g}_m} - \theta_{ij}\right)\right). \quad \text{(Eq. 7)}$$

The adhesion parameters of each cell edge $\beta_{ij}(t)$ were the summation of the adhesion parameters of 2 cells $n$ and $m$ facing their cell edge. The adhesion parameters of each cell $n$ or $m$ were determined by the difference between the direction of cell polarity $\theta_{\vec{g}_n}$ or $\theta_{\vec{g}_m}$ and the direction of cell edge facing these cells $\theta_{ij}$ ($-180^\circ < \theta_{\vec{g}_n}, \theta_{\vec{g}_m}, \theta_{ij} \leq 180^\circ$). At the connecting edges between vertices $i$ and $j$, the direction of cell edge from $i$ to $j$ is the opposite direction from $j$ to $i$ ($\cos\theta_{ij} = -\cos\theta_{ji}$). $G$ denotes the strength of the cell polarity, which affects the cell edge adhesion parameter. In germ band formation, initial cell polarities are only set in cells on the rim of the germ disc, and the cell polarities of other cells are set to $\vec{g}_n(t=0) = 0$. The initial directions of cell polarity rely on the orientation of the anterior–posterior and dorsal–ventral axes at the germ disc; $\vec{g}_n(t=0) = \left(\frac{\sqrt{y_n^2+z_n^2}}{R_{0i}}\left(1+\frac{z_n}{4R_{0i}}\right), \frac{x_n}{\sqrt{2}R_{0i}} - \frac{2z_n}{R_{0i}}, \frac{x_n}{\sqrt{2}R_{0i}} + \frac{2y_nz_n}{R_{0i}\sqrt{y_n^2+z_n^2}}\right)$ in cells on the rim of the germ disc, where $x_n$, $y_n$, and $z_n$ are coordinates of the geometric center of cells.

## 2.4 Mechanical parameter setting

For the contraction phase (germ disc formation), we set the cell mechanical parameters in Eq. 3 using an expansion parameter $\alpha_n = 1\ \mu m^{-2}$, an adhesion parameter $\beta_{0ij} = 1\ \mu m$, and a contraction parameter $\gamma_n = 2.5$ in embryonic cells, and to $\alpha_n = 1\ \mu m^{-2}$, $\beta_{0ij} = 1\ \mu m$, and $\gamma_n = 0.5$ in abembryonic cells. The adhesion parameter of the cell edge between the embryonic and abembryonic cells was $\beta_{0ij} = 40\ \mu m$.

For the embryo elongation phase (germ band formation), we set the cell mechanical parameters in Eq. 3 using an expansion parameter $\alpha_n = 1\ \mu m^{-2}$, an adhesion parameter $\beta_{0ij} = 1\ \mu m$, and a contraction parameter $\gamma_n = 0.5$ in embryonic cells, and to $\alpha_n = 0.1\ \mu m^{-2}$, $\beta_{0ij} = 0.1\ \mu m$ and $\gamma_n = 0.15$ in extraembryonic cells. The adhesion parameter of the cell edge between the embryonic and extraembryonic cells was $\beta_{0ij} = 40\ \mu m$. The feedback strength of cell polarity $k_{fd}$ in Eq. 6 was 0.1 in embryonic cells but 0 in extraembryonic cells. The strength of the effect of cell polarity on cell adhesion $G$ in Eq. 7 was 10 in embryonic cells but 0 in extraembryonic cells.

## 2.5 Cell division and cell growth

The cell division plane was automatically determined based on the geometric shape of the cell by dividing along the short axis direction of the approximate ellipse for the cell through the geometric center of the cell. The developmental times during germ disc or germ band formation ranged from $t = 0$ (start) to $t = 1.0$ (end). During germ disc formation, the number of embryonic cells increased from $n = 64$ to $n = 1500$ by cell division (where cell cycles follow a normal distribution with mean $t = 0.2$ and variance 0.05). During germ band formation, cell numbers increased again from $n = 1500$ to $n = 6000$ by cell division (where cell cycles follow a normal distribution with mean $t = 0.5$ and variance 0.1). The variation in the timing of the first cell divisions followed a uniform distribution and a range of a quarter of the time ($t = 0.25$) it took for germ disc or germ band formation.

The initial ideal cell area in Eq. 3 was set to $A_{0n} = 6,400\ \mu m^2$ for all cells in germ disc formation and $A_{0n} = 200\ \mu m^2$ for all cells in germ band formation. Embryonic cells have no cell area growth, but $A_{0n}$ splits by one half in each cell division step. The abembryonic cells set in a part of embryonic cells ($n = 100$ at $t = 0.5$) and grow by $\frac{dA_{0n}}{dt} = 0.001 \times 200$ during germ disc formation, and the extraembryonic cells grow by $\frac{dA_{0n}}{dt} = 0.009 \times 200$ during germ band formation without cell division. The ideal cell perimeter in Eq. 3 was set to $P_{0n} = 0\ \mu m$ for all cells during both germ disc formation and germ band formation.

## 2.6 Cell rearrangement and cell extrusion

Cell rearrangement was implemented through cell neighbor exchange (also called a T1 transition). The T1 transition occurs when the distance between two connected vertices becomes less than a minimum threshold distance (<3 μm), much smaller than a typical edge length (~10 μm). The connections of vertices are switched as illustrated in Figure 2B(5).

Cell extrusion was implemented by removing the shrunk cell (also called a T2 transition). The T2 transition occurs when the cell area became less than a minimum threshold area (<50 $\mu m^2$) at a triangular cell. The cell was removed, and the geometric center of the removed cell was added to vertices of neighboring cells as a new vertex; cell edges were then connected between the new vertex and its nearest vertices of neighboring cells, as illustrated in Figure 2B(6).

## 2.7 Embedding a reaction and diffusion system

We embedded a reaction and diffusion system in the cell vertex model. Each cell includes concentrations of three types of

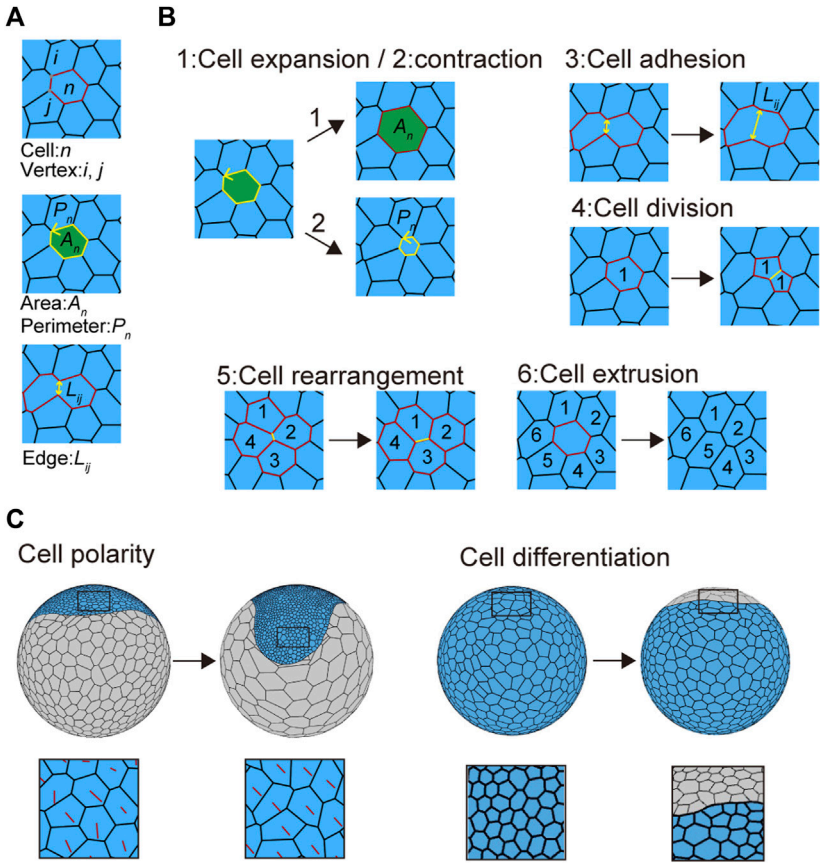


FIGURE 2
Mechanical cell properties in embryos. **(A)** Virtual cells in the vertex model. The letters *n*, (*i*, *j*), $A_n$, $P_n$, and $L_{ij}$ in the panels represent the cell number, vertex number, cell area, cell perimeter, and cell edge length, respectively. **(B)** Cell behaviors introduced into the cell vertex model. Three cell mechanics are modeled: 1) cell expansion, 2) cell contraction, and 3) cell adhesion. 1) Cell expansion and 2) cell contraction mainly contribute to increasing or decreasing cell area ($A_n$) and perimeter ($P_n$), whereas 3) cell adhesion mainly contributes to increasing or decreasing cell edge length ($L_{ij}$; see in Eq. 3 in Methods). Three types of context-dependent cellular events are modeled: 4) cell division, 5) cell rearrangement, and 6) cell extrusion. Numbers in the panels indicate cell positional relationships. Black arrows indicate time advanced. See Supplementary Movie S3 for details. **(C)** Cell polarity (left) and cell differentiation (right) associated with cell shaping. Red lines indicate cell polarity direction (left bottom), while blue and gray cells indicate embryonic and abembryonic cell populations, respectively (right).

molecules ($X_n \geq 0$, $Y_n \geq 0$, and $Z_n \geq 0$). These molecules react according to the molecular network in each cell (Eq. 9 and Figure 7C) and diffuse between neighboring cells. The reaction–diffusion equations are written as follows:

$$\begin{aligned}\frac{dX_n}{dt} &= R_x(X_n, Y_n, Z_n) + D_x\frac{\partial X^2}{\partial^2 r},\\ \frac{dY_n}{dt} &= R_Y(X_n, Y_n, Z_n) + D_Y\frac{\partial Y^2}{\partial^2 r},\\ \frac{dZ_n}{dt} &= R_Z(X_n, Y_n, Z_n) + D_Z\frac{\partial Z^2}{\partial^2 r}.\end{aligned} \quad \text{(Eq. 8)}$$

In the simulation, we set the reaction equation of the molecular network as an example of wave traveling and subsequent wave splitting by:

$$\begin{aligned}R_X(X_n, Y_n, Z_n) &= A_X X_0 - B_X Y_n,\\ R_Y(X_n, Y_n, Z_n) &= A_Y Y_n - (Y_n - Y_0)^3 - B_Y X_n + C_y Z_n,\\ R_Z(X_n, Y_n, Z_n) &= A_Z X_n - B_Z Y_n - C_Z Z_n.\end{aligned} \quad \text{(Eq. 9)}$$

The parameters were $A_X = 1.2$, $B_X = 1.0$, $A_Y = 0.2$, $B_Y = 1.0$, $C_Y = 1.2$, $A_Z = 1.0$, $B_Z = 1.0$, $C_Z = 0.5$, and $Y_0 = 1.0$.

During germ band formation, the initial pattern of these molecules was $X_0 = 1.0$ on the rim of the embryo. Under these parameter settings, the gene expression waves exhibited oscillations and wave-splitting patterns (Figure 7B). The distance related to diffusion $\partial^2 r$ in Eq. 8 was calculated by the square differential distance $\partial r$ between the geometric center of cell $n$ and the geometric centers of its neighboring cells. The diffusion coefficients were $D_X = 20$, $D_Y = 5$, and $D_Z = 0$; thus, $X_n$ and $Y_n$ are diffused, but $Z_n$ is not diffused.

## 2.8 Code for the spherical-surfaced vertex model

The spherical-surfaced vertex model code was written in C++. The code is available at GitHub with the following URL: https://github.com/Motohiro-Fujiwara/spherical_vertex model_spider.git.

Operation checks were made using operating systems for Mac and Linux.

## 2.9 Spiders and culture conditions

Animal experiments were reviewed and approved by the Institutional Animal Care and Use Committee of the JT Biohistory Research Hall (No. 2020–1). Laboratory stocks of the spider *Parasteatoda tepidariorum* (syn. *Achaearanea tepidariorum*) were maintained at 25°C in a 16 h light/8 h dark cycle. The developmental stages have been described previously (Akiyama-Oda and Oda, 2003).

## 2.10 Live imaging and image processing

The developmental stages of the spider embryos were assessed at the start of stage 2 (10 h after egg laying: AEL), stage 5 (30 h AEL), and stage 6 (40 h AEL). Live embryos were dechorionated with 100% commercial bleach, transferred onto heptane-extracted glue in the intended region of a specially designed glass slide, and covered with halocarbon oil 700 (Sigma-Aldrich H8898). Glass capillaries (Drummond 2-000-075) were pulled using a puller (PN-3; Narishige) to make injection needles. Vital fluorescent dyes SPY505-DNA and SPY555-actin (Spiro Chrome), each of which dissolved in DMSO, were mixed at a 1:1 ratio and microinjected into the perivitelline space of the embryos using a needle. The embryos were examined using a Zeiss Axio Zoom.V16 equipped with a digital camera Zeiss Axiocam 506, 2 or 3 hours after injection. Optical sections were made at 4-μm thickness for DNA images (Figure 1A), and 2-μm optical sections from the same embryos were collected for actin and DNA images using an ApoTome3 sectioning unit (Figures 1B and C). Time-lapse images of 2-μm optical sections for DNA and actin were taken at 5 min intervals for 2 h (from 53 to 55 h AEL) using the ApoTome3 sectioning unit (Figures 1D and E). The observed embryos were further examined if embryogenesis had proceeded.

The acquired Z-series images at each time point were processed with ImageJ (FIJI) extended depth of field plugin to generate in-focus single images. Images taken without ApoTome3 were processed using a real wavelet transform with the parameter settings spline order 3 and number of scales 11, while images taken with ApoTome3 used a complex wavelet transform with the parameter settings filter length 6 and number of scales 3. The resultant images were adjusted for brightness and contrast using ImageJ, and the DNA and actin images were merged (Figures 1C–E).

Images of 5-μm optical sections were taken using the same microscope with bright light at 5 min intervals for 3 days. The images at each time point were processed with the ImageJ plugin for the following method and settings: real wavelet, spline order 3, and number of scales 7. The resulting images are compiled to generate Supplementary Movie S1.

# 3 Results and discussion

## 3.1 Observation of the multicellular architecture of the developing spider embryo

We observed the multicellular architecture development of the spider *P. tepidariorum* embryo from early to mid-stages using vital fluorescent dye-labeled DNA and F-actin (Figures 1A–C and Supplementary Movie S1). The spherically symmetric blastoderm forms around 10 h AEL, with approximately 64 cells evenly distributed on the surface of the egg. Two cell populations appeared approximately 15 h AEL, manifesting an axis of radial symmetry in the embryo. One cell population showed stronger concentrations of cortical F-actin and an increasingly denser distribution of cells, whereas the other showed little cortical F-actin and an increasingly sparse distribution of cells. Most of the former cell population participated in the formation of a germ disc, which was a single layer of more than 1,000 epithelial cells that mostly contributed to the ectoderm. Further separation of the germ disc epithelial cell population occurs in the following stages. A small cluster of cells called cumulus mesenchymal (CM) cells was internalized at the center of the germ disc, followed by symmetry-breaking migration along the basal side of the germ-disc epithelium that reached the rim of the germ disc (Akiyama-Oda and Oda, 2010). In a peripheral region of the germ disc where the CM cells arrived, they induced the differentiation of extraembryonic cells (Akiyama-Oda and Oda, 2006), which had progressively larger apical surface areas and less prominent cortical F-actin. Simultaneously, the remaining ectoderm underwent remodeling to form a segmented germ band (Hemmi et al., 2018). During this remodeling process, mediolaterally oriented cell intercalations and variously oriented cell divisions were observed (Figures 1D and E and Supplementary Movie S2), which was consistent with previous reports (Hemmi et al., 2018). These cell dynamics promote tissue deformation to shape the whole embryo.

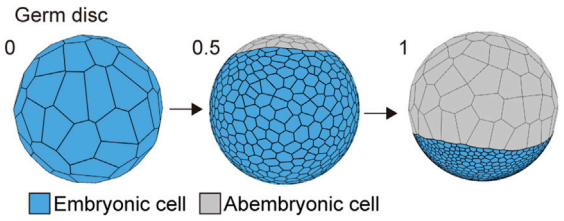


FIGURE 3
Spherical to germ disc embryo shaping in *P. tepidariorum*. The embryo size was 570 μm diameter, and the cell number ranged from 64 ($t$ = 0) to 1,500 ($t$ = 1) epithelial cells. When the cell number reached approximately 1,000 cells by cell division ($t$ = 0.5), the cells differentiated into two typed-cell populations that were embryonic (blue) and abembryonic (gray) cells.

## 3.2 Constructing a cell vertex model of the spherical epithelial multicell that corresponds to the hierarchical structure of the embryo

The characteristic shape of a developing spider embryo was composed of outer epithelial tissues, which were deformed by epithelial cell dynamics on the spherical surface during embryogenesis (Figure 1A; Akiyama-Oda and Oda, 2010). To reproduce this embryonic shaping process, we constructed a spherical-surfaced vertex model as a virtual multicellular platform (Figure 1F; Honda, 1983; Farhadifar et al., 2007; Fletcher et al., 2014). One advantage of the spherical-surfaced vertex model that distinguishes it from an ordinary 2D sheet vertex model is that it adopts a closed structure system and does not require cell-free boundaries of tissues (Figure 1F). In the constructed vertex model, each polygon represents the apical area of an individual epithelial cell on the embryo surface, and the collective polygons represent the multicellular architecture of the outer epithelial tissue (Figure 1F). We assumed that a whole embryo consisted of one or more tissue types, and that each tissue type consisted of homogeneous cells with certain cell properties. This hierarchical framework of an actual embryo (Figure 1F) was retained in our modeling scheme using object-oriented programming in C++. We also assumed a spherical radius constraint on each vertex to maintain an elastic spherical shape (Eq. 1), which represented the epithelial cell populations attached to inner spherical structures such as the yolk. The connections of polygon edges at each vertex were flexible, and the vertices could increase or decrease in number. These geometric properties allowed the vertex model to express cellular dynamics, such as cell division and cell–cell interactions (Figure 1F and Supplementary Movie S1), as seen in actual embryonic development (Figures 1D and E).

To determine the mechanical properties of individual cell units, we assumed the presence of three sources of potential energy: 1) area elasticity, 2) perimeter contraction, and 3) line adhesion (Figures 2A and B and Supplementary Movie S3). These were expressed in the motion equations for each vertex (Eq. 3; Farhadifar et al., 2007; Fletcher et al., 2014). In addition to these mechanical properties, three types of context-dependent cellular events were included in the model: 4) cell division, 5) cell rearrangement, and 6) cell extrusion, by setting cell cycle periods and transition thresholds (Figure 2B, Supplementary Movie S3 and Methods Section 2.5 and Section 2.6; Farhadifar et al., 2007; Fletcher et al., 2014). Cell shapes were determined by regulating these six cell properties. Changing some of these parameters led to various phenotypic consequences. For example, when it was difficult for cell rearrangements to occur, the embryonic cells showed aberrant shapes (Supplementary Figure S1A).

To reflect global polarity that forms in the cell population along the future anterior–posterior (A-P) and dorsal–ventral (D-V) axes at earlier stages of embryonic development (Akiyama-Oda and Oda, 2006; Akiyama-Oda and Oda, 2020), we assumed that embryonic cells develop a planar cell polarity (Figure 2C). This polarity parameter, which was included in the adhesion term of the vertex motion equation, was initially set along the primary body axes (A-P and D-V axes) but changed over time in a self-determining mode depending on the neighboring cells (Figure 2C; Eq. 6). The cell polarity orientation determined the anisotropic adhesion at the cell edges (Eq. 7). We also introduced cell differentiation by defining two cell types with distinct mechanical properties, cell size characteristics, and cell division frequencies (Figure 2C). However, the cell division plane was automatically determined based on the geometric shape of the cell to divide the cell along the short axis through its geometric center. Given the two cell-type populations with differing cell mechanical properties, the spherical vertex model could represent various embryo shapes, including disc (germ disc) and band (germ band) shapes.

## 3.3 Germ disc formation is achieved by defining two cell populations with distinct mechanical properties

The first morphogenetic process following the formation of a spherically symmetric blastoderm in the *P. tepidariorum* embryo was the formation of a germ disc (Akiyama-Oda and Oda, 2003; Pechmann, 2016). To mimic this morphogenetic process, we used the cell differentiation for two types of cell populations with distinct mechanical properties when the cell number increased from 64 to 1,000 in the spherical embryo (Figure 3). These two cell populations corresponded to abembryonic and embryonic cells that could form a germ disc. The embryo size (570 μm diameter), cell number, and mechanical parameters for each cell population (differentiation to 900 embryonic cells and 100 abembryonic cells; Methods)

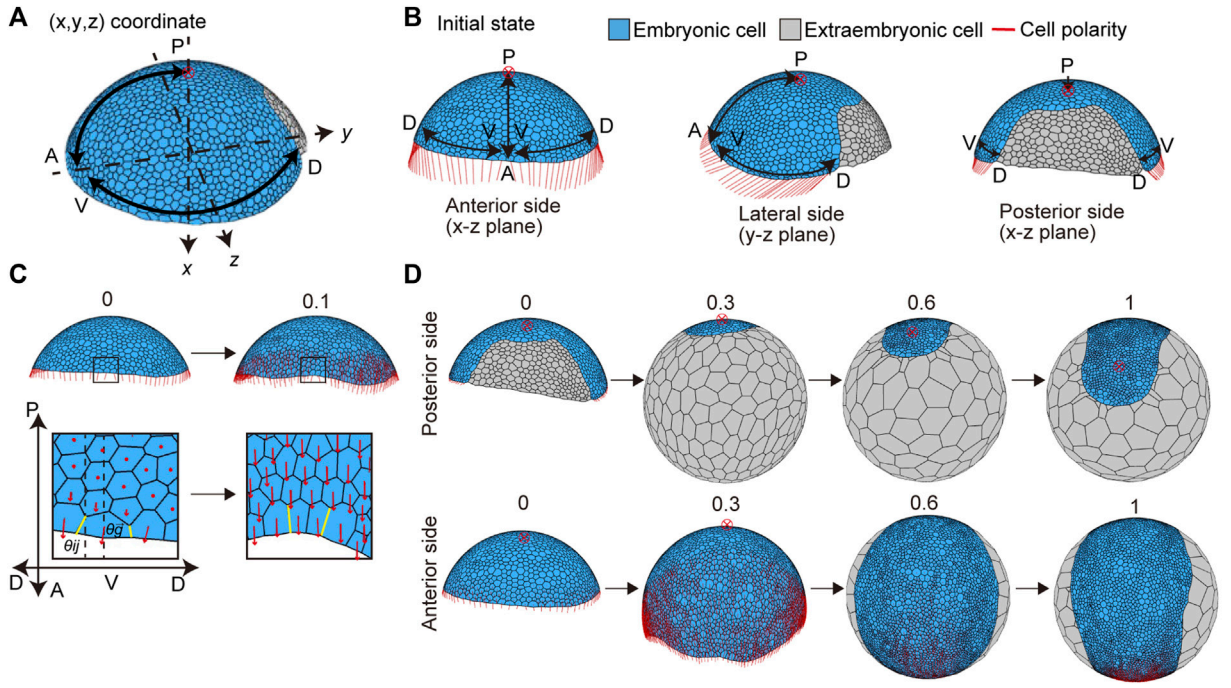


FIGURE 4
Initial settings for cell polarity and cell differentiation, and the deformation from the germ disc to germ band *in silico*. **(A)** Direction of two body axes (anterior–posterior (A-P) and dorsal–ventral (D-V) axes) defined in the germ disc. The A-P axis is on the x-y plane, and the D-V axis is on the y-z plane in the Cartesian coordinate system (x, y, z). The red cross with a circle indicates the position of a posterior pole in **(A,B,D)**. Embryonic and extraembryonic cells are depicted in blue and gray, respectively in **(A,B,D)**. **(B)** Initial setting for cell polarity, viewed from three different sides of the embryo: the anterior side (left), lateral side (center), and dorsal side (right). Initial cell polarities were only set in embryonic cells located at the rim of the embryo (red line). **(C)** Initial cell polarity defined by the initial direction of the A-P and D-V axes ($t$ = 0, left), and changes in the cell polarity over development are shown ($t$ = 0.1, right). The boxes in the embryo are magnified in the lower panels. The strengths of cell adhesion tension change depending on different angles between cell edge orientation (yellow line, $\theta_{ij}$) and the cell polarity direction ($\theta_{\vec{g}_n}$; see in Methods). **(D)** Model simulation over time. Initial cell polarities were set as shown in **(B)**. Numbers on each panel represent the developmental time. The virtual disc-like cell assembly (blue) was deformed into a band-like shape, similar to that observed in *P. tepidariorum* embryos.

were adjusted to achieve a similar morphogenetic process that formed a germ disc (Figure 3; Kanayama et al., 2010). Consistent with the F-actin observation (Figures 1B and C), the embryonic cell population was given a greater adhesion tension and cell contraction strength, while the abembryonic cell population was given a smaller adhesion tension strength. The abembryonic cell population shifted to a non-proliferative state upon differentiation. The adhesion tensions on the cell edges between embryonic and abembryonic cell populations were higher than the adhesion tensions between homogeneous cell populations, which was a requirement for developing a smooth boundary between the two cell populations (Supplementary Figure S1B). These cell mechanics successfully mimicked germ disc formation independent of cell polarity and the emerging axis of radial symmetry. Given that these two cell populations exhibited distinct mechanical properties with appropriate adhesion tension and contraction, a disc-shaped tissue could develop in the spherical-surfaced vertex model.

## 3.4 Germ band formation is achieved by setting two distinct cell types and global polarity

The *P. tepidariorum* germ disc stage embryo undergoes a dynamic transition process to form a germ band immediately after the signal-sending CM cells arrive at the rim of the germ disc (Akiyama-Oda and Oda, 2006; Hemmi et al., 2018). To mimic this process, the mathematical model assumed two initial conditions for the germ disc cell population (Figure 4A). The first condition was the differentiation of an extraembryonic cell population on the future dorsal side of the germ disc, where the signal-sending CM cells had arrived (Figure 4A). These newly differentiated extraembryonic cells were set to have no proliferative activity and distinct mechanical properties and cell-size characteristics from those of the remaining germ disc cells (Methods). The second condition applied planar cell polarity to reflect the mutually orthogonal A-P and D-V axes of the embryo

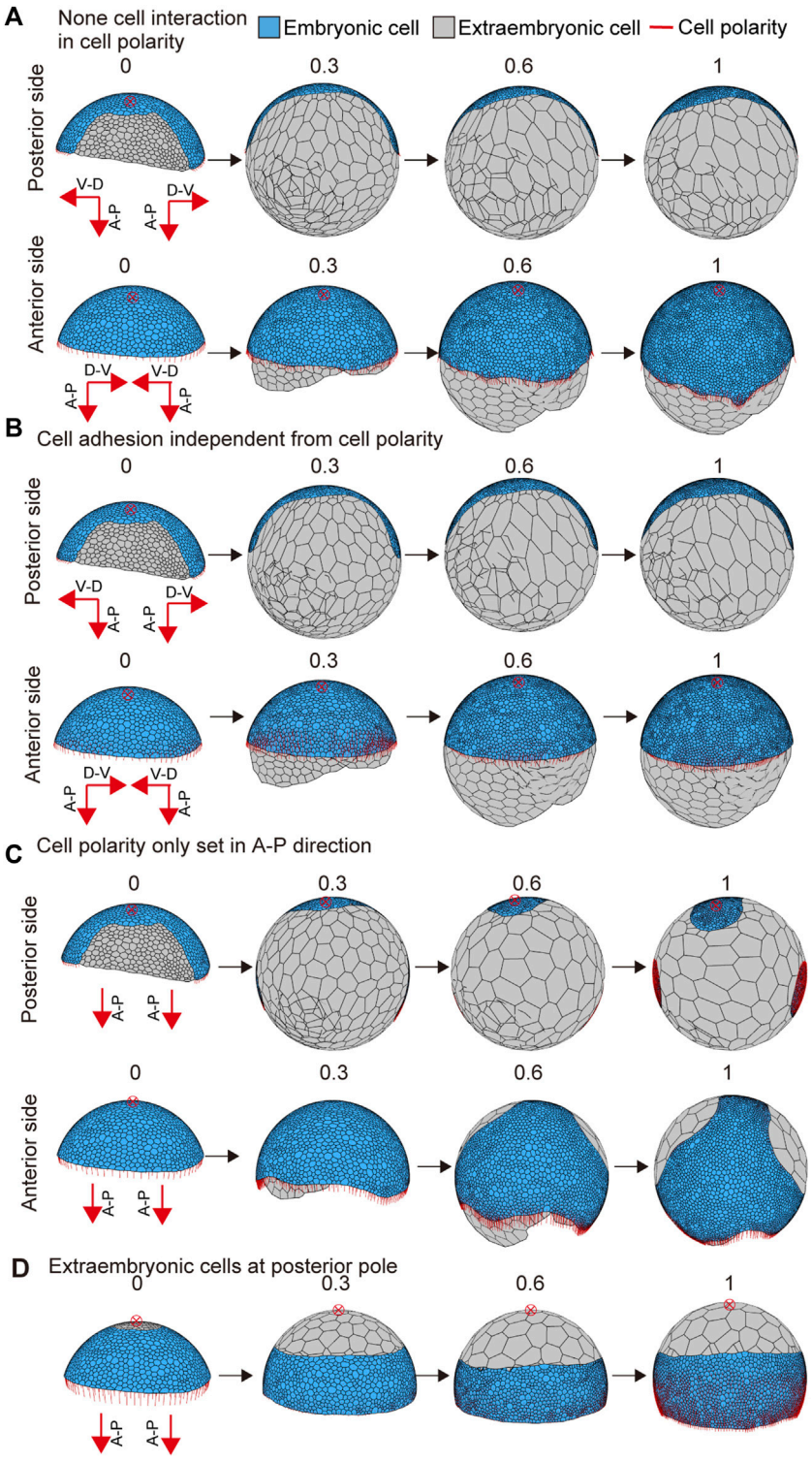


FIGURE 5
Embryo shape change as affected by parameter values or initial conditions. **(A)** Blocking the interaction between neighboring cells in cell polarity ($k_{fd}$ = 0 in Eq. 6). The initial conditions for cell polarity are the same as shown in Figure 4B. **(B)** Interrupting the dependency between cell polarity and cell adhesion ($G$ = 0 in Eq. 7). The initial conditions for cell polarity are the same as shown in Figure 4B. **(C)** Changing the initial conditions for cell polarity shown in Figure 4B. The development time of embryo shaping when cell polarity was only set in the A-P axis direction. **(D)** Changing the initial conditions for cell differentiation shown in Figure 4B. The development time of embryo shaping when the extraembryonic cells were positioned around the posterior pole of the embryo (red cross with a circle). The red cross with a circle indicates the posterior pole position. Numbers on each panel represent the developmental time (initial state $t$ = 0 to after the deformation $t$ = 1.0). See Supplementary Movie S4 for details.

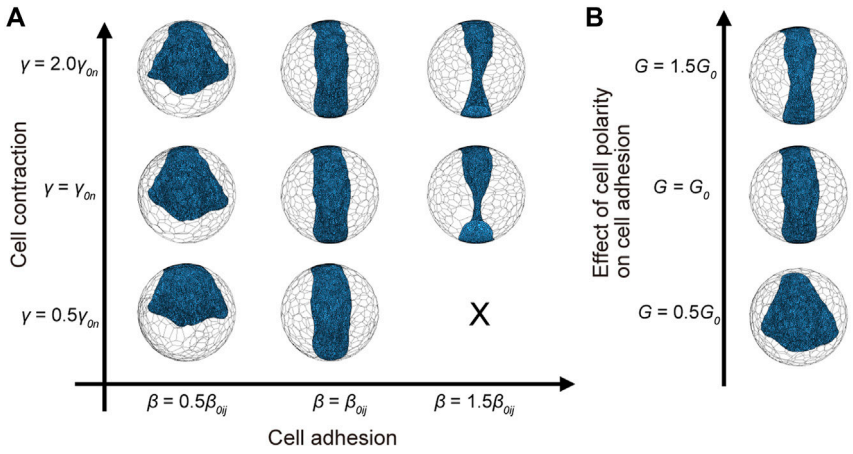


FIGURE 6
Embryo shape as affected by altering cell mechanical parameters. **(A)** Changing mechanical parameters for cell adhesion $\beta_{0ij}$ in Eq. 7 (horizontal axis) and cell contraction $\gamma_n$ in Eq. 3 (vertical axis). Reference parameters in germ band formation as $\beta_{0ij}$= 1 μm and $\gamma_{0n}$= 0.5 in embryonic cells. In $\beta$= 1.5$\beta_{0ij}$ and $\gamma$= 0.5$\gamma_{0n}$, the numerical calculation was halted before completion (x symbol). In cell adhesion $\beta$= $\beta_{0ij}$, the widths of germ band at the midpoint were 226 μm at $\gamma$ = 0.5$\gamma_{0n}$, 206 μm at $\gamma$ = $\gamma_{0n}$, and 180 μm at $\gamma$ = 2.0$\gamma_{0n}$. **(B)** Changing the strength of the effect of cell polarity on cell adhesion $G$ in Eq. 7. Reference parameters in germ band formation as $G_0$= 10 in embryonic cells. The blue cells represent embryonic cells, and the colorless cells represent extraembryonic cells in **(A,B)**.

(Figures 4A and B). Oriented cell polarity was initially set only in the germ disc rim cells (Figure 4B). The directions of cell polarity were interactive among the neighboring cells over time (Eq. 7), which allowed for the effects to spread across the tissue and promote collective cell movement and oriented cell intercalation (Figure 4C). The time evolution of the modeled germ disc started under these two initial conditions (Figures 4B,C) and then mimicked the coordinated dynamics of extraembryonic tissue expansion and germ band formation (Figure 4D and Supplementary Movie S4; center top). The virtual germ band elongated along the emerging A-P axis with frequent mediolaterally oriented intercalations of cells (Figure 4D and Supplementary Movie S1), which was observed in the *P. tepidariorum* embryos (Figure 1D). In this model, cell division frequencies were virtually uniform among the germ band cells, suggesting that locally enhanced cell proliferation is not essential for mimicking germ band formation in spider embryos.

To examine the effects of interactive cell polarity and polarity-dependent cell adhesion on embryo shaping, we altered the parameter values to block the respective functions. When the feedback parameter $k_{fd}$ in Eq. 6 was set to zero to block the interaction between neighboring cells for cell polarity regulation, the embryo was slightly elongated, but no band-like form developed (Figure 5A and Supplementary Movie S4; left bottom). When the polarity dependence parameter for adhesion $G$ in Eq. 7 was set to zero, the germ disc did not show any elongation behavior (Figure 5B and Supplementary Movie S4; center bottom). Next, to test the applicability of different initial conditions, we changed the initial cell polarity setting. The polarity of circumferential cells along the rim of the germ disc was set to orient parallel to the A-P axis of the embryo but ignored the global polarity of the D-V axis, with the extraembryonic cell population in the same region (Figure 5C). Under this condition, the simulation of the modeled germ disc resulted in embryo elongation in a direction other than the A-P axis (Figure 5C and Supplementary Movie S4; right top). In another condition, the extraembryonic cell population was initially placed around the center of the germ disc, with the polarity oriented parallel to the A-P axis of the embryo (Figure 5D). The resulting virtual embryo was barrel-shaped (Figure 5D and Supplementary Movie S4; right bottom), mimicking the development of *Pt-patched* knockdown embryos that have signal-sending CM cells that fail to move from the center of the germ disc but still induce differentiation of the extraembryonic cell population (Akiyama-Oda and Oda, 2010). These mathematical simulations using the spherical-surfaced vertex model suggested that spider-like embryonic development can be reproduced with relatively simple model settings. It was also suggested that modifying settings of cell polarity and cell differentiation can cause variation in morphogenetic processes.

Next, we examined the impact of the cell adhesion parameter $\beta_{0ij}$ (in Eq. 7) and the cell contraction parameter $\gamma_n$ (in Eq. 3) on the simulation of germ band formation. The parameter $\beta$ was shifted to 0.5 $\beta_{0ij}$ and to 1.5 $\beta_{0ij}$, whereas the parameter $\gamma$ was shifted to 0.5 $\gamma_{0n}$ and to 2.0 $\gamma_{0n}$ (Figure 6A).

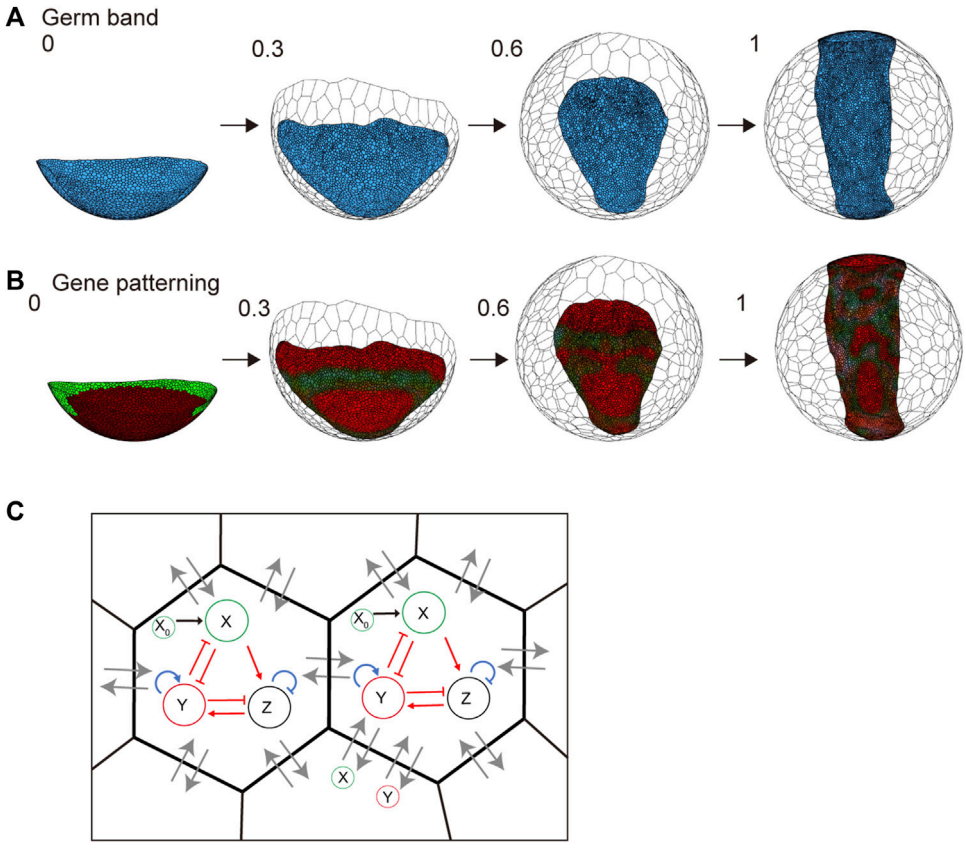


FIGURE 7
Embryo shaping and gene patterning during germ disc development. **(A)** Body axis formation of the germ band in *P. tepidariorum*. The embryo size is 570 μm diameter, composed of 1,500 ($t$ = 0) to 6,000 ($t$ = 1.0) epithelial cells. The settings for each cell parameter are described in the Methods section. The blue colored cells represent embryonic cells, and the colorless cells represent extraembryonic cells. **(B)** Gene expression patterning during embryo shaping. The collars indicate the molecules $X$ (green) and $Y$ (red) defined in **(C)** and Methods section. Numbers on each panel represent the developmental time (initial state $t$ = 0 to after the deformation $t$ = 1.0). See Supplementary Movie S5 for details. **(C)** Gene expression network in a cell and diffusion between neighboring cells. Red arrows indicate the regulations between two molecules, while blue arrows indicate self-regulation. Black arrows indicate the input from the initial pattern of $X = X_O$ (**(B)** left). Lines with arrowheads indicate promotion; those with end bars indicate inhibition. Gray arrows indicate molecular diffusion ($X$ and $Y$) between neighboring cells.

When the parameter $\beta$ was 0.5 $\beta_{0ij}$, the elongation of the forming germ band did not fully occur regardless of the value of the parameter $\gamma$ (Figure 6A). Conversely, when the parameter $\beta$ was 1.5 $\beta_{0ij}$, the formation and elongation of the germ band progressed, but too rapidly, resulting in a germ band being abnormally narrow at the midpoint (Figure 6A). Additionally, we also altered the strength of the effect of cell polarity on cell adhesion $G$ (in Eq. 7). When the parameter $G$ was 0.5 $G_0$, the elongation of the forming germ band did not fully occur (Figure 6B). Conversely, when the parameter $G$ was 1.5 $G_0$, the formation and elongation of the germ band progressed, resulting in a germ band being long and narrow (Figure 6B). Taken together, changing the parameters of cell adhesion and cell contraction deformed the germ band outlines, and the strength of cell adhesion was responsible for embryo elongation.

## 3.5 Embedding a genetic network in the spherical-surfaced vertex model

In spider embryogenesis, gene expression patterning occurs simultaneously with embryonic shaping (Hemmi et al., 2018). One of the most important goals worth pursuing when using the spherical-surfaced vertex model is to reconstruct the various patterning processes that are controlled by different genetic networks in the field of virtual cells undergoing active rearrangement. Hence, we embedded a simple genetic network with three variables that corresponded to gene activities in the individual cells that form the germ band (Figures 7A–C and Methods). We assumed that the protein products of genes were diffusible with different diffusion coefficients like those in ordinary reaction and diffusion systems that generate stripes, spots, or other patterns (Kondo and Miura, 2010). The embedded

genetic network was intended to mimic the wave traveling and splitting of the expression of the spider *hedgehog* (*hh*) homolog (*Pt-hh*), which originates at the rim of the germ disc (Kanayama et al., 2011; Hemmi et al., 2018). The initial gene expression values were set on the embryo edges, as observed in previous studies (Hemmi et al., 2018). Simulations showed that the gene expression wave was followed by splitting when the virtual cellular field underwent germ band formation (Figure 7B and Supplementary Movie S5). However, the integrity of the linear configuration of the transverse gene expression waves was not stably maintained. Cell rearrangements within the plane of the germ band-forming field appeared to cause fluctuations in wave behavior. These cellular dynamics in the patterning field are not usually considered when simulating pattern formation using ordinary reaction and diffusion systems.

In the late *P. tepidariorum* germ disc, differential concentric gene expressions are established along the central–peripheral direction that reflects the future A-P axis under the control of Hedgehog (Hh) signaling. However, the genetic network embedded in the current vertex model does not use this spatial information. This condition may limit the model's ability to computationally reproduce the pattern-forming behaviors of gene expression waves during germ band formation. In *Drosophila* embryos, regulatory coordination between positional information in a tissue and cell behavior that drives convergent extension has been suggested (Paré et al., 2014). Such a regulatory connection between the emerging rough positional information and cell mechanical parameters should be incorporated to improve our vertex model. Quantitative data on cell position, cell behavior, and gene expression can now be obtained from spider embryos using live imaging, multicolor fluorescent *in situ* hybridization, and single-cell/nuclear transcriptomes (Hemmi et al., 2018; Akiyama-Oda et al., 2022). Analyses of such quantitative data may help us understand the mechanical regulations and genetic networks underlying the pattern-forming processes in the spider embryo.

### 3.6 Future directions for *in silico* evolutionally testing of the body axis formation process in arthropod-like embryos

We have shown that computational simulations using a two-dimensional vertex model modified to operate on a spherical surface can reproduce dynamic cell behaviors that drive the formation of a germ disc and the transition of the germ disc to a germ band similar to those observed in *P. tepidariorum* embryos (Figures 1, 3, 4). In our current model, however, symmetry-breaking steps prior to the two morphogenetic processes are ignored, with the spatial asymmetries given as initial conditions instead. In early spider embryos, there may be localized maternal factors and/or self-determination systems mediated by cell–cell interactions. Regulation of symmetry-breaking CM cell migration is key to achieving continuity during germ disc to germ band development. Although signal-sending CM cells are an internal cell cluster that originates at the polar site, our spherical-surfaced vertex model can be modified to have a signal source that moves below the surface cell layer in response to emerging cues. Previous studies have suggested that these cues are regulated by a genetic network involving Hh signaling in the *P. tepidariorum* embryo (Akiyama-Oda and Oda, 2010). In addition, competence to respond to a signal is an essential property of embryonic cells, and it may be spatially regulated as part of the patterning mechanism. Future models should consider this response as well as a dynamic source of signal.

Hh signaling activity in *P. tepidariorum* embryonic development not only mediates the formation of global polarity but also contributes to the subsequent steps of body axis segmentation (Akiyama-Oda and Oda, 2010; Hemmi et al., 2018; Akiyama-Oda and Oda, 2020). The later activities of Hh signaling, at least in part, may be comparable to those of segment polarity genes in *Drosophila* segmentation. The formation of a spatially periodic striped pattern of *hh* expression is a highly conserved feature in embryonic development in arthropods. Downstream effectors of Hh signaling are involved in regulating the sorting behavior of cells (Larsen et al., 2003), which indicates its potential link to the regulation of cell mechanical properties. This aspect could be incorporated into the cell vertex model. Constructing mathematical models that can reproduce a continuous process by which a spherically symmetric multicellular assembly develops into an arthropod-like segmented body pattern is a long-term goal in future studies.

The germ disc stage, such as in *P. tepidariorum*, is missing in other spider embryos. There are variations in the early embryonic developmental process in many animals, even among spider species (Oda et al., 2020). The virtual multicellular platform proposed in this work is rudimentary but adjustable to different conditions and can be improved. For example, egg shape can be easily modified to test the robustness of a pattern-forming system (Supplementary Figure S1C). Another long-term goal for future studies will be to mathematically test the evolution of arthropod-like embryos.

## 4 Conclusion

We propose a cell vertex model that operates on a spherical surface, where the virtual multicellular system could represent spider-like embryonic development based on the regulation of cell mechanics. The vertex model was implemented with an interactive cell polarity parameter associated with adhesion tension. This implementation

allowed for mimicking of the formation of a germ band in spider embryos. This vertex model serves as a virtual multicellular platform to test various spider-like embryonic morphogenetic processes by modifying the parameters and conditions for cell polarity, cell differentiation, and cell mechanical properties. In addition, this multicellular platform has the potential to embed a gene regulatory network that generates waves of gene expression. Further development of the vertex model could contribute to improved reconstruction of arthropod body pattern development and evolution.

## Data availability statement

The raw data supporting the conclusion of this article will be made available by the authors, without undue reservation.

## Author contributions

Conceptualization: MF, YA, and HO. Methodology: MF and YA. Investigation: MF and YA. Formal analysis: MF and YA. Software: MF. Writing—original draft preparation: MF and HO. Writing—review and editing: MF, YA, and HO. Supervision: HO. All authors discussed and approved the results.

## Funding

This work was supported by the JT Biohistory Research Hall and JST (PRESTO Grant Number: JPMJPR2041 to YA).

## Acknowledgments

The authors thank Koichi Fujimoto, Katsuyoshi Matsushita, and other members of Fujimoto's laboratory (Osaka University, Japan) for discussions and technical advice on the cell vertex model. The authors also thank Akiko Noda for technical assistance and Takanori Akaiwa, Kazuhiro Nagata and other members of the JT Biohistory Research Hall (Takatsuki, Japan) for discussions.

## Conflict of interest

The authors declare that the research was conducted in the absence of any commercial or financial relationships that could be construed as a potential conflict of interest.

## Publisher's note

All claims expressed in this article are solely those of the authors and do not necessarily represent those of their affiliated organizations, or those of the publisher, the editors, and the reviewers. Any product that may be evaluated in this article, or claim that may be made by its manufacturer, is not guaranteed or endorsed by the publisher.

## Supplementary material

The Supplementary Material for this article can be found online at: https://www.frontiersin.org/articles/10.3389/fcell.2022.932814/full#supplementary-material

## References

Akiyama-Oda, Y., Akaiwa, T., and Oda, H. (2022). Reconstruction of the global polarity of an early spider embryo by single-cell and single-nucleus transcriptome analysis. *Front. Cell Dev. Biol.* 10, 933220 doi:10.3389/fcell.2022.933220

Akiyama-Oda, Y., and Oda, H. (2006). Axis specification in the spider embryo: dpp is required for radial-to-axial symmetry transformation and sog for ventral patterning. *Development* 133, 2347–2357. doi:10.1242/dev.02400

Akiyama-Oda, Y., and Oda, H. (2010). Cell migration that orients the dorsoventral axis is coordinated with anteroposterior patterning mediated by Hedgehog signaling in the early spider embryo. *Development* 137, 1263–1273. doi:10.1242/dev.045625

Akiyama-Oda, Y., and Oda, H. (2003). Early patterning of the spider embryo: a cluster of mesenchymal cells at the cumulus produces dpp signals received by germ disc epithelial cells. *Development* 130, 1735–1747. doi:10.1242/dev.00390

Akiyama-Oda, Y., and Oda, H. (2020). Hedgehog signaling controls segmentation dynamics and diversity via msx1 in a spider embryo. *Sci. Adv.* 6, eaba7261. doi:10.1126/sciadv.aba7261

Aliee, M., Röper, J.-C., Landsberg, K. P., Pentzold, C., Widmann, T. J., Jülicher, F., et al. (2012). Physical mechanisms shaping the Drosophila dorsoventral compartment boundary. *Curr. Biol.* 22, 967–976. doi:10.1016/j.cub.2012.03.070

Alt, S., Ganguly, P., and Salbreux, G. (2017). Vertex models: from cell mechanics to tissue morphogenesis. *Philos. Trans. R. Soc. Lond. B Biol. Sci.* 372, 20150520. doi:10.1098/rstb.2015.0520

Benton, M. A., Akam, M., and Pavlopoulos, A. (2013). Cell and tissue dynamics during Tribolium embryogenesis revealed by versatile fluorescence labeling approaches. *Development* 140, 3210–3220. doi:10.1242/dev.096271

Benton, M. A. (2018). A revised understanding of Tribolium morphogenesis further reconciles short and long germ development. *PLoS Biol.* 16, e2005093. doi:10.1371/journal.pbio.2005093

Bertet, C., Sulak, L., and Lecuit, T. (2004). Myosin-dependent junction remodelling controls planar cell intercalation and axis elongation. *Nature* 429, 667–671. doi:10.1038/nature02590

Blankenship, J. T., Backovic, S. T., Sanny, J. S. P., Weitz, O., and Zallen, J. A. (2006). Multicellular rosette formation links planar cell polarity to tissue morphogenesis. *Dev. Cell* 11, 459–470. doi:10.1016/j.devcel.2006.09.007

Brusca, R. C., and Brusca, G. J. (2003). *Invertebrates*. Second Edition. Sunderland, Massachusetts: Sinauer Associates.

Farhadifar, R., Röper, J.-C., Aigouy, B., Eaton, S., and Jülicher, F. (2007). The influence of cell mechanics, cell-cell interactions, and proliferation on epithelial packing. *Curr. Biol.* 17, 2095–2104. doi:10.1016/j.cub.2007.11.049

Fletcher, A. G., Osterfield, M., Baker, R. E., and Shvartsman, S. Y. (2014). Vertex models of epithelial morphogenesis. *Biophys. J.* 106, 2291–2304. doi:10.1016/j.bpj.2013.11.4498

Forgacs, G., and Newman, S. A. (2005). *Biological physics of the developing embryo*. Cambridge: Cambridge University Press. doi:10.1017/CBO9780511755576

Galis, F., van Dooren, T. J. M., and Metz, J. A. J. (2002). Conservation of the segmented germband stage: robustness or pleiotropy? *Trends Genet.* 18, 504–509. doi:10.1016/S0168-9525(02)02739-7

Goriely, A. (2017). "Discrete computational models," in *The mathematics and mechanics of biological growth interdisciplinary applied mathematics*. Editor A. Goriely (New York, NY: Springer), 51–59. doi:10.1007/978-0-387-87710-5_3

Heer, N. C., and Martin, A. C. (2017). Tension, contraction and tissue morphogenesis. *Development* 144, 4249–4260. doi:10.1242/dev.151282

Hemmi, N., Akiyama-Oda, Y., Fujimoto, K., and Oda, H. (2018). A quantitative study of the diversity of stripe-forming processes in an arthropod cell-based field undergoing axis formation and growth. *Dev. Biol.* 437, 84–104. doi:10.1016/j.ydbio.2018.03.001

Honda, H. (1983). "Geometrical models for cells in tissues," in *International review of cytology*. Editors G. H. Bourne, J. F. Danielli, and K. W. Jeon (Cambridge: Academic Press), 191–248. doi:10.1016/S0074-7696(08)62339-6

Honda, H., Motosugi, N., Nagai, T., Tanemura, M., and Hiiragi, T. (2008). Computer simulation of emerging asymmetry in the mouse blastocyst. *Development* 135, 1407–1414. doi:10.1242/dev.014555

Hubaud, A., and Pourquié, O. (2014). Signalling dynamics in vertebrate segmentation. *Nat. Rev. Mol. Cell Biol.* 15, 709–721. doi:10.1038/nrm3891

Irvine, K. D., and Wieschaus, E. (1994). Cell intercalation during Drosophila germband extension and its regulation by pair-rule segmentation genes. *Development* 120, 827–841. doi:10.1242/dev.120.4.827

Kanayama, M., Akiyama-Oda, Y., Nishimura, O., Tarui, H., Agata, K., and Oda, H. (2011). Travelling and splitting of a wave of hedgehog expression involved in spider-head segmentation. *Nat. Commun.* 2, 500. doi:10.1038/ncomms1510

Kanayama, M., Akiyama-Oda, Y., and Oda, H. (2010). Early embryonic development in the spider Achaearanea tepidariorum: microinjection verifies that cellularization is complete before the blastoderm stage. *Arthropod Struct. Dev.* 39, 436–445. doi:10.1016/j.asd.2010.05.009

Keller, R. (2006). Mechanisms of elongation in embryogenesis. *Development* 133, 2291–2302. doi:10.1242/dev.02406

Kondo, S., and Miura, T. (2010). Reaction-diffusion model as a framework for understanding biological pattern formation. *Science* 329, 1616–1620. doi:10.1126/science.1179047

Kong, D., Wolf, F., and Großhans, J. (2017). Forces directing germ-band extension in Drosophila embryos. *Mech. Dev.* 144, 11–22. doi:10.1016/j.mod.2016.12.001

Landsberg, K. P., Farhadifar, R., Ranft, J., Umetsu, D., Widmann, T. J., Bittig, T., et al. (2009). Increased cell bond tension governs cell sorting at the Drosophila anteroposterior compartment boundary. *Curr. Biol.* 19, 1950–1955. doi:10.1016/j.cub.2009.10.021

Larsen, C. W., Hirst, E., Alexandre, C., and Vincent, J.-P. (2003). Segment boundary formation in Drosophila embryos. *Development* 130, 5625–5635. doi:10.1242/dev.00867

Lecuit, T., and Lenne, P.-F. (2007). Cell surface mechanics and the control of cell shape, tissue patterns and morphogenesis. *Nat. Rev. Mol. Cell Biol.* 8, 633–644. doi:10.1038/nrm2222

Liu, P. Z., and Kaufman, T. C. (2005). Short and long germ segmentation: unanswered questions in the evolution of a developmental mode. *Evol. Dev.* 7, 629–646. doi:10.1111/j.1525-142X.2005.05066.x

Oda, H., and Akiyama-Oda, Y. (2020). The common house spider Parasteatoda tepidariorum. *EvoDevo* 11, 6. doi:10.1186/s13227-020-00152-z

Oda, H., Iwasaki-Yokozawa, S., Usui, T., and Akiyama-Oda, Y. (2020). Experimental duplication of bilaterian body axes in spider embryos: holm's organizer and self-regulation of embryonic fields. *Dev. Genes Evol.* 230, 49–63. doi:10.1007/s00427-019-00631-x

Okuda, S., Miura, T., Inoue, Y., Adachi, T., and Eiraku, M. (2018). Combining Turing and 3D vertex models reproduces autonomous multicellular morphogenesis with undulation, tubulation, and branching. *Sci. Rep.* 8, 2386. doi:10.1038/s41598-018-20678-6

Paluch, E., and Heisenberg, C.-P. (2009). Biology and physics of cell shape changes in development. *Curr. Biol.* 19, R790–R799. doi:10.1016/j.cub.2009.07.029

Paré, A. C., Vichas, A., Fincher, C. T., Mirman, Z., Farrell, D. L., Mainieri, A., et al. (2014). A positional Toll receptor code directs convergent extension in Drosophila. *Nature* 515, 523–527. doi:10.1038/nature13953

Pechmann, M. (2016). Formation of the germ-disc in spider embryos by a condensation-like mechanism. *Front. Zool.* 13, 35. doi:10.1186/s12983-016-0166-9

Peel, A. D., Chipman, A. D., and Akam, M. (2005). Arthropod segmentation: beyond the Drosophila paradigm. *Nat. Rev. Genet.* 6, 905–916. doi:10.1038/nrg1724

Raff, R. A. (2012). *The shape of life: genes, development, and the evolution of animal form*. Chicago: University of Chicago Press.

Richardson, M. K. (1995). Heterochrony and the phylotypic period. *Dev. Biol.* 172, 412–421. doi:10.1006/dbio.1995.8041

Sachs, L., Chen, Y.-T., Drechsler, A., Lynch, J. A., Panfilio, K. A., Lässig, M., et al. (2015). Dynamic BMP signaling polarized by toll patterns the dorsoventral axis in a hemimetabolous insect. *eLife* 4, e05502. doi:10.7554/eLife.05502

Sarrazin, A. F., Peel, A. D., and Averof, M. (2012). A segmentation clock with two-segment periodicity in insects. *Science* 336, 338–341. doi:10.1126/science.1218256

Sato, K., Hiraiwa, T., and Shibata, T. (2015). Cell chirality induces collective cell migration in epithelial sheets. *Phys. Rev. Lett.* 115, 188102. doi:10.1103/PhysRevLett.115.188102

Scholtz, G., and Wolff, C. (2013). "Arthropod embryology: Cleavage and germ band development," in *Arthropod biology and evolution: molecules, development, morphology*. Editors A. Minelli, G. Boxshall, and G. Fusco (Berlin, Heidelberg: Springer), 63–89. doi:10.1007/978-3-642-36160-9_4

Stansbury, M. S., and Moczek, A. P. (2013). "The evolvability of arthropods," in *Arthropod biology and evolution: molecules, development, morphology*. Editors A. Minelli, G. Boxshall, and G. Fusco (Berlin, Heidelberg: Springer), 479–493. doi:10.1007/978-3-642-36160-9_18

Sun, D. A., and Patel, N. H. (2019). The amphipod crustacean Parhyale hawaiensis: an emerging comparative model of arthropod development, evolution, and regeneration. *Wiley Interdiscip. Rev. Dev. Biol.* 8, e355. doi:10.1002/wdev.355

Thomas, G. W. C., Dohmen, E., Hughes, D. S. T., Murali, S. C., Poelchau, M., Glastad, K., et al. (2020). Gene content evolution in the arthropods. *Genome Biol.* 21, 15. doi:10.1186/s13059-019-1925-7

Valentine, J. W. (2004). *On the origin of phyla*. Chicago: University of Chicago Press.

Willmore, K. E. (2012). The body plan concept and its centrality in evo-devo. *Evo. Edu. Outreach* 5, 219–230. doi:10.1007/s12052-012-0424-z

frontiers | Frontiers in Cell and Developmental Biology

TYPE Review
PUBLISHED 12 September 2022
DOI 10.3389/fcell.2022.966662



OPEN ACCESS

EDITED BY
Hiroaki Hirata,
Kanazawa Institute of Technology, Japan

REVIEWED BY
Kazumasa Ohashi,
Tohoku University, Japan
Dominique Alfandari,
University of Massachusetts Amherst, United States

*CORRESPONDENCE
Srikala Raghavan,
srikala_raghavan@asrl.a-star.edu.sg

†These authors have contributed equally to this work

SPECIALTY SECTION
This article was submitted to Cell Adhesion and Migration, a section of the journal Frontiers in Cell and Developmental Biology

RECEIVED 11 June 2022
ACCEPTED 18 July 2022
PUBLISHED 12 September 2022

CITATION
Lim R, Banerjee A, Biswas R, Chari AN and Raghavan S (2022), Mechanotransduction through adhesion molecules: Emerging roles in regulating the stem cell niche. *Front. Cell Dev. Biol.* 10:966662. doi: 10.3389/fcell.2022.966662



# Mechanotransduction through adhesion molecules: Emerging roles in regulating the stem cell niche

Ryan Lim[1†], Avinanda Banerjee[1†], Ritusree Biswas[2,3†], Anana Nandakumar Chari[1] and Srikala Raghavan[1,2*]

[1]A*STAR Skin Research Lab (ASRL), Agency for Science, Technology and Research (A*STAR) 8A Biomedical Grove, Singapore, Singapore, [2]Institute for Stem Cell Science and Regenerative Medicine (inStem), GKVK Campus, Bangalore, India, [3]Sastra University, Thanjavur, TN, India

Stem cells have been shown to play an important role in regenerative medicine due to their proliferative and differentiation potential. The challenge, however, lies in regulating and controlling their potential for this purpose. Stem cells are regulated by growth factors as well as an array of biochemical and mechanical signals. While the role of biochemical signals and growth factors in regulating stem cell homeostasis is well explored, the role of mechanical signals has only just started to be investigated. Stem cells interact with their niche or to other stem cells via adhesion molecules that eventually transduce mechanical cues to maintain their homeostatic function. Here, we present a comprehensive review on our current understanding of the influence of the forces perceived by cell adhesion molecules on the regulation of stem cells. Additionally, we provide insights on how this deeper understanding of mechanobiology of stem cells has translated toward therapeutics.

KEYWORDS

**mechanotransduction, stem cell niche, adhesion molecules, adherens junctions, focal adhesion, disease and regenerative therapeutics**

## 1 Introduction

Regenerative Medicine, which deals with the restoration of tissues/organs upon injury or chronic disease, is a promising and emerging branch of medical research (Mason and Dunnill, 2008; Mahla, 2016). It is well known that stem cells in our body hold the capability of self-renewal and differentiation into other types of cells, which makes it an ideal candidate for regenerative medicine. Though the term stem cell (original: 'Stammzelle') appeared in the scientific literature in the mid-19th century by famous German biologist Ernst Haeckel (Haeckel, 1868); major breakthroughs in the stem cell research only happened a century later. However, over the past 20 years, there have been immense advancements in the field of stem cell research, in elucidating their characteristics and potential for regenerative medicine (Mahla, 2016; Liu et al., 2020).

Although there are different types of stem cells, they all share common characteristics of self-renewal and the ability to differentiate into different cell types. Among many types

of stem cell classifications, two common ways to classify them are 1) based on their origin or residency, known as tissue-specific stem cells and 2) based on their potency, which refers to their ability to differentiate into various cell types.

Stem cells isolated from mammalian blastocysts are also known as embryonic stem cells (ESCs) (Evans and Kaufman, 1981; Thomson, 1998; Smith, 2001). Stem cells isolated from the epiblast stage of embryos are termed epiblast stem cells (EpiSCs) and primordial germ cells (embryogenic germ cells EGCs) (Shamblott et al., 1998; Yu and Thomson, 2008). In contrast to ESCs, adult stem cells are found in various tissues and are alternatively termed as somatic stem cells (Leblond, 1964; Robey, 2000). Hematopoietic stem cells (HSC) were amongst the first identified adult stem cells and the most widely studied (Seita & Weissman, 2010). Some of the tissues where pools of adult stem cells have been identified include 1) The nervous system which includes parts of brain, 2) Bone marrow and blood which consist of bone marrow, peripheral blood, dental pulp and spinal cord, blood vessels, 3) Endothelial Progenitor Cells, 4) Skeletal Muscle Stem Cells, 5) Epithelial Cell Precursors in the Skin and Digestive System as well as from parts of cornea, retina, liver, and pancreas. These tissue specific stem cells (TSSCs) behave differently depending on their local environment and the homeostatic requirement of the body.

Stem cells (SCs) often reside in tissue-specific microenvironments termed as the stem cell niche, that play an important role in regulating the proliferation and differentiation of these cells, thereby maintain tissue homeostasis (Schofield, 1978). The concept and significance of the stem cell niche was first proposed by Scholfield in 1978, when he demonstrated that removing these cells from their niche resulted in their differentiation (Schofield, 1978). Stem cell fates are regulated by both intrinsic and extrinsic factors. Cell-intrinsic factors include specific transcription factors, microRNAs, epigenetic regulators and secreted signaling molecules such as Wnts and BMPs (Watt and Hogan, 2000; Nusse, 2008; Gangaraju and Lin, 2009; Wang and Wagers, 2011; Li et al., 2017; Chacón-Martínez et al., 2018; Rigillo et al., 2021). Extrinsic factors include the regulation of stem cells with through cell-cell and cell-substratum interactions (Watt and Huck, 2013; Gattazzo et al., 2014). In addition to the above-mentioned niche factors, mechanical signals originating from cell-intrinsic and externally applied forces also have major implications on the behavior of the SCs (Vining and Mooney, 2017). Force generation by actomyosin contractility and cytoskeletal assembly impinge on mechanisms by which the cells exert intrinsic forces on its extracellular milieu and neighboring cells. In contrast, cell-extrinsic forces arise from the rigidity, topography and composition of the ECM that exerts shear, tensile and compressive forces on the stem cells (Lo et al., 2000; Even-Ram et al., 2006; Dupont et al., 2011; Li et al., 2011; Wolfenson et al., 2019). Transmission of these mechanical forces through cell-cell junctions and cell-substratum adhesions plays a key role in regulating intracellular signaling pathways, eventually determining stem cell fate (Vining and Mooney, 2017). Although the role of cell-intrinsic factors and signaling molecules regulating the quiescence of the stem cells have been extensively studied, the mechanical function of the cell-cell adhesion molecules in maintaining the stem cell homeostasis is less well explored. Cells typically sense and transmit external forces to specialized structures at the cell periphery. These structures then transduce the forces into a biochemically detectable signal, and ultimately the response of the cell is transcribed by the nucleus. These are commonly referred to as mechanotransmission, mechanosensing, and mechanoresponse, respectively or as a whole, mechanotransduction (Ingber, 2006; Jansen et al., 2017). Recent studies have highlighted the importance of biophysical attributes of the microenvironment, including mechanical loading and substrate material property, in determining the self-renewal and commitment of SCs required for its maintenance and differentiation respectively. External forces applied to the SCs from its niche generates traction forces as well as compressive forces through the cytoskeleton. These forces are then transmitted from the cytoskeleton to other cellular components inside or outside of the SCs. This concept of organizing and stabilizing the cytoskeleton by the living cells in response to applied external forces is based on the model of tensegrity, which was first described by D. Ingber (Chen and Ingber, 1999; Ingber, 2003). The cellular tensegrity model describes the cell as a mechanical force bearing structure that is composed of compression resistant components and tension bearing cables. These cables create a pre-stress state in the cell, which is opposed by the compression resistant components known as struts, that aids in the maintenance of the mechanical equilibrium of the cell. This tensegrity-based model highlights the integration of cytoplasmic mechanotransduction and biological responses that are critical for determining the proliferative and differentiative characteristics of SCs, gene expression, as well as its role in organ development (Chowdhury et al., 2010; Engler et al., 2004; 2006). The 2 cell junctions that regulate mechanotransduction of the SCs within its niche are, the cadherin mediated Adherens Junctions (AJs) and the integrin mediated Focal Adhesions (FAs).

# 2 Role of extracellular matrix molecule and adhesion molecules in regulating mechanotransduction of stem cell niche

## 2.1 Extracellular matrix and matrix metalloproteinases as a niche factor

### 2.1.1 Extracellular matrix

The ECM comprises of noncellular components surrounding all the cells in the body, and provides mechanical support via a structural macromolecular network (Murphy-Ullrich & Sage,

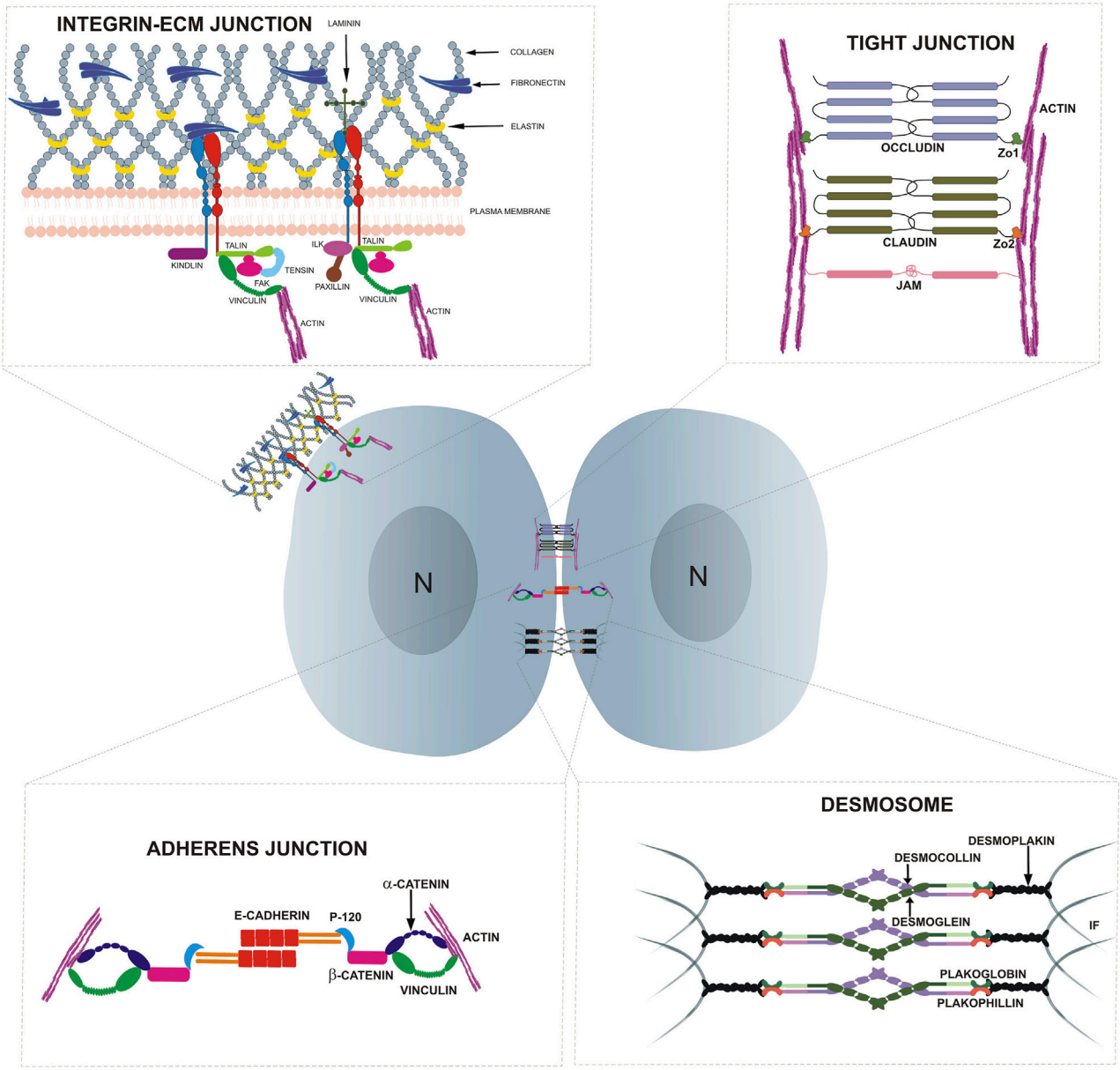


FIGURE 1
Highlights the cell adhesion molecules present at cell-cell and cell-substratum junctions in epithelial cells.

2014; Theocharis et al., 2016; Stanton et al., 2019). Mechanical cues from the ECM help to regulate cell phenotypes, motility, biochemistry and matrix production and therefore plays an essential role in tissue remodeling (Jaalouk and Lammerding, 2009; Akhmanova et al., 2015). The components of the ECM that mediate signaling in cells include: collagen, elastin, laminin, fibronectin, hyaluronic acid, chondroitin sulfate and syndecans, as well as soluble components such as cytokines, matrix metalloproteinases, growth factors and proteases (Figure 1) (Hynes, 2009; Mohammed et al., 2019). The physical properties of the ECM such as its rigidity, viscosity, porosity and topography are influenced by the concentration, type, and arrangement of macromolecules (fibers, proteoglycans and glycoproteins). As a result, the ECM may present as a soft or hard substrate (Yue, 2014; Jansen et al., 2015). Multiple studies have suggested the role of ECM stiffness as a major regulatory physical factor in determining stem cell fate (Discher et al., 2005; Paszek et al., 2005; Engler et al., 2006; Even-Ram et al., 2006; Hamidouche et al., 2009; Li et al., 2011; Gandavarapu et al., 2014).

#### 2.1.1.1 Collagen

About 30% of the total protein mass in mammals is constituted by collagen, which is also one of the most abundant components of the ECM (Shoulders and Raines, 2009; Ricard-Blum, 2011). The collagen super family comprises 28 members with at least 46 distinct polypeptide chains in vertebrates (Brinckmann, 2005). The primary component of the ECM in vertebrates is collagen I, which consists of stiff, thick and long fibrils that contribute to the structural architecture, shape and mechanical properties of tissues such as tensile strength in skin and resistance to traction in ligaments (Ricard-Blum, 2011). Different collagen types are reported to perform tissue-specific functions. For example, collagen XXII which is present only at tissue junctions (skeletal and heart muscles) and in the skin epithelia acts as an adhesion ligand (Koch et al., 2004). Collagen XIII in bone regulates its formation by coupling bone mass to mechanical use (Ylönen et al., 2005) and collagen VII in skin is critical for maintaining dermal-epidermal adhesion, thus affecting its integrity (Bruckner-Tuderman et al., 1987).

Collagen in the ECM of the stem cell niche plays an important role in determining the proliferative and differentiation potential of the stem cells. Studies have shown that type IV collagen in the basement membrane and hair follicles of the skin provides mechanical support as well as an increase in the proliferative potential of normal human basal keratinocytes (Breitkreutz et al., 2013; Choi et al., 2014). Likewise, in muscle stem cells (satellite cells), alterations of muscle stiffness which is mediated by collagen VI deposition by fibroblasts affects the self-renewal and maintenance of these stem cells (Urciuolo et al., 2013). The mechanical microenvironment of the intestinal crypt cells has been shown to be primarily regulated by type VI collagen via its interaction with the RGD domain of fibronectin (Groulx et al., 2011; Benoit et al., 2012). Altered tissue stiffness in the intestinal crypt cells is associated with increased type VI collagen secretion into the basal lamina. This alteration of the tissue stiffness, in turn, affects integrin focal adhesions, growth factor receptor signaling and acto-myosin and cytoskeletal-dependent cellular contractility (Handorf et al., 2015). Collagen has also been shown to support stem cell properties such as clonogenicity, cell growth and osteogenic differentiation potential (Chen et al., 2007; Linsley et al., 2013; Somaiah et al., 2015; Akhir and Teoh, 2020). The absence of collagen III in mice affects osteoblast differentiation (Volk et al., 2014) whereas the denaturation of collagen I promotes osteoblastic differentiation (Tsai et al., 2010). Taken together, these studies suggested that the structural integrity conferred by collagen in the ECM is implicated in the fate of stem cell proliferation and differentiation in different niches.

#### 2.1.1.2 Elastin

Another important component factor of the ECM along with collagen are the elastin networks that are predominantly found in soft elastic tissues like the skin, blood vessels and lungs (Rosenbloom et al., 1993; Li & Daggett, 2002). Elastin is formed from its monomer, tropoelastin. Tropoelastin is crosslinked at its lysine residues, thereby forming elastic fibers along with microfibrillar proteins such as fibrillin. These elastic fibers are the major contributors to the mechanical properties of elastin (Aaron and Gosline, 1981; Ozsvar et al., 2015). Elastin is predominantly deposited during prenatal development and childhood and is rarely synthesized during adulthood (Ozsvar et al., 2015). 90% of elastin comprises elastic fibers, with the remaining 10% consisting of fibrillin glycoprotein (Mecham, 1991). The primary role of these elastic fibers is to undergo constant stretch-recoil cycles, thus maintaining the structural and functional integrity of the elastic tissues throughout the organism's lifetime (Ozsvar et al., 2015).

Studies have shown that tropoelastin can promote cell attachment and migration of various cell types such as fibroblasts, mesenchymal stem cells (MSCs) and endothelial cells (Ozsvar et al., 2015). Additionally, tropoelastin has been shown to interact and bind with one of the major cell adhesion proteins, integrins, to promote proliferation in MSCs and HSCs. Specifically, elastin's interaction with αvβ3 and αvβ5 integrins on the surface of MSCs, either as surface-bound or as soluble tropoelastin, promotes MSC proliferation. This was attributed to the ability of elastin to convey mechanical signals and modulate gene expression that supports proliferation (Rodgers and Weiss, 2004; Yeo and Weiss, 2019). Tropoelastin-integrin interactions partially contribute to the wound healing process by remodeling the ECM (Ozsvar et al., 2021). Likewise, in the hematopoietic stem cell (HSC) compartment, mechanical characteristics of tropoelastin in the ECM has been shown to be associated with its differentiation (Holst et al., 2010). The tunable elasticity of elastin plays an important role in regulating cell proliferation, differentiation, adhesion and migration.

#### 2.1.1.3 Laminin

Laminins are a family of large multidomain, heterotrimeric glycoproteins that are composed of three different subunits, the α, β, and γ chains. These chains are encoded by 11 genes in humans and form at least 15 trimeric combinations of subunits throughout different tissues (Aumailley et al., 2005). Different combinations of these three subunits confer upon laminins its nomenclature. For example, laminin composed of α2, β1, and γ1 chains is laminin 211 and so on (Kaur and Reinhardt, 2015). Each laminin subunit consists of tandem LE repeats (laminin-type epidermal growth factor-like domains), globular domains interspersed within the LE domains and an α-helical domain which follows after the LE repeats (Beck et al., 1990; Hamill et al., 2009). The α-helical domains of the α, β, and γ subunits wind around each other to produce a trimeric coiled-coil structure

(Beck et al., 1990). Laminins (with other components) maintain the structural and functional integrity of the ECM, ultimately affecting cell viability (Armony et al., 2016). Additionally, laminins also influence cell adhesion and migration (Domogatskaya et al., 2012).

Laminins are well known for regulating different stem cell functions such as cell-substratum adhesion, proliferation, migration and differentiation (Iorio et al., 2015). However, there are very few *in-vivo* reports that highlight the mechanical properties of laminin in maintaining stem cell function. In contrast, *in-vitro* studies that modulate substrate stiffness and ligand composition to mimic the native elasticity of the stem cell niches have highlighted the role of laminin as a stem cell niche factor. For example, satellite cell renewal from skeletal muscle was promoted when cultured on laminin crosslinked hydrogels (with a stiffness of ~12 kPa) which mimics the native elasticity of skeletal muscles. This study further reported that muscle satellite cells cultured on laminin functionalized hydrogels contributed to muscle regeneration when grafted into immune deficient mice that partially lacked endogenous satellite cells (Gilbert et al., 2010). Different isoforms of laminin have been shown to be able to direct the differentiation of human induced pluripotent stem cells (hiPSCs) into multiple eye-like tissues. Of note, the E8 fragments of laminin 511 enables the dense concentration of hiPSCs colonies due to actomyosin contraction, which results in cell density YAP inactivation and ultimately leading to retinal differentiation in these colony centers (Shibata et al., 2018). Neural stem and progenitor cells (NSPCs) differentiation towards the oligodendrocyte lineage have been shown to be favored when cultured on laminin coated substrate over fibronectin coated substrate and along with mechanical stimulation by subjecting the cells to a single static stretch (Arulmoli et al., 2015). This oligodendrocyte lineage specific differentiation is preferentially mediated by the integrin α6 laminin binding. These findings correlate with what is known *in vivo* as laminin is found in high concentrations in a developing brain and is also expressed in the NSPC niches such as the subventricular zone (SVZ) of the lateral ventricles and dentate gyrus (DG) of the hippocampus in an adult brain (Chen et al., 2003; Lathia et al., 2007; Relucio et al., 2012). Thus, mechanical forces resulting from robust cell movements during development and tissue folding of the brain may thus be implicated together with laminin in the ECM to direct NSPC differentiation towards the oligodendrocyte lineage within this niche.

#### 2.1.1.4 Fibronectin

Fibronectin (FN) is a large 440 kDa, multidomain, dimeric glycoprotein which is found in the extracellular milieu of different tissues (Proctor, 1987; Parisi et al., 2020). It is composed of two identical subunits that are joined together by disulfide bonds near the C-terminal regions. Each subunit monomer consists of three different types of repeats, namely FNI, FNII and FNIII (Hynes, 1986; Pankov and Yamada, 2002; To and Midwood, 2011; Adams et al., 2015). FN exists in both soluble and insoluble forms. The soluble FN, also known as plasma fibronectin, circulates in the blood and contributes primarily to tissue repair by forming fibrin blood clots (To and Midwood, 2011). On the other hand, the insoluble FN, also known as cellular FN, is found on cell surfaces and in the ECM (Proctor, 1987; To and Midwood, 2011). FN is also considered as the 'master organizer' of the ECM since it helps in organizing other matrix proteins such as collagen, heparin, fibrillin and fibulins (Morla and Ruoslahti, 1992; Chung and Erickson, 1997; Klass et al., 2000; Woods, 2001; Galante and Schwarzbauer, 2007; Kaur and Reinhardt, 2015). The tripeptide sequence Arg-Gly-Asp or RGD present on the FNIII repeat, binds to different integrin subunits and aids in the assembly of FN (Goodman, 2021). These non-covalent interactions help in forming a matured FN network.

Interaction of FN with cell surface receptors such as integrins and syndecans aid in cell adhesion and migration as well as determining cell shape and differentiation. Human mesenchymal stem cells (hMSCs) are known to utilize their own contractile forces and translate environmental cues such as variations in substrate rigidity into differential biochemical signals with the help of stretched FN fibers. hMSCs mediated osteogenesis was shown to be increased upon inhibition of αvβ3 integrin on relaxed FN fibers whereas osteogenesis was decreased upon inhibition of αvβ1 on stretched FN fibers. Thus, the mechanical strain of these FN fibers serves as a checkpoint, where they act as a crucial mechano-chemical signal converter that help the hMSCs to differentiate (Li et al., 2013). Osteogenic differentiation is known to be enhanced with increasing higher substrate stiffness ranging from 0.7 to 80 kPa. Interestingly, when polyacrylamide gels were coated with fibronectin, it stimulated osteogenic differentiation even at a lower substrate stiffness of 25 kPa, at a comparable differentiation rate to that of 80 kPa. These studies indicate that the mechanical properties of ECM components like fibronectin might play a significant role in determining the fate of stem cells (Rowlands et al., 2008). In embryonic stem cells (ES) fibronectin-mediated upregulation of the expression αvβ1 has been shown to promote the fate of cells towards a meso-endodermal lineage (Hayashi et al., 2007; Pimton et al., 2011). Additionally, in adult stem cells, fibronectin can promote differentiation towards a skeletal lineage as opposed to an adipogenic fate (Ogura et al., 2004; Martino et al., 2009; Wang et al., 2010). Interestingly, when differentiated 3T3 adipocytes were cultured on fibronectin, a reduction in the lipogenic gene expression was observed, suggesting that fibronectin also affects the fate of these cells (Spiegelman and Ginty, 1983). In mammalian skin, FN is also known to contribute to the wound healing process. The FN pericellular matrix assembled by fibroblasts senses strain

caused by a disruption in tensile homeostasis during wounding. Mechanically regulated interaction between FN and collagen drives the deposition of collagen over FN matrices at the wound bed, which protects the FN matrix from the microenvironmental forces (Patten and Wang, 2021). Although it is known that the interaction between FN and collagen is mechanically regulated, the mechanism for the unfolding of the FN fibrils is less well understood (Gee et al., 2008; Ponmurugan and Vemparala, 2012; Früh et al., 2015; Szymanski et al., 2017a; Szymanski et al., 2017b).

### 2.1.2 Matrix metalloproteinases

Matrix metalloproteinases (MMPs) are enzymes that cleave components of the ECM such as collagen and laminin, and play an important role in embryonic development, morphogenesis and tissue remodeling (Brenner et al., 1989; Matrisian and Hogan, 1990; Woessner, 1991; Tyagi et al., 1995). MMPs are a growing family of metallo endopeptidases and can be classified as collagenases, gelatinases, stromelysins, matrilysins and, enamelysins (Jabłońska-Trypuć et al., 2016). During development, MMPs help in regulating biophysical cues by degrading and modulating the stiffness of the ECM in different stem cell niches such as MSCs and HSCs (Caiazzo et al., 2016; Saw et al., 2019). MSCs play an active and significant role in bone regeneration due to their ability to migrate to injured sites and differentiate into osteocytes. Additionally, MMPs are also involved in bone regeneration as it has been shown that inhibition of MMPs, in particular MMP-13, led to perturbations in the migration, proliferation and osteogenic differentiation capabilities of the MSCs (Kasper et al., 2007). It was further demonstrated in the same study that mechanical loading also played a role in regulating the expression of MMPs, which may be an important factor in regulating levels of MMPs to direct MSC osteogenic differentiation. The conditional ablation of MMP-14 from mouse dermal fibroblasts results in enhanced accumulation of collagen I in the ECM, resulting in a fibrotic skin condition associated with an increase in stiffness and tensile strength. This study suggested that MMP-14 contributes to collagen remodeling in adult skin, and plays a crucial role in maintaining dermal homeostasis (Zigrino et al., 2016). The migration of muscle stem cells (MuSCs) and progenitors to appropriate sites require physical interaction with its niche (Smith, et al., 2017). During this migration, cells experience mechanical resistance from the matrix, causing the cells to escape from their basement membrane. This process requires the expression of MMPs (MMP-1, MMP-14) from muscle progenitors to degrade the ECM in their path of migration (Wang et al., 2009; Xiaoping and Yong, 2009; Lund et al., 2014). Taken together, these studies show that MMPs play a critical role in modulating the physical properties of ECM to affect a variety of stem cell functions.

## 2.2 Cell-substrate adhesions as niche factor

In multicellular organisms, adhesion molecules help to maintain tissue architecture, generate forces for cell movement and ensure the functionality of tissues by creating barriers (Vleminckx, 2017). Adhesion molecules bind to various ligands and receptors and the resulting signals are critical to many physiological processes such as cell growth, differentiation, contact inhibition and apoptosis (Vleminckx, 2017). The cytoplasmic domain of adhesion molecules bind indirectly to the cytoskeletal proteins such as actin and intermediate filaments, whereas their extracellular domain, via homophilic or heterophilic adhesion, interact with adhesion receptors on neighboring cells or ECM ligands. Furthermore, these adhesion molecules often cluster at specific restricted areas in the membrane, commonly termed as junctional complexes. The linkage to the cytoskeleton coupled with its clustering enhances the strength of adhesion forces nucleated by these adhesion molecules. Adhesion molecules are classified into five major groups based on their mode of interaction, function, structure and location. These groups are integrins, cadherins, selectins, proteoglycans and the immunoglobulin (Ig) superfamily (Samanta and Almo, 2015; Vleminckx, 2017). In this section, we will focus on the role of integrins, involved in cell-ECM interactions via the focal adhesions (FA) and cadherin, that mediate cell-cell interactions at the adherens junction (AJ) in stem cell functions. Junction complexes induced by cadherin and integrins can initiate signal transduction that facilitates niche signaling, in turn regulating stem cell properties such as self-renewal, proliferation and survival (Chen et al., 2013). The role of mechanical signals in regulating stem cell function, has been recently reviewed (Shih et al., 2011; Vining and Mooney, 2017; Naqvi and McNamara, 2020). However, the molecular mechanisms underpinning the mechanical activation of adhesion molecules and their roles in regulating stem cell fate are still less well understood.

### 2.2.1 Integrin

Integrins are transmembrane heterodimeric receptors consisting of α and β subunits that function as a mechanical link between the cellular cytoskeleton and the ECM (Figure 1) (Sun et al., 2016). The engagement of integrins with their extracellular ligands initiates intracellular biochemical responses (Hynes, 1992; Arnaout et al., 2007). In mammals, there are eight β-subunits and 18 α-subunits resulting in 24 distinct integrin receptors (Hynes, 2002). These receptors bind to different ECM ligands such as laminin, fibronectin and collagen IV, with specific heterodimers playing important roles in stem cell maintenance in different tissue niches. For example, $\alpha_2$ integrin regulates the osteogenic differentiation in hMSCs and is upregulated in MSCs plated on stiffer matrices (42.1 kPa). On the other hand, the knockdown of $\alpha_2$ integrin in these MSCs

decreased osteogenic induction, suggesting a role for this integrin in mechanotransduction during osteogenic differentiation (Shih et al., 2011). The reduction in quiescence of neural stem cells (NSCs) is associated with a lower expression of β1 integrin, which, in turn, results in a reduced interaction of the β1 integrin on the NSCs to the laminin-rich microenvironment (Shen et al., 2008; Nascimento et al., 2018). On the other hand, bifunctional hydrogels with different stiffnesses (2 and 20 kPa) that are engineered with laminin peptide (IKVAV) and poly-lysine led to neurogenesis in embryonic cortical progenitors and adult NSCs respectively via β1 integrin. These data suggest that substrate stiffness and ligand specificity of integrin contribute to different stem cell behavior (Farrukh et al., 2017). Although integrin is a well-known mechanotransmitter, integrin-mediated mechanosensing in regulating the stem cell microenvironment is still being explored.

### 2.2.2 Integrin-associated proteins

Focal adhesions (FAs) are one of the key junctions involved in mechanosensing at the cell periphery. FAs comprise multimeric protein complexes which integrate both inside-out and outside-in signals and involve both mechanical and biochemical cues to regulate cellular functions (Vogel and Sheetz, 2006; Schiller and Fässler, 2013; Oakes and Gardel, 2014). FAs are nucleated by integrin receptors that form a mechanical link between the cytoskeleton and the ECM (Kanchanawong et al., 2010). Initially, integrins bind to the ligands found in the matrix, following which the cytoplasmic domain of the integrin subunit recruits multiple intracellular anchoring proteins such as talin, kindlin, paxillin, FAK, ILK, tensin etc (Figure 1). This anchorage can either result in the recruitment of vinculin, further linking this complex to the actin cytoskeleton, or result in direct engagement with the actin cytoskeleton (Alberts et al., 2002). Perturbations of these integrin-associated proteins have revealed their critical role in maintaining the stem cell niche.

Talin is an integrin-associated protein that is critical for integrin activation at the FA (Chinthalapudi et al., 2018). The lack of talin in embryonic stem cells in mice leads to the failure in the association of integrin with the cytoskeleton, resulting in embryonic lethality during gastrulation. This defect arises due to perturbed cell migration and cytoskeletal organization in the stem cell niche (Monkley et al., 2000). On the other hand, knockdown of talin in the testis results in disrupted adhesion within the germline stem cell (GSC) niche of *Drosophila*. This niche comprises stromal hub cells, GSCs and somatic cyst stem cells (CySCs). The adhesion between the hub cells and GSCs is required to maintain the undifferentiated state of GSCs, therefore the knock down of talin leads to an accumulation of differentiated GSCs (Raymond et al., 2009). A similar study in *C. elegans* showed that talin plays an important role in organizing the cytoskeleton, stabilizing adhesive contacts in muscle and modulating dynamic integrin signaling during migration (Cram et al., 2003).

Integrin-linked kinase (ILK) is a focal adhesion protein that interacts with the cytoplasmic tail of integrin β subunits and links them to the actin cytoskeleton. In the hair follicle stem cell (HFSC) niche, studies have pointed to the importance of ILK in maintaining quiescence of these cells. Deletion of ILK from the *epidermis* resulted in remodeling of the ECM and led to compensatory binding to laminin-511 over laminin-332 due to fragmentation and reduction of the latter. This imbalance caused an increase in Wnt and Tgf-β2 signaling and led to aberrant differentiation of HFSCs (Morgner et al., 2015). ILK has also been shown to be a key player during cardiomyogenesis. A decrease in ILK expression by siRNA resulted in a reduction in human fetal cardiomyogenesis, which could be attributed to an enhancement in Wnt signaling (Traister et al., 2012). Although the role of mechanotransduction in fetal cardiomyogenesis has not been directly investigated, it would be interesting to study if these dysregulations are mediated by forces generated by ILK. Lastly, mechanical stimulation of MSCs derived from mouse limb buds led to an increase in activation AKT/mTOR pathway which required ILK, ultimately resulting in an increase in differentiation and collagen expression in the niche of tendon cells (Mousavizadeh et al., 2020).

Focal Adhesion Kinase (FAK) is regulated by integrins and functions as a force sensor. Physically stretching cells causes cellular strain, increasing the force experienced at FAs, thereby activating FAK by phosphorylation at the Tyr397 residue (Schlaepfer et al., 1994; Calalb et al., 1995; Polte and Hanks, 1997). Forces experienced in focal adhesions are positively correlated with Tyr397 phosphorylated in FAK, suggesting that lower force results in reduced FAK activation (Torsoni et al., 2003). FAK activity is positively regulated by Rho-associated kinases and non-muscle myosin II. Cytoskeletal contractility along with FA formation decreased upon inhibition of the Rho-associated kinases (Seo et al., 2011). FAK activation is required for osteogenic differentiation (Salasznyk et al., 2007; Shih et al., 2011; Mathieu and Loboa, 2012) and is further correlated with myosin II being involved in osteogenic differentiation. Additionally, force-mediated activation of FAK results in activation of Rho which can then result in force-mediated adult stem cell differentiation (Thompson et al., 2012).

Tensin is known to interact with actin as well as integrins at the FAs and establishes a crucial connection between the cytoskeletal network and the ECM. Tensin three is widely expressed in tonsil-derived MSCs (TMSCs), where it plays an important role in the proliferation and differentiation of TMSCs by regulating the levels of β1-integrin (Park et al., 2019). The Ivaska's group demonstrated the role of the energy sensor AMP-activated protein kinase (AMPK) that worked in association with tensin to increase the activity of integrins. Mechanistically, AMPK negatively regulates tensin 1 and tensin 3, which in

the absence of AMPK, binds to β1-integrin, thereby regulating integrin dependent processes like cell adhesion, mechanotransduction and cell matrix formation (Georgiadou et al., 2017). Although not much is known about the role of tensin in mechanotransduction, future studies will be needed to address its role in stem cell homeostasis.

Kindlin is a scaffold protein, required for several protein-protein interactions in the FA complex. Recent studies have identified Kindlin 2 as a critical mechanosensor in MSCs. Kindlin 2 plays an important role in regulating YAP/TAZ expression and localization to regulate the fate of the MSCs. Mechanistically, kindlin-2 interacts with Myosin Light Chain Kinases (MLCKs), which controls the MSC microenvironment and intracellular signaling through RhoA activation and phosphorylation of MLC. This interaction controls the actin organization and YAP/TAZ phosphorylation, ultimately controlling YAP/TAZ mediated gene expression to regulate the MSC differentiation (Guo et al., 2018). Kindlin-2 is also reported to regulate chondrogenesis, osteogenesis and osteocyte survival. Deleting kindlin-2 from osteocytes, which are the mechanosensors of bone, has been shown to impair bone homeostasis, disrupt FA formation, cytoskeletal organization and cell orientation in bone. Loss of kindlin 2 also induced apoptosis in osteocytes and resulted in the abnormal expression of sclerostin, a negative regulator of bone formation under mechanical stimulation (Qin et al., 2021).

Paxillin is a phosphotyrosine-containing docking protein that is primarily localized to the FA complex (Glenney and Zokas, 1989; Schaller, 2001). Paxillin interacts with FAK and other signaling molecules, associated with integrin signaling and membrane trafficking (Wade et al., 2002). The mechanosensing properties of paxillin are enabled by its binding to activated vinculin that stabilizes the FA-cytoskeleton interaction. Both paxillin null mouse embryonic stem (ES) cells and paxillin null differentiated cells display defects in focal adhesion and cell spreading, coupled with an observed reduction in FAK phosphorylation (Wade et al., 2002). As studies have only begun to scratch the surface, research demonstrating a direct link between mechanotransduction and maintenance of the stem cell niche via paxillin requires further investigation.

The FA protein vinculin, which is associated with the actin cytoskeleton, is also present at the cell-cell junction (AJ). Vinculin is a well-known mechanotransducer that directly interacts with talin, α-actinin and paxillin at the FAs and α-catenin at the AJs. Various studies have shown the mechanotransduction role of vinculin at the cellular level. Only a few studies have highlighted the mechanotransduction role of vinculin in maintaining the SC niche. A study by Holle et al. showed that KD of vinculin in hMSCs resulted in a reduction of cytoplasmic and FA vinculin (Holle et al., 2013). Vinculin KD also led to a reduction in myoblast determination protein 1 (MyoD) expression in the nucleus. MyoD is the transcription factor which induces stem cell differentiation into a myoblast lineage. Re-expression of the full length or head domain of vinculin was sufficient to restore MyoD expression allowing cells to return to their myogenic state. Additionally, vinculin KD cells displayed hampered durotaxis or cell migration towards a stiffer, more myogenic-permissive matrix as opposed to control cells, which assembled preferentially at the myogenic-permissive matrix. Another transcription factor, Myogenic factor 5 (Myf5), regulates muscle differentiation along with MyoD. Studies have shown that vinculin KD resulted in the loss of stiffness-mediated expression of MyoD and Myf5 hindering myogenic differentiation. Recently, our group has shown the role of vinculin in maintaining HFSC quiescence (Biswas et al., 2021). Usually HFSCs are maintained in a quiescence state which is achieved by the cell to cell contact mediated inhibition of proliferation (Fan and Meyer, 2021). Conditional KO of vinculin in murine *epidermis* resulted in mechanically weak AJs which failed to sequester YAP at the junctions and led to increased proliferation of the HFSCs. Mechanistically, our work showed that, in contact-inhibited (quiescent) bulge stem cells, vinculin was critical in maintaining α-catenin in a stretched/open conformation reinforcing the junction which in turn kept YAP sequestered at the AJs. These studies highlight the crucial role of mechanotransduction through vinculin at the FAs and AJs for maintaining the SCs niche.

## 2.3 Cell-cell adhesions as niche factor

So far, we have discussed how integrins and integrin associated proteins at the FAs play an active role in mechanotransduction. Cells also interact with each other by forming cell-cell junctions including AJs, desmosomes, tight junctions and gap junctions (Figure 1). Among these, AJs are the key adhesion structures that interact with the cytoskeleton of neighboring cells to enable mechanical force transduction (Pannekoek et al., 2019).

### 2.3.1 Adherens junction

AJs mediate adhesion through homotypic interactions of cadherins such as E-cadherin which are calcium-dependent, transmembrane proteins (Figure 1). E-cadherin associates with the catenin family of proteins such as β-catenin, α-catenin, and p120 via its cytoplasmic domain. This forms an E-cadherin-catenin complex that interacts with the F-actin cytoskeleton by either direct binding to α-catenin or an indirect association via vinculin (Koirala et al., 2021). AJs regulate cell-cell adhesion within the stem cell niche thereby affecting stem cell fate.

#### 2.3.1.1 E-cadherin

E-cadherins are critical to the formation and maintenance of cell junctions, and for the proliferation, survival and differentiation of cells to maintain tissue integrity. Cell-cell adhesion mediated by E-cadherin is linked to signaling pathways that transduce signals to the cytoplasm and nucleus (Stepniak et al., 2009). Studies have also shed light on the importance of E-cadherin mediated stem cell niche maintenance in regulating the self-renewal of NSCs (Karpowicz et al., 2009). E-cadherin has also been shown to be crucial in maintaining the pluripotency of mESCs as the disruption in E-cadherin leads to increased Epithelial-Mesenchymal Transition (EMT) and differentiation of these cells (Redmer et al., 2011). The deletion of the E-cadherin gene in mESCs leads to the failure of cell compaction in the embryonic blastocyst that is important for maintaining the epithelial subcellular structures i.e., cellular junctions, during early mammalian development (Larue et al., 1994). Additionally, E-cadherin induces conformational changes in α-catenin through the transmission of adhesion forces from the cell-cell junctions. This leads to strengthened binding of α-catenin to F-actin and the recruitment of vinculin to the site where these forces are applied.

#### 2.3.1.2 β-catenin

In epithelial tissue, β-catenin is one of the crucial components of the AJ, where it links cadherins to the cytoskeleton of the cell, thus establishing cell adhesion. Subcellular localization of β-catenin is known to determine its function within the cell (Dietrich et al., 2002). When β-catenin localizes in the cytoplasm or nucleus, it functions as a major signaling hub for the Wnt/β-catenin signaling pathway, where it acts as a transcriptional co-activator of T cell factor/lymphoid enhancer factor family (TCF/LEF) target genes (Kim et al., 2019). β-Catenin also acts as a mechanotransducer (Benham-Pyle et al., 2016), where mechanical cues induce its nuclear accumulation and enhance transcriptional activity (Benham-Pyle et al., 2015). Additionally, it has also been reported that mechanical perturbation of *Drosophila* embryos causes increased β-catenin signaling and upregulation of its downstream target genes (Farge, 2003). The Wnt/β-catenin signaling pathway is known to respond to ECM stiffness (Du et al., 2016), which ultimately affects cellular functions such as proliferation, differentiation, migration, genetic stability, apoptosis, and stem cell renewal (Pai et al., 2017).

Jansen and co-workers demonstrated that the biphasic effects of mechanical loading on β-catenin resulted in negative effects on Wnt signaling in osteoblast differentiation and mineralization (Jansen et al., 2010). Murine embryonic stem cells (mESCs) showed enhanced expression of various pluripotency markers Oct4, Sox2, Nanog, LIF (also known as mechanopluripotency) when cultured in a stirred suspension bioreactor. Mechanical cues promoted by fluid shear induces the nuclear translocation of β-catenin. This causes a concomitant increase of c-Myc, which is an upstream regulator of these pluripotency markers, ultimately promoting mESCs mechanopluripotency (Nath et al., 2021). This study indicates that mechanotransduction through the AJ complex is critical for mESC pluripotency maintenance. In inner ear progenitor cells (IEPCs), external mechanical signals from ECM can be transduced through the RhoA-YAP-β-catenin signaling cascade to regulate its survival, proliferation and differentiation (Xia et al., 2020). Taken together, β-catenin functions as a mechanical regulator that controls cellular functions important for maintaining stem cell homeostasis.

#### 2.3.1.3 α-catenin

α-Catenin is another key molecule in the AJ, that links to the actin cytoskeleton and the cadherin complex via β-catenin (Niessen & Gottardi, 2008). The association of α-catenin with the actin cytoskeleton, allows it to sense the changes in tissue tension during cytoskeletal contraction. α-Catenin thus acts as a mechanosensor, where it converts mechanical cues into biochemical signals that control cell proliferation and cell death (Yonemura et al., 2010; Sarpal et al., 2019). The Conditional KO of α-catenin in the skin *epidermis* results in abnormal hair morphogenesis, along with defective AJ formation and cell polarity (Vasioukhin et al., 2001). Additionally, the loss of α-catenin from the *epidermis* results in hyperproliferation of the interfollicular *epidermis* (IFE) and the presence of multinucleated cells. This, in turn, leads to a precancerous skin condition with characteristics similar to squamous cell carcinoma. A follow-up study by Vasioukhin's group in 2011 showed that specific deletion of α-catenin from the HFSC compartment led to the development of squamous cell carcinomas. This was due to the direct interaction of the transcriptional co-activator YAP1 with α-catenin. The cKO of α-catenin from the HFSC leads to translocation of YAP to the nucleus, thereby promoting cell proliferation and forming pre-cancerous lesions (Silvis et al., 2011). It was later demonstrated that the interaction of 14-3-3 and the PP2A phosphatase with α-catenin led to the phosphorylation of YAP1, sequestering it to the junctions, and preventing hyperproliferation (Schlegelmilch et al., 2011). This suggested that α-catenin acts not only as a tumor-suppressor, but also as a sensor of cell density in the skin. Knockdown of α-catenin in human embryonic SCs (hESCs) results in the induction of endodermal differentiation due to ubiquitylation and proteolysis of β-catenin. This inhibits repression of Wnt target genes in the transformed cells (Choi et al., 2013). Association of α-catenin with the adenomatous polyposis coli (APC) tumor suppressor, a component of the Wnt/β-catenin pathway, was shown to control the ubiquitination of β-catenin via the APC destruction complex. Therefore, the reduction of α-catenin

levels in hESCs leads to a failure in proteolytic destruction of β-catenin, inducing differentiation of the endoderm. Studies on the process of mechano-sensing of α-catenin have only recently started to be investigated. However, the force-dependent conformational change of α-catenin has been shown to activate proteins that facilitate binding with the dynamic actin cytoskeletal network.

#### 2.3.1.4 p120

p120 catenin is one of the catenins that interacts with E-cadherin at the AJ (Reynolds et al., 1994; Kourtidis et al., 2013). The localization of p120 catenin from the AJ to the cytoplasm upon mechanical stress sensing results in the increased turnover of E-cadherin, which in turn promotes wing development in *Drosophila*, suggesting the importance of p120 as a mechanotransducer at the junctions (Iyer et al., 2019). Several other studies have also described the role of p120 in SC maintenance. During early embryogenesis in mice, p120 null mutant mouse embryonic SCs (mESCs) failed to differentiate completely. The absence of p120 in mESCs leads to the destabilization of E-cadherin at the AJs, causing defective formation of the primitive endoderm (Pieters et al., 2016). A study on mESCs by Pierre D. McCrea's group showed that p120 catenin negatively regulates a repressive transcriptional complex, RE1-silencing transcription factor/co-repressor (REST/coREST), that plays a critical role in stem cell fate determination. Direct binding of p120 to the REST/coREST complex prevented proper differentiation of the mESCs towards neural fate, thereby uncovering a role for p120 in modulating SC differentiation (Lee et al., 2014). p120 catenin acts as a mediator in cellular positioning and organ patterning during fate determination of pancreatic progenitors in mice by regulating the differential expression of E-cadherin. This in turn drives cellular motility and directs cells towards specific niches to determine their cellular fate (Nyeng et al., 2019). Taken together, p120 not only acts as a mediator for E-cadherin function but also plays an important role in lineage commitment. Further studies are required to fully understand how mechanotransduction by p120 regulates the SC niche.

### 2.3.2 Desmosomes

Desmosomes are intercellular cadherin-mediated cell-cell junctions that couples to the intermediate filaments and confer mechanical stability when cells are exposed to tensile and mechanical stress (Figure 1). Specifically, desmosomal cadherins are formed by desmogleins 1-4 and desmocollin 1–3, which bind to armadillo proteins plakoglobin and plakophilins via their cytoplasmic tails and subsequently binds to intermediate filaments via Desmoplakin (Angulo-Urarte et al., 2020). The KO of DSG2 results in peri-implantation lethality and also led to a decrease in embryonic stem cell proliferation (Eshkind et al., 2002). DSG2 was shown to be important for regulating the self-renewal and differentiation capacity of pluripotent stem cells (PSCs). Depletion of DSG2 using monoclonal antibodies in hPSCs resulted in decreased proliferation and reduced expression of pluripotency markers (Park et al., 2018). These results implicate a role of desmosomes in regulating stem cell proliferation and differentiation, however, more work is needed to ascertain how mechanical signals regulate this process. Different compositions of desmosomes lead to a difference in the strength of cell-cell adhesion in different layers of the skin, which in turn, correlates with different levels of proliferation and differentiation. The basal proliferating keratinocytes express desmocollin 2/3 (DSC2/3) and desmoglobin 2/3 (DSG2/3) which displayed the weakest binding out of all the different desmosomal proteins. In contrast, the differentiated cells in the suprabasal layers such as the cornified layer contain a higher composition of DSC1 and DSG1/4, which provided the strongest binding strength. This correlates with the need for differentiated keratinocytes to form strong and stable cell-cell adhesions to maintain a physical barrier that protects the *epidermis* from mechanical and chemical stresses (Harrison et al., 2016; Green et al., 2019). Taken together, studies on desmosomes have begun to shed some light in understanding its role along with other adhesion proteins in maintaining the proliferative capacity of stem cells in its niche. However, more studies are needed to fully understand its role in mechanical transduction and maintaining other stem cell niches.

### 2.3.3 Tight junctions

Tight junction (TJ) proteins are a branching network of intercellular adhesion complexes that controls the permeability of the tissue. TJs are present on epithelial and endothelial cells (Figure 1). In the epithelium, tight junction structures form partitions between the apical and the basolateral domains that prevent the intermixing of both the transmembrane components, thereby supporting cell polarity. TJ proteins are categorized into two groups depending on their functionality: integral transmembrane protein and peripheral membrane proteins or plaque proteins. Four transmembrane proteins namely claudins, occludin, tricellulin and junctional adhesion molecule (JAM) aids in forming tightly regulated networks between the peripheral membrane proteins. On the other hand, peripheral adapter proteins such as zona-occludens 1 (ZO-1), ZO-2 and ZO-3 play a role in connecting the transmembrane proteins to the cytoskeleton and other signaling molecules (Lee et al., 2018). Differences in expression of these TJ proteins play an important role in regulating the barrier integrity of the membrane.

Studies have shown that TJ proteins play an important role in controlling the biological functions of several stem cells. For example, occluding junctions have been shown to play a novel role in regulating the niche of the hematopoietic stem cells when induced with a bacterial infection (Khadilkar et al., 2017). In *Drosophila*, an immune response is triggered upon infection that

leads to barrier breaks due to modulations in the occluding junctions. This in turn helps in prohemocyte differentiation that eventually induced immune cell production, thereby activating the immune response. TJ proteins like occludins, ZO-1, caludins present in human NSCs (hNSCs) are known to help in the formation of hNSC clusters known as neurospheres. The formation of these neurospheres are critical for maintaining the stemness of hNSCs. TJ proteins were downregulated upon induction of differentiation in NSCs, further corroborating the fact that they are important in maintaining the stemness of the NSCs (Watters et al., 2015). This suggests a plausible connection between TJ protein levels and their regulation of the NSC niche. However, further studies are required to establish the direct interaction of NSCs and the TJ protein complex that might play a role in this cluster formation.

# 3 Implication of adhesion molecules in diseases

Several diseases have been linked to changes in the expression or function of various adhesion molecules (Table 1).

## 3.1 Inflammatory bowel disease

One of the roles of the intestinal epithelium is to prevent the exposure of the gastrointestinal tract to foreign antigens and harmful microbiota. This is achieved by the formation of tightly regulated cell junctions and organization of the epithelium to establish a barrier. This epithelial barrier integrity is maintained by the TJ proteins that consist of both transmembrane and peripheral membrane proteins like occludin, zonula occludens and claudins that are linked to the cytoskeleton of the cell (Landy et al., 2016; Chelakkot et al., 2018). Defects in maintaining this barrier function leads to pathological conditions like inflammatory bowel disease (IBD).

IBD is a chronic inflammatory disease that causes severe inflammation of the gastrointestinal tract. The disease is mainly categorized into two types depending on the part of the inflamed intestine: Ulcerative colitis (UC) and Crohn's disease (CD) (Chelakkot et al., 2018; Binienda et al., 2020). The characteristic symptoms of IBD are a leaky gut that is caused by the apoptotic and ulcerative intestinal epithelium, resulting in severe inflammation. Previous studies have shown that over-expression of a TJ protein claudin 2 in UC patients increased pore formation in their epithelium. On the other hand, claudins 3, 4 and 7 which help in tightening the epithelial junctions were found to be reduced in these patients (Prasad et al., 2005; Oshima et al., 2008). This suggested differential expression of several TJ proteins might be a major cause of increased permeability of the intestinal epithelium that leads to defective barrier function. Similarly, in CD, perturbed organization of the TJ proteins was observed in inflamed areas. Several studies showed claudin 2 to also be upregulated in the CD patients with a concomitant downregulation of claudin 3,5,8 (Kucharzik et al., 2001; Zeissig et al., 2007; Das et al., 2012). In addition to TJ proteins, AJ proteins have also been shown to be involved in a relapse of this disease. Downregulation of the E-cadherin-catenin complex led to the loss of cell-cell junctions in the gut that exposed the luminal content to the immune cells thereby increasing the relapse of CD (Wyatt et al., 1993; Arnott et al., 2000).

Treatment options for IBD have substantially improved over the past few decades. Several drugs have been developed to target interleukins (ILs), tumor necrosis factor (TNF) as well as JAK signaling that regulates several cytokines, for treating both the types of IBD. Even though there has been advancement in the drug discovery and delivery process, some patients still do not respond to the drugs and display a relapse of the symptoms. SC based therapy is a promising treatment option that has started to develop. Somatic SCs such as HSCs and MSCs have already been used for treating IBD patients (Shimizu et al., 2019). The HSC transplantation process requires rebooting the immune system by lymph ablation followed by reconstruction of the immune system. A pilot study based on autologous HSC transplantation showed regaining of responsiveness to the drugs as well as sustained remission in about 80% of the patients suffering from refractory CD (López-García et al., 2017). Even though there was an improvement after the transplantation, CD relapsed in most of the patients in a span of 5 years. In addition, severe adverse events occurred in many patients who received HSCT compared to the control group. Taken together, this study suggested HSCT to be one of the methods that can be used for treating patients with severe CD but requires improvement compared to the conventional methods.

Mesenchymal stem cell therapy is another technique that has been used for treating active CD fistula (Misselwitz et al., 2020). MSCs have been reported to show immunosuppressive behavior as well as decreased the effect of the lymphocytes, thereby modulating the immune system (Aggarwal and Pittenger, 2005; Corcione et al., 2006; Ren et al., 2008). Clinical studies have already been conducted using bone marrow derived MSC transplantation (MSCT) as well as adipose derived MSC transplantation (ASCT) (Shimizu et al., 2019). In a phase 2 trial of allogeneic mesenchymal stromal cell transplantation, the Crohn's disease activity index (CDAI) was reduced in patients suffering from luminal CD (Forbes et al., 2014). Almost 53% of the patients had clinical remission within 42 days of receiving the treatment. In this study, only one case of severe adverse effect was reported, which led to the occurrence of stage 1 adenocarcinoma after 3 weeks of the treatment. Even though MSCT seemed better than the HSCT, long term efficacy of this treatment to maintain long-term disease remission needs further investigation. On the other hand, in a phase 3 randomized, double-blind study, ASCT was shown to be

an effective treatment for patients with complex perianal fistula associated with Crohn's disease (Panés et al., 2016). Among the 212 patients randomly divided into treatment and placebo groups, almost 50% of the ASCT treated patients attained remission. Adverse effect cases that included anal abscess and proctalgia were almost similar in number for both the treated and placebo patients. This suggested both ASCT and MSCT to be safer treatment options for IBD patients who failed to respond to conventional treatments.

In 2012, Yui et al. developed intestinal organoid models and transplanted intestinal stem cells (ISC) in mice with colitis (Yui et al., 2012). Based on this study, Ryuichi Okamoto's group is now using ISC transplantation (ISCT) to study this potential treatment method to cure patients with refractory IBD. ISCs have been isolated from patient derived biopsies that are now being tested for therapeutic potential (Shimizu et al., 2019). These cells have the potential to proliferate and reestablish the wound bed in these patients, thereby protecting the organ from mechanical and pathogenic insults. This method is awaiting clinical trials but has the potential to directly cause mucosal healing. In addition to the stem cell-based treatments, given the importance of maintaining barrier function in IBD, identifying the mechanism of the cell-cell junctions regulation might aid in improving these therapeutics.

## 3.2 Epidermolysis bullosa

Epidermolysis bullosa (EB) is a group of rare diseases caused by mutations in genes that encode for both ECM and focal adhesion proteins and is estimated to affect 1 in 30,000 people worldwide (Bruckner et al., 2020). It is characterized by fragile skin and severe blistering and lesions that can occur from as early as childbirth. The most common type of EB is Epidermolysis Bullosa Simplex (EBS), and can be caused by autosomal recessive mutation of the desmoplakin gene in the suprabasal cells or autosomal dominant mutations in the keratin 5/14 genes in the basal cells. Junctional Epidermolysis Bullosa (JEB), which occurs due to an autosomal recessive mutation in an array of ECM and hemidesmosome proteins such as Laminin-332 and α6β4 and BP230 integrin along the basement membrane. Dystrophic Epidermolysis Bullosa (DEB) occurs due to a mutation in Collagen VII, which is localized below the basement membrane (Bruckner-Tuderman, 2019). These molecular mutations impair the structure and functional integrity within highly specialized interfaces of the skin, that are important for cell adhesion, tissue repair and barrier function. Ultimately, this leads to a diminished resistance to mechanical stress and shearing forces, which causes subsequent cell and tissue damage (Uitto and Richard, 2004; Fine et al., 2008; Bruckner-Tuderman et al., 2013).

EB poses as a potentially life-threatening disease as the perpetual and progressive scarring triggered by skin blistering and lesions leads to chronic wounds. These chronic wounds are coupled with increased bacterial colonization, fibrosis, inflammation, and a systemic development of cutaneous squamous cell carcinoma (Guerra et al., 2017). Mutations in the genes are not restricted to the skin but also in other epithelialized (gastrointestinal, urogenital tract, respiratory) or mesenchymal (skeletal muscle) organs (Prodinger et al., 2019). EB with Pyloric atresia in patients affects both the skin and digestive tract, causing severe blistering and also an obstruction of the pylorus (Nakano et al., 2001). There are no direct cures for any of the EB subtypes, and current treatment strategies are only useful in managing the wounds and pain caused by EB. Numerous preclinical research and developments using gene correction, protein replacement and cell-based treatments such as bone marrow transplantation and mesenchymal stem cell therapy have pointed to new therapeutic avenues and have entered early clinical trials.

Stem cells present a promising avenue to reverse some of the damage caused by Recessive Dystrophic Epidermolysis Bullosa (RDEB) and early research in animal models suggest that hematopoietic cell transplantation (HCT) from WT donor-derived cells to RDEB mice improved its survival and skin strength (Tolar et al., 2009). These positive results spurred the development of a small clinical trial involving allogeneic HCT in 6 children with RDEB. Overall, the trial showed promising results as 5 out of 6 of the patients displayed an increase in collagen VII deposition in the Dermal Epidermal Junction (DEJ), improved wounding healing and a decrease in blister formation (Tolar and Wagner, 2013). Additional trials have been conducted with varying outcomes (Petrof et al., 2015; Rashidghamat and McGrath, 2017). Current phase 2 clinical trials include further testing of healthy donor mesenchymal stem cell infusions into EB patients. These developments are promising and provide potentially better therapeutic treatments forEB. (https://clinicaltrials.gov/ct2/show/NCT02582775; https://clinicaltrials.gov/ct2/show/NCT01033552). Additionally, studies from other groups have successfully employed *ex vivo* cell and gene therapy to treat intermediate JEB caused by mutations in Laminin β3. In an initial study, epidermal stem cells from an adult patient affected by Laminin β3 deficient JEB were transduced with a retroviral vector expressing Laminin β3 cDNA encoding functional Laminin β3 and applied to the affected skin area as cohesive epidermal sheets made from a plastic substrate (Mavilio et al., 2006). The study proved to be efficacious during a 6.5 years follow up, where the *epidermis* became fully functional and restored with no adverse reaction (De Rosa et al., 2014). This positive response spurred further testing on a 7-year-old boy in 2015 with EB and epidermal loss in 80% of his body using the same gene therapy to produce functional laminin 332 from transgenic cultured *epidermis* using a fibrin substrate (Hirsch et al., 2017). Similarly, the patient displayed good results after the treatment, with his newly formed

*epidermis* expressing normal levels of laminin 332, displaying a functional basement membrane that remained resistant to mechanical stress and blistering. In the long run, gene therapy to correct mutations causing EB might prove useful. Further scrutiny and hopes can be pinned onto these 2 patients as they continue to undergo observational studies to monitor the efficacy of this treatment method (https://clinicaltrials.gov/ct2/show/NCT05111600).

## 3.3 Breast cancer

Breast cancer is the most common cancer occurring in women globally. Annually, about 1.7 million new cases are recorded in the world (Hai-Ying et al., 2020). The mammary gland is the milk-producing organ in animals, which continuously develops after birth and fully differentiates upon pregnancy and lactation. During postnatal development and onset of reproductive cycles, the mammary gland is dynamically remodeled and undergoes morphological changes due to changes in cell proliferation, differentiation, migration and apoptosis. This inherent plasticity has been suggested to increase the susceptibility of the organ to carcinogenesis (Paavolainen and Peuhu, 2021).

Mechanical signals that cells receive from their surroundings are emerging as key players and contributors to tumor progression (Humphrey et al., 2014; Panciera et al., 2017). These mechanical signals change with the composition of the ECM during mammary development. Tumor progression of mammary cells can be characterized by increased ECM deposition, also known as desmoplasia. Collagen V is increased in desmoplastic stroma in human breast carcinoma (Barsky et al., 1982). Clinically, desmoplastic stroma is associated with a 4–6 fold increased relative risk of developing breast carcinoma, with poor prognosis (Boyd et al., 2001; Guo et al., 2001).

Recent studies have begun to highlight the importance of external mechanical signals that mammary gland cells receive in driving tumorigenesis. Initially, it was shown that primary luminal mammary gland cells were able to form self-renewing colonies in the presence of oncogenic factors such as EGFR and activated HER2 (Panciera et al., 2020). This led to the development of solid organoids composed entirely of K8+ luminal cells which are a hallmark of human HER2+ breast cancer. However, when these cells were plated on a soft adhesive hydrogel of 0.5 kPa which phenocopies the external environment of the normal mammary gland, the presence of the same oncogenic factors were insufficient to develop into self-renewing solid organoids reminiscent in breast cancers. However, when the primary luminal cells were plated on the hydrogels of higher rigidity (40 kPa), the growth of these organoids was observed. Mechanistically, this was shown to be due to the mechanical cues conferred from a stiffer environment, that ultimately led to increased YAP/TAZ signaling and increased proliferation and self-renewal (Panciera et al., 2020). YAP activation also causes remodeling of the surrounding ECM and this favored tumor spreading (Calvo et al., 2013).

Other studies have also begun to highlight the role of various cell adhesion molecules in the development of breast cancer, such as the activation of intracellular FAK (dos Santos et al., 2012; Provenzano and Keely, 2009). In particular, change to a stiffer ECM has been found to correlate with increased FAK activation and increase tumorigenesis in mammary cells. Integrin αvβ3 was also found to be significantly elevated in metastatic tumors compared to primary pancreatic and breast tumors. Mechanistically, this seemed to occur by the recruitment of Src kinase that promotes migration of the cancer cells (Ghajar & Bissell, 2008; Desgrosellier et al., 2010). Studies from multiple groups have described potential therapeutic modalities such as integrin β1 blocking antibodies, since tumors derived from human xenograft models and transgenic models displayed significant growth inhibition upon treatment with an integrin β1 inhibitory antibody (White et al., 2004; Park et al., 2006). As the ECM is increasingly recognized as the master regulator of cell response and behavior, an increase in the knowledge and understanding of the dynamic role that ECM plays in cancer biology, both in terms of its architectural complexity and how this affects the tumor progression in breast cancer, will be valuable. Biomimetic models such as the decellularized ECM recapitulates the complex ECM microenvironment of the mammary glands and can be useful tools to allow a better understanding of cell-ECM interactions. Although these approaches to treating breast cancer are still new, it may shed light on the tumorigenesis of the mammary gland cancer and open new treatment paradigms (Wishart et al., 2020; Tamayo-Angorrilla et al., 2021).

# 4 Discussion, perspectives and future directions

The connection between cells and ECM through FA and the cell to cell junction through AJ, both serve as mechanosensitive hubs. In this review, we have discussed how mechanotransduction through these hubs contribute to maintaining various stem cell niches. Additionally, we have discussed upcoming stem cell-based therapeutics for several diseases which are associated with the adhesion molecules. Another major player involved in the mechanotransduction process is the nucleus and the nuclear envelope (NE), which is gaining importance as mechanosensory organelles. The Linker of Nucleoskeleton and Cytoskeleton (LINC) complexes at the NE, serves as mechanosensory hubs which connects between various cytoskeletal components of the cell (actin, microtubules and intermediate filaments) and nucleoskeletal system of the nucleus (lamins). Specifically, mutations in the lamin A, which is present at the inner nuclear membrane results in various laminopathies such as progeria (Gotzmann and Foisner,

TABLE 1 Diseases associated with cell adhesion molecules.

| Type of cell adhesion molecule | Disease | Mechanism of the disease | Distribution | Therapy |
|---|---|---|---|---|
| Focal adhesion proteins (cell-substratum) | Junctional Epidermolysis Bullosa | Laminin 5, α3β1 integrin and α6β4 integrin | Basement membrane of skin | *ex vivo* cell and gene therapy De Rosa et al. (2014), Hirsch et al. (2017), Mavilio et al. (2006) |
| | Dystrophic Epidermolysis Bullosa | Collagen VII | Below the basement membrane of skin | Hematopoietic cell transplantation (HCT) Petrof et al. (2015), Rashidghamat and McGrath (2017), Tolar and Wagner (2013) (https://clinicaltrials.gov/ct2/show/NCT02582775) (https://clinicaltrials.gov/ct2/show/NCT01033552) |
| | Mammary Gland Cancer | Integrin β1, Collagen V, FAK | Mammary Gland | Targeting signaling pathways in cancer stem cells (CSCs) Yang et al. (2017) Targeting integrin β1 in mice xenograft models Park et al. (2006), White et al. (2004) |
| | Atherosclerosis | Collagen I, III | Heart | MSC therapy: Gorabi et al. (2019), Lin et al. (2020), Zhang et al. (2014) |
| | Osteoporosis | Collagen I | Bone and skeletal | MSC therapy Arjmand et al. (2020), Jiang et al. (2021), Kangari et al. (2020), Pouikli et al. (2021) |
| | Alport Syndrome | Collagen IV | Kidneys (Glomeruli) | Stem cell Therapy: LeBleu et al. (2009) Stem Cell Therapy - Alport Syndrome News |
| | Ullrich congenital muscular dystrophy | Collagen 6α1, α2, α3 | Skeletal muscles | Collagen supplementation: Takenaka-Ninagawa et al. (2021); Yonekawa and Nishino (2015) |
| | Glanzmann thrombasthenia | Integrin α11b3 | Platelets | Hematopoietic stem cell therapy Crone and James (2019), Connor et al. (2008) https://rarediseases.org/rare-diseases/glanzmann-thrombasthenia/ |
| | Leukocyte Adhesion Deficiency 1 | Integrin β2 | Leukocytes (T and B cells) | Hematopoietic stem cell therapy Qasim et al. (2009) |
| | Leukocyte Adhesion Deficiency 3 | Kindlin 3 | Leukocytes (T and B cells) | Hematopoietic stem cell therapy Stepensky et al. (2015) |
| | Fibronectin glomerulopathy | Fibronectin | Kidney | Symptoms are treated currently Ishimoto et al. (2013) |
| | Williams Beuren syndrome | Elastin | Lungs, blood vessels, skin, gastrointestinal, genitourinary | Symptoms are currently treated Duque Lasio & Kozel (2018) |
| | Laminin-α2-related congenital muscular dystrophy (LAMA2-CMD) | Laminin α2 | Muscle | Protein replacement therapy Barraza-Flores et al. (2020) |

(Continued on following page)

TABLE 1 (*Continued*) Diseases associated with cell adhesion molecules.

| Type of cell adhesion molecule | Disease | Mechanism of the disease | Distribution | Therapy |
|---|---|---|---|---|
| Desmosomes (cell-cell junction) | Epidermolysis Bullosa Simplex | Desmoplakin | Intra-epidermal region | Gene therapy<br>Marinkovich and Tang (2019) |
| | Arrhythmogenic cardiomyopathy | Plakophilin-2, Desmoplakin, Desmoglein-2 and Desmocollin-2 | Heart | Stem cell therapy<br>Liu et al. (2021) ,<br>campos de carvalho et al. 2021 |
| Adherens Junction (cell-cell junction) | Oral cancer, Basal cell adenoma (BCA), Mucoepidermoid Carcinoma (MEC), Adenoid Cystic Carcinoma, Colorectal cancer | β-catenin | Oral cancer: Mouth<br>BCA: Skin<br>MEC: Salivary gland<br>Adenoid Cystic Carcinoma: Salivary gland, Head and neck<br>Colorectal cancer: Colon | Stem cell therapy<br>Suma et al. (2015), Baniebrahimi et al. (2020), Shahoumi (2021), Yuan et al. (2021) |
| | Squamous cell carcinoma | α-catenin | Head and Neck, Skin | Stem cell Therapy<br>Affolter et al. (2021), Chen and Wang (2019) |
| | Cardiomyopathy | αE-catenin | Heart muscles | Stem cell therapy:<br>Diaz-Navarro et al. (2021), Jiao et al. (2014), Tripathi et al. (2021) |
| | Hereditary Diffuse Gastric Cancer (HDGC), Breast cancer, Epithelial ovarian cancer | E-cadherin (CDH1) | HDGC: Stomach<br>Breast cancer: Breast<br>Epithelial ovarian cancer: Ovaries | HDGC: Currently, no SC therapies are available<br>Breast cancer: Stem cell Therapy:<br>Khan et al. (2021), Kitamura et al., 2021<br>Epithelial ovarian cancer: Currently, no SC therapies are available |
| | Dilated cardiomyopathy (DCM) and hypertrophic cardiomyopathy (HCM) | Vinculin | Heart | DCM: Stem cell-based therapies<br>Catelain et al. (2013), Diaz-Navarro et al. (2021)<br>Stem cell breakthrough unlocks mysteries associated with inherited heart condition -- ScienceDaily<br>Regenerative Therapy for Cardiomyopathies -PMC (nih.gov)<br>Stem cell therapy<br>Wang et al. (2018)<br>Gene therapy: Vinculin Over expression<br>Kaushik et al. (2015) |
| | Atopic dermatitis | p120 catenin | Cutaneous disorder, skin | Mesenchymal stem cell Therapy:<br>Daltro et al. (2020), Guan et al. (2022)<br>www.sciencedaily.com/releases/2016/06/160607080935.htm |
| Tight Junctions (cell-cell junctions) | Inflammatory bowel disease (IBD) | Claudins 2, 3,4 5,7,8 | Intestine | Stem cell therapy<br>Sawada (2013); Shimizu et al. (2019) |
| | Congenital deafness | Claudin 14 and Claudin 11 | Ears | IPSC based therapy:<br>He et al. (2021), Peng et al. (2014) |
| | Multiple Sclerosis | Claudin 11 | Central nervous system | Currently, no SC therapies are available |

2006), and muscular dystrophies which affects the functions of stem cell pools such as MSCs and muscle stem cells respectively (Favreau et al., 2004; Frock et al., 2006).

While several studies have highlighted the importance of these molecules and their involvement in a plethora of human diseases, there are very few studies that directly correlate mechanical signaling and disease progression. It is therefore crucial to bridge this gap in order to identify new therapeutic interventions that will increase clinical success in treating these diseases. The role of mechanotransduction in the field of regenerative medicine is starting to gain importance. Beyond regenerative medicine, the implication of microenvironmental factors that regulates both mechanical and biochemical signaling to improve the disease outcome remains largely unexplored and opens up an exciting domain of research.

## Author contributions

This review was conceptualised by RL, AB, RB, AC and SR. This was written by RL, AB, RB, AC and SR. The figure was put together by RL, AB and RB and these 3 authors contributed equally.

## Funding

The Raghavan Lab at ASRL is funded through the AMBM Grant A18A8b0059 and ASRL Core funds.

## Conflict of interest

The authors declare that the research was conducted in the absence of any commercial or financial relationships that could be construed as a potential conflict of interest.

## Publisher's note



## References

Aaron, B. B., and Gosline, J. M. (1981). Elastin as a random-network elastomer: A mechanical and optical analysis of single elastin fibers. *Biopolymers* 20, 1247–1260. doi:10.1002/bip.1981.360200611

Adams, J. C., Chiquet-Ehrismann, R., and Tucker, R. P. (2015). The evolution of tenascins and fibronectin. *Cell. adh. Migr.* 9, 22–33. doi:10.4161/19336918.2014.970030

Affolter, A., Lammert, A., Kern, J., Scherl, C., and Rotter, N. (2021). Precision medicine gains momentum: Novel 3D models and stem cell-based approaches in head and neck cancer. *Front. Cell. Dev. Biol.* 9, 666515. doi:10.3389/fcell.2021.666515

Aggarwal, S., and Pittenger, M. F. (2005). Human mesenchymal stem cells modulate allogeneic immune cell responses. *Blood* 105, 1815–1822. doi:10.1182/blood-2004-04-1559

Akhir, H. M., and Teoh, P. L. (2020). Collagen type I promotes osteogenic differentiation of amniotic membrane-derived mesenchymal stromal cells in basal and induction media. *Biosci. Rep.* 40, BSR20201325. doi:10.1042/BSR20201325

Akhmanova, M., Osidak, E., Domogatsky, S., Rodin, S., and Domogatskaya, A. (2015). Physical, spatial, and molecular aspects of extracellular matrix of *in vivo* niches and artificial scaffolds relevant to stem cells research. *Stem Cells Int.*, 167025. doi:10.1155/2015/167025

Alberts, B., Johnson, A., and Lewis, J. (2002). "Molecular biology of the cell," in *The self-assembly and dynamic structure of cytoskeletal filaments*. 4th edition (New York: Garland Science).

Angulo-Urarte, A., van der Wal, T., and Huveneers, S. (2020). Cell-cell junctions as sensors and transducers of mechanical forces. *Biochim. Biophys. Acta. Biomembr.* 1862, 183316. doi:10.1016/j.bbamem.2020.183316

Arjmand, B., Sarvari, M., Alavi-Moghadam, S., Payab, M., Goodarzi, P., Gilany, K., et al. (2020). Prospect of stem cell therapy and regenerative medicine in osteoporosis. *Front. Endocrinol.* 11, 430. doi:10.3389/fendo.2020.00430

Armony, G., Jacob, E., Moran, T., Levin, Y., Mehlman, T., Levy, Y., et al. (2016). Cross-linking reveals laminin coiled-coil architecture. *Proc. Natl. Acad. Sci. U. S. A.* 113, 13384–13389. doi:10.1073/pnas.1608424113

Arnaout, M. A., Goodman, S. L., and Xiong, J. P. (2007). Structure and mechanics of integrin-based cell adhesion. *Curr. Opin. Cell. Biol.* 19, 495–507. doi:10.1016/j.ceb.2007.08.002

Arnott, I. D. R., Kingstone, K., and Ghosh, S. (2000). Abnormal intestinal permeability predicts relapse in inactive Crohn disease. *Scand. J. Gastroenterol.* 35, 1163–1169. doi:10.1080/003655200750056637

Arulmoli, J., Pathak, M. M., McDonnell, L. P., Nourse, J. L., Tombola, F., Earthman, J. C., et al. (2015). Static stretch affects neural stem cell differentiation in an extracellular matrix-dependent manner. *Sci. Rep.* 5, 8499. doi:10.1038/srep08499

Aumailley, M., Bruckner-Tuderman, L., Carter, W. G., Deutzmann, R., Edgar, D., Ekblom, P., et al. (2005). A simplified laminin nomenclature. *Matrix Biol.* 24, 326–332. doi:10.1016/j.matbio.2005.05.006

Baniebrahimi, G., Mir, F., and Khanmohammadi, R. (2020). Cancer stem cells and oral cancer: Insights into molecular mechanisms and therapeutic approaches. *Cancer Cell. Int.* 20, 113. doi:10.1186/s12935-020-01192-0

Barraza-Flores, P., Hermann, H. J., Bates, C. R., Allen, T. G., Grunert, T. T., and Burkin, D. J. (2020). Human laminin-111 and laminin-211 protein therapy prevents muscle disease progression in an immunodeficient mouse model of LAMA2-CMD. *Skelet. Muscle* 10, 18. doi:10.1186/s13395-020-00235-4

Barsky, S. H., Rao, C. N., Grotendorst, G. R., and Liotta, L. A. (1982). Increased content of type V collagen in desmoplasia of human breast carcinoma. *Am. J. Pathology*.

Beck, K., Hunter, I., and Engel, J. (1990). Structure and function of laminin: Anatomy of a multidomain glycoprotein. *FASEB J.* 4, 148–160. doi:10.1096/fasebj.4.2.2404817

Benham-Pyle, B. W., Pruitt, B. L., and Nelson, W. J. (2015). Cell adhesion. Mechanical strain induces E-cadherin-dependent Yap1 and β-catenin activation to drive cell cycle entry. *Science* 348, 1024–1027. doi:10.1126/science.aaa4559

Benham-Pyle, B. W., Sim, J. Y., Hart, K. C., Pruitt, B. L., and Nelson, W. J. (2016). Increasing β-catenin/Wnt3A activity levels drive mechanical strain-induced cell cycle progression through mitosis. *ELife* 5, e19799. doi:10.7554/eLife.19799

Benoit, Y. D., Groulx, J.-F., Gagné, D., and Beaulieu, J.-F. (2012). RGD-dependent epithelial cell-matrix interactions in the human intestinal crypt. *J. Signal Transduct.*, 248759. doi:10.1155/2012/248759

Binienda, A., Ziolkowska, S., Hauge, I. H., and Salaga, M. (2020). The role of immune and epithelial stem cells in inflammatory bowel disease therapy. *Curr. Drug Targets* 21, 1405–1416. doi:10.2174/1389450121666200504074922

Biswas, R., Banerjee, A., Lembo, S., Zhao, Z., Lakshmanan, V., Lim, R., et al. (2021). Mechanical instability of adherens junctions overrides intrinsic quiescence of hair follicle stem cells. *Dev. Cell.* 56, 761–780.e7. doi:10.1016/j.devcel.2021.02.020

Boyd, N. F., Martin, L. J., Stone, J., Greenberg, C., Minkin, S., and Yaffe, M. J. (2001). Mammographic densities as a marker of human breast cancer risk and their use in chemoprevention. *Curr. Oncol. Rep.* 3, 314–321. doi:10.1007/s11912-001-0083-7

Breitkreutz, D., Koxholt, I., Thiemann, K., and Nischt, R. (2013). Skin basement membrane: The foundation of epidermal integrity - BM functions and diverse roles of bridging molecules nidogen and perlecan. *Biomed. Res. Int.*, 179784. doi:10.1155/2013/179784

Brenner, C. A., Adler, R. R., Rappolee, D. A., Pedersen, R. A., and Werb, Z. (1989). Genes for extracellular-matrix-degrading metalloproteinases and their inhibitor, TIMP, are expressed during early mammalian development. *Genes and Development* 3, 848–859. doi:10.1101/gad.3.6.848

Brinckmann, J. (2005). Collagens at a glance. *Top. Curr. Chem. (Cham).* 2005, 1–6. doi:10.1007/b103817

Bruckner, A. L., Losow, M., Wisk, J., Patel, N., Reha, A., Lagast, H., et al. (2020). The challenges of living with and managing epidermolysis bullosa: Insights from patients and caregivers. *Orphanet J. Rare Dis.* 15, 1. doi:10.1186/s13023-019-1279-y

Bruckner-Tuderman, L., Mcgrath, J. A., Robinson, E. C., and Uitto, J. (2013). Progress in epidermolysis Bullosa research: Summary of DEBRA international research conference 2012. *J. Invest. Dermatol.* 133, 2121–2126. doi:10.1038/jid.2013.127

Bruckner-Tuderman, L. (2019). Newer treatment modalities in epidermolysis bullosa. *Indian dermatol. Online J.* 10, 244–250. doi:10.4103/idoj.idoj_287_18

Bruckner-Tuderman, L., Schynder, U. W., Winterhalter, K. H., and Bruckner, P. (1987). Tissue form of type VII collagen from human skin and dermal fibroblasts in culture. *Eur. J. Biochem.* 165 (3), 607–611. doi:10.1111/j.1432-1033.1987.tb11483.x

Caiazzo, M., Okawa, Y., Ranga, A., Piersigilli, A., Tabata, Y., and Lutolf, M. P. (2016). Defined three-dimensional microenvironments boost induction of pluripotency. *Nat. Mat.* 15, 344–352. doi:10.1038/nmat4536

Calalb, M. B., Polte, T. R., and Hanks, S. K. (1995). Tyrosine phosphorylation of focal adhesion kinase at sites in the catalytic domain regulates kinase activity: A role for src family kinases. *Mol. Cell. Biol.* 15, 954–963. doi:10.1128/mcb.15.2.954

Calvo, F., Ege, N., Grande-Garcia, A., Hooper, S., Jenkins, R. P., Chaudhry, S. I., et al. (2013). Mechanotransduction and YAP-dependent matrix remodelling is required for the generation and maintenance of cancer-associated fibroblasts. *Nat. Cell. Biol.* 15, 637–646. doi:10.1038/ncb2756

Campos de Carvalho, A. C., Kasai-Brunswick, T. H., and Bastos Carvalho, A. (2021). Cell-Based therapies for heart failure. *Front. Pharmacol.* 12, 641116. doi:10.3389/fphar.2021.641116

Catelain, C., Riveron, S., Papadopoulos, A., Mougenot, N., Jacquet, A., Vauchez, K., et al. (2013). Myoblasts and embryonic stem cells differentially engraft in a mouse model of genetic dilated cardiomyopathy. *Mol. Ther.* 21, 1064–1075. doi:10.1038/mt.2013.15

Chacón-Martínez, C. A., Koester, J., and Wickström, S. A. (2018). Signaling in the stem cell niche: Regulating cell fate, function and plasticity. *Development* 145, dev165399. doi:10.1242/dev.165399

Chelakkot, C., Ghim, J., and Ryu, S. H. (2018). Mechanisms regulating intestinal barrier integrity and its pathological implications. *Exp. Mol. Med.* 50, 1–9. doi:10.1038/s12276-018-0126-x

Chen, C. S., and Ingber, D. E. (1999). Tensegrity and mechanoregulation: From skeleton to cytoskeleton. *Osteoarthr. Cartil.* 7, 81–94. doi:10.1053/joca.1998.0164

Chen, D., and Wang, C.-Y. (2019). Targeting cancer stem cells in squamous cell carcinoma. *Precis. Clin. Med.* 2, 152–165. doi:10.1093/pcmedi/pbz016

Chen, S., Lewallen, M., and Xie, T. (2013). Adhesion in the stem cell niche: Biological roles and regulation. *Dev. Camb.* 140, 255–265. doi:10.1242/dev.083139

Chen, X. D., Dusevich, V., Feng, J. Q., Manolagas, S. C., and Jilka, R. L. (2007). Extracellular matrix made by bone marrow cells facilitates expansion of marrow-derived mesenchymal progenitor cells and prevents their differentiation into osteoblasts. *J. Bone Min. Res.* 22, 1943–1956. doi:10.1359/jbmr.070725

Chen, Z. L., Indyk, J. A., and Strickland, S. (2003). The hippocampal laminin matrix is dynamic and critical for neuronal survival. *Mol. Biol. Cell.* 14, 2665–2676. doi:10.1091/mbc.E02-12-0832

Chinthalapudi, K., Rangarajan, E. S., and Izard, T. (2018). The interaction of talin with the cell membrane is essential for integrin activation and focal adhesion formation. *Proc. Natl. Acad. Sci. U. S. A.* 115, 10339–10344. doi:10.1073/pnas.1806275115

Choi, H. R., Nam, K. M., Park, S. J., Kim, D. S., Huh, C. H., Park, W. Y., et al. (2014). Suppression of miR135b increases the proliferative potential of normal human keratinocytes. *J. Invest. Dermatol.* 134, 1161–1164. doi:10.1038/jid.2013.427

Choi, S. H., Estarás, C., Moresco, J. J., Yates, J. R., and Jones, K. A. (2013). α-Catenin interacts with APC to regulate β-catenin proteolysis and transcriptional repression of Wnt target genes. *Genes. Dev.* 27, 2473–2488. doi:10.1101/gad.229062.113

Chowdhury, F., Na, S., Li, D., Poh, Y. C., Tanaka, T. S., Wang, F., et al. (2010). Material properties of the cell dictate stress-induced spreading and differentiation in embryonic stemcells. *Nat. Mat.* 9, 82–88. doi:10.1038/nmat2563

Chung, C. Y., and Erickson, H. P. (1997). Glycosaminoglycans modulate fibronectin matrix assembly and are essential for matrix incorporation of tenascin-C. *J. Cell. Sci.* 110 ( Pt 12), 1413–1419. doi:10.1242/jcs.110.12.1413

Connor, P., Khair, K., Liesner, R., Amrolia, P., Veys, P., Ancliff, P., et al. (2008). Stem cell transplantation for children with Glanzmann thrombasthenia. *Br. J. Haematol.* 140, 568–571. doi:10.1111/j.1365-2141.2007.06890.x

Corcione, A., Benvenuto, F., Ferretti, E., Giunti, D., Cappiello, V., Cazzanti, F., et al. (2006). Human mesenchymal stem cells modulate B-cell functions. *Blood* 107, 367–372. doi:10.1182/blood-2005-07-2657

Cram, E. J., Clark, S. G., and Schwarzbauer, J. E. (2003). Talin loss-of-function uncovers roles in cell contractility and migration in *C. elegans*. *J. Cell. Sci.* 116, 3871–3878. doi:10.1242/jcs.00705

Crone, C., and James, B. (2019). Haemopoietic stem cell transplantation is a curative treatment option with minimal transplant-related complications for patients with severe Glanzmann's thrombasthenia. *Clin. Med. N.* 19, s34. doi:10.7861/clinmedicine.19-2-s34

Daltro, S. R. T., Meira, C. S., Santos, I. P., Ribeiro dos Santos, R., and Soares, M. B. P. (2020). Mesenchymal stem cells and atopic dermatitis: A review. *Front. Cell. Dev. Biol.* 8, 326. doi:10.3389/fcell.2020.00326

Das, P., Goswami, P., Das, T. K., Nag, T., Sreenivas, V., Ahuja, V., et al. (2012). Comparative tight junction protein expressions in colonic crohn's disease, ulcerative colitis, and tuberculosis: A new perspective. *Virchows Arch.* 460, 261–270. doi:10.1007/s00428-012-1195-1

De Rosa, L., Carulli, S., Cocchiarella, F., Quaglino, D., Enzo, E., Franchini, E., et al. (2014). Long-term stability and safety of transgenic cultured epidermal stem cells in gene therapy of junctional epidermolysis bullosa. *Stem Cell. Rep.* 2, 1–8. doi:10.1016/j.stemcr.2013.11.001

Desgrosellier, J. S., Seguin, L., Barnes, L. A., Shields, D. J., Huang, M., Lau, S. K., et al. (2010). Abstract 3841: An integrin αvβ3/c-Src oncogenic unit promotes anchorage independence and tumor progression. *Cancer Res.* 70, 3841. doi:10.1158/1538-7445.am10-3841

Diaz-Navarro, R., Urrútia, G., Cleland, J. G. F., Poloni, D., Villagran, F., Acosta-Dighero, R., et al. (2021). Stem cell therapy for dilated cardiomyopathy. *Cochrane Database Syst. Rev.* 7, CD013433. doi:10.1002/14651858.CD013433.pub2

Dietrich, C., Scherwat, J., Faust, D., and Oesch, F. (2002). Subcellular localization of β-catenin is regulated by cell density. *Biochem. Biophys. Res. Commun.* 292 (1), 195–199. doi:10.1006/BBRC.2002.6625

Discher, D. E., Janmey, P., and Wang, Y. L. (2005). Tissue cells feel and respond to the stiffness of their substrate. *Science* 310, 1139–1143. doi:10.1126/science.1116995

Domogatskaya, A., Rodin, S., and Tryggvason, K. (2012). Functional diversity of laminins. *Annu. Rev. Cell. Dev. Biol.* 28, 523–553. doi:10.1146/annurev-cellbio-101011-155750

dos Santos, P. B., Zanetti, J. S., Ribeiro-Silva, A., and Beltrão, E. I. C. (2012). Beta 1 integrin predicts survival in breast cancer: A clinicopathological and immunohistochemical study. *Diagn. Pathol.* 7, 104. doi:10.1186/1746-1596-7-104

Du, J., Zu, Y., Li, J., Du, S., Xu, Y., Zhang, L., et al. (2016). Extracellular matrix stiffness dictates Wnt expression through integrin pathway. *Sci. Rep.* 6, 20395. doi:10.1038/srep20395

Dupont, S., Morsut, L., Aragona, M., Enzo, E., Giulitti, S., Cordenonsi, M., et al. (2011). Role of YAP/TAZ in mechanotransduction. *Nature* 474, 179–183. doi:10.1038/nature10137

Duque Lasio, M. L., and Kozel, B. A. (2018). Elastin-driven genetic diseases. *Matrix Biol.* 71-72, 144–160. doi:10.1016/j.matbio.2018.02.021

Engler, A. J., Griffin, M. A., Sen, S., Bönnemann, C. G., Sweeney, H. L., and Discher, D. E. (2004). Myotubes differentiate optimally on substrates with tissue-like stiffness: Pathological implications for soft or stiff microenvironments. *J. Cell. Biol.* 166, 877–887. doi:10.1083/jcb.200405004

Engler, A. J., Sen, S., Sweeney, H. L., and Discher, D. E. (2006). Matrix elasticity directs stem cell lineage specification. *Cell.* 126, 677–689. doi:10.1016/j.cell.2006.06.044

Eshkind, L., Tian, Q., Schmidt, A., Franke, W. W., Windoffer, R., and Leube, R. E. (2002). Loss of desmoglein 2 suggests essential functions for early embryonic development and proliferation of embryonal stem cells. *Eur. J. Cell. Biol.* 81, 592–598. doi:10.1078/0171-9335-00278

Evans, M. J., and Kaufman, M. H. (1981). Establishment in culture of pluripotential cells from mouse embryos. *Nature* 292, 154–156. doi:10.1038/292154a0

Even-Ram, S., Artym, V., and Yamada, K. M. (2006). Matrix control of stem cell fate. *Cell.* 126, 645–647. doi:10.1016/j.cell.2006.08.008

Fan, Y., and Meyer, T. (2021). Molecular control of cell density-mediated exit to quiescence. *Cell. Rep.* 36, 109436. doi:10.1016/j.celrep.2021.109436

Farge, E. (2003). Mechanical induction of Twist in the Drosophila foregut/stomodeal primordium. *Curr. Biol.* 13, 1365–1377. doi:10.1016/S0960-9822(03)00576-1

Farrukh, A., Ortega, F., Fan, W., Marichal, N., Paez, J. I., Berninger, B., et al. (2017). Bifunctional hydrogels containing the laminin motif IKVAV promote neurogenesis. *Stem Cell. Rep.* 9, 1432–1440. doi:10.1016/j.stemcr.2017.09.002

Favreau, C., Higuet, D., Courvalin, J.-C., and Buendia, B. (2004). Expression of a mutant lamin A that causes emery-dreifuss muscular dystrophy inhibits in vitro differentiation of C2C12 myoblasts. *Mol. Cell. Biol.* 24, 1481–1492. doi:10.1128/mcb.24.4.1481-1492.2004

Fine, J. D., Eady, R. A. J., Bauer, E. A., Bauer, J. W., Bruckner-Tuderman, L., Heagerty, A., et al. (2008). The classification of inherited epidermolysis bullosa (EB): Report of the third international consensus meeting on diagnosis and classification of EB. *J. Am. Acad. Dermatol.* 58, 931–950. doi:10.1016/j.jaad.2008.02.004

Forbes, G. M., Sturm, M. J., Leong, R. W., Sparrow, M. P., Segarajasingam, D., Cummins, A. G., et al. (2014). A phase 2 study of allogeneic mesenchymal stromal cells for luminal crohn's disease refractory to biologic therapy. *Clin. Gastroenterol. Hepatol.* 12, 64–71. doi:10.1016/j.cgh.2013.06.021

Frock, R. L., Kudlow, B. A., Evans, A. M., Jameson, S. A., Hauschka, S. D., and Kennedy, B. K. (2006). Lamin A/C and emerin are critical for skeletal muscle satellite cell differentiation. *Genes. Dev.* 20, 486–500. doi:10.1101/gad.1364906

Früh, S. M., Schoen, I., Ries, J., and Vogel, V. (2015). Molecular architecture of native fibronectin fibrils. *Nat. Commun.* 6, 7275. doi:10.1038/ncomms8275

Galante, L. L., and Schwarzbauer, J. E. (2007). Requirements for sulfate transport and the diastrophic dysplasia sulfate transporter in fibronectin matrix assembly. *J. Cell. Biol.* 179, 999–1009. doi:10.1083/jcb.200707150

Gandavarapu, N. R., Alge, D. L., and Anseth, K. S. (2014). Osteogenic differentiation of human mesenchymal stem cells on α5 integrin binding peptide hydrogels is dependent on substrate elasticity. *Biomater. Sci.* 2, 352–361. doi:10.1039/c3bm60149h

Gangaraju, V. K., and Lin, H. (2009). MicroRNAs: Key regulators of stem cells. *Nat. Rev. Mol. Cell. Biol.* 10, 116–125. doi:10.1038/nrm2621

Gattazzo, F., Urciuolo, A., and Bonaldo, P. (2014). Extracellular matrix: A dynamic microenvironment for stem cell niche. *Biochim. Biophys. Acta* 1840, 2506–2519. doi:10.1016/j.bbagen.2014.01.010

Gee, E. P. S., Ingber, D. E., and Stultz, C. M. (2008). Fibronectin unfolding revisited: Modeling cell traction-mediated unfolding of the tenth type-III repeat. *PLoS ONE* 3, e2373. doi:10.1371/journal.pone.0002373

Georgiadou, M., Lilja, J., Jacquemet, G., Guzmán, C., Rafaeva, M., Alibert, C., et al. (2017). AMPK negatively regulates tensin-dependent integrin activity. *J. Cell. Biol.* 216, 1107–1121. doi:10.1083/jcb.201609066

Ghajar, C. M., and Bissell, M. J. (2008). Extracellular matrix control of mammary gland morphogenesis and tumorigenesis: Insights from imaging. *Histochem. Cell. Biol.* 130, 1105–1118. doi:10.1007/s00418-008-0537-1

Gilbert, P. M., Havenstrite, K. L., Magnusson, K. E. G., Sacco, A., Leonardi, N. A., Kraft, P., et al. (2010). Substrate elasticity regulates skeletal muscle stem cell self-renewal in culture. *Science* 329, 1078–1081. doi:10.1126/science.1191035

Glenney, J. R., and Zokas, L. (1989). Novel tyrosine kinase substrates from Rous sarcoma virus-transformed cells are present in the membrane skeleton. *J. Cell. Biol.* 108, 2401–2408. doi:10.1083/jcb.108.6.2401

Goodman, S. R. (2021). Cell adhesion and the extracellular matrix. *Goodman's Med. Cell. Biol.*. doi:10.1016/b978-0-12-817927-7.00007-7

Gorabi, A. M., Banach, M., Reiner, Ž., Pirro, M., Hajighasemi, S., Johnston, T. P., et al. (2019). The role of mesenchymal stem cells in atherosclerosis: Prospects for therapy via the modulation of inflammatory milieu. *J. Clin. Med.* 8, E1413. doi:10.3390/jcm8091413

Gotzmann, J., and Foisner, R. (2006). A-Type lamin complexes and regenerative potential: A step towards understanding laminopathic diseases? *Histochem. Cell. Biol.* 125, 33–41. doi:10.1007/s00418-005-0050-8

Green, K. J., Jaiganesh, A., and Broussard, J. A. (2019). Desmosomes: Essential contributors to an integrated intercellular junction network. *F1000Res.* 8, F1000. doi:10.12688/f1000research.20942.1

Groulx, J. F., Gagné, D., Benoit, Y. D., Martel, D., Basora, N., and Beaulieu, J. F. (2011). Collagen VI is a basement membrane component that regulates epithelial cell-fibronectin interactions. *Matrix Biol.* 30, 195–206. doi:10.1016/j.matbio.2011.03.002

Guan, J., Li, Y., Lu, F., and Feng, J. (2022). Adipose-derived stem cells ameliorate atopic dermatitis by suppressing the IL-17 expression of Th17 cells in an ovalbumin-induced mouse model. *Stem Cell. Res. Ther.* 13, 98. doi:10.1186/s13287-022-02774-7

Guerra, L., Odorisio, T., Zambruno, G., and Castiglia, D. (2017). Stromal microenvironment in type VII collagen-deficient skin: The ground for squamous cell carcinoma development. *Matrix Biol.* 63, 1–10. doi:10.1016/j.matbio.2017.01.002

Guo, L., Cai, T., Chen, K., Wang, R., Wang, J., Cui, C., et al. (2018). Kindlin-2 regulates mesenchymal stem cell differentiation through control of YAP1/TAZ. *J. Cell. Biol.* 217, 1431–1451. doi:10.1083/jcb.201612177

Guo, Y. P., Martin, L. J., Hanna, W., Banerjee, D., Miller, N., Fishell, E., et al. (2001). Growth factors and stromal matrix proteins associated with mammographic densities. *Cancer Epidemiol. Biomarkers Prev.*.

Haeckel, E. (1868). Natürliche schöpfungsgeschichte: Gemeinverständliche wissenschaftliche - ernst haeckel - google books. Available at: https://books.google.co.in/books?hl=en&lr=&id=Kh4fdEy0OWYC&oi=fnd&pg=PA1&ots=hRgBU1dzQy&sig=uujYiG2vSGZkjHgaWh_p1KMuOdI&redir_esc=y#v=onepage&q&f=false.

Hai-Ying, C., Tanaka, Y., Hifumi, T., Shoji, K., Kayesh, M. E. H., Hashem, M. A., et al. (2020). Pathological and genetic aspects of spontaneous mammary gland tumor in Tupaia belangeri (tree shrew). *PLoS ONE* 15, e0233232. doi:10.1371/journal.pone.0233232

Hamidouche, Z., Fromigué, O., Ringe, J., Häupl, T., Vaudin, P., Pagès, J. C., et al. (2009). Priming integrin alpha5 promotes human mesenchymal stromal cell osteoblast differentiation and osteogenesis. *Proc. Natl. Acad. Sci. U. S. A.* 106, 18587–18591. doi:10.1073/pnas.0812334106

Hamill, K. J., Kligys, K., Hopkinson, S. B., and Jones, J. C. R. (2009). Laminin deposition in the extracellular matrix: A complex picture emerges. *J. Cell. Sci.* 122, 4409–4417. doi:10.1242/jcs.041095

Handorf, A. M., Zhou, Y., Halanski, M. A., and Li, W. J. (2015). Tissue stiffness dictates development, homeostasis, and disease progression. *Organogenesis* 11, 1–15. doi:10.1080/15476278.2015.1019687

Harrison, O. J., Brasch, J., Lasso, G., Katsamba, P. S., Ahlsen, G., Honig, B., et al. (2016). Structural basis of adhesive binding by desmocollins and desmogleins. *Proc. Natl. Acad. Sci. U. S. A.* 113, 7160–7165. doi:10.1073/pnas.1606272113

Hayashi, Y., Furue, M. K., Okamoto, T., Ohnuma, K., Myoishi, Y., Fukuhara, Y., et al. (2007). Integrins regulate mouse embryonic stem cell self-renewal. *Stem Cells* 25, 3005–3015. doi:10.1634/stemcells.2007-0103

He, Z., Ding, Y., Mu, Y., Xu, X., Kong, W., Chai, R., et al. (2021). Stem cell-based therapies in hearing loss. *Front. Cell. Dev. Biol.* 9, 730042. doi:10.3389/fcell.2021.730042

Hirsch, T., Rothoeft, T., Teig, N., Bauer, J. W., Pellegrini, G., De Rosa, L., et al. (2017). Regeneration of the entire human epidermis using transgenic stem cells. *Nature* 551, 327–332. doi:10.1038/nature24487

Holle, A. W., Tang, X., Vijayraghavan, D., Vincent, L. G., Fuhrmann, A., Choi, Y. S., et al. (2013). *In situ* mechanotransduction via vinculin regulates stem cell differentiation. *Stem Cells* 31, 2467–2477. doi:10.1002/stem.1490

Holst, J., Watson, S., Lord, M. S., Eamegdool, S. S., Bax, D. V., Nivison-Smith, L. B., et al. (2010). Substrate elasticity provides mechanical signals for the expansion of hemopoietic stem and progenitor cells. *Nat. Biotechnol.* 28, 1123–1128. doi:10.1038/nbt.1687

Humphrey, J. D., Dufresne, E. R., and Schwartz, M. A. (2014). Mechanotransduction and extracellular matrix homeostasis. *Nat. Rev. Mol. Cell. Biol.* 15, 802–812. doi:10.1038/nrm3896

Hynes, R. O. (1986). Fibronectins. *Sci. Am.* 254, 42–51. doi:10.1038/scientificamerican0686-42

Hynes, R. O. (2002). Integrins: Bidirectional, allosteric signaling machines. *Cell.* 110, 673–687. doi:10.1016/S0092-8674(02)00971-6

Hynes, R. O. (1992). Integrins: Versatility, modulation, and signaling in cell adhesion. *Cell.* 69, 11–25. doi:10.1016/0092-8674(92)90115-S

Hynes, R. O. (2009). The extracellular matrix: Not just pretty fibrils. *Science* 326, 1216–1219. doi:10.1126/science.1176009

Ingber, D. E. (2006). Cellular mechanotransduction: Putting all the pieces together again. *FASEB J.* 20, 811–827. doi:10.1096/fj.05-5424rev

Ingber, D. E. (2003). Tensegrity I. Cell structure and hierarchical systems biology. *J. Cell. Sci.* 116, 1157–1173. doi:10.1242/jcs.00359

Iorio, V., Troughton, L. D., and Hamill, K. J. (2015). Laminins: Roles and utility in wound repair. *Adv. Wound Care* 4, 250–263. doi:10.1089/wound.2014.0533

Ishimoto, I., Sohara, E., Ito, E., Okado, T., Rai, T., and Uchida, S. (2013). Fibronectin glomerulopathy. *Clin. Kidney J.* 6, 513–515. doi:10.1093/ckj/sft097

Iyer, K. V., Piscitello-Gómez, R., Paijmans, J., Jülicher, F., and Eaton, S. (2019). Epithelial viscoelasticity is regulated by mechanosensitive E-cadherin turnover. *Curr. Biol.* 29, 578–591.e5. doi:10.1016/j.cub.2019.01.021

Jaalouk, D. E., and Lammerding, J. (2009). Mechanotransduction gone awry. *Nat. Rev. Mol. Cell. Biol.* 10, 63–73. doi:10.1038/nrm2597

Jabłońska-Trypuć, A., Matejczyk, M., and Rosochacki, S. (2016). Matrix metalloproteinases (MMPs), the main extracellular matrix (ECM) enzymes in collagen degradation, as a target for anticancer drugs. *J. Enzyme Inhib. Med. Chem.* 31, 177–183. doi:10.3109/14756366.2016.1161620

Jansen, J. H. W., Eijken, M., Jahr, H., Chiba, H., Verhaar, J. A. N., Van Leeuwen, J. P. T. M., et al. (2010). Stretch-induced inhibition of Wnt/beta-catenin signaling in mineralizing osteoblasts. *J. Orthop. Res.* 28, 390–396. doi:10.1002/jor.20991

Jansen, K. A., Atherton, P., and Ballestrem, C. (2017). Mechanotransduction at the cell-matrix interface. *Semin. Cell. Dev. Biol.* 71, 75–83. doi:10.1016/j.semcdb.2017.07.027

Jansen, K. A., Donato, D. M., Balcioglu, H. E., Schmidt, T., Danen, E. H. J., and Koenderink, G. H. (2015). A guide to mechanobiology: Where biology and physics meet. *Biochim. Biophys. Acta* 1853, 3043–3052. doi:10.1016/j.bbamcr.2015.05.007

Jiang, Y., Zhang, P., Zhang, X., Lv, L., and Zhou, Y. (2021). Advances in mesenchymal stem cell transplantation for the treatment of osteoporosis. *Cell. Prolif.* 54, e12956. doi:10.1111/cpr.12956

Jiao, R., Liu, Y., Yang, W. J., Zhu, X. Y., Li, J., and Tang, Q. Z. (2014). Effects of stem cell therapy on dilated cardiomyopathy. *Saudi Med. J.* 35, 1463–1468.

Kanchanawong, P., Shtengel, G., Pasapera, A. M., Ramko, E. B., Davidson, M. W., Hess, H. F., et al. (2010). Nanoscale architecture of integrin-based cell adhesions. *Nature* 468, 580–584. doi:10.1038/nature09621

Kangari, P., Talaei-Khozani, T., Razeghian-Jahromi, I., and Razmkhah, M. (2020). Mesenchymal stem cells: Amazing remedies for bone and cartilage defects. *Stem Cell. Res. Ther.* 11, 492. doi:10.1186/s13287-020-02001-1

Karpowicz, P., Willaime-Morawek, S., Balenci, L., Deveale, B., Inoue, T., and Van Der Kooy, D. (2009). E-Cadherin regulates neural stem cell self-renewal. *J. Neurosci.* 29, 3885–3896. doi:10.1523/JNEUROSCI.0037-09.2009

Kasper, G., Glaeser, J. D., Geissler, S., Ode, A., Tuischer, J., Matziolis, G., et al. (2007). Matrix metalloprotease activity is an essential link between mechanical stimulus and mesenchymal stem cell behavior. *Stem Cells* 25, 1985–1994. doi:10.1634/stemcells.2006-0676

Kaur, J., and Reinhardt, D. P. (2015). Extracellular matrix (ECM) molecules. *Stem Cell. Biol. Tissue Eng. Dent. Sci.*, 25–45. doi:10.1016/B978-0-12-397157-9.00003-5

Kaushik, G., Spenlehauer, A., Sessions, A. O., Trujillo, A. S., Fuhrmann, A., Fu, Z., et al. (2015). Vinculin network-mediated cytoskeletal remodeling regulates contractile function in the aging heart. *Sci. Transl. Med.* 7, 292ra99. doi:10.1126/scitranslmed.aaa5843

Khadilkar, R. J., Vogl, W., Goodwin, K., and Tanentzapf, G. (2017). Modulation of occluding junctions alters the hematopoietic niche to trigger immune activation. *ELife* 6, e28081. doi:10.7554/eLife.28081

Khan, S., Suryavanshi, M., Kaur, J., Nayak, D., Khurana, A., Manchanda, R. K., et al. (2021). Stem cell therapy: A paradigm shift in breast cancer treatment. *World J. Stem Cells* 13, 841–860. doi:10.4252/wjsc.v13.i7.841

Kim, E., Lisby, A., Ma, C., Lo, N., Ehmer, U., Hayer, K. E., et al. (2019). Promotion of growth factor signaling as a critical function of β-catenin during HCC progression. *Nat. Commun.* 10, 1909. doi:10.1038/s41467-019-09780-z

Kitamura, Y., Kanaya, N., Moleirinho, S., Du, W., Reinshagen, C., Attia, N., et al. (2021). Anti-EGFR VHH-armed death receptor ligand–engineered allogeneic stem cells have therapeutic efficacy in diverse brain metastatic breast cancers. *Sci. Adv.* 7, eabe8671. doi:10.1126/sciadv.abe8671

Klass, C. M., Couchman, J. R., and Woods, A. (2000). Control of extracellular matrix assembly by syndecan-2 proteoglycan. *J. Cell. Sci.* 113 (3), 493–506. doi:10.1242/jcs.113.3.493

Koch, M., Schulze, J., Hansen, U., Ashwodt, T., Keene, D. R., Brunken, W. J., et al. (2004). A novel marker of tissue junctions, collagen XXII. *J. Biol. Chem.* 279, 22514–22521. doi:10.1074/jbc.M400536200

Koirala, R., Priest, A. V., Yen, C. F., Cheah, J. S., Pannekoek, W. J., Gloerich, M., et al. (2021). Inside-out regulation of E-cadherin conformation and adhesion. *Proc. Natl. Acad. Sci. U. S. A.* 118, e2104090118. doi:10.1073/pnas.2104090118

Kourtidis, A., Ngok, S. P., and Anastasiadis, P. Z. (2013). P120 catenin: An essential regulator of cadherin stability, adhesion-induced signaling, and cancer progression. *Prog. Mol. Biol. Transl. Sci.* 116, 409–432. doi:10.1016/B978-0-12-394311-8.00018-2

Kucharzik, T., Walsh, S. V., Chen, J., Parkos, C. A., and Nusrat, A. (2001). Neutrophil transmigration in inflammatory bowel disease is associated with differential expression of epithelial intercellular junction proteins. *Am. J. Pathol.* 159–2009. doi:10.1016/S0002-9440(10)63051-9

Landy, J., Ronde, E., English, N., Clark, S. K., Hart, A. L., Knight, S. C., et al. (2016). Tight junctions in inflammatory bowel diseases and inflammatory bowel disease associated colorectal cancer. *World J. Gastroenterol.* 22, 3117–3126. doi:10.3748/wjg.v22.i11.3117

Larue, L., Ohsugi, M., Hirchenhain, J., and Kemler, R. (1994). E-cadherin null mutant embryos fail to form a trophectoderm epithelium. *Proc. Natl. Acad. Sci. U. S. A.* 91, 8263–8267. doi:10.1073/pnas.91.17.8263

Lathia, J. D., Patton, B., Eckley, D. M., Magnus, T., Mughal, M. R., Sasaki, T., et al. (2007). Patterns of laminins and integrins in the embryonic ventricular zone of the CNS. *J. Comp. Neurol.* 505, 630–643. doi:10.1002/cne.21520

LeBleu, V., Sugimoto, H., Mundel, T. M., Gerami-Naini, B., Finan, E., Miller, C. A., et al. (2009). Stem cell therapies benefit Alport syndrome. *J. Am. Soc. Nephrol.* 20, 2359–2370. doi:10.1681/ASN.2009010123

Leblond, C. P. (1964). Classification of cell populations on the basis of their proliferative behavior. *Natl. Cancer Inst. Monogr.* 14, 119–150.

Lee, B., Moon, K. M., and Kim, C. Y. (2018). Tight junction in the intestinal epithelium: Its association with diseases and regulation by phytochemicals. *J. Immunol. Res.* 2018, 2645465. doi:10.1155/2018/2645465

Lee, M., Ji, H., Furuta, Y., Park, J. I., and McCrea, P. D. (2014). p120-catenin regulates REST and CoREST, and modulates mouse embryonic stem cell differentiation. *J. Cell. Sci.* 127, 4037–4051. doi:10.1242/jcs.151944

Li, B., and Daggett, V. (2002). Molecular basis for the extensibility of elastin. *J. Muscle Res. Cell. Motil.* 23, 561–573. doi:10.1023/A:1023474909980

Li, B., Moshfegh, C., Lin, Z., Albuschies, J., and Vogel, V. (2013). Mesenchymal stem cells exploit extracellular matrix as mechanotransducer. *Sci. Rep.* 3, 2425. doi:10.1038/srep02425

Li, D., Zhou, J., Chowdhury, F., Cheng, J., Wang, N., and Wang, F. (2011). Role of mechanical factors in fate decisions of stem cells. *Regen. Med.* 6, 229–240. doi:10.2217/rme.11.2

Li, N., Long, B., Han, W., Yuan, S., and Wang, K. (2017). MicroRNAs: Important regulators of stem cells. *Stem Cell. Res. Ther.* 8, 110. doi:10.1186/s13287-017-0551-0

Lin, Y., Zhu, W., and Chen, X. (2020). The involving progress of MSCs based therapy in atherosclerosis. *Stem Cell. Res. Ther.* 11, 216. doi:10.1186/s13287-020-01728-1

Linsley, C., Wu, B., and Tawil, B. (2013). The effect of fibrinogen, collagen type I, and fibronectin on mesenchymal stem cell growth and differentiation into osteoblasts. *Tissue Eng. Part A* 19, 1416–1423. doi:10.1089/ten.tea.2012.0523

Liu, C., Han, D., Liang, P., Li, Y., and Cao, F. (2021). The current dilemma and breakthrough of stem cell therapy in ischemic heart disease. *Front. Cell. Dev. Biol.* 9, 636136. doi:10.3389/fcell.2021.636136

Liu, G., David, B. T., Trawczynski, M., and Fessler, R. G. (2020). Advances in pluripotent stem cells: History, mechanisms, technologies, and applications. *Stem Cell. Rev. Rep.* 16, 3–32. doi:10.1007/s12015-019-09935-x

Lo, C. M., Wang, H. B., Dembo, M., and Wang, Y. L. (2000). Cell movement is guided by the rigidity of the substrate. *Biophys. J.* 79, 144–152. doi:10.1016/S0006-3495(00)76279-5

López-García, A., Rovira, M., Jauregui-Amezaga, A., Marín, P., Barastegui, R., Salas, A., et al. (2017). Autologous haematopoietic stem cell transplantation for refractory crohn's disease: Efficacy in a single-centre cohort. *J. Crohns Colitis* 11, 1161–1168. doi:10.1093/ecco-jcc/jjx054

Lund, D. K., Mouly, V., and Cornelison, D. D. W. (2014). MMP-14 is necessary but not sufficient for invasion of three-dimensional collagen by human muscle satellite cells. *Am. J. Physiol. Cell. Physiol.* 307, C140–C149. doi:10.1152/ajpcell.00032.2014

Mahla, R. S. (2016). Stem cells applications in regenerative medicine and disease therapeutics. *Int. J. Cell. Biol.* 2016, 6940283. doi:10.1155/2016/6940283

Marinkovich, M. P., and Tang, J. Y. (2019). Gene therapy for epidermolysis bullosa. *J. Invest. Dermatol.* 139, 1221–1226. doi:10.1016/j.jid.2018.11.036

Martino, M. M., Mochizuki, M., Rothenfluh, D. A., Rempel, S. A., Hubbell, J. A., and Barker, T. H. (2009). Controlling integrin specificity and stem cell differentiation in 2D and 3D environments through regulation of fibronectin domain stability. *Biomaterials* 30, 1089–1097. doi:10.1016/j.biomaterials.2008.10.047

Mason, C., and Dunnill, P. (2008). A brief definition of regenerative medicine. *Regen. Med.* 3, 1–5. doi:10.2217/17460751.3.1.1

Mathieu, P. S., and Loboa, E. G. (2012). Cytoskeletal and focal adhesion influences on mesenchymal stem cell shape, mechanical properties, and differentiation down osteogenic, adipogenic, and chondrogenic pathways. *Tissue Eng. Part B Rev.* 18, 436–444. doi:10.1089/ten.teb.2012.0014

Matrisian, L. M., and Hogan, B. L. M. (1990). Growth factor-regulated proteases and extracellular matrix remodeling during mammalian development. *Curr. Top. Dev. Biol.* 24, 219–259. doi:10.1016/S0070-2153(08)60089-7

Mavilio, F., Pellegrini, G., Ferrari, S., Di Nunzio, F., Di Iorio, E., Recchia, A., et al. (2006). Correction of junctional epidermolysis bullosa by transplantation of genetically modified epidermal stem cells. *Nat. Med.* 12, 1397–1402. doi:10.1038/nm1504

Mecham, R. P. (1991). Elastin synthesis and fiber assembly. *Ann. N. Y. Acad. Sci.* 624, 137–146. doi:10.1111/j.1749-6632.1991.tb17013.x

Misselwitz, B., Juillerat, P., Sulz, M. C., Siegmund, B., and Brand, S.Swiss IBDnet, an official working group of the Swiss Society of Gastroenterology (2020). Emerging treatment options in inflammatory bowel disease: Janus kinases, stem cells, and more. *Digestion* 101, 69–82. doi:10.1159/000507782

Mohammed, D., Versaevel, M., Bruyère, C., Alaimo, L., Luciano, M., Vercruysse, E., et al. (2019). Innovative tools for mechanobiology: Unraveling outside-in and inside-out mechanotransduction. *Front. Bioeng. Biotechnol.* 7, 162. doi:10.3389/fbioe.2019.00162

Monkley, S. J., Zhou, X. H., Kinston, S. J., Giblett, S. M., Hemmings, L., Priddle, H., et al. (2000). Disruption of the talin gene arrests mouse development at the gastrulation stage. *Dev. Dyn.* 219, 560–574. doi:10.1002/1097-0177(2000)9999:9999<::AID-DVDY1079>3.0.CO;2-Y

Morgner, J., Ghatak, S., Jakobi, T., Dieterich, C., Aumailley, M., and Wickström, S. A. (2015). Integrin-linked kinase regulates the niche of quiescent epidermal stem cells. *Nat. Commun.* 6, 8198. doi:10.1038/ncomms9198

Morla, A., and Ruoslahti, E. (1992). A fibronectin self-assembly site involved in fibronectin matrix assembly: Reconstruction in a synthetic peptide. *J. Cell. Biol.* 118, 421–429. doi:10.1083/jcb.118.2.421

Mousavizadeh, R., Hojabrpour, P., Eltit, F., McDonald, P. C., Dedhar, S., McCormack, R. G., et al. (2020). β1 integrin, ILK and mTOR regulate collagen synthesis in mechanically loaded tendon cells. *Sci. Rep.* 10, 12644. doi:10.1038/s41598-020-69267-6

Murphy-Ullrich, J. E., and Sage, E. H. (2014). Revisiting the matricellular concept. *Matrix Biol.* 37, 1–14. doi:10.1016/j.matbio.2014.07.005

Nakano, A., Pulkkinen, L., Murrell, D., Rico, J., Lucky, A. W., Garzon, M., et al. (2001). Epidermolysis bullosa with congenital pyloric atresia: Novel mutations in the β4 integrin gene (ITGB4) and genotype/phenotype correlations. *Pediatr. Res.* 49, 618–626. doi:10.1203/00006450-200105000-00003

Naqvi, S. M., and McNamara, L. M. (2020). Stem cell mechanobiology and the role of biomaterials in governing mechanotransduction and matrix production for tissue regeneration. *Front. Bioeng. Biotechnol.* 8, 597661. doi:10.3389/fbioe.2020.597661

Nascimento, M. A., Sorokin, L., and Coelho-Sampaio, T. (2018). Fractone bulbs derive from ependymal cells and their laminin composition influence the stem cell niche in the subventricular zone. *J. Neurosci.* 38, 3880–3889. doi:10.1523/JNEUROSCI.3064-17.2018

Nath, S. C., Day, B., Harper, L., Yee, J., Hsu, C. Y. M., Larijani, L., et al. (2021). Fluid shear stress promotes embryonic stem cell pluripotency via interplay between β-catenin and vinculin in bioreactor culture. *Stem Cells* 39, 1166–1177. doi:10.1002/stem.3382

Niessen, C. M., and Gottardi, C. J. (2008). Molecular components of the adherens junction. *Biochim. Biophys. Acta* 1778, 562–571. doi:10.1016/j.bbamem.2007.12.015

Nusse, R. (2008). Wnt signaling and stem cell control. *Cell. Res.* 18, 523–527. doi:10.1038/cr.2008.47

Nyeng, P., Heilmann, S., Löf-Öhlin, Z. M., Pettersson, N. F., Hermann, F. M., Reynolds, A. B., et al. (2019). p120ctn-Mediated organ patterning precedes and determines pancreatic progenitor fate. *Dev. Cell.* 49, 31–47.e9. doi:10.1016/j.devcel.2019.02.005

Oakes, P. W., and Gardel, M. L. (2014). Stressing the limits of focal adhesion mechanosensitivity. *Curr. Opin. Cell. Biol.* 30, 68–73. doi:10.1016/j.ceb.2014.06.003

Ogura, N., Kawada, M., Chang, W. J., Zhang, Q., Lee, S. Y., Kondoh, T., et al. (2004). Differentiation of the human mesenchymal stem cells derived from bone marrow and enhancement of cell attachment by fibronectin. *J. Oral Sci.* 46, 207–213. doi:10.2334/josnusd.46.207

Oshima, T., Miwa, H., and Joh, T. (2008). Changes in the expression of claudins in active ulcerative colitis. *J. Gastroenterol. Hepatol.* 23, S146–S150. doi:10.1111/j.1440-1746.2008.05405.x

Ozsvar, J., Mithieux, S. M., Wang, R., and Weiss, A. S. (2015). Elastin-based biomaterials and mesenchymal stem cells. *Biomater. Sci.* 3, 800–809. doi:10.1039/c5bm00038f

Ozsvar, J., Yang, C., Cain, S. A., Baldock, C., Tarakanova, A., and Weiss, A. S. (2021). Tropoelastin and elastin assembly. *Front. Bioeng. Biotechnol.* 9, 643110. doi:10.3389/fbioe.2021.643110

Paavolainen, O., and Peuhu, E. (2021). Integrin-mediated adhesion and mechanosensing in the mammary gland. *Semin. Cell. Dev. Biol.* 114, 113–125. doi:10.1016/j.semcdb.2020.10.010

Pai, S. G., Carneiro, B. A., Mota, J. M., Costa, R., Leite, C. A., Barroso-Sousa, R., et al. (2017). Wnt/beta-catenin pathway: Modulating anticancer immune response. *J. Hematol. Oncol.* 10, 101. doi:10.1186/s13045-017-0471-6

Panciera, T., Azzolin, L., Cordenonsi, M., and Piccolo, S. (2017). Mechanobiology of YAP and TAZ in physiology and disease. *Nat. Rev. Mol. Cell. Biol.* 18, 758–770. doi:10.1038/nrm.2017.87

Panciera, T., Citron, A., Di Biagio, D., Battilana, G., Gandin, A., Giulitti, S., et al. (2020). Publisher Correction: Reprogramming normal cells into tumour precursors requires ECM stiffness and oncogene-mediated changes of cell mechanical properties. *Nat. Mat.* 19, 475. doi:10.1038/s41563-020-0615-x10.1038/s41563-020-0644-5

Panés, J., García-Olmo, D., Van Assche, G., Colombel, J. F., Reinisch, W., Baumgart, D. C., et al. (2016). Expanded allogeneic adipose-derived mesenchymal stem cells (Cx601) for complex perianal fistulas in crohn's disease: A phase 3 randomised, double-blind controlled trial. *Lancet* 388, 1281–1290. doi:10.1016/S0140-6736(16)31203-X

Pankov, R., and Yamada, K. M. (2002). Fibronectin at a glance. *J. Cell. Sci.* 115, 3861–3863. doi:10.1242/jcs.00059

Pannekoek, W. J., de Rooij, J., and Gloerich, M. (2019). Force transduction by cadherin adhesions in morphogenesis. In *F1000Research* 8, F1000. doi:10.12688/f1000research.18779.1

Parisi, L., Toffoli, A., Ghezzi, B., Mozzoni, B., Lumetti, S., and Macaluso, G. M. (2020). A glance on the role of fibronectin in controlling cell response at biomaterial interface. *Jpn. Dent. Sci. Rev.* 56, 50–55. doi:10.1016/j.jdsr.2019.11.002

Park, C. C., Zhang, H., Pallavicini, M., Gray, J. W., Baehner, F., Park, C. J., et al. (2006). Beta1 integrin inhibitory antibody induces apoptosis of breast cancer cells, inhibits growth, and distinguishes malignant from normal phenotype in three dimensional cultures and *in vivo*. *Cancer Res.* 66, 1526–1535. doi:10.1158/0008-5472.CAN-05-3071

Park, G. C., Kim, H. S., Park, H. Y., Seo, Y., Kim, J. M., Shin, S. C., et al. (2019). Tensin-3 regulates integrin-mediated proliferation and differentiation of tonsil-derived mesenchymal stem cells. *Cells* 9, E89. doi:10.3390/cells9010089

Park, J., Son, Y., Lee, N. G., Lee, K., Lee, D. G., Song, J., et al. (2018). DSG2 is a functional cell surface marker for identification and isolation of human pluripotent stem cells. *Stem Cell. Rep.* 11, 115–127. doi:10.1016/j.stemcr.2018.05.009

Paszek, M. J., Zahir, N., Johnson, K. R., Lakins, J. N., Rozenberg, G. I., Gefen, A., et al. (2005). Tensional homeostasis and the malignant phenotype. *Cancer Cell.* 8, 241–254. doi:10.1016/j.ccr.2005.08.010

Patten, J., and Wang, K. (2021). Fibronectin in development and wound healing. *Adv. Drug Deliv. Rev.* 170, 353–368. doi:10.1016/j.addr.2020.09.005

Peng, T., Dong, Y., Zhu, G., and Xie, D. (2014). Induced pluripotent stem cells: Landscape for studying and treating hereditary hearing loss. *J. Otology* 9, 151–155. doi:10.1016/j.joto.2015.02.001

Petrof, G., Lwin, S. M., Martinez-Queipo, M., Abdul-Wahab, A., Tso, S., Mellerio, J. E., et al. (2015). Potential of systemic allogeneic mesenchymal stromal cell therapy for children with recessive dystrophic epidermolysis bullosa. *J. Invest. Dermatol.* 135, 2319–2321. doi:10.1038/jid.2015.158

Pieters, T., Goossens, S., Haenebalcke, L., Andries, V., Stryjewska, A., De Rycke, R., et al. (2016). p120 catenin-mediated stabilization of E-cadherin is essential for primitive endoderm specification. *PLoS Genet.* 12, e1006243. doi:10.1371/journal.pgen.1006243

Pimton, P., Sarkar, S., Sheth, N., Perets, A., Marcinkiewicz, C., Lazarovici, P., et al. (2011). Fibronectin-mediated upregulation of α5β1 integrin and cell adhesion during differentiation of mouse embryonic stem cells. *Cell. adh. Migr.* 5, 73–82. doi:10.4161/cam.5.1.13704

Polte, T. R., and Hanks, S. K. (1997). Complexes of focal adhesion kinase (FAK) and Crk-associated substrate (p130(Cas)) are elevated in cytoskeleton-associated fractions following adhesion and Src transformation. Requirements for Src kinase

activity and FAK proline-rich motifs. *J. Biol. Chem.* 272, 5501–5509. doi:10.1074/jbc.272.9.5501

Ponmurugan, M., and Vemparala, S. (2012). Studies on structural and average unfolding behaviours of FNIII domain of Contactin-1 protein by molecular dynamics simulation. *Front. Life Sci.* 6, 33–45. doi:10.1080/21553769.2013.776995

Pouikli, A., Parekh, S., Maleszewska, M., Nikopoulou, C., Baghdadi, M., Tripodi, I., et al. (2021). Chromatin remodeling due to degradation of citrate carrier impairs osteogenesis of aged mesenchymal stem cells. *Nat. Aging* 1, 810–825. doi:10.1038/s43587-021-00105-8

Prasad, S., Mingrino, R., Kaukinen, K., Hayes, K. L., Powell, R. M., MacDonald, T. T., et al. (2005). Inflammatory processes have differential effects on claudins 2, 3 and 4 in colonic epithelial cells. *Lab. Invest.* 85, 1139–1162. doi:10.1038/labinvest.3700316

Proctor, R. A. (1987). Fibronectin: A brief overview of its structure, function, and physiology. *Rev. Infect. Dis.* 9, S317–S321. doi:10.1093/clinids/9.supplement_4.s317

Prodinger, C., Reichelt, J., Bauer, J. W., and Laimer, M. (2019). Epidermolysis bullosa: Advances in research and treatment. *Exp. Dermatol.* 28, 1176–1189. doi:10.1111/exd.13979

Provenzano, P. P., and Keely, P. J. (2009). The role of focal adhesion kinase in tumor initiation and progression. *Cell. adh. Migr.* 3, 347–350. doi:10.4161/cam.3.4.9458

Qasim, W., Cavazzana-Calvo, M., Davies, E. G., Davis, J., Duval, M., Eames, G., et al. (2009). Allogeneic hematopoietic stem-cell transplantation for leukocyte adhesion deficiency. *Pediatrics* 123, 836–840. doi:10.1542/peds.2008-1191

Qin, L., Fu, X., Ma, J., Lin, M., Zhang, P., Wang, Y., et al. (2021). Kindlin-2 mediates mechanotransduction in bone by regulating expression of Sclerostin in osteocytes. *Commun. Biol.* 4, 402. doi:10.1038/s42003-021-01950-4

Rashidghamat, E., and McGrath, J. A. (2017). Novel and emerging therapies in the treatment of recessive dystrophic epidermolysis bullosa. *Intractable Rare Dis. Res.* 6, 6–20. doi:10.5582/irdr.2017.01005

Raymond, K., Deugnier, M. A., Faraldo, M. M., and Glukhova, M. A. (2009). Adhesion within the stem cell niches. *Curr. Opin. Cell. Biol.* 21, 623–629. doi:10.1016/j.ceb.2009.05.004

Redmer, T., Diecke, S., Grigoryan, T., Quiroga-Negreira, A., Birchmeier, W., and Besser, D. (2011). E-cadherin is crucial for embryonic stem cell pluripotency and can replace OCT4 during somatic cell reprogramming. *EMBO Rep.* 12, 720–726. doi:10.1038/embor.2011.88

Relucio, J., Menezes, M. J., Miyagoe-Suzuki, Y., Takeda, S., and Colognato, H. (2012). Laminin regulates postnatal oligodendrocyte production by promoting oligodendrocyte progenitor survival in the subventricular zone. *GLIA* 60, 1451–1467. doi:10.1002/glia.22365

Ren, G., Zhang, L., Zhao, X., Xu, G., Zhang, Y., Roberts, A. I., et al. (2008). Mesenchymal stem cell-mediated immunosuppression occurs via concerted action of chemokines and nitric oxide. *Cell. Stem Cell.* 2, 141–150. doi:10.1016/j.stem.2007.11.014

Reynolds, A. B., Daniel, J., McCrea, P. D., Wheelock, M. J., Wu, J., and Zhang, Z. (1994). Identification of a new catenin: The tyrosine kinase substrate p120cas associates with E-cadherin complexes. *Mol. Cell. Biol.* 14, 8333–8342. doi:10.1128/mcb.14.12.8333-8342.1994

Ricard-Blum, S. (2011). The collagen family. *Cold Spring Harb. Perspect. Biol.* 3, a004978. doi:10.1101/cshperspect.a004978

Rigillo, G., Basile, V., Belluti, S., Ronzio, M., Sauta, E., Ciarrocchi, A., et al. (2021). The transcription factor NF-Y participates to stem cell fate decision and regeneration in adult skeletal muscle. *Nat. Commun.* 12, 6013. doi:10.1038/s41467-021-26293-w

Robey, P. G. (2000). Series Introduction: Stem cells near the century mark. *J. Clin. Invest.* 105, 1489–1491. doi:10.1172/jci10256

Rodgers, U. R., and Weiss, A. S. (2004). Integrin αvβ3 binds a unique non-RGD site near the C-terminus of human tropoelastin. *Biochimie* 86, 173–178. doi:10.1016/j.biochi.2004.03.002

Rosenbloom, J., Abrams, W. R., and Mecham, R. (1993). Extracellular matrix 4: The elastic fiber. *FASEB J.* 7, 1208–1218. doi:10.1096/fasebj.7.13.8405806

Rowlands, A. S., George, P. A., and Cooper-White, J. J. (2008). Directing osteogenic and myogenic differentiation of MSCs: Interplay of stiffness and adhesive ligand presentation. *Am. J. Physiol. Cell. Physiol.* 295, C1037–C1044. doi:10.1152/ajpcell.67.2008

Salasznyk, R. M., Klees, R. F., Boskey, A., and Plopper, G. E. (2007). Activation of FAK is necessary for the osteogenic differentiation of human mesenchymal stem cells on laminin-5. *J. Cell. Biochem.* 100, 499–514. doi:10.1002/jcb.21074

Samanta, D., and Almo, S. C. (2015). Nectin family of cell-adhesion molecules: Structural and molecular aspects of function and specificity. *Cell. Mol. Life Sci.* 72, 645–658. doi:10.1007/s00018-014-1763-4

Sarpal, R., Yan, V., Kazakova, L., Sheppard, L., Yu, J. C., Fernandez-Gonzalez, R., et al. (2019). Role of α-Catenin and its mechanosensing properties in regulating Hippo/YAP-dependent tissue growth. *PLoS Genet.* 15, e1008454. doi:10.1371/journal.pgen.1008454

Saw, S., Weiss, A., Khokha, R., and Waterhouse, P. D. (2019). Metalloproteases: On the watch in the hematopoietic niche. *Trends Immunol.* 40, 1053–1070. doi:10.1016/j.it.2019.09.006

Sawada, N. (2013). Tight junction-related human diseases. *Pathol. Int.* 63, 1–12. doi:10.1111/pin.12021

Schaller, M. D. (2001). Paxillin: A focal adhesion-associated adaptor protein. *Oncogene* 20, 6459–6472. doi:10.1038/sj.onc.1204786

Schiller, H. B., and Fässler, R. (2013). Mechanosensitivity and compositional dynamics of cell-matrix adhesions. *EMBO Rep.* 14, 509–519. doi:10.1038/embor.2013.49

Schlaepfer, D. D., Hanks, S. K., Hunter, T., and Geer, P. Van Der. (1994). Integrin-mediated signal transduction linked to Ras pathway by GRB2 binding to focal adhesion kinase. *Nature* 372, 786–791. doi:10.1038/372786a0

Schlegelmilch, K., Mohseni, M., Kirak, O., Pruszak, J., Rodriguez, J. R., Zhou, D., et al. (2011). Yap1 acts downstream of α-catenin to control epidermal proliferation. *Cell.* 144, 782–795. doi:10.1016/j.cell.2011.02.031

Schofield, R. (1978). The relationship between the spleen colony-forming cell and the haemopoietic stem cell. A hypothesis. *Blood Cells.*

Seita, J., and Weissman, I. L. (2010). Hematopoietic stem cell: Self-renewal versus differentiation. *Wiley Interdiscip. Rev. Syst. Biol. Med.* 2, 640–653. doi:10.1002/wsbm.86

Seo, C. H., Furukawa, K., Montagne, K., Jeong, H., and Ushida, T. (2011). The effect of substrate microtopography on focal adhesion maturation and actin organization via the RhoA/ROCK pathway. *Biomaterials* 32, 9568–9575. doi:10.1016/j.biomaterials.2011.08.077

Shahoumi, L. A. (2021). Oral cancer stem cells: Therapeutic implications and challenges. *Front. Oral Health* 2, 685236. doi:10.3389/froh.2021.685236

Shamblott, M. J., Axelman, J., Wang, S., Bugg, E. M., Littlefield, J. W., Donovan, P. J., et al. (1998). Derivation of pluripotent stem cells from cultured human primordial germ cells. *Proc. Natl. Acad. Sci. U. S. A.* 95, 13726–13731. doi:10.1073/pnas.95.23.13726

Shen, Q., Wang, Y., Kokovay, E., Lin, G., Chuang, S. M., Goderie, S. K., et al. (2008). Adult SVZ stem cells lie in a vascular niche: A quantitative analysis of niche cell-cell interactions. *Cell. Stem Cell.* 3, 289–300. doi:10.1016/j.stem.2008.07.026

Shibata, S., Hayashi, R., Okubo, T., Kudo, Y., Katayama, T., Ishikawa, Y., et al. (2018). Selective laminin-directed differentiation of human induced pluripotent stem cells into distinct ocular lineages. *Cell. Rep.* 25, 1668–1679.e5. doi:10.1016/j.celrep.2018.10.032

Shih, Y. R. V., Tseng, K. F., Lai, H. Y., Lin, C. H., and Lee, O. K. (2011). Matrix stiffness regulation of integrin-mediated mechanotransduction during osteogenic differentiation of human mesenchymal stem cells. *J. Bone Min. Res.* 26, 730–738. doi:10.1002/jbmr.278

Shimizu, H., Suzuki, K., Watanabe, M., and Okamoto, R. (2019). Stem cell-based therapy for inflammatory bowel disease. *Intest. Res.* 17, 311–316. doi:10.5217/ir.2019.00043

Shoulders, M. D., and Raines, R. T. (2009). Collagen structure and stability. *Annu. Rev. Biochem.* 78, 929–958. doi:10.1146/annurev.biochem.77.032207.120833

Silvis, M. R., Kreger, B. T., Lien, W. H., Klezovitch, O., Rudakova, G. M., Camargo, F. D., et al. (2011). α-catenin is a tumor suppressor that controls cell accumulation by regulating the localization and activity of the transcriptional coactivator yap1. *Sci. Signal.* 4, ra33. doi:10.1126/scisignal.2001823

Smith, A. G. (2001). Embryo-derived stem cells: Of mice and men. *Annu. Rev. Cell. Dev. Biol.* 17, 435–462. doi:10.1146/annurev.cellbio.17.1.435

Smith, L., Cho, S., and Discher, D. E. (2017). Mechanosensing of matrix by stem cells: From matrix heterogeneity, contractility, and the nucleus in pore-migration to cardiogenesis and muscle stem cells *in vivo*. *Semin. Cell. Dev. Biol.* 71, 84–98. doi:10.1016/j.semcdb.2017.05.025

Somaiah, C., Kumar, A., Mawrie, D., Sharma, A., Patil, S. D., Bhattacharyya, J., et al. (2015). Collagen promotes higher adhesion, survival and proliferation of mesenchymal stem cells. *PLoS ONE* 10, e0145068. doi:10.1371/journal.pone.0145068

Spiegelman, B. M., and Ginty, C. A. (1983). Fibronectin modulation of cell shape and lipogenic gene expression in 3t3-adipocytes. *Cell.* 35, 657–666. doi:10.1016/0092-8674(83)90098-3

Stanton, A. E., Tong, X., and Yang, F. (2019). Extracellular matrix type modulates mechanotransduction of stem cells. *Acta Biomater.* 96, 310–320. doi:10.1016/j.actbio.2019.06.048

Stepensky, P. Y., Wolach, B., Gavrieli, R., Rousso, S., Ami, T. B., Goldman, V., et al. (2015). Leukocyte adhesion deficiency type III: Clinical features and treatment with stem cell transplantation. *J. Pediatr. Hematol. Oncol.* 37, 264–268. doi:10.1097/MPH.0000000000000228

Stepniak, E., Radice, G. L., and Vasioukhin, V. (2009). Adhesive and signaling functions of cadherins and catenins in vertebrate development. *Cold Spring Harb. Perspect. Biol.* 1, a002949. doi:10.1101/cshperspect.a002949

Suma, G., Arora, M., and Lakhanpal, M. (2015). Stem cell therapy: A novel treatment approach for oral mucosal lesions. *J. Pharm. Bioallied Sci.* 7, 2–8. doi:10.4103/0975-7406.149809

Sun, Z., Guo, S. S., and Fässler, R. (2016). Integrin-mediated mechanotransduction. *J. Cell. Biol.* 215, 445–456. doi:10.1083/jcb.201609037

Szymanski, J. M., Sevcik, E. N., Zhang, K., and Feinberg, A. W. (2017). Stretch-dependent changes in molecular conformation in fibronectin nanofibers. *Biomater. Sci.* 5, 1629–1639. doi:10.1039/c7bm00370f

Szymanski, J. M., Zhang, K., and Feinberg, A. W. (2017). Measuring the Poisson's ratio of fibronectin using engineered nanofibers. *Sci. Rep.* 7, 13413. doi:10.1038/s41598-017-13866-3

Takenaka-Ninagawa, N., Kim, J., Zhao, M., Sato, M., Jonouchi, T., Goto, M., et al. (2021). Collagen-VI supplementation by cell transplantation improves muscle regeneration in Ullrich congenital muscular dystrophy model mice. *Stem Cell. Res. Ther.* 12, 446. doi:10.1186/s13287-021-02514-3

Tamayo-Angorrilla, M., López de Andrés, J., Jiménez, G., and Marchal, J. A. (2021). The biomimetic extracellular matrix: A therapeutic tool for breast cancer research. *Transl. Res.* 247, 117–136. doi:10.1016/J.TRSL.2021.11.008

Theocharis, A. D., Skandalis, S. S., Gialeli, C., and Karamanos, N. K. (2016). Extracellular matrix structure. *Adv. Drug Deliv. Rev.* 97, 4–27. doi:10.1016/j.addr.2015.11.001

Thompson, W. R., Rubin, C. T., and Rubin, J. (2012). Mechanical regulation of signaling pathways in bone. *Gene* 503, 179–193. doi:10.1016/j.gene.2012.04.076

Thomson, J. A., Itskovitz-Eldor, J., Shapiro, S. S., Waknitz, M. A., Swiergiel, J. J., Marshall, V. S., et al. (1998). Embryonic stem cell lines derived from human blastocysts. *Science* 282, 1145–1147. doi:10.1126/science.282.5391.1145

To, W. S., and Midwood, K. S. (2011). Plasma and cellular fibronectin: Distinct and independent functions during tissue repair. *Fibrogenes. Tissue Repair* 4, 21. doi:10.1186/1755-1536-4-21

Tolar, J., Akemi, I. Y., Riddle, M., McElmurry, R. T., Osborn, M., Xia, L., et al. (2009). Amelioration of epidermolysis bullosa by transfer of wild-type bone marrow cells. *Blood* 113, 1167–1174. doi:10.1182/blood-2008-06-161299

Tolar, J., and Wagner, J. E. (2013). Allogeneic blood and bone marrow cells for the treatment of severe epidermolysis bullosa: Repair of the extracellular matrix. *Lancet* 382, 1214–1223. doi:10.1016/S0140-6736(13)61897-8

Torsoni, A. S., Constancio, S. S., Nadruz, W., Hanks, S. K., and Franchini, K. G. (2003). Focal adhesion kinase is activated and mediates the early hypertrophic response to stretch in cardiac myocytes. *Circ. Res.* 93, 140–147. doi:10.1161/01.RES.0000081595.25297.1B

Traister, A., Aafaqi, S., Masse, S., Dai, X., Li, M., Hinek, A., et al. (2012). ILK induces cardiomyogenesis in the human heart. *PLoS ONE* 7, e37802. doi:10.1371/journal.pone.0037802

Tripathi, A., Khan, M. S., Khan, A. R., Vaughn, V. M., and Bolli, R. (2021). Cell therapy for nonischemic dilated cardiomyopathy: A systematic review and meta-analysis of randomized controlled trials. *Stem Cells Transl. Med.* 10, 1394–1405. doi:10.1002/sctm.21-0094

Tsai, S. W., Cheng, Y. H., Chang, Y., Liu, H. L., and Tsai, W. B. (2010). Type I collagen structure modulates the behavior of osteoblast-like cells. *J. Taiwan Inst. Chem. Eng.* 41, 247–251. doi:10.1016/j.jtice.2009.10.002

Tyagi, S. C., Kumar, G., S., and Glover, G. (1995). Induction of tissue inhibitor and matrix metalloproteinase by serum in human heart-derived fibroblast and endomyocardial endothelial cells. *J. Cell. Biochem.* 58, 360–371. doi:10.1002/jcb.240580309

Uitto, J., and Richard, G. (2004). Progress in epidermolysis bullosa: Genetic classification and clinical implications. *Am. J. Med. Genet. C Semin. Med. Genet.* 131C, 61–74. doi:10.1002/ajmg.c.30035

Urciuolo, A., Quarta, M., Morbidoni, V., Gattazzo, F., Molon, S., Grumati, P., et al. (2013). Collagen VI regulates satellite cell self-renewal and muscle regeneration. *Nat. Commun.* 4, 1964. doi:10.1038/ncomms2964

Vasioukhin, V., Bauer, C., Degenstein, L., Wise, B., and Fuchs, E. (2001). Hyperproliferation and defects in epithelial polarity upon conditional ablation of α-catenin in skin. *Cell.* 104, 605–617. doi:10.1016/S0092-8674(01)00246-X

Vining, K. H., and Mooney, D. J. (2017). Mechanical forces direct stem cell behaviour in development and regeneration. *Nat. Rev. Mol. Cell. Biol.* 18, 728–742. doi:10.1038/nrm.2017.108

Vleminckx, K. (2017). "Cell adhesion molecules," in *Encyclopedia of cancer*. Editor M. Schwab (Berlin Heidelberg: Springer), 885–891. doi:10.1007/978-3-662-46875-3_989

Vogel, V., and Sheetz, M. (2006). Local force and geometry sensing regulate cell functions. *Nat. Rev. Mol. Cell. Biol.* 7, 265–275. doi:10.1038/nrm1890

Volk, S. W., Shah, S. R., Cohen, A. J., Wang, Y., Brisson, B. K., Vogel, L. K., et al. (2014). Type III collagen regulates osteoblastogenesis and the quantity of trabecular bone. *Calcif. Tissue Int.* 94, 621–631. doi:10.1007/s00223-014-9843-x

Wade, R., Bohl, J., and Vande Pol, S. (2002). Paxillin null embryonic stem cells are impaired in cell spreading and tyrosine phosphorylation of focal adhesion kinase. *Oncogene* 21, 96–107. doi:10.1038/sj.onc.1205013

Wang, L. D., and Wagers, A. J. (2011). Dynamic niches in the origination and differentiation of haematopoietic stem cells. *Nat. Rev. Mol. Cell. Biol.* 12, 643–655. doi:10.1038/nrm3184

Wang, W., Pan, H., Murray, K., Jefferson, B. S., and Li, Y. (2009). Matrix metalloproteinase-1 promotes muscle cell migration and differentiation. *Am. J. Pathol.* 174, 541–549. doi:10.2353/ajpath.2009.080509

Wang, Y., Zhao, L., Smas, C., and Sul, H. S. (2010). Pref-1 interacts with fibronectin to inhibit adipocyte differentiation. *Mol. Cell. Biol.* 30, 3480–3492. doi:10.1128/mcb.00057-10

Wang, Z., Su, X., Ashraf, M., Kim, I. M., Weintraub, N. L., Jiang, M., et al. (2018). Regenerative therapy for cardiomyopathies. *J. Cardiovasc. Transl. Res.* 11 (5), 357–365. doi:10.1007/s12265-018-9807-z

Watt, F. M., and Hogan, B. L. M. (2000). Out of eden: Stem cells and their niches. *Science* 287, 1427–1430. doi:10.1126/science.287.5457.1427

Watt, F. M., and Huck, W. T. S. (2013). Role of the extracellular matrix in regulating stem cell fate. *Nat. Rev. Mol. Cell. Biol.* 14, 467–473. doi:10.1038/nrm3620

Watters, A. K., Rom, S., Hill, J. D., Dematatis, M. K., Zhou, Y., Merkel, S. F., et al. (2015). Identification and dynamic regulation of tight junction protein expression in human neural stem cells. *Stem Cells Dev.* 24, 1377–1389. doi:10.1089/scd.2014.0497

White, D. E., Kurpios, N. A., Zuo, D., Hassell, J. A., Blaess, S., Mueller, U., et al. (2004). Targeted disruption of beta1-integrin in a transgenic mouse model of human breast cancer reveals an essential role in mammary tumor induction. *Cancer Cell.* 6, 159–170. doi:10.1016/j.ccr.2004.06.025

Wishart, A. L., Conner, S. J., Guarin, J. R., Fatherree, J. P., Peng, Y., McGinn, R. A., et al. (2020). Decellularized extracellular matrix scaffolds identify full-length collagen VI as a driver of breast cancer cell invasion in obesity and metastasis. *Sci. Adv.* 6, eabc3175. doi:10.1126/sciadv.abc3175

Woessner, J. F. (1991). Matrix metalloproteinases and their inhibitors in connective tissue remodeling. *FASEB J.* 5, 2145–2154. doi:10.1096/fasebj.5.8.1850705

Wolfenson, H., Yang, B., and Sheetz, M. P. (2019). Steps in mechanotransduction pathways that control cell morphology. *Annu. Rev. Physiol.* 81, 585–605. doi:10.1146/annurev-physiol-021317-121245

Woods, A. (2001). Syndecans: Transmembrane modulators of adhesion and matrix assembly. *J. Clin. Invest.* 107, 935–941. doi:10.1172/JCI12802

Wyatt, J., Vogelsang, H., Hübl, W., Waldhoer, T., and Lochs, H. (1993). Intestinal permeability and the prediction of relapse in Crohri's disease. *Lancet* 341, 1437–1439. doi:10.1016/0140-6736(93)90882-H

Xia, M., Chen, Y., He, Y., Li, H., and Li, W. (2020). Activation of the RhoA-YAP-β-catenin signaling axis promotes the expansion of inner ear progenitor cells in 3D culture. *Stem Cells* 38, 860–874. doi:10.1002/stem.3175

Xiaoping, C., and Yong, L. (2009). Role of matrix metalloproteinases in skeletal muscle: Migration, differentiation, regeneration and fibrosis. *Cell. Adh. Migr.* 3 (4), 337–341. doi:10.4161/cam.3.4.9338

Yang, X., Wang, H., and Jiao, B. (2017). Mammary gland stem cells and their application in breast cancer. *Oncotarget* 8, 10675–10691. doi:10.18632/oncotarget.12893

Yeo, G. C., and Weiss, A. S. (2019). Soluble matrix protein is a potent modulator of mesenchymal stem cell performance. *Proc. Natl. Acad. Sci. U. S. A.* 116, 2042–2051. doi:10.1073/pnas.1812951116

Ylönen, R., Kyrönlahti, T., Sund, M., Ilves, M., Lehenkari, P., Tuukkanen, J., et al. (2005). Type XIII collagen strongly affects bone formation in transgenic mice. *J. Bone Min. Res.* 20, 1381–1393. doi:10.1359/JBMR.050319

Yonekawa, T., and Nishino, I. (2015). Ullrich congenital muscular dystrophy: Clinicopathological features, natural history and pathomechanism(s). *J. Neurol. Neurosurg. Psychiatry* 86, 280–287. doi:10.1136/jnnp-2013-307052

Yonemura, S., Wada, Y., Watanabe, T., Nagafuchi, A., and Shibata, M. (2010). alpha-Catenin as a tension transducer that induces adherens junction development. *Nat. Cell. Biol.* 12, 533–542. doi:10.1038/ncb2055

Yu, J., and Thomson, J. A. (2008). Pluripotent stem cell lines. *Genes. Dev.* 22, 1987–1997. doi:10.1101/gad.1689808

Yuan, J., Wei, Z., Xu, X., Ocansey, D. K. W., Cai, X., and Mao, F. (2021). The effects of mesenchymal stem cell on colorectal cancer. *Stem Cells Int.*, 9136583. doi:10.1155/2021/9136583

Yue, B. (2014). Biology of the extracellular matrix: An overview. *J. Glaucoma* 23, S20–S23. doi:10.1097/IJG.0000000000000108

Yui, S., Nakamura, T., Sato, T., Nemoto, Y., Mizutani, T., Zheng, X., et al. (2012). Functional engraftment of colon epithelium expanded *in vitro* from a single adult $Lgr5^{+}$ stem cell. *Nat. Med.* 18, 618–623. doi:10.1038/nm.2695

Zeissig, S., Bürgel, N., Günzel, D., Richter, J., Mankertz, J., Wahnschaffe, U., et al. (2007). Changes in expression and distribution of claudin 2, 5 and 8 lead to discontinuous tight junctions and barrier dysfunction in active Crohn's disease. *Gut* 56, 61–72. doi:10.1136/gut.2006.094375

Zhang, N., Xie, X., Chen, H., Chen, H., Yu, H., and Wang, J. A. (2014). Stem cell-based therapies for atherosclerosis: Perspectives and ongoing controversies. *Stem Cells Dev.* 23, 1731–1740. doi:10.1089/scd.2014.0078

Zigrino, P., Brinckmann, J., Niehoff, A., Lu, Y., Giebeler, N., Eckes, B., et al. (2016). Fibroblast-Derived MMP-14 regulates collagen homeostasis in adult skin. *J. Invest. Dermatol.* 136, 1575–1583. doi:10.1016/j.jid.2016.03.036

frontiers | Frontiers in Cell and Developmental Biology

TYPE Review
PUBLISHED 02 December 2022
DOI 10.3389/fcell.2022.1038107



OPEN ACCESS

EDITED BY
Naotaka Nakazawa,
Kindai University, Japan

REVIEWED BY
Ariella Shikanov,
University of Michigan, United States
Christiani A. Amorim,
Université Catholique de Louvain, Belgium

*CORRESPONDENCE
Chii Jou Chan,
dbschii@nus.edu.sg

SPECIALTY SECTION
This article was submitted to Cell Adhesion and Migration, a section of the journal Frontiers in Cell and Developmental Biology

RECEIVED 06 September 2022
ACCEPTED 16 November 2022
PUBLISHED 02 December 2022

CITATION
Biswas A, Ng BH, Prabhakaran VS and Chan CJ (2022), Squeezing the eggs to grow: The mechanobiology of mammalian folliculogenesis. *Front. Cell Dev. Biol.* 10:1038107. doi: 10.3389/fcell.2022.1038107



# Squeezing the eggs to grow: The mechanobiology of mammalian folliculogenesis

Arikta Biswas[1], Boon Heng Ng[1], Vinod S/O Prabhakaran[1] and Chii Jou Chan[1,2]*

[1]Mechanobiology Institute, National University of Singapore, Singapore, Singapore, [2]Department of Biological Sciences, National University of Singapore, Singapore, Singapore

The formation of functional eggs (oocyte) in ovarian follicles is arguably one of the most important events in early mammalian development since the oocytes provide the bulk genetic and cytoplasmic materials for successful reproduction. While past studies have identified many genes that are critical to normal ovarian development and function, recent studies have highlighted the role of mechanical force in shaping folliculogenesis. In this review, we discuss the underlying mechanobiological principles and the force-generating cellular structures and extracellular matrix that control the various stages of follicle development. We also highlight emerging techniques that allow for the quantification of mechanical interactions and follicular dynamics during development, and propose new directions for future studies in the field. We hope this review will provide a timely and useful framework for future understanding of mechano-signalling pathways in reproductive biology and diseases.

KEYWORDS

**folliculogenesis, mechanobiology, oocyte, mechanotransduction, mammalian reproduction, theca cell**

## 1 Introduction

In mammals, the ovarian follicles housing the oocytes are the functional units for female reproduction. The maturation of follicles, or folliculogenesis, is not only essential for supporting oogenesis, but also triggers the production of hormones for female sexual characteristics and early pregnancy. The developmental stages of follicles, loosely defined by the follicle size, the number of cells at the follicular envelope and the morphology, can be classified into the primordial, primary, secondary and antral follicle stage (Hertig and Adams, 1967) (Figure 1A). Folliculogenesis begins with the primordial follicle stage, which consists of an oocyte surrounded by a single layer of somatic granulosa cells (GCs). Upon activation, the primordial follicles develop into the primary follicles, which are characterised by the formation of cuboidal-shaped GCs and the zona pellucida (ZP) that encapsulates the oocyte while maintaining transzonal projections between the oocyte and the GCs. These primary follicles then grow into secondary follicles characterised by multiple layers of GCs and an outer layer of theca cells (TCs). Multiple pockets of fluid-

filled lumens form within the GCs as the secondary follicles increase in size and acquire stratified layers of GCs and TCs. These lumen eventually resolve into a single antrum that grows in size. Under the action of luteinizing hormone, the theca wall undergoes extensive extracellular matrix (ECM) remodelling, which, together with antrum expansion, lead to follicle rupture and the release of oocytes out of the ovary, a process known as ovulation.

Early work on ovarian folliculogenesis was largely descriptive, relying on histology, histochemistry and electron microscopy (Hertig and Adams, 1967). There were extensive functional studies using molecular genetics and transgenics approaches, which revealed key genes and proteins that are required for primary follicle activation and growth (Choi and Rajkovic, 2006; França and Mendonca, 2022). The advancement of immunofluorescence imaging further enables the visualisation of follicular cells and the cytoskeletal proteins during development (Da Silva-Buttkus et al., 2008; Mora et al., 2012), paving the way for a more quantitative approach to understand follicular morphogenesis. Along with these studies, novel approaches were developed to culture follicles *ex vivo*, such as the seminal work by Eppig *et al.* on 2D systems and organ culture (Eppig, 1977; Eppig and Schroeder, 1989; Eppig and O'Brien, 1996). In the 2000s, a series of works on culturing follicles in 3D using novel biomaterials were introduced (Pangas et al., 2003; Xu et al., 2006a; West et al., 2007; Hornick et al., 2012), which provide a more native follicle environment with tunable stiffness for optimal follicle growth and survival.

While these studies revealed key paracrine and autocrine signalling patterns in the mammalian ovary, the biomechanics and the roles of mechanical signalling during folliculogenesis have not been investigated as much. It is known that mechanical forces play an integral role in controlling cellular dynamics and functions in development, tissue homeostasis and cancer growth (Heisenberg and Bellaïche, 2013; Hannezo and Heisenberg, 2019). Effective coordination of long-range force transmission and mechanosensing of cells do not only lead to robust tissue morphogenesis, they also impact cell fate specification and tissue patterning *via* mechanotransduction (Chan et al., 2017). In recent years, new evidence has emerged showing that mechanical cues play a critical role in regulating ovarian folliculogenesis. *Ex vivo* culture of follicles revealed that the follicle growth is sensitive to the surrounding matrix stiffness, and compressive stress exerted by the matrix can act against follicle expansion and development. Fragmentation of the ovary, which releases tissue mechanical tension and disrupts F-actin, can promote follicle activation and growth *via* Hippo signalling pathway, a well known mechanotransduction pathway (Kawamura et al., 2013). It has also been hypothesised that the regional difference in ECM stiffness at the outer cortex and the inner medulla may contribute to differential follicle growth or migration (Woodruff and Shea, 2011), which was supported by recent studies on primate (rhesus monkey) and bovine ovaries (Hornick et al., 2012; Henning and Laronda, 2021). These studies highlight the importance of applying tissue mechanics to understand how the follicle size, number and positioning are controlled robustly during ovarian development.

Follicle development is often associated with extensive tissue remodelling (Smith et al., 1999), and changes in tissue mechanical properties have been implicated to influence oocyte quality and fertility. Indeed, ovarian ageing is highly correlated with increased fibrosis and tissue stiffness (Amargant et al., 2020) due to increased expression or altered composition of ECM in the stroma (Briley et al., 2016). Interestingly, ovarian diseases such as polycystic ovarian syndrome (PCOS) (Wood et al., 2015) have densely collagenized and thickened cortex, and are characterised by anovulation, probably due to the lack of ECM degradation or abnormal ECM architecture. Similarly, endometriosis was shown to be associated with abnormal mechanical rigidity in the ECM (Huang et al., 2022). These studies suggest that proper follicle growth requires a biomechanically permissive environment, and calls for a need to better understand the mechanobiological principles governing folliculogenesis.

In this review, we first introduce the various stages of ovarian development and the classical molecular signalling pathways associated with each stage. We then discuss how mechanical stress may be generated by cells within the follicle, and the ECM and stromal cells at the extra-follicular level to impact follicle activation, growth and tissue patterning during ovarian development. We will also introduce the relevant biophysical techniques and reconstitutive biomimetic approaches that allow us to better investigate the underlying mechano-signalling pathways regulating folliculogenesis. Finally, we provide some future perspectives and highlight open questions for the field of ovarian mechanobiology.

## 2 Primordial follicle dormancy and activation

Prior to the primordial follicle formation, the female primordial germ cells first form cell cysts during embryonic development. In mouse, following birth, cyst breakdown occurs due to the invading GCs, which eventually surround the germ cells to form dormant primordial follicles (Lei and Spradling, 2013; Lei and Spradling, 2016). Bidirectional communication between the oocyte and the GCs has been shown to be essential at this stage, as the absence of either the oocyte or the GCs lead to follicle death (Eppig, 1979). The oocyte controls glycolysis within the GCs *via* the expression levels of glycolytic genes (Sugiura et al., 2005) and influences the level of luteinizing hormone receptor (LHR) in the GCs (Eppig et al., 1997). The GCs, on the other hand, play an active role in modulating the transcriptional activity and chromatin remodelling of the oocyte (De La Fuente

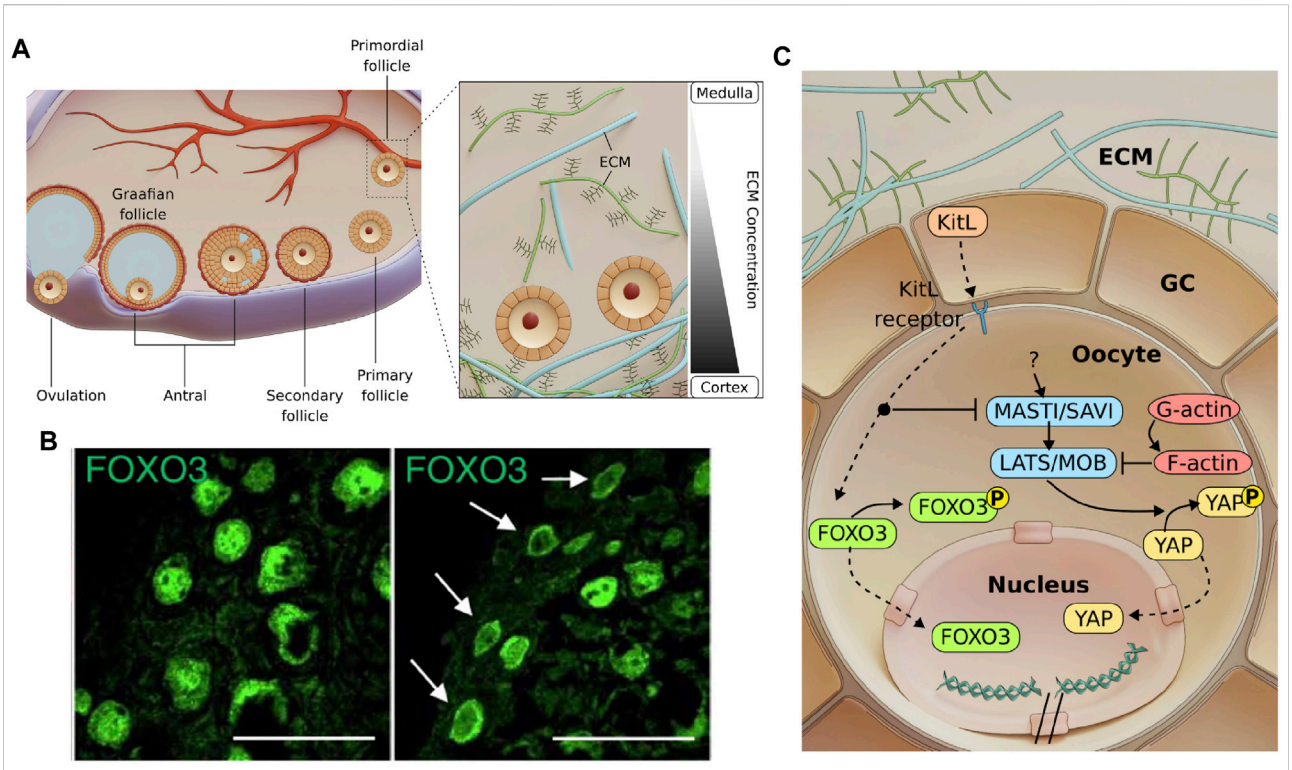


FIGURE 1
Follicle development and possible mechano-signalling pathways involved in primordial follicle activation. **(A)**. Mammalian folliculogenesis is classified into the primordial, primary, secondary and antral follicle stage. Antral follicles undergo ovulation to release the cumulus-oocyte complex before forming a corpus luteum. Inset: A gradient of ECM stiffness was proposed to extend from the soft ovarian medulla to the stiffer cortex where the dormant primordial follicles predominantly reside. **(B)**. Images showing that primordial follicles can be activated *via* ECM degradation (right), as indicated by FOXO3 cytoplasmic localisation compared to the nuclear localisation of FOXO3 in dormant primordial follicles (left). Scale bar: 50 μm. Images from (Nagamatsu et al., 2019). **(C)**. Mechanosensitive Akt and Hippo pathways govern primordial follicle activation. GCs express Kit ligands (KitL), which are bound to the Kit receptors on the oocyte. Activating the Akt pathway leads to phosphorylation of FOXO3 in the cytoplasm. The Akt pathway also disrupts the Hippo pathway at MST1 to allow for YAP nuclear localisation and downstream activation and growth of follicle. Mechanical stress exerted by the GCs may independently activate mechanosensitive proteins and contribute to dormancy.

and Eppig, 2001), and express Kit ligand (KitL) which binds to the c-Kit receptors on the oocyte to initiate AKT-mediated follicle activation (Jones and Pepling, 2013). The activation of dormant primordial follicles may also involve protein interactions from within the cell or across cell-cell junctions. In this section, we focus on the PI3K/Akt and Hippo pathways, two signalling pathways that have been identified as major regulators of primordial follicle activation. These pathways may be triggered by extrinsic mechanical stress imposed by the surrounding GCs and the ECM (Figure 1A, inset), which helps to maintain primordial follicle dormancy and ensure sufficient ovarian follicle reserve throughout the fertility period.

The Akt pathway is a well-established signalling pathway that responds to extracellular signals and promotes growth and survival (Hemmings and Restuccia, 2012). In response to a KitL, KIT proto-oncogene receptor tyrosine kinases (c-Kit) induce a kinase cascade, which in turn phosphorylates and activates AKT. Phosphorylated AKT then phosphorylates the transcription factor FOXO3 (Forkhead Box O3), leading to cytoplasmic localisation of FOXO3. It was demonstrated that FOXO3 nuclear export coincides with primordial follicle activation (John et al., 2008) and FOXO3 overexpression leads to increased reproductive capability in mice (Pelosi et al., 2013). Constitutively active FOXO3 was found to cause infertility (Liu et al., 2007), suggesting that nuclear FOXO3 is essential for dormancy regulation but only at a sufficient level. In contrast, the lack of FOXO3 resulted in uncontrolled follicle activation and early infertility (Castrillon et al., 2003), but did not affect follicular growth after activation (John et al., 2007). This suggests that FOXO3 specifically regulates the primordial follicle dormancy, and can be used as a reliable marker for primordial follicle activation.

Primordial follicles are mainly found at the cortex of the ovary, surrounded by abundant ECM. Recent work by Nagamatsu *et. al.* demonstrated that the cortical ECM of mouse ovaries provides mechanical stress to maintain the primordial follicles in their dormant state (Nagamatsu et al., 2019) (Figure 1B). In this study, they showed that the disruption

of collagen leads to FOXO3 translocation to the cytoplasm in primordial follicles, while application of external pressure restores nuclear FOXO3 and dormancy. Notably, primordial follicles that are under mechanical stress exhibit nuclear rotation. However, the mechanosensing mechanism for FOXO3 dynamics and how forces are related to nuclear rotation remains unknown. Of note, the oocytes expanded in size upon ECM abolishment, suggesting that they are physically compressed in their dormant state. The transient change in oocyte volume also implies fluid exchange between the oocyte and the surrounding GCs and possible volume regulation by hydraulic stress.

Apart from the Akt pathway, the Hippo pathway is another well known mechano-signalling pathway. The Hippo pathway can respond to various signals, such as ECM stiffness (Dupont et al., 2011), substrate stiffness (Thomasy et al., 2013), stretching (Aragona et al., 2013), cell geometry (Dupont et al., 2011), cell density (Zhao et al., 2007), cellular tension (Perez Gonzalez et al., 2018) and shear stress (Lee et al., 2017). These factors were integrated by the Hippo pathway to regulate various cellular processes such as growth, development and homeostasis (Wu and Guan, 2021). When the Hippo pathway is activated, the Yes-associated protein (YAP) becomes phosphorylated and localises to the cytoplasm, where it remains non-functional or gets degraded. However, when the Hippo pathway is disrupted, non-phosphorylated YAP translocates to the nucleus to form a transcription activation complex with TEA domain family members (TEAD 1-4), leading to expression of downstream genes. The Hippo pathway was found to play a role in follicle growth. Disruption of the Hippo pathway caused a primary ovarian insufficiency (POI)-like phenotype (St John et al., 1999), indicating that YAP might be necessary for follicle activation. This is further corroborated by a study of Kawamura *et al.*, who demonstrated that ovarian fragmentation can lead to F-actin polymerisation, increased nuclear YAP localisation and primordial follicle activation (Kawamura et al., 2013). Moreover, F-actin polymerisation itself leads to increased nuclear YAP localisation and follicle growth (Cheng et al., 2015), highlighting YAP's mechanosensing capability and its role in follicle activation.

Given that the dormant oocytes with nuclear FOXO3 are mechanically compressed (Nagamatsu et al., 2019), and that compressive stress is implicated in YAP signalling, this suggests a potential crosstalk between Akt pathway and Hippo pathway. There is evidence that the Hippo pathway functions downstream of the Akt pathway. In *Drosophila*, Borreguero-Muñoz et al. showed that AKT can directly disrupt the Hippo pathway (Figure 1C) (Borreguero-Muñoz et al., 2019). In mouse ovaries, the use of MK2206 (AKT inhibitor) not only suppressed follicle activation, but also led to an increase in pYAP-to-YAP ratio (Hu et al., 2019). This implies that AKT can disrupt Hippo signalling and trigger YAP nuclear localisation and follicle activation. This evidence points to the existence of a crosstalk between the Akt and Hippo pathways and should be carefully examined together in the context of primordial follicle activation.

The GCs surrounding the oocyte may also directly regulate oocyte functions through mechanotransduction (Figure 1C). Notably, the squamous GCs exhibit contractile stress fibres at the primordial follicle stage (Nagamatsu et al., 2019), and have flat morphology compared to the cuboidal GCs at the primary follicle stage. Is this change in morphology during activation a result of reduced compressive stress from ECM remodelling, or due to intrinsic change in GC contractility? Furthermore, since flat cells are often associated with high surface tension (Lecuit and Lenne, 2007), does it imply that the squamous GCs exert significant forces on the oocyte during dormancy, and the release of mechanical tension leads to follicle activation? Another open question is whether the GC mechanics can directly trigger the expression of KitL and downstream AKT-mediated activation in the oocyte. These questions will likely be addressed in the near future with the application of novel biophysical tools and *ex vivo* reconstitution approaches (see Section 6).

# 3 Mechano-signalling in pre-antral follicle development

Secondary follicle development is characterised by the development of the spindle shaped TCs overlying the basement membrane (BM) around the GCs (Figure 2A). It takes more than 30 days for primordial follicles to become secondary follicles in rat ovaries, and 120 days in the case of human ovaries (McGee and Hsueh, 2000). Sizes of secondary follicles range from 59 to 303 μm in diameter as measured across multiple species (Griffin et al., 2006). Secondary folliculogenesis is also marked by a rapid increase in oocyte volume, although the oocyte is observed to remain in meiotic arrest (DiLuigi et al., 2008). The ZP surrounding the oocyte becomes thicker and more prominent at this stage for most organisms (Albertini et al., 2001). Here we focus our discussion on three key components in secondary follicles that may potentially regulate their development *via* mechanical signalling.

## 3.1 Basement membrane

One of the most crucial internal components of the follicle is the BM. The basal lamina separating the TCs from the GCs is typically composed of isoforms of collagen IV and laminin (O'Shea et al., 1978), but the relative compositions change during folliculogenesis (Rodgers et al., 2003; Berkholtz et al., 2006). Fibronectin is not prominent in the BM of primordial and primary follicles, but its expression becomes stronger at the secondary follicle stage (Akkoyunlu et al., 2003; Heeren et al., 2015). BM is nano-porous and can allow size-dependent passage of molecules across it. Molecules with molecular weights lower

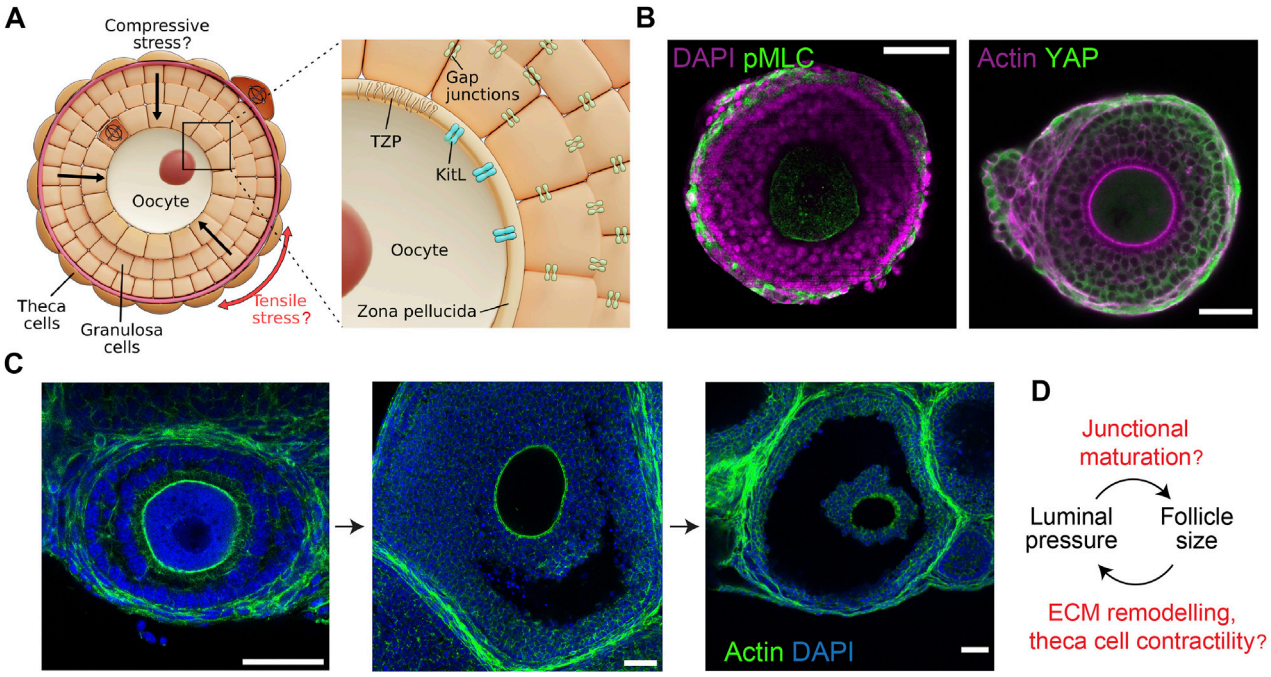


FIGURE 2
Mechano-hydraulic control of secondary and antral follicle development. **(A)**. During secondary follicle development, spindle-shaped TCs form around the basement membrane (dark red) and the GCs, potentially generating compressive stress within the follicle. Anisotropic stress pattern may guide cell division orientation in the TCs (circumferential) and the GCs (radial). Inset: Compressive stress may affect oocyte growth by modifying the oocyte-granulosa interactions mediated by the TZP and Kit ligands. Mechanical stress may also influence the GC proliferation *via* gap junction activities. **(B)**. Left: Isolated follicle immuno-stained for nuclei (DAPI) and phosphorylated-myosin light chain (pMLC), showing contractile TCs. Right: Follicle immuno-stained for actin and YAP, showing YAP nuclear localisation in the TCs only. Scale bar: 50 μm. **(C)**. Antral follicles immuno-stained for nuclei (DAPI) and actin. Luminal fluid accumulates at the intercellular space, eventually merging into a singly-resolved antrum that continues to expand till ovulation. Scale bar: 40 μm. **(D)**. Potential feedback loop between luminal pressure and follicle size: increased luminal pressure may trigger junctional maturation and follicle expansion through mechanosensing, while TC stiffening may control the final size of the follicles.

than 100 kDa can move freely through the BM, while those larger than 500 kDa cannot (Perloff et al., 1954; Shalgi et al., 1973). There exist reports on the pore size and thickness of BM in non-ovarian models (Abrams et al., 2000; Nicholas and Jacques, 2005; Halfter et al., 2013; Gaiko-Shcherbak et al., 2015), but these parameters have not been characterised in ovarian follicles. It is suggested that the composition, geometry, and crosslinking of the different proteins can dictate the BM mechanical properties (Miller, 2017; Ramos-Lewis and Page-McCaw, 2019), but the physical properties and mechanical functions of BM in folliculogenesis remain poorly characterised.

BM is common in most tissues in the body and is involved in a variety of diseases (Christensen et al., 2015). The thickness of the reticular BM (Saglani et al., 2006) and capillary BM (Ganda et al., 1983) has been implicated in asthma and diabetes respectively. It has been shown in epithelial cancers that cells can generate physical forces to invade the BM, leading to metastasis (Chang and Chaudhuri, 2019). Cancer-associated fibroblasts, myoepithelial cells and immune cells have also been implicated to regulate cell invasion. It is possible that similar conditions may apply to ovarian cancers. Hence, a deeper understanding of BM mechanics may inspire new approaches to modify the BM and help to prevent cancer progression.

The stiffness of the BM provides another key mechanical cue that may impact follicle development. The values of BM stiffness vary, ranging from ~55 kPa in mouse mesentery to 400-3,000 kPa in mouse renal tubules (Bhave et al., 2017; Glentis et al., 2017). In *Drosophila*, BM stiffness has been shown to determine the shape of developing egg chambers (Crest et al., 2017; Chen et al., 2019) and in altering cell migration *in vivo* in the central nervous system (Kim et al., 2014; Sánchez-Sánchez et al., 2017). Softer BM in the *Drosophila* wing disc allowed the wing disc to expand and flatten (Ramos-Lewis and Page-McCaw, 2019). Increased niche-derived mechanical stress due to increased BM stiffness in aged murine hair follicle stem cells has been observed to repress transcription, silence bivalent promoters and compromise stem cell potential (Koester et al., 2021). Recently it has also been shown that the intricate interplay between cell-cell and cell-BM interactions can contribute to stratified epithelial budding and branching morphogenesis of murine embryonic salivary glands (Wang et al., 2021).

In ovarian development, the BM has been suggested to protect ovarian follicles from physical damage (Figueiredo et al., 1995). It was proposed that the stiff basal lamina acts as a mechanical barrier for the proliferation and inward division of GCs (Da Silva-Buttkus et al., 2008): the GCs become more densely packed when they divide in a radial fashion within the follicles, thereby leading to the emergence of multi-layered GCs at this stage (Da Silva-Buttkus et al., 2008). Here we speculate that as the follicles grow in size, the BM may deform or undergo active remodelling to accommodate for the growing number of GCs contained within. How this changes the BM mechanical properties and regulates TC and GC functions will constitute an exciting topic for future research.

## 3.2 Granulosa cells

The internal geometry of a follicle loosely resembles that of a multicellular spheroid and it is plausible that mechanical cues affecting spheroid growth could also play a role in folliculogenesis. Increased mechanical stress inside tumour spheroids have been shown to lead to reduced cellular proliferation (Delarue et al., 2014; Dolega et al., 2017). As the spheroids grow, compressive stress can build up and promote cancer cell migration (Tse et al., 2012). It has been shown that the tumour spheroid growth responds to the stiffer mechano-environment through cytoskeletal remodelling and ROCK signalling pathway (Taubenberger et al., 2019). In the developing wing imaginal disc of *Drosophila*, the varied stress patterns between cells at the periphery (tension) and the cells in the centre (compression) lead to differential cell shape and division orientation (LeGoff et al., 2013). In secondary follicles, a similar mechanism may operate where follicle growth leads to the emergence of anisotropic stress pattern, characterised by radial compressive stress in the GC layer and tangential tensile stress at the theca layer. This may in turn direct cell division pattern and follicle morphogenesis (Figure 2A).

GCs secrete mucopolysaccharides which thicken and rigidify the ZP during follicle growth, thereby changing the mechanical environment around the oocytes (Ouni et al., 2020). Transzonal projections (TZPs) are hair-like projections from the GCs which invade the ZP and maintain direct contact with the oocyte (El-Hayek et al., 2018). The communication between the oocyte and its surrounding GCs is also mediated by connexin 37, a gap junction protein that is present at the tip of the TZPs (Simon et al., 1997; Ackert et al., 2001). Among the GCs, it is known that another type of gap junction proteins, connexin 43, connect the GCs and help with the exchange of nutrients like amino acids, glucose, ions, and cGMP in order to maintain cellular osmolarity and metabolism (Eppig, 1991; Winterhager and Kidder, 2015). Gene knockout studies have shown that connexin 37 are not only essential for oocyte maturation, they are also required for the luteinisation of GCs prior to ovulation (Simon et al., 1997). Loss of connexin 43 in mutant ovaries showed impaired GC proliferation, absence of antrum and developmentally incompetent oocytes (Ackert et al., 2001). Connexins in endothelial cells are known to be affected by shear stress and connexin 43 hemichannels in osteocytes are known to be opened by mechanical loading which helps in bone formation (Islam and Steward, 2019; Riquelme et al., 2020; Zhao et al., 2020). Whether connexins respond to mechanical stimuli and regulate follicle growth requires further investigation.

As the GCs become multi-layered, several signalling molecules–namely, BMP-15 and GDF-9—secreted by the oocyte start to impact this process (Dong et al., 1996; Moore et al., 2003). As described in the previous section, both these factors along with the Kit ligands and their receptors are believed to take part in a feedback loop between the oocyte and the GCs during this developmental stage (Eppig, 2001; Otsuka and Shimasaki, 2002). A similar bidirectional communication also exists between the GCs and TCs. While the Kit ligands and other growth factors from the GCs can prompt TC proliferation (Huang et al., 2001; Matsuura et al., 2002; Field et al., 2014; Shiomi-Sugaya et al., 2015), several BMPs secreted by the TCs are shown to impact GC proliferation (Lee et al., 2001; Glister et al., 2005) through the Wnt (Wang et al., 2010), Notch (Trombly et al., 2009), and Hedgehog (Wijgerde et al., 2005) signalling pathways. Though some of the signalling pathways have been implicated in tissue mechanics in non-ovarian developmental systems (Bonewald and Johnson, 2008; Brunt et al., 2017; Stassen et al., 2020; Yang et al., 2021), definitive evidence on potential mechano-regulation of these signalling pathways in the ovary remains to be established.

## 3.3 Theca cells

TCs are observed to appear at the periphery of secondary follicles that have at least two layers of GCs (Figure 2A) (Magoffin and Weitsman, 1994), and the process is gonadotropin independent. However, the origin of these cells remains debatable. While some believe that they originate from putative stem cells in ovaries (Honda et al., 2007), others suggest that they are derived from progenitor cells at the embryonic stage (Liu et al., 2015). Though not characterised, it is hypothesised that the cells are recruited from the ovarian stroma mediated by oocyte or GC secreted factors (Orisaka et al., 2009). TCs provide structural integrity to the follicles and produce important endocrine regulatory factors like androgens and other growth regulatory factors (Erickson et al., 1985; Young and McNeilly, 2010). Malfunction of TCs such as overproduction of TC-secreted androgens leads to PCOS (Azziz et al., 2009; Huang et al., 2010), which is a leading cause of female infertility that

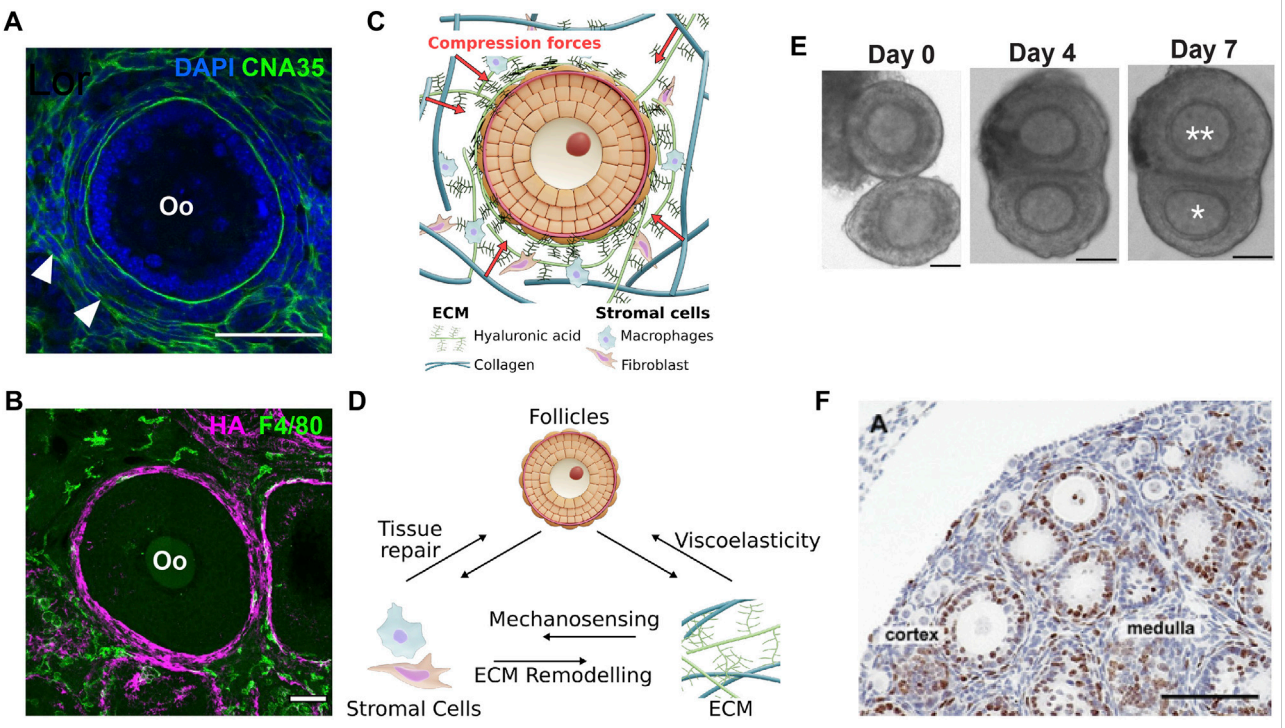


FIGURE 3
Stromal mechanics and inter-follicle dynamics in ovary development. **(A)**. Labelling of CNA35, a collagen-binding protein, shows the presence of basement membrane within the follicle and at the interstitial tissue (white arrowhead). Scale bar: 50 μm. **(B)**. Macrophages labelled with F4/80 were observed at the interstitial matrix, while the hyaluronic acid (HA) was highly expressed at the TC layer. Scale bar: 50 μm. **(C)**. Growing follicles may be mechanically confined by the surrounding ECM that comprises mainly of collagen and HA. **(D)**. Potential feedback interactions between stromal cells, ECM and follicle growth during ovarian development and ageing. Changes in ECM composition and mechanical properties may activate immune response from macrophages *via* mechanosensing pathways, or the stromal cells may actively remodel the ECM or participate in tissue repair during follicle death or post-ovulation. Changes in ECM viscoelastic properties may directly influence follicle growth. (**E–F**). Follicle-follicle interactions may provide additional mechanical signals to influence follicle growth. **(E)**. *In vitro* culture of follicle doublet shows that the follicles can merge over the course of 7 days to generate a dominant, growing follicle (double asterisks) and a "subordinate" follicle with limited growth (single asterisk). Scale bar: 50 μm. **(F)**. Evidence of close contact among pre-antral follicles in a P12 mouse ovary. Scale bar: 100 μm. Image from (Da Silva-Buttkus et al., 2008).

affects 4-20% of reproductively aged women worldwide (Deswal et al., 2020).

The theca layer is not homogeneous. The layer consists of the inner cells bordering the BM, also known as the *theca interna*, which secrete steroids that serve as substrates for estrogen production from the GCs (Magoffin et al., 1995). The outermost layers of TCs, the *theca externa*, are fibroblast-like in nature. They emerge at the later stages of follicle development, and are believed to play a role during ovulation. During follicle expansion in this growth phase, the theca layers are known to provide nutrients by developing vasculature through secreting vascular endothelial growth factor (VEGF) (Jones and Shikanov, 2019), thereby leading to increased oxygenation in the follicle (Shin et al., 2005).

While the role of TCs in steroid production and hormonal regulation is well documented, the structural and mechanical functions of these cells are less well understood. Recently, cancer-associated fibroblasts have been shown to self-organise to form a capsule around tumour cells and initiate mechanotransduction through active compression (Barbazan et al., 2021). The contractile TCs may wrap around the follicles in a similar fashion and provide compressive stress to coordinate signalling and growth within the follicle (Figure 2B). A recent study revealed the presence of mechanical heterogeneity within the follicle, where the TCs were shown to have a higher loss tangent (>20%) than the GCs, particularly during the antral follicle stage (Chan et al., 2021). The loss tangent here can be understood as the ratio between the cell's effective micro-viscosity and stiffness. A higher loss tangent of TCs therefore indicates greater energy dissipation and a more viscous response when subjected to mechanical stress. This may be associated with the increased hyaluronan production by the TCs (Figure 3B) (Amargant et al., 2020).

Despite growing evidence that mechanical signalling can impact follicle development, questions remain on how these mechanical forces are generated and maintained within the follicles. In particular, it is not known how GC proliferation, which may generate tissue pressure, is coupled to BM remodelling and TC-generated compressive stress during follicle development. Addressing this will require novel methods to quantify cellular dynamics, tissue mechanics and mechanosensing activities in the ovarian follicles (see Section 6).

## 4 Tissue hydraulics during antral follicle development and ovulation

A key morphological event is the emergence of a fluid-filled cavity (lumen) in the antral follicles (Figure 2C). Fluid cavity can generate hydrostatic pressure that can modulate cell-cell junctional remodelling or ion pump activities that in turn leads to organ or embryo size control and tissue patterning (Chan et al., 2019; Mosaliganti et al., 2019). A similar feedback mechanism may operate during antral follicle morphogenesis (Figure 2D). In addition, the lumen can act as a signalling hub to drive cell differentiation and cell shape changes around the lumen (Durdu et al., 2014; Ryan et al., 2019). In mammalian species, the antrum size varies from species to species: larger species such as human and bovine have larger follicles with the fluid comprising a substantial volume fraction (>95%) of the follicles at ovulation (Rodgers et al., 2001), while follicles of smaller species such as rats and mice contain less follicular fluid (Rodgers and Irving-Rodgers, 2010). Despite previous reports showing a correlation between antrum formation and oocyte maturation (Dumesic et al., 2015), the potential mechano-chemical functions of antrum in folliculogenesis remain enigmatic. Similarly, there remains limited studies on how the micro-lumen first emerge and coalesce into a single antrum, which is essential for late ovulation. One likely mechanism is osmotic regulation, where the antrum fluid could be sourced externally from the blood vessels formed around the TCs that encapsulate the antral follicles. Since the GCs lack functional tight junctions (Mora et al., 2012), it would not be possible to establish an osmotic gradient across the membrane granulosa with small ions like sodium. Instead, larger molecules such as hyaluronan and proteoglycans appeared to be trapped in the antrum which may generate a significant osmotic gradient to draw in fluid from the theca capillary (Clarke et al., 2006; Rodgers and Irving-Rodgers, 2010). However it remains unclear how the GCs actively secrete osmotically active molecules into the antrum, and if this is triggered by some signalling molecules released by the oocyte. One possible hypothesis is that some GCs within the follicle undergo apoptosis and are eliminated, thereby creating a hollow space that is filled with fluid. This process is also known as 'cavitation' (Sigurbjörnsdóttir et al., 2014). Cell death releases DNA fragments which, by virtue of their high molecular weights, may generate strong osmotic force to drive lumen expansion and coalescence (Clarke et al., 2006).

As mentioned, the GCs lack functional tight junctions but are connected by the gap junctions (Mora et al., 2012). This suggests that antrum development is not likely mediated by directed fluid transport through apico-basal polarity establishment, a mechanism widely reported in epithelial tissues and *in vitro* (Roignot et al., 2013). It is however worth noting that fluid accumulation can occur at the basolateral compartment through exocytosis or programmed cell shape changes (Schliffka and Maître, 2019). For example, during mouse blastocyst development, cytoplasmic vesicles are secreted and transported into intercellular space, leading to fluid accumulation at the onset of blastocoel formation (Ryan et al., 2019). During zebrafish gastrulation, mitotic rounding during cell divisions drive cell-cell contact disassembly in the deep cells, leading to increased interstitial fluid that translates to global tissue fluidization at the animal pole (Petridou et al., 2019). Whether these mechanisms operate during antral folliculogenesis constitute exciting topics for future research.

As the follicle matures into the Graafian follicle, it undergoes ovulation, which is characterised by a series of biochemical and morphological events that lead to its ultimate rupture and discharge of the mature oocyte out of the ovary. While it is known that elevated levels of luteinizing and follicle-stimulating hormones are required for ovulation, the precise mechanisms underlying this process remain unknown. Early studies pointed to both mechanical and enzymatic activities in follicle rupture during ovulation. Biophysical studies of follicle wall tension showed a large increase in wall extensibility prior to follicle rupture (Espey and Lipner, 1963), which is associated with the thinning of the theca wall due to ECM degradation by multiple proteolytic enzymes such as matrix metalloproteinases and plasmin (Curry and Smith, 2006). Interestingly, endothelin was proposed as a mechanotransduction gene that may facilitate follicular rupture and ovulation by binding to the smooth muscle at the theca externa, thereby leading to the contractile activity necessary for follicular rupture (Ko et al., 2006). Early studies on antrum fluid mechanics revealed no significant change in the hydrostatic pressure during antrum development (Espey and Lipner, 1963; Rondell, 1964; Bronson et al., 1979), potentially due to species difference and technical limitations. However, recent studies using servo-null micropressure system detects more than 40% increase in luminal pressure from preovulatory to late ovulatory phase in rat ovaries after human chorionic gonadotropin (hCG) stimulation (Matousek et al., 2001). Future studies leveraging on *ex vivo* culture and live imaging will provide better spatiotemporal dynamics of ovulation and will help to address how coordinated changes in lumen pressure, tissue mechanics and ECM remodelling lead to robust biophysical control of ovulation.

# 5 Mechanical signalling from extra-follicular environment

In addition to intra-follicular mechanical interactions, extra-follicular mechanical signals from the ovarian stroma also play a significant role in regulating follicle growth. The stroma is highly complex, consisting of nerves, vasculature, ECM, immune and fibroblast-like cells (Kinnear et al., 2020). In this section, we discuss how the ECM, stromal cells and follicle-follicle interactions may dynamically modulate the follicle's mechanical environment to orchestrate its development.

## 5.1 Interstitial extracellular matrix

It is well established that the ECM can initiate both mechanical and biochemical signalling cues. Historically, the role of ovarian fibrillar ECM such as collagen, laminin and fibronectin, and their changes during follicular progression were the focus of in-depth characterisation (Berkholtz et al., 2006). Across species, collagen IV is consistently expressed in the basal lamina throughout follicle development (Irving-Rodgers and Rodgers, 2005; Ouni et al., 2020). They were also detected in the BM of atretic follicles (Nakano et al., 2007) and the theca shell (Figure 3A). However, type IV alpha chains 3-6 in the BM decreases after the primary follicle stage (Irving-Rodgers and Rodgers, 2005). Collagen I and VI are expressed throughout the ovary (Woodruff and Shea, 2007; Ouni et al., 2019), with type I mainly located at the ovarian surface epithelium (Woodruff and Shea, 2007). Spatially, decellularized human and bovine ovarian tissues show that the collagen fibres are radially aligned at the cortex and anisotropic at the medulla (Laronda et al., 2015), suggesting a difference in ECM mechanics between the cortex and the medulla, possibly associated with the cortex having a higher stiffness. Recent work on human ovaries also revealed a significant thickening of ECM fibre bundles and increased ECM pore size from prepuberty to reproductive ageing, which is also associated with increased fibre orientation and straightness (Ouni et al., 2021). Similar to collagen, fibronectin was reported to increase in the stroma and theca layer during follicle growth (Woodruff and Shea, 2007). Laminin was also found to increase in the BM along with follicle development (Irving-Rodgers and Rodgers, 2005), with some isoforms present in the ovarian surface epithelium and TC layer (Rodgers et al., 2003).

Apart from fibrillar proteins, a key component of the ECM is hyaluronan or hyaluronic acid (HA), which is an anionic glycosaminoglycan (GAG) matrix with high molecular weight (typically 1,000-8,000 kDa) (Cowman et al., 2015; Monslow et al., 2015). Their ability to trap fluid and swell by osmotic pressure generates mechanical stress to influence the form and function of the tissue microenvironment (Voutouri and Stylianopoulos, 2018). In zebrafish, HA provides anisotropic extracellular stress to guide otic bud morphogenesis (Munjal et al., 2021) or cardiac valve development (Vignes et al., 2022). In murine adenocarcinoma models, administration of hyaluronidase resulted in tumour relaxation, indicating that HA provides tissue compressive resistance (Stylianopoulos et al., 2012; Voutouri and Stylianopoulos, 2018). In bovine and porcine ovaries, HA was localised at the theca layer, stroma, and vasculature (Parkes et al., 2021), similar to our observation in mice (Figure 3B). HA concentrations are known to surge and accumulate in the cumulus cell-oocyte complexes (COC) (Salustri et al., 1999), potentially related to their soft nature (Chen et al., 2016). In contrast to collagen, the roles of HA mechanics in regulating folliculogenesis and ovarian functions are relatively understudied.

There has been recent progress in understanding the spatio-temporal dynamics of interstitial ECM in the context of ovarian ageing, fibrosis, and inflammation. During ovarian ageing, the overall collagen deposition increases while the total HA content decreases, with no significant change in the molecular weights (Amargant et al., 2020). This fibrotic trend was again observed in human samples, indicating that the phenomenon may be conserved across species during ageing (Manuel et al., 2019). A recent study has also shown that this ageing-associated reduction in female reproductive lifespan can be rescued by reversing collagen fibrosis in mouse ovaries (Umehara et al., 2022). It is known that fibrosis mechanically alters the organ by significantly increasing tissue stiffness (Wells, 2013). However, it remains unclear as to how fibrotic ECM remodelling of the ovarian stroma mechanistically modulates follicle development in disease and ageing (Figure 3C).

## 5.3 Stromal cells

Apart from the ECM, the ovarian stroma is also populated with diverse cell types with myriad functions. Amongst the stromal cells, fibroblasts (Sahai et al., 2020) and macrophages (Kim and Nair, 2019) are known to have the capability to remodel ECM. Indeed, there have been extensive reports of ECM remodelling *via* matrix metalloproteinases, plasminogens, and associated enzymes in ovaries (Smith et al., 1999; Curry and Smith, 2006). However, which stromal cells are specifically involved during ECM deposition and degradation is not fully understood.

Macrophages make up the largest sub-population of immune cells in the ovaries (Kinnear et al., 2020), and are known to possess ECM remodelling capabilities which can enhance ovarian cancer progression (Busuttil et al., 2014; Cheng et al., 2019). In aged ovaries, it was reported that there was a shift in macrophage polarisation towards pro-tissue regenerative type (M2 polarisation) (Zhang et al., 2020) which is coherent with the observed inflammatory fibrotic ECM structure in aged ovaries (Briley et al., 2016; Rowley et al., 2020; Lliberos et al.,

2021), although the underlying mechanotransduction pathways remain unknown. Fibroblasts, in their highly contractile state, are generally associated with ECM deposition and remodelling (Sahai et al., 2020). While there have been several reports linking cancer-associated fibroblasts with ovarian cancer progression and tumour-ECM remodelling (Kenny et al., 2007; Thuwajit et al., 2018), little is known about how the ovarian fibroblast-like cells modulate the ovarian matrix during folliculogenesis. The study of ovarian fibroblasts is challenging due to a lack of suitable experimental platforms (Quiros et al., 2008). This is further compounded by the fact that fibroblasts lack a clear biomarker, and have been shown to be highly heterogeneous between and within organs (Chang et al., 2002).

## 5.4 Stromal cell-ECM-follicle feedback

While the stromal cells can actively remodel the ECM, ECM biomechanics can also reciprocally impact the stromal cell functions (Figure 3D). It has been shown that macrophage function, polarisation, and migration are influenced by ECM biomechanical and physical properties (McWhorter et al., 2015; Sridharan et al., 2019). For example, macrophages seeded onto stiff polyacrylamide gels were primed towards pro-inflammatory polarisation and exhibit podosome-dependent migration whereas on soft gels, macrophages were anti-inflammatory and showed fast ameboid-like migration (Petersen et al., 2012). Likewise, the ECM remodelling capability of fibroblasts is also dependent on physical cues from the environment–it was observed that high stiffness scaffolds increased fibroblast secretion of matrix metalloproteinase-1 (Petersen et al., 2012). Interestingly, we identified F4/80+ macrophages to be spatially associated with the HA 'shell' at the theca layer (Figure 3B), suggesting possible crosstalk between macrophage and HA. Active remodelling of ECM by the stromal cells may lead to changes in the ECM biomechanical properties, which will ultimately impact follicle growth and oocyte quality (Figure 3D). The stromal cells, particularly the macrophages, are known to be associated with atretic follicles across different species (Kasuya, 1995; Best et al., 1996; Petrovská et al., 1996; Gaytán et al., 1998) and in the ovulatory process (Brännström et al., 1993; Takaya et al., 1997), which suggests that the macrophages may play an active role in tissue clearing and wound healing processes during ovarian development and homeostasis. Ultimately, a system-level understanding of the feedback interactions between the stromal cells, ECM, and the follicles will help illuminate the underlying mechanobiological principles regulating ovarian folliculogenesis (Figure 3D).

## 5.5 Follicle-follicle interactions

Another source of mechanical signalling *in vivo* could be the direct contact between the follicles. In a seminal work by Spears *et al.* (Spears et al., 1996), they demonstrated that co-culture of two mouse follicles in contact can lead to follicle dominance, where one follicle invariably grows and becomes dominant while the other one shows arrested growth, as shown in Figure 3E. Notably, the suppressed follicles are not dying, as manual removal of the dominant follicle can induce subsequent growth of the suppressed follicle. In a follow-up paper, the authors further demonstrated that the dominant follicles also render the subordinate follicles more susceptible to lowered FSH concentrations, thereby inducing atresia in these follicles (Baker et al., 2001). These findings on how follicle-follicle contact determines follicle selection and fate may answer the question why only a certain number of follicles undergo size amplification and eventually ovulate during each reproductive cycle (6-7 ovulatory follicles in the case of mouse and only one in human). These findings are physiologically relevant as histological studies revealed that preantral follicles are often found in close contact with each other (Da Silva-Buttkus et al., 2008) (Figure 3F), and preovulatory follicles are found alongside less-developed antral follicles (Baker and SpearsN., 1999). These studies also prompt speculation if differential follicle growth can lead to distinct follicle positioning within the ovary during development. For example, in very young ovaries, the small primordial follicles are often found at the ovarian cortex while the larger growing follicles are found in the inner medulla. Later, as the mice grow past puberty, the ovary is characterised by numerous antral follicles that are found to be close to the ovarian surface, ready for ovulation. Whether such tissue patterning is mediated by follicle-follicle interactions and if these interactions play a similar role in human ovaries are exciting questions for the future.

In the above studies, the authors proposed the existence of a contact-mediated mechanism for follicle dominance and suppression, although the molecular mechanism was not addressed. Others have proposed that the growing follicles may secrete inhibitory signals such as anti-Müllerian hormone (AMH) and activin to maintain primordial or pre-antral follicle dormancy (Durlinger et al., 1999; Mizunuma et al., 1999). Here we propose that in addition to paracrine signalling, mechanical signals, such as the compressive stress exerted by one follicle on another, may provide further inhibitory signals to break the initial size symmetry and trigger differential growth. This corroborates with a recent atomic force microscopy (AFM) study which revealed that the large follicles are the mechanically dominant structures in the ovary that may transmit mechanical stress to the surrounding follicles (Hopkins et al., 2021).

# 6 Approaches to study ovarian mechanobiology

## 6.1 Biomechanical characterisation of ovarian mechanics

The concept of mechanobiology in ovarian biology is relatively new, and biophysical studies to quantify tissue mechanical properties in ovaries remain scarce. To date, AFM remains the primary tool to measure the ovarian biomechanical properties, such as the follicle and stromal stiffness during reproductive ageing and menopause (Amargant et al., 2020; Hopkins et al., 2021; Ouni et al., 2021). Here, the sample is indented with a cantilever attached to an AFM tip of known geometry and the applied force is measured from the bending angle of the cantilever. The surface stiffness is calculated by fitting the force indentation curves to known mechanical models. Of note, while these studies were conducted on different layers of tissues, tissue sectioning itself may potentially release tissue stress and perturb the mechanical state of the ovaries (Stylianopoulos et al., 2012). Micropipette aspiration is another technique that can be used to probe the surface tension of a cell or tissue, based on the Laplace Law (Maître et al., 2016; Chan et al., 2019). Furthermore, by tracking the dynamics of the aspirated 'tongue' of the tissue, the tissue viscosity can be extracted (Guevorkian et al., 2010). Another well established technique to infer cellular or tissue tension is laser ablation. Here, UV or femtosecond-pulsed near-infrared lasers are used to cut biological tissues locally. Upon disruption, the speed and direction of recoil of the cell-cell junctions or tissue segment can be used to infer the magnitude and orientation of local cell or tissue tension (Sugimura et al., 2016).

The above-mentioned techniques are mostly confined to measuring the surface mechanics of tissues. To quantify mechanical properties within the tissues, other tools such as magnetic tweezer have been developed. Here, magnetic beads or ferrofluid oil droplets are introduced into tissues, which can be manipulated in the presence of an externally applied magnetic field. If the magnetic properties of the beads or droplets is known, the force-displacement profiles can be used to calculate the local stiffness and viscosity of the tissue (Mongera et al., 2018; Zhu et al., 2020; D'Angelo and Solon, 2020). In recent years, label-free, non-invasive approaches have also been developed to directly 'image' the mechanical landscape of tissue interior. For example, Brillouin microscopy has been developed to measure micro-viscoelasticity of cells and tissues with high spatial resolution in 3D (Prevedel et al., 2019). It relies on the interaction and inelastic scattering of monochromatic laser light from thermally driven acoustic phonons at high frequencies. The scattered light spectrum is indicative of the material's local mechanical properties, as shown by recent work on mouse ovaries and living embryos (Chan et al., 2021; Bevilacqua et al., 2022). Another imaging technique is second harmonic generation microscopy, which probes the tissue composition and the molecular structure of collagen with high sensitivity and specificity. It has been used extensively to study alterations in fibrillar collagens in scar tissues of skin, lung, heart and eyes (Mostaço-Guidolin et al., 2017), as well as in mouse ovaries (Watson et al., 2012; Bochner et al., 2015).

Besides measuring tissue material properties, another important parameter that remains poorly characterised is the mechanical stress within ovaries. To evaluate mechanical stress in tissue interior, several techniques have been developed in recent years. For example, hydrogel-based deformable beads have been developed, which allows ones to quantify the local stress fields in living tissues, as demonstrated in zebrafish and *in vitro* cell aggregates (Dolega et al., 2017; Mohagheghian et al., 2018; Träber et al., 2019; Souchaud et al., 2022). Larger beads have been used to infer the contractile stress exerted by cells. For example, a recent study shows that the compressive stress exerted by contractile cardiomyocytes can be quantified by measuring the change in volume of large gelatin beads of known compressibility, before and after cardiomyocyte enwrapment (He et al., 2021). To quantify tissue pressure in 3D tissues, laser ablation, combined with the tracking of tissue outflow from the abscission site, allows one to compare the mechanical state of compressed tumour aggregates (Barbazan et al., 2021). While many of these techniques have yet to be applied to mammalian ovaries, we foresee that such quantitative studies will yield important insights to advance the field of ovarian biology.

## 6.2 Quantitative imaging of ovarian dynamics

Recent advancement in deep tissue imaging has allowed us to gain insights into follicle dynamics within the ovary. One such tool is light-sheet microscopy. This technique has been increasingly used in the last few years for rapid visualisation of live specimens, particularly for deep tissues where a single sample plane is excited optically by a light sheet and fluorescent images are captured by a camera placed perpendicular to the excitation (Power and Huisken, 2017). This technique allows an enhanced image quality and does not rely on physical sectioning of the tissues. Combined with tissue clearing, light-sheet microscopy has been used to quantify follicle morphometrics in pig ovaries (Lin et al., 2017) and human ovaries that revealed marked architectural remodelling in certain ECM biomarkers at prepubertal, reproductive-age and menopausal stages (Ouni et al., 2022). Another powerful tool for studying follicle development *in vivo* is optical coherence tomography, which allows imaging of ovaries *in situ* and in real time with micron-scale imaging resolution (Wang et al., 2015; Watanabe et al., 2015). Widely used in ophthalmology and

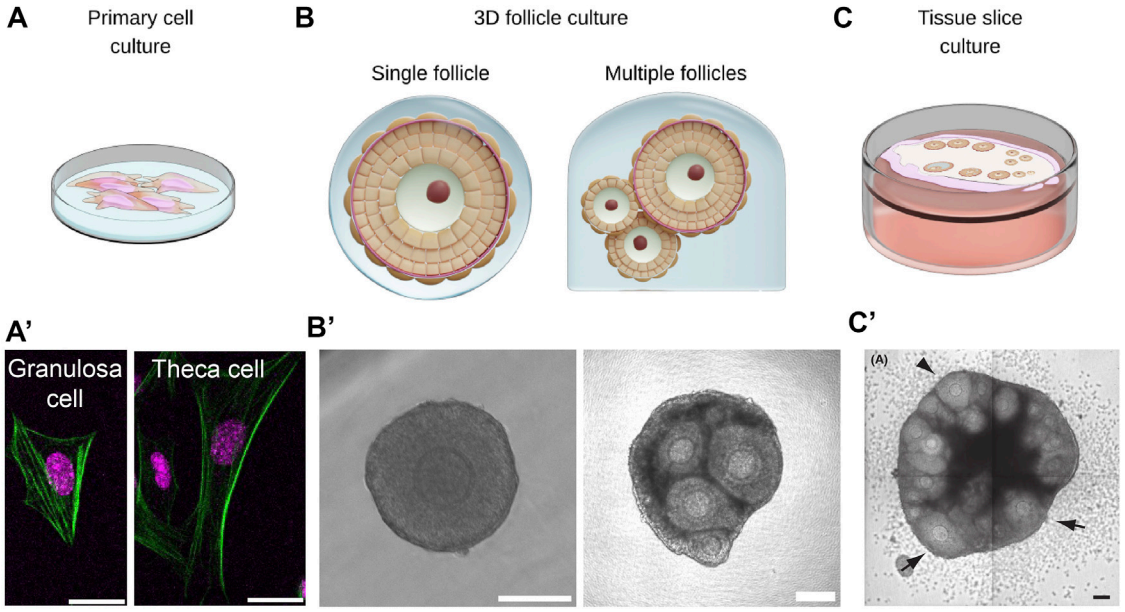


FIGURE 4
Multiscale *ex vivo* reconstitution approaches are required for integrative understanding of ovarian mechanobiology. **(A,A')**. Primary cells such as the theca cells and the granulosa cells can be isolated from bulk ovaries for studying single cell mechanics or cell-cell interactions in co-culture systems. Scale bar: 20 μm. **(B,B')**. Isolated follicles can be cultured in 3D hydrogel for studying morphogenesis and the impact of mechanical confinement on follicle growth. Aggregates of follicles can also be cultured in 3D to study follicle-follicle interactions. Scale bar: 100 μm. **(C,C')**. Ovarian tissue slices can be cultured *ex vivo* to study collective dynamics of follicles and ovulation during development. Scale bar: 100 μm. Image from (Komatsu and Masubuchi, 2017).

endoscopic studies of luminal organ systems (Swanson et al., 1993; Fujimoto et al., 2000), there has been a growing number of work utilising this approach to study reproductive events when combined with intra-vital imaging, such as in mouse ovary and oviduct (Burton et al., 2015), co-operative sperm flow (Wang and Larina, 2018), and oocyte and embryo transport during pre-implantation development (Wang and Larina, 2021).

## 6.3 *Ex vivo* reconstitution

Owing to the multifactorial complexity in the tissue microenvironment, it is challenging to dissect the individual contribution of mechanical signals on follicle growth. Here, *ex vivo* reconstitution of follicles provides a bottom-up approach to understand how the follicle's mechanical environment impacts its maturation. For example, when cultured in 3D alginate hydrogel (Figure 4B,B′), secondary follicles in the softer matrix showed increased follicle growth, theca development, antrum formation and higher oocyte quality, suggesting that mechanical confinement can regulate follicle development (Xu et al., 2006b; West et al., 2007; West-Farrell et al., 2009). To allow follicle expansion at later stages of development, degradable hydrogel was developed, such as the fibrin-alginate interpenetrating network (Shikanov et al., 2011). Recently, poly(ethylene glycol) (PEG) hydrogels have also been developed to allow better control of matrix stiffness and pore size that promotes optimal follicle growth (Kim et al., 2016). Others have further incorporated mechanical heterogeneities within the gel, where microfluidics was employed to encapsulate follicles within a gel that is made of a soft inner core of collagen and stiff alginate shell (Choi et al., 2014; He, 2017). This was proposed to better mimic the supposedly soft medulla and stiffer cortex of the ovary that are required for follicles to develop to the antrum stage.

In addition to stiffness, ovarian tissues may be viscoelastic and exhibit stress relaxation, which measures how fast the material dissipates its internal stress in response to externally applied deformation. Recent studies demonstrated that hydrogels that exhibit slow relaxation provide greater mechanical confinement to hinder spheroid growth and cell proliferation (Nam et al., 2019; Indana et al., 2021). As discussed before (see Section 5), HA is a major component of ovarian ECM that is highly expressed in the ovarian stroma and TCs. Their ability to trap interstitial fluid and resist compression (Irving-Rodgers and Rodgers, 2005) may generate a slow stress relaxation environment to confine follicle growth. In future, it will be instructive to study follicle growth when cultured in gels of different stress relaxation profiles. Also, how HA remodelling impacts follicle growth and oocyte functions during ovarian ageing will be an exciting topic for future research.

Moving beyond single follicle studies, other works have attempted to study follicle dynamics using ovarian tissue slices (Komatsu and Masubuchi, 2017; Komatsu et al., 2018). By growing tissues on culture inserts, the authors were able to image and quantify pre-antral follicle development, ovulation and atresia (Figure 4C,C′). This approach may provide a good platform to study collective dynamics of follicles, such as differential growth and follicle dominance as discussed in previous sections.

To investigate mechanical interactions between the oocyte and somatic cells, it is noteworthy that there exist protocols for isolating and culturing primary GCs and TCs *in vitro* (Li and Hearn, 2000; Choi et al., 2014; Tian et al., 2015) (Figure 4A,A′). This provides a unique opportunity to probe their biomechanical properties and mechanosensing properties, which is not easily accessible *in vivo*. By adding complexity to such systems, such as TC-follicle or GC-oocyte co-culture systems, one could also gain new insights into how the follicle components mechanically interact with each other.

## 7 Conclusion

With the advancements in mechanobiology and experimental tools, we are now at a unique position to address how mechanical signals act in concert with hormonal signalling to control robust mammalian folliculogenesis. While we have discussed new biophysical techniques that allow us to dissect the intricate mechanical interactions at the intra- and extra-follicular level, *in vivo* perturbations remain challenging given the multiscale complexity of the organ. An attractive approach to address these experimental limitations is theoretical modelling and computational simulations (Johnson et al., 2015; Fischer et al., 2021; Fischer-Holzhausen and Röblitz, 2022), which allow us to tune mechanical parameters and 'perturb' the system *in silico* in order to assess functional sufficiency of these mechanical signals in ovarian growth.

Understanding ovarian mechanobiology has profound implications in understanding ovarian ageing, cancer, and disease, which are often associated with impaired tissue mechanics and misregulated mechano-signalling pathways. From the clinical perspective, a 'mechanical' understanding of follicular development has important implications in assisted reproductive technology such as *in vitro* fertilisation (IVF) and *in vitro* maturation (IVM). Both approaches generate relatively low success rates, potentially due to the removal of the follicle's mechanical environment that helps to ensure oocyte health. The design of novel biomaterials to provide appropriate mechanical signals may contribute to future improvement of IVF and IVM and even oocyte rejuvenation. Of note, the ovaries are similar to many organs in terms of tissue architecture and functions, and similar biophysical principles may operate in these diverse systems. Indeed, recent work revealed the role of mechanics in lymphocyte infiltration and stromal remodelling during lymph node expansion (Assen et al., 2022; Horsnell et al., 2022) and mammalian kidney development (Viola et al., 2022).

We end this review by proposing several questions for future research. Does mechanotransduction play a role in regulating oocyte growth? If so, what are the key mechanosensors involved in the process? How are the various mechanical signals integrated across multiple scales to influence follicle maturation? At the tissue level, how are mechanics and hormonal signalling coupled to generate robust follicle patterns in terms of their number, size and positions? Finally, does follicle-follicle interactions play a role in follicle death (atresia) that is known to take place during ovarian development? Recent work revealed that cell-cell fluid exchange can lead to collective cell death and the selection of functional eggs in *C. elegans* during oogenesis (Chartier et al., 2021), suggesting that germ cell fate can be controlled by environmental factors. Ultimately, it will be exciting to explore if the different spatiotemporal dynamics of follicle development in diverse mammalian species are governed by the same underlying mechanobiological principles.

## Author contributions

All authors participated in the writing process. CC conceptualized the review.

## Funding

CC. is supported by the Ministry of Education under the Research Centres of Excellence programme through the Mechanobiology Institute and the Department of Biological Sciences at the National University of Singapore (A-0003467-27-00, A-0007085-00-00), and the Bia-Echo Asia Centre for Female Reproductive Longevity & Equality at the National University of Singapore (A-0006323-00-00).

## Acknowledgments

We thank members of the Chan laboratory, Tsuyoshi Hirashima and Yuchen Long for helpful comments on the manuscript, and Diego Pitta de Araujo for illustration. We apologise to the authors whose work could not be highlighted due to space limitations.

## Conflict of interest

The authors declare that the research was conducted in the absence of any commercial or financial relationships that could be construed as a potential conflict of interest.

## Publisher's note



## References

Abrams, G. A., Goodman, S. L., Nealey, P. F., Franco, M., and Murphy, C. J. (2000). Nanoscale topography of the basement membrane underlying the corneal epithelium of the rhesus macaque. *Cell Tissue Res.* 299 (1), 39–46. doi:10.1007/s004419900074

Ackert, C. L., Gittens, J. E., O'Brien, M. J., Eppig, J. J., and Kidder, G. M. (2001). Intercellular communication via connexin43 gap junctions is required for ovarian folliculogenesis in the mouse. *Dev. Biol.* 233 (2), 258–270. doi:10.1006/dbio.2001.0216

Akkoyunlu, G., Demir, R., and Üstünel, İ. (2003). Distribution patterns of TGF-α, laminin and fibronectin and their relationship with folliculogenesis in rat ovary. *Acta Histochem.* 105 (4), 295–301. doi:10.1078/0065-1281-00717

Albertini, D. F., Combelles, C. M., Benecchi, E., and Carabatsos, M. J. (2001). Cellular basis for paracrine regulation of ovarian follicle development. *Reproduction* 121 (5), 647–653. doi:10.1530/rep.0.1210647

Amargant, F., Manuel, S. L., Tu, Q., Parkes, W. S., Rivas, F., Zhou, L. T., et al. (2020). Ovarian stiffness increases with age in the mammalian ovary and depends on collagen and hyaluronan matrices. *Aging Cell* 19 (11), e13259. doi:10.1111/acel.13259

Aragona, M., Panciera, T., Manfrin, A., Giulitti, S., Michielin, F., Elvassore, N., et al. (2013). A mechanical checkpoint controls multicellular growth through YAP/TAZ regulation by actin-processing factors. *Cell* 154 (5), 1047–1059. doi:10.1016/j.cell.2013.07.042

Assen, F. P., Abe, J., Hons, M., Hauschild, R., Shamipour, S., Kaufmann, W. A., et al. (2022). Multitier mechanics control stromal adaptations in the swelling lymph node. *Nat. Immunol.* 23 (8), 1246–1255. doi:10.1038/s41590-022-01257-4

Azziz, R., Carmina, E., Dewailly, D., Diamanti-Kandarakis, E., Escobar-Morreale, H. F., Futterweit, W., et al. (2009). The androgen excess and PCOS society criteria for the polycystic ovary syndrome: The complete task force report. *Fertil. Steril.* 91 (2), 456–488. doi:10.1016/j.fertnstert.2008.06.035

Baker, S. J., Sršeň, V., Lapping, R., and Spears, N. (2001). Combined effect of follicle-follicle interactions and declining follicle-stimulating hormone on murine follicle health *in vitro*. *Biol. Reprod.* 65 (4), 1304–1310. doi:10.1095/biolreprod65.4.1304

Baker, S., and SpearsN. (1999). The role of intra-ovarian interactions in the regulation of follicle dominance. *Hum. Reprod. Update* 5 (2), 153–165. doi:10.1093/humupd/5.2.153

Barbazan, J., Pérez-González, C., Gómez-González, M., Dedenon, M., Richon, S., Latorre, E., et al. (2021). Cancer-associated fibroblasts actively compress cancer cells and modulate mechanotransduction. *Cell Biol*. doi:10.1101/2021.04.05.438443

Berkholtz, C. B., Shea, L. D., and Woodruff, T. K. (2006). Extracellular matrix functions in follicle maturation. *Semin. Reprod. Med.* 24 (4), 262–269. doi:10.1055/s-2006-948555

Best, C. L., Pudney, J., Welch, W. R., Burger, N., and Hill, J. A. (1996). Localization and characterization of white blood cell populations within the human ovary throughout the menstrual cycle and menopause. *Hum. Reprod.* 11 (4), 790–797. doi:10.1093/oxfordjournals.humrep.a019256

Bevilacqua, C., Gomez, J. M., Fiuza, U. M., Chan, C. J., Wang, L., Hambura, S., et al. (2022). High-resolution line-scan Brillouin microscopy for live-imaging of mechanical properties during embryo development. *Bioengineering*. doi:10.1101/2022.04.25.489364

Bhave, G., Colon, S., and Ferrell, N. (2017). The sulfilimine cross-link of collagen IV contributes to kidney tubular basement membrane stiffness. *Am. J. Physiol. Ren. Physiol.* 313 (3), F596–F602. doi:10.1152/ajprenal.00096.2017

Bochner, F., Fellus-Alyagor, L., Kalchenko, V., Shinar, S., and Neeman, M. (2015). A novel intravital imaging window for longitudinal microscopy of the mouse ovary. *Sci. Rep.* 5 (1), 12446. doi:10.1038/srep12446

Bonewald, L. F., and Johnson, M. L. (2008). Osteocytes, mechanosensing and Wnt signaling. *Bone* 42 (4), 606–615. doi:10.1016/j.bone.2007.12.224

Borreguero-Muñoz, N., Fletcher, G. C., Aguilar-Aragon, M., Elbediwy, A., Vincent-Mistiaen, Z. I., and Thompson, B. J. (2019). The Hippo pathway integrates PI3K-Akt signals with mechanical and polarity cues to control tissue growth. *PLoS Biol.* 17 (10), e3000509. doi:10.1371/journal.pbio.3000509

Brännström, M., Mayrhofer, G., and Robertson, S. A. (1993). Localization of leukocyte subsets in the rat ovary during the periovulatory period. *Biol. Reprod.* 48 (2), 277–286. doi:10.1095/biolreprod48.2.277

Briley, S. M., Jasti, S., McCracken, J. M., Hornick, J. E., Fegley, B., Pritchard, M. T., et al. (2016). Reproductive age-associated fibrosis in the stroma of the mammalian ovary. *Reproduction* 152 (3), 245–260. doi:10.1530/REP-16-0129

Bronson, R. A., Bryant, G., Balk, M. W., and Emanuele, N. (1979). Intrafollicular pressure within preovulatory follicles of the pig. *Fertil. Steril.* 31 (2), 205–213. doi:10.1016/s0015-0282(16)43824-0

Brunt, L. H., Begg, K., Kague, E., Cross, S., and Hammond, C. L. (2017). Wnt signalling controls the response to mechanical loading during Zebrafish joint development. *Development* 144, 2798–2809. doi:10.1242/dev.153528

Burton, J. C., Wang, S., Stewart, C. A., Behringer, R. R., and Larina, I. V. (2015). High-resolution three-dimensional *in vivo* imaging of mouse oviduct using optical coherence tomography. *Biomed. Opt. Express* 6 (7), 2713–2723. doi:10.1364/BOE.6.002713

Busuttil, R. A., George, J., Tothill, R. W., Ioculano, K., Kowalczyk, A., Mitchell, C., et al. (2014). A signature predicting poor prognosis in gastric and ovarian cancer represents a coordinated macrophage and stromal response. *Clin. Cancer Res.* 20 (10), 2761–2772. doi:10.1158/1078-0432.CCR-13-3049

Castrillon, D. H., Miao, L., Kollipara, R., Horner, J. W., and DePinho, R. A. (2003). Suppression of ovarian follicle activation in mice by the transcription factor Foxo3a. *Science* 301 (5630), 215–218. doi:10.1126/science.1086336

Chan, C. J., Bevilacqua, C., and Prevedel, R. (2021). Mechanical mapping of mammalian follicle development using Brillouin microscopy. *Commun. Biol.* 4 (1), 1133. doi:10.1038/s42003-021-02662-5

Chan, C. J., Costanzo, M., Ruiz-Herrero, T., Mönke, G., Petrie, R. J., Bergert, M., et al. (2019). Hydraulic control of mammalian embryo size and cell fate. *Nature* 571 (7763), 112–116. doi:10.1038/s41586-019-1309-x

Chan, C. J., Heisenberg, C. P., and Hiiragi, T. (2017). Coordination of morphogenesis and cell-fate specification in development. *Curr. Biol.* 27 (18), R1024–R1035. doi:10.1016/j.cub.2017.07.010

Chang, H. Y., Chi, J. T., Dudoit, S., Bondre, C., van de Rijn, M., Botstein, D., et al. (2002). Diversity, topographic differentiation, and positional memory in human fibroblasts. *Proc. Natl. Acad. Sci. U. S. A.* 99 (20), 12877–12882. doi:10.1073/pnas.162488599

Chang, J., and Chaudhuri, O. (2019). Beyond proteases: Basement membrane mechanics and cancer invasion. *J. Cell Biol.* 218 (8), 2456–2469. doi:10.1083/jcb.201903066

Chartier, N. T., Mukherjee, A., Pfanzelter, J., Fürthauer, S., Larson, B. T., Fritsch, A. W., et al. (2021). A hydraulic instability drives the cell death decision in the nematode germline. *Nat. Phys.* 17 (8), 920–925. doi:10.1038/s41567-021-01235-x

Chen, D. Y., Crest, J., Streichan, S. J., and Bilder, D. (2019). Extracellular matrix stiffness cues junctional remodeling for 3D tissue elongation. *Nat. Commun.* 10 (1), 3339. doi:10.1038/s41467-019-10874-x

Chen, X., Bonfiglio, R., Banerji, S., Jackson, D. G., Salustri, A., and Richter, R. P. (2016). Micromechanical analysis of the hyaluronan-rich matrix surrounding the oocyte reveals a uniquely soft and elastic composition. *Biophys. J.* 110 (12), 2779–2789. doi:10.1016/j.bpj.2016.03.023

Cheng, H., Wang, Z., Fu, L., and Xu, T. (2019). Macrophage polarization in the development and progression of ovarian cancers: An overview. *Front. Oncol.* 9, 421. doi:10.3389/fonc.2019.00421

Cheng, Y., Feng, Y., Jansson, L., Sato, Y., Deguchi, M., Kawamura, K., et al. (2015). Actin polymerization-enhancing drugs promote ovarian follicle growth mediated by the Hippo signaling effector YAP. *FASEB J.* 29 (6), 2423–2430. doi:10.1096/fj.14-267856

Choi, J. K., Agarwal, P., Huang, H., Zhao, S., and He, X. (2014). The crucial role of mechanical heterogeneity in regulating follicle development and ovulation with

engineered ovarian microtissue. *Biomaterials* 35 (19), 5122–5128. doi:10.1016/j.biomaterials.2014.03.028

Choi, Y., and Rajkovic, A. (2006). Genetics of early mammalian folliculogenesis. *Cell. Mol. Life Sci.* 63 (5), 579–590. doi:10.1007/s00018-005-5394-7

Christensen, A. P., Patel, S. H., Grasa, P., Christian, H. C., and Williams, S. A. (2015). Oocyte glycoproteins regulate the form and function of the follicle basal lamina and theca cells. *Dev. Biol.* 401 (2), 287–298. doi:10.1016/j.ydbio.2014.12.024

Clarke, H. G., Hope, S. A., Byers, S., and Rodgers, R. J. (2006). Formation of ovarian follicular fluid may be due to the osmotic potential of large glycosaminoglycans and proteoglycans. *Reproduction* 132 (1), 119–131. doi:10.1530/rep.1.00960

Cowman, M. K., Schmidt, T. A., Raghavan, P., and Stecco, A. (2015). Viscoelastic properties of hyaluronan in physiological conditions. *F1000Res.* 4, 622. doi:10.12688/f1000research.6885.1

Crest, J., Diz-Muñoz, A., Chen, D. Y., Fletcher, D. A., and Bilder, D. (2017). Organ sculpting by patterned extracellular matrix stiffness. *eLife* 6, e24958. doi:10.7554/eLife.24958

Curry, T., and Smith, M. (2006). Impact of extracellular matrix remodeling on ovulation and the folliculo-luteal transition. *Semin. Reprod. Med.* 24 (4), 228–241. doi:10.1055/s-2006-948552

Da Silva-Buttkus, P., Jayasooriya, G. S., Mora, J. M., Mobberley, M., Ryder, T. A., Baithun, M., et al. (2008). Effect of cell shape and packing density on granulosa cell proliferation and formation of multiple layers during early follicle development in the ovary. *J. Cell Sci.* 121 (23), 3890–3900. doi:10.1242/jcs.036400

D'Angelo, A., and Solon, J. (2020). Application of mechanical forces on Drosophila embryos by manipulation of microinjected magnetic particles. *Bio. Protoc.* 10 (9), e3608. doi:10.21769/BioProtoc.3608

De La Fuente, R., and Eppig, J. J. (2001). Transcriptional activity of the mouse oocyte genome: Companion granulosa cells modulate transcription and chromatin remodeling. *Dev. Biol.* 229 (1), 224–236. doi:10.1006/dbio.2000.9947

Delarue, M., Montel, F., Vignjevic, D., Prost, J., Joanny, J. F., and Cappello, G. (2014). Compressive stress inhibits proliferation in tumor spheroids through a volume limitation. *Biophys. J.* 107 (8), 1821–1828. doi:10.1016/j.bpj.2014.08.031

Deswal, R., Narwal, V., Dang, A., and Pundir, C. S. (2020). The prevalence of polycystic ovary syndrome: A brief systematic review. *J. Hum. Reprod. Sci.* 13 (4), 261–271. doi:10.4103/jhrs.JHRS_95_18

DiLuigi, A., Weitzman, V. N., Pace, M. C., Siano, L. J., Maier, D., and Mehlmann, L. M. (2008). Meiotic arrest in human oocytes is maintained by a Gs signaling pathway. *Biol. Reprod.* 78 (4), 667–672. doi:10.1095/biolreprod.107.066019

Dolega, M. E., Delarue, M., Ingremeau, F., Prost, J., Delon, A., and Cappello, G. (2017). Cell-like pressure sensors reveal increase of mechanical stress towards the core of multicellular spheroids under compression. *Nat. Commun.* 8 (1), 14056. doi:10.1038/ncomms14056

Dong, J., Albertini, D. F., Nishimori, K., Kumar, T. R., Lu, N., and Matzuk, M. M. (1996). Growth differentiation factor-9 is required during early ovarian folliculogenesis. *Nature* 383 (6600), 531–535. doi:10.1038/383531a0

Dumesic, D. A., Meldrum, D. R., Katz-Jaffe, M. G., Krisher, R. L., and Schoolcraft, W. B. (2015). Oocyte environment: Follicular fluid and cumulus cells are critical for oocyte health. *Fertil. Steril.* 103 (2), 303–316. doi:10.1016/j.fertnstert.2014.11.015

Dupont, S., Morsut, L., Aragona, M., Enzo, E., Giulitti, S., Cordenonsi, M., et al. (2011). Role of YAP/TAZ in mechanotransduction. *Nature* 474 (7350), 179–183. doi:10.1038/nature10137

Durdu, S., Iskar, M., Revenu, C., Schieber, N., Kunze, A., Bork, P., et al. (2014). Luminal signalling links cell communication to tissue architecture during organogenesis. *Nature* 515 (7525), 120–124. doi:10.1038/nature13852

Durlinger, A. L. L., Kramer, P., Karels, B., Jong, F. H. D., Uilenbroek, J. T. J., Grootegoed, J. A., et al. (1999). Control of primordial follicle recruitment by anti-Müllerian hormone in the mouse ovary. *Endocrinology* 140 (12), 5789–5796. doi:10.1210/endo.140.12.7204

El-Hayek, S., Yang, Q., Abbassi, L., FitzHarris, G., and Clarke, H. J. (2018). Mammalian oocytes locally remodel follicular architecture to provide the foundation for germline-soma communication. *Curr. Biol.* 28 (7), 1124–1131. e3. doi:10.1016/j.cub.2018.02.039

Eppig, J. J. (1979). A comparison between oocyte growth in coculture with granulosa cells and oocytes with granulosa cell-oocyte junctional contact maintained *in vitro*. *J. Exp. Zool.* 209 (2), 345–353. doi:10.1002/jez.1402090216

Eppig, J. J. (1991). Intercommunication between mammalian oocytes and companion somatic cells. *Bioessays* 13 (11), 569–574. doi:10.1002/bies.950131105

Eppig, J. J. (1977). Mouse oocyte development *in vitro* with various culture systems. *Dev. Biol.* 60 (2), 371–388. doi:10.1016/0012-1606(77)90135-x

Eppig, J. J., and O'Brien, M. J. (1996). Development *in vitro* of mouse oocytes from primordial follicles. *Biol. Reprod.* 54 (1), 197–207. doi:10.1095/biolreprod54.1.197

Eppig, J. J. (2001). Oocyte control of ovarian follicular development and function in mammals. *Reproduction* 122 (6), 829–838. doi:10.1530/rep.0.1220829

Eppig, J. J., and Schroeder, A. C. (1989). Capacity of mouse oocytes from preantral follicles to undergo embryogenesis and development to live young after growth, maturation, and fertilization *in vitro*. *Biol. Reprod.* 41 (2), 268–276. doi:10.1095/biolreprod41.2.268

Eppig, J. J., Wigglesworth, K., Pendola, F., and Hirao, Y. (1997). Murine oocytes suppress expression of luteinizing hormone receptor messenger ribonucleic acid by granulosa cells. *Biol. Reprod.* 56 (4), 976–984. doi:10.1095/biolreprod56.4.976

Erickson, G. F., Magoffin, D. A., Dyer, C. A., and Hofeditz, C. (1985). The ovarian androgen producing cells: A review of structure/function relationships. *Endocr. Rev.* 6 (3), 371–399. doi:10.1210/edrv-6-3-371

Espey, L. L., and Lipner, H. (1963). Measurements of intrafollicular pressures in the rabbit ovary. *Am. J. Physiol.* 205 (6), 1067–1072. doi:10.1152/ajplegacy.1963.205.6.1067

Field, S. L., Dasgupta, T., Cummings, M., and Orsi, N. M. (2014). Cytokines in ovarian folliculogenesis, oocyte maturation and luteinisation: Cytokines in folliculogenesis. *Mol. Reprod. Dev.* 81 (4), 284–314. doi:10.1002/mrd.22285

Figueiredo, J. R., Hulshof, S. C., Thiry, M., Van den Hurk, R., Bevers, M. M., Nusgens, B., et al. (1995). Extracellular matrix proteins and basement membrane: Their identification in bovine ovaries and significance for the attachment of cultured preantral follicles. *Theriogenology* 43 (5), 845–858. doi:10.1016/0093-691x(95)00036-8

Fischer, S., Ehrig, R., Schäfer, S., Tronci, E., Mancini, T., Egli, M., et al. (2021). Mathematical modeling and simulation provides evidence for new strategies of ovarian stimulation. *Front. Endocrinol.* 12, 613048. doi:10.3389/fendo.2021.613048

Fischer-Holzhausen, S., and Röblitz, S. (2022). Hormonal regulation of ovarian follicle growth in humans: Model-based exploration of cycle variability and parameter sensitivities. *J. Theor. Biol.* 547, 111150. doi:10.1016/j.jtbi.2022.111150

França, M. M., and Mendonca, B. B. (2022). Genetics of ovarian insufficiency and defects of folliculogenesis. *Best. Pract. Res. Clin. Endocrinol. Metab.* 36 (1), 101594. doi:10.1016/j.beem.2021.101594

Fujimoto, J. G., Pitris, C., Boppart, S. A., and Brezinski, M. E. (2000). Optical coherence tomography: An emerging technology for biomedical imaging and optical biopsy. *Neoplasia* 2 (1–2), 9–25. doi:10.1038/sj.neo.7900071

Gaiko-Shcherbak, A., Fabris, G., Dreissen, G., Merkel, R., Hoffmann, B., and Noetzel, E. (2015). The acinar cage: Basement membranes determine molecule exchange and mechanical stability of human breast cell acini. *PLoS One* 10 (12), e0145174. doi:10.1371/journal.pone.0145174

Ganda, O. P., Williamson, J. R., Soeldner, J. S., Gleason, R. E., Kilo, C., Kaldany, A., et al. (1983). Muscle capillary basement membrane width and its relationship to diabetes mellitus in monozygotic twins. *Diabetes* 32 (6), 549–556. doi:10.2337/diab.32.6.549

Gaytán, F., Morales, C., Bellido, C., Aguilar, E., and Sánchez-Criado, J. E. (1998). Ovarian follicle macrophages: Is follicular atresia in the immature rat a macrophage-mediated Event?1. *Biol. Reprod.* 58 (1), 52–59. doi:10.1095/biolreprod58.1.52

Glentis, A., Oertle, P., Mariani, P., Chikina, A., El Marjou, F., Attieh, Y., et al. (2017). Author Correction: Cancer-associated fibroblasts induce metalloprotease-independent cancer cell invasion of the basement membrane. *Nat. Commun.* 8 (1), 1036. doi:10.1038/s41467-018-03304-x

Glister, C., Richards, S. L., and Knight, P. G. (2005). Bone morphogenetic proteins (BMP) -4, -6, and -7 potently suppress basal and luteinizing hormone-induced androgen production by bovine theca interna cells in primary culture: Could ovarian hyperandrogenic dysfunction be caused by a defect in thecal BMP signaling? *Endocrinology* 146 (4), 1883–1892. doi:10.1210/en.2004-1303

Griffin, J., Emery, B. R., Huang, I., Peterson, C. M., and Carrell, D. T. (2006). Comparative analysis of follicle morphology and oocyte diameter in four mammalian species (mouse, hamster, pig, and human). *J. Exp. Clin. Assist. Reprod.* 3, 2. doi:10.1186/1743-1050-3-2

Guevorkian, K., Colbert, M. J., Durth, M., Dufour, S., and Brochard-Wyart, F. (2010). Aspiration of biological viscoelastic drops. *Phys. Rev. Lett.* 104 (21), 218101. doi:10.1103/PhysRevLett.104.218101

Halfter, W., Candiello, J., Hu, H., Zhang, P., Schreiber, E., and Balasubramani, M. (2013). Protein composition and biomechanical properties of *in vivo*-derived basement membranes. *Cell adh. Migr.* 7 (1), 64–71. doi:10.4161/cam.22479

Hannezo, E., and Heisenberg, C. P. (2019). Mechanochemical feedback loops in development and disease. *Cell* 178 (1), 12–25. doi:10.1016/j.cell.2019.05.052

He, C., Wei, X., Liang, T., Liu, M., Jiang, D., Zhuang, L., et al. (2021). Quantifying the compressive force of 3D cardiac tissues via calculating the volumetric deformation of built-in elastic gelatin microspheres. *Adv. Healthc. Mat.* 10 (16), 2001716. doi:10.1002/adhm.202001716

He, X. (2017). Microfluidic encapsulation of ovarian follicles for 3D culture. *Ann. Biomed. Eng.* 45 (7), 1676–1684. doi:10.1007/s10439-017-1823-7

Heeren, A. M., van Iperen, L., Klootwijk, D. B., de Melo Bernardo, A., Roost, M. S., Gomes Fernandes, M. M., et al. (2015). Development of the follicular basement membrane during human gametogenesis and early folliculogenesis. *BMC Dev. Biol.* 15 (1), 4. doi:10.1186/s12861-015-0054-0

Heisenberg, C. P., and Bellaïche, Y. (2013). Forces in tissue morphogenesis and patterning. *Cell* 153 (5), 948–962. doi:10.1016/j.cell.2013.05.008

Hemmings, B. A., and Restuccia, D. F. (2012). PI3K-PKB/Akt pathway. *Cold Spring Harb. Perspect. Biol.* 4 (9), a011189. doi:10.1101/cshperspect.a011189

Henning, N. F. C., and Laronda, M. (2021). The matrisome contributes to the increased rigidity of the bovine ovarian cortex and provides a source of new bioengineering tools to investigate ovarian biology. *SSRN J.* doi:10.2139/ssrn.3943652

Hertig, A. T., and Adams, E. C. (1967). Studies on the human oocyte and its follicle. I. Ultrastructural and histochemical observations on the primordial follicle stage. *J. Cell Biol.* 34 (2), 647–675. doi:10.1083/jcb.34.2.647

Honda, A., Hirose, M., Hara, K., Matoba, S., Inoue, K., Miki, H., et al. (2007). Isolation, characterization, and *in vitro* and *in vivo* differentiation of putative thecal stem cells. *Proc. Natl. Acad. Sci. U. S. A.* 104 (30), 12389–12394. doi:10.1073/pnas.0703787104

Hopkins, T. I. R., Bemmer, V. L., Franks, S., Dunlop, C., Hardy, K., and Dunlop, I. E. (2021). Micromechanical mapping of the intact ovary interior reveals contrasting mechanical roles for follicles and stroma. *Biomaterials* 277, 121099. doi:10.1016/j.biomaterials.2021.121099

Hornick, J. E., Duncan, F. E., Shea, L. D., and Woodruff, T. K. (2012). Isolated primate primordial follicles require a rigid physical environment to survive and grow *in vitro*. *Hum. Reprod.* 27 (6), 1801–1810. doi:10.1093/humrep/der468

Horsnell, H. L., Tetley, R. J., De Belly, H., Makris, S., Millward, L. J., Benjamin, A. C., et al. (2022). Lymph node homeostasis and adaptation to immune challenge resolved by fibroblast network mechanics. *Nat. Immunol.* 23 (8), 1169–1182. doi:10.1038/s41590-022-01272-5

Hu, L., Su, T., Luo, R., Zheng, Y., Huang, J., Zhong, Z., et al. (2019). Hippo pathway functions as a downstream effector of AKT signaling to regulate the activation of primordial follicles in mice. *J. Cell. Physiol.* 234 (2), 1578–1587. doi:10.1002/jcp.27024

Huang, A., Brennan, K., and Azziz, R. (2010). Prevalence of hyperandrogenemia in the polycystic ovary syndrome diagnosed by the National Institutes of Health 1990 criteria. *Fertil. Steril.* 93 (6), 1938–1941. doi:10.1016/j.fertnstert.2008.12.138

Huang, C. T. F., Weitsman, S. R., Dykes, B. N., and Magoffin, D. A. (2001). Stem cell factor and insulin-like growth factor-I stimulate luteinizing hormone-independent differentiation of rat ovarian theca cells. *Biol. Reprod.* 64 (2), 451–456. doi:10.1095/biolreprod64.2.451

Huang, Q., Liu, X., and Guo, S. (2022). Higher fibrotic content of endometriotic lesions is associated with diminished prostaglandin E2 signaling. *Reprod. Med. Biol.* 21 (1), e12423. doi:10.1002/rmb2.12423

Indana, D., Agarwal, P., Bhutani, N., and Chaudhuri, O. (2021). Viscoelasticity and adhesion signaling in biomaterials control human pluripotent stem cell morphogenesis in 3D culture. *Adv. Mat.* 33 (43), 2101966. doi:10.1002/adma.202101966

Irving-Rodgers, H. F., and Rodgers, R. J. (2005). Extracellular matrix in ovarian follicular development and disease. *Cell Tissue Res.* 322 (1), 89–98. doi:10.1007/s00441-005-0042-y

Islam, M. M., and Steward, R. L. (2019). Probing endothelial cell mechanics through connexin 43 disruption. *Exp. Mech.* 59 (3), 327–336. doi:10.1007/s11340-018-00445-4

John, G. B., Gallardo, T. D., Shirley, L. J., and Castrillon, D. H. (2008). Foxo3 is a PI3K-dependent molecular switch controlling the initiation of oocyte growth. *Dev. Biol.* 321 (1), 197–204. doi:10.1016/j.ydbio.2008.06.017

John, G. B., Shirley, L. J., Gallardo, T. D., and Castrillon, D. H. (2007). Specificity of the requirement for Foxo3 in primordial follicle activation. *Reproduction* 133 (5), 855–863. doi:10.1530/REP-06-0051

Johnson, J., Chen, X., Xu, X., and Emerson, J. W. (2015). ŏvSim: A simulation of the population dynamics of mammalian ovarian follicles. *Physiology*. [Internet] [cited 2022 Jun 26]. doi:10.1101/034249

Jones, A. S. K., and Shikanov, A. (2019). Follicle development as an orchestrated signaling network in a 3D organoid. *J. Biol. Eng.* 13, 2. doi:10.1186/s13036-018-0134-3

Jones, R. L., and Pepling, M. E. (2013). KIT signaling regulates primordial follicle formation in the neonatal mouse ovary. *Dev. Biol.* 382 (1), 186–197. doi:10.1016/j.ydbio.2013.06.030

Kasuya, K. (1995). The process of apoptosis in follicular epithelial cells in the rabbit ovary, with special reference to involvement by macrophages. *Arch. Histol. Cytol.* 58 (2), 257–264. doi:10.1679/aohc.58.257

Kawamura, K., Cheng, Y., Suzuki, N., Deguchi, M., Sato, Y., Takae, S., et al. (2013). Hippo signaling disruption and Akt stimulation of ovarian follicles for infertility treatment. *Proc. Natl. Acad. Sci. U. S. A.* 110 (43), 17474–17479. doi:10.1073/pnas.1312830110

Kenny, H. A., Krausz, T., Yamada, S. D., and Lengyel, E. (2007). Use of a novel 3D culture model to elucidate the role of mesothelial cells, fibroblasts and extra-cellular matrices on adhesion and invasion of ovarian cancer cells to the omentum. *Int. J. Cancer* 121 (7), 1463–1472. doi:10.1002/ijc.22874

Kim, J., Perez, A. S., Claflin, J., David, A., Zhou, H., and Shikanov, A. (2016). Synthetic hydrogel supports the function and regeneration of artificial ovarian tissue in mice. *NPJ Regen. Med.* 1 (1), 16010. doi:10.1038/npjregenmed.2016.10

Kim, S. N., Jeibmann, A., Halama, K., Witte, H. T., Wälte, M., Matzat, T., et al. (2014). ECM stiffness regulates glial migration in *Drosophila* and mammalian glioma models. *Development* 141 (16), 3233–3242. doi:10.1242/dev.106039

Kim, S. Y., and Nair, M. G. (2019). Macrophages in wound healing: Activation and plasticity. *Immunol. Cell Biol.* 97 (3), 258–267. doi:10.1111/imcb.12236

Kinnear, H. M., Tomaszewski, C. E., Chang, F. L., Moravek, M. B., Xu, M., Padmanabhan, V., et al. (2020). The ovarian stroma as a new frontier. *Reproduction* 160 (3), R25–R39. doi:10.1530/REP-19-0501

Ko, C., Gieske, M. C., Al-Alem, L., Hahn, Y., Su, W., Gong, M. C., et al. (2006). Endothelin-2 in ovarian follicle rupture. *Endocrinology* 147 (4), 1770–1779. doi:10.1210/en.2005-1228

Koester, J., Miroshnikova, Y. A., Ghatak, S., Chacón-Martínez, C. A., Morgner, J., Li, X., et al. (2021). Niche stiffening compromises hair follicle stem cell potential during ageing by reducing bivalent promoter accessibility. *Nat. Cell Biol.* 23 (7), 771–781. doi:10.1038/s41556-021-00705-x

Komatsu, K., Iwase, A., Murase, T., and Masubuchi, S. (2018). Ovarian tissue culture to visualize phenomena in mouse ovary. *J. Vis. Exp.* (136), 57794. doi:10.3791/57794

Komatsu, K., and Masubuchi, S. (2017). Observation of the dynamics of follicular development in the ovary. *Reprod. Med. Biol.* 16 (1), 21–27. doi:10.1002/rmb2.12010

Laronda, M. M., Jakus, A. E., Whelan, K. A., Wertheim, J. A., Shah, R. N., and Woodruff, T. K. (2015). Initiation of puberty in mice following decellularized ovary transplant. *Biomaterials* 50, 20–29. doi:10.1016/j.biomaterials.2015.01.051

Lecuit, T., and Lenne, P. F. (2007). Cell surface mechanics and the control of cell shape, tissue patterns and morphogenesis. *Nat. Rev. Mol. Cell Biol.* 8 (8), 633–644. doi:10.1038/nrm2222

Lee, H. J., Diaz, M. F., Price, K. M., Ozuna, J. A., Zhang, S., Sevick-Muraca, E. M., et al. (2017). Fluid shear stress activates YAP1 to promote cancer cell motility. *Nat. Commun.* 8 (1), 14122. doi:10.1038/ncomms14122

Lee, W. S., Otsuka, F., Moore, R. K., and Shimasaki, S. (2001). Effect of bone morphogenetic protein-7 on folliculogenesis and ovulation in the rat. *Biol. Reprod.* 65 (4), 994–999. doi:10.1095/biolreprod65.4.994

LeGoff, L., Rouault, H., and Lecuit, T. (2013). A global pattern of mechanical stress polarizes cell divisions and cell shape in the growing *Drosophila* wing disc. *Development* 140 (19), 4051–4059. doi:10.1242/dev.090878

Lei, L., and Spradling, A. C. (2016). Mouse oocytes differentiate through organelle enrichment from sister cyst germ cells. *Science* 352, 95–99. doi:10.1126/science.aad2156

Lei, L., and Spradling, A. C. (2013). Mouse primordial germ cells produce cysts that partially fragment prior to meiosis. *Development* 140 (10), 2075–2081. doi:10.1242/dev.093864

Li, S. K. B., and Hearn, M. T. W. (2000). Isolation of thecal cells: An assessment of purity and steroidogenic potential. *J. Biochem. Biophys. Methods* 45 (2), 169–181. doi:10.1016/s0165-022x(00)00107-x

Lin, H. C. A., Dutta, R., Mandal, S., Kind, A., Schnieke, A., and Razansky, D. (2017). "Light-sheet microscopy for quantitative ovarian folliculometry," in *San francisco*. Editors M. C. Skala and P. J. Campagnola (California: United States), 100430K. doi:10.1117/12.2252242

Liu, C., Peng, J., Matzuk, M. M., and Yao, H. H. C. (2015). Lineage specification of ovarian theca cells requires multicellular interactions via oocyte and granulosa cells. *Nat. Commun.* 6, 6934. doi:10.1038/ncomms7934

Liu, L., Rajareddy, S., Reddy, P., Du, C., Jagarlamudi, K., Shen, Y., et al. (2007). Infertility caused by retardation of follicular development in mice with oocyte-

specific expression of Foxo3a. *Development* 134 (1), 199–209. doi:10.1242/dev.02667

Lliberos, C., Liew, S. H., Zareie, P., La Gruta, N. L., Mansell, A., and Hutt, K. (2021). Evaluation of inflammation and follicle depletion during ovarian ageing in mice. *Sci. Rep.* 11 (1), 278. doi:10.1038/s41598-020-79488-4

Magoffin, D. A., Hubert-Leslie, D., and Zachow, R. J. (1995). Estradiol-17 beta, insulin-like growth factor-I, and luteinizing hormone inhibit secretion of transforming growth factor beta by rat ovarian theca-interstitial cells. *Biol. Reprod.* 53 (3), 627–635. doi:10.1095/biolreprod53.3.627

Magoffin, D. A., and Weitsman, S. R. (1994). Insulin-like growth factor-I regulation of luteinizing hormone (LH) receptor messenger ribonucleic acid expression and LH-stimulated signal transduction in rat ovarian theca-interstitial cells. *Biol. Reprod.* 51 (4), 766–775. doi:10.1095/biolreprod51.4.766

Maître, J. L., Turlier, H., Illukkumbura, R., Eismann, B., Niwayama, R., Nédélec, F., et al. (2016). Asymmetric division of contractile domains couples cell positioning and fate specification. *Nature* 536 (7616), 344–348. doi:10.1038/nature18958

Manuel, S. L., Antonova, E., Hornick, J. E., Riera, F. A., Wei, J. J., Pavone, M. E., et al. (2019). Collagen and hyaluronan matrices undergo age-related changes in the human ovary. *Fertil. Steril.* 112 (3), e252–e253. doi:10.1016/j.fertnstert.2019.07.1406

Matousek, M., Carati, C., Gannon, B., and Brännström, M. (2001). Novel method for intrafollicular pressure measurements in the rat ovary: Increased intrafollicular pressure after hCG stimulation. *Reproduction* 8, 307–314. doi:10.1530/rep.0.1210307

Matsuura, T., Sugimura, M., Iwaki, T., Ohashi, R., Kanayama, N., and Nishihira, J. (2002). Anti-macrophage inhibitory factor antibody inhibits PMSG-hCG-induced follicular growth and ovulation in mice. *J. Assist. Reprod. Genet.* 19 (12), 591–595. doi:10.1023/a:1021219317155

McGee, E. A., and Hsueh, A. J. (2000). Initial and cyclic recruitment of ovarian follicles. *Endocr. Rev.* 21 (2), 200–214. doi:10.1210/edrv.21.2.0394

McWhorter, F. Y., Davis, C. T., and Liu, W. F. (2015). Physical and mechanical regulation of macrophage phenotype and function. *Cell. Mol. Life Sci.* 72 (7), 1303–1316. doi:10.1007/s00018-014-1796-8

Miller, R. T. (2017). Mechanical properties of basement membrane in health and disease. *Matrix Biol.* 57 (58), 366–373. doi:10.1016/j.matbio.2016.07.001

Mizunuma, H., Liu, X., Andoh, K., Abe, Y., Kobayashi, J., Yamada, K., et al. (1999). Activin from secondary follicles causes small preantral follicles to remain dormant at the resting stage. *Endocrinology* 140 (1), 37–42. doi:10.1210/endo.140.1.6409

Mohagheghian, E., Luo, J., Chen, J., Chaudhary, G., Chen, J., Sun, J., et al. (2018). Quantifying compressive forces between living cell layers and within tissues using elastic round microgels. *Nat. Commun.* 9 (1), 1878. doi:10.1038/s41467-018-04245-1

Mongera, A., Rowghanian, P., Gustafson, H. J., Shelton, E., Kealhofer, D. A., Carn, E. K., et al. (2018). A fluid-to-solid jamming transition underlies vertebrate body axis elongation. *Nature* 561 (7723), 401–405. doi:10.1038/s41586-018-0479-2

Monslow, J., Govindaraju, P., and Puré, E. (2015). Hyaluronan - a functional and structural sweet spot in the tissue microenvironment. *Front. Immunol.* 6, 231. doi:10.3389/fimmu.2015.00231

Moore, R. K., Otsuka, F., and Shimasaki, S. (2003). Molecular basis of bone morphogenetic protein-15 signaling in granulosa cells. *J. Biol. Chem.* 278 (1), 304–310. doi:10.1074/jbc.M207362200

Mora, J. M., Fenwick, M. A., Castle, L., Baithun, M., Ryder, T. A., Mobberley, M., et al. (2012). Characterization and significance of adhesion and junction-related proteins in mouse ovarian follicles. *Biol. Reprod.* 86 (5153), 1–14. doi:10.1095/biolreprod.111.096156

Mosaliganti, K. R., Swinburne, I. A., Chan, C. U., Obholzer, N. D., Green, A. A., Tanksale, S., et al. (2019). Size control of the inner ear via hydraulic feedback. *eLife* 8, e39596. doi:10.7554/eLife.39596

Mostaço-Guidolin, L., Rosin, N., and Hackett, T. L. (2017). Imaging collagen in scar tissue: Developments in second harmonic generation microscopy for biomedical applications. *Int. J. Mol. Sci.* 18 (8), 1772. doi:10.3390/ijms18081772

Munjal, A., Hannezo, E., Tsai, T. Y. C., Mitchison, T. J., and Megason, S. G. (2021). Extracellular hyaluronate pressure shaped by cellular tethers drives tissue morphogenesis. *Cell* 184 (26), 6313–6325.e18. e18. doi:10.1016/j.cell.2021.11.025

Nagamatsu, G., Shimamoto, S., Hamazaki, N., Nishimura, Y., and Hayashi, K. (2019). Mechanical stress accompanied with nuclear rotation is involved in the dormant state of mouse oocytes. *Sci. Adv.* 5 (6), eaav9960. doi:10.1126/sciadv.aav9960

Nakano, K., Naito, I., Momota, R., Sado, Y., Hasegawa, H., Ninomiya, Y., et al. (2007). The distribution of type IV collagen alpha chains in the mouse ovary and its correlation with follicular development. *Arch. Histol. Cytol.* 70 (4), 243–253. doi:10.1679/aohc.70.243

Nam, S., Gupta, V. K., Leepyo, H., Lee, J. Y., Wisdom, K. M., Varma, S., et al. (2019). Cell cycle progression in confining microenvironments is regulated by a growth-responsive TRPV4-PI3K/Akt-p27 $^{Kip1}$ signaling axis. *Sci. Adv.* 5 (8), eaaw6171. doi:10.1126/sciadv.aaw6171

Nicholas, A. K., and Jacques, P. B. (2005). "Morphology and ultrastructure of basement membranes," in *Current topics in membranes* (Elsevier), 19–42.

Orisaka, M., Jiang, J. Y., Orisaka, S., Kotsuji, F., and Tsang, B. K. (2009). Growth differentiation factor 9 promotes rat preantral follicle growth by up-regulating follicular androgen biosynthesis. *Endocrinology* 150 (6), 2740–2748. doi:10.1210/en.2008-1536

O'Shea, J. D., Cran, D. G., Hay, M. F., and Moor, R. M. (1978). Ultrastructure of the theca interna of ovarian follicles in sheep. *Cell Tissue Res.* 187 (3), 457–472. doi:10.1007/BF00229610

Otsuka, F., and Shimasaki, S. (2002). A negative feedback system between oocyte bone morphogenetic protein 15 and granulosa cell kit ligand: Its role in regulating granulosa cell mitosis. *Proc. Natl. Acad. Sci. U. S. A.* 99 (12), 8060–8065. doi:10.1073/pnas.122066899

Ouni, E., Bouzin, C., Dolmans, M. M., Marbaix, E., Pyr Dit Ruys, S., Vertommen, D., et al. (2020). Spatiotemporal changes in mechanical matrisome components of the human ovary from prepuberty to menopause. *Hum. Reprod.* 35 (6), 1391–1410. doi:10.1093/humrep/deaa100

Ouni, E., Nedbal, V., Da Pian, M., Cao, H., Haas, K. T., Peaucelle, A., et al. (2022). Proteome-wide and matrisome-specific atlas of the human ovary computes fertility biomarker candidates and open the way for precision oncofertility. *Matrix Biol.* 109, 91–120. doi:10.1016/j.matbio.2022.03.005

Ouni, E., Peaucelle, A., Haas, K. T., Van Kerk, O., Dolmans, M. M., Tuuri, T., et al. (2021). A blueprint of the topology and mechanics of the human ovary for next-generation bioengineering and diagnosis. *Nat. Commun.* 12 (1), 5603. doi:10.1038/s41467-021-25934-4

Ouni, E., Vertommen, D., Chiti, M. C., Dolmans, M. M., and Amorim, C. A. (2019). A draft map of the human ovarian proteome for tissue engineering and clinical applications. *Mol. Cell. Proteomics* 18, S159–S173. doi:10.1074/mcp.RA117.000469

Pangas, S. A., Saudye, H., Shea, L. D., and Woodruff, T. K. (2003). Novel approach for the three-dimensional culture of granulosa cell–oocyte complexes. *Tissue Eng.* 9 (5), 1013–1021. doi:10.1089/107632703322495655

Parkes, W. S., Amargant, F., Zhou, L. T., Villanueva, C. E., Duncan, F. E., and Pritchard, M. T. (2021). Hyaluronan and collagen are prominent extracellular matrix components in bovine and porcine ovaries. *Genes* 12 (8), 1186. doi:10.3390/genes12081186

Pelosi, E., Omari, S., Michel, M., Ding, J., Amano, T., Forabosco, A., et al. (2013). Constitutively active Foxo3 in oocytes preserves ovarian reserve in mice. *Nat. Commun.* 4 (1), 1843. doi:10.1038/ncomms2861

Perez Gonzalez, N., Tao, J., Rochman, N. D., Vig, D., Chiu, E., Wirtz, D., et al. (2018). Cell tension and mechanical regulation of cell volume. *Mol. Biol. Cell* 29 (21), 0. doi:10.1091/mbc.E18-04-0213

Perloff, W. H., Schultz, J., Farris, E. J., and Balin, H. (1954). Some aspects of the chemical nature of human ovarian follicular fluid. *Fertil. Steril.* 6 (1), 11–17. doi:10.1016/s0015-0282(16)31861-1

Petersen, A., Joly, P., Bergmann, C., Korus, G., and Duda, G. N. (2012). The impact of substrate stiffness and mechanical loading on fibroblast-induced scaffold remodeling. *Tissue Eng. Part A* 18 (17–18), 1804–1817. doi:10.1089/ten.TEA.2011.0514

Petridou, N. I., Grigolon, S., Salbreux, G., Hannezo, E., and Heisenberg, C. P. (2019). Fluidization-mediated tissue spreading by mitotic cell rounding and non-canonical Wnt signalling. *Nat. Cell Biol.* 21 (2), 169–178. doi:10.1038/s41556-018-0247-4

Petrovská, M., Dimitrov, D. G., and Michael, S. D. (1996). Quantitative changes in macrophage distribution in normal mouse ovary over the course of the estrous cycle examined with an image analysis system. *Am. J. Reprod. Immunol.* 36 (3), 175–183. doi:10.1111/j.1600-0897.1996.tb00159.x

Power, R. M., and Huisken, J. (2017). A guide to light-sheet fluorescence microscopy for multiscale imaging. *Nat. Methods* 14 (4), 360–373. doi:10.1038/nmeth.4224

Prevedel, R., Diz-Muñoz, A., Ruocco, G., and Antonacci, G. (2019). Brillouin microscopy: An emerging tool for mechanobiology. *Nat. Methods* 16 (10), 969–977. doi:10.1038/s41592-019-0543-3

Quiros, R. M., Valianou, M., Kwon, Y., Brown, K. M., Godwin, A. K., and Cukierman, E. (2008). Ovarian normal and tumor-associated fibroblasts retain *in vivo* stromal characteristics in a 3-D matrix-dependent manner. *Gynecol. Oncol.* 110 (1), 99–109. doi:10.1016/j.ygyno.2008.03.006

Ramos-Lewis, W., and Page-McCaw, A. (2019). Basement membrane mechanics shape development: Lessons from the fly. *Matrix Biol.* 75–76, 72–81. doi:10.1016/j.matbio.2018.04.004

Riquelme, M. A., Cardenas, E. R., Xu, H., and Jiang, J. X. (2020). The role of connexin channels in the response of mechanical loading and unloading of bone. *Int. J. Mol. Sci.* 21 (3), E1146. doi:10.3390/ijms21031146

Rodgers, R. J., and Irving-Rodgers, H. F. (2010). formation of the ovarian follicular antrum and follicular fluid. *Biol. Reprod.* 82 (6), 1021–1029. doi:10.1095/biolreprod.109.082941

Rodgers, R. J., Irving-Rodgers, H. F., and Russell, D. L. (2003). Extracellular matrix of the developing ovarian follicle. *Reproduction* 126 (4), 415–424. doi:10.1530/rep.0.1260415

Rodgers, R. J., Irving-Rodgers, H. F., van Wezel, I. L., Krupa, M., and Lavranos, T. C. (2001). Dynamics of the membrana granulosa during expansion of the ovarian follicular antrum. *Mol. Cell. Endocrinol.* 171 (1–2), 41–48. doi:10.1016/s0303-7207(00)00430-5

Roignot, J., Peng, X., and Mostov, K. (2013). Polarity in mammalian epithelial morphogenesis. *Cold Spring Harb. Perspect. Biol.* 5 (2), a013789. doi:10.1101/cshperspect.a013789

Rondell, P. (1964). Follicular pressure and distensibility in ovulation. *Am. J. Physiology* 5.

Rowley, J. E., Amargant, F., Zhou, L. T., Galligos, A., Simon, L. E., Pritchard, M. T., et al. (2020). Low molecular weight hyaluronan induces an inflammatory response in ovarian stromal cells and impairs gamete development *in vitro*. *Int. J. Mol. Sci.* 21 (3), 1036. doi:10.3390/ijms21031036

Ryan, A. Q., Chan, C. J., Graner, F., and Hiiragi, T. (2019). Lumen expansion facilitates epiblast-primitive endoderm fate specification during mouse blastocyst formation. *Dev. Cell* 51 (6), 684–697. e4. doi:10.1016/j.devcel.2019.10.011

Saglani, S., Molyneux, C., Gong, H., Rogers, A., Malmström, K., Pelkonen, A., et al. (2006). Ultrastructure of the reticular basement membrane in asthmatic adults, children and infants. *Eur. Respir. J.* 28 (3), 505–512. doi:10.1183/09031936.06.00056405

Sahai, E., Astsaturov, I., Cukierman, E., DeNardo, D. G., Egeblad, M., Evans, R. M., et al. (2020). A framework for advancing our understanding of cancer-associated fibroblasts. *Nat. Rev. Cancer* 20 (3), 174–186. doi:10.1038/s41568-019-0238-1

Salustri, A., CamAioni, A., Fulop, C., and Hascall, V. C. (1999). Hyaluronan and proteoglycans in ovarian follicles. *Hum. Reprod. Update* 5 (4), 293–301. doi:10.1093/humupd/5.4.293

Sánchez-Sánchez, B. J., Urbano, J. M., Comber, K., Dragu, A., Wood, W., Stramer, B., et al. (2017). Drosophila embryonic hemocytes produce laminins to strengthen migratory response. *Cell Rep.* 21 (6), 1461–1470. doi:10.1016/j.celrep.2017.10.047

Schliffka, M. F., and Maître, J. L. (2019). Stay hydrated: Basolateral fluids shaping tissues. *Curr. Opin. Genet. Dev.* 57, 70–77. doi:10.1016/j.gde.2019.06.015

Shalgi, R., Kraicer, P., Rimon, A., Pinto, M., and Soferman, N. (1973). Proteins of human follicular fluid: The blood-follicle barrier. *Fertil. Steril.* 24 (6), 429–434. doi:10.1016/s0015-0282(16)39730-8

Shikanov, A., Xu, M., Woodruff, T. K., and Shea, L. D. (2011). A method for ovarian follicle encapsulation and culture in a proteolytically degradable 3 dimensional system. *J. Vis. Exp.* (49), 2695. doi:10.3791/2695

Shin, S. Y., Lee, H. J., Ko, D. S., Lee, H. C., and Park, W. I. (2005). The regulators of VEGF expression in mouse ovaries. *Yonsei Med. J.* 46 (5), 679–686. doi:10.3349/ymj.2005.46.5.679

Shiomi-Sugaya, N., Komatsu, K., Wang, J., Yamashita, M., Kikkawa, F., and Iwase, A. (2015). Regulation of secondary follicle growth by theca cells and insulin-like growth factor 1. *J. Reprod. Dev.* 61 (3), 161–168. doi:10.1262/jrd.2014-107

Sigurbjörnsdóttir, S., Mathew, R., and Leptin, M. (2014). Molecular mechanisms of de novo lumen formation. *Nat. Rev. Mol. Cell Biol.* 15 (10), 665–676. doi:10.1038/nrm3871

Simon, A. M., Goodenough, D. A., Li, E., and Paul, D. L. (1997). Female infertility in mice lacking connexin 37. *Nature* 385 (6616), 525–529. doi:10.1038/385525a0

Smith, M. F., McIntush, E. W., Ricke, W. A., Kojima, F. N., and Smith, G. W. (1999). Regulation of ovarian extracellular matrix remodelling by metalloproteinases and their tissue inhibitors: Effects on follicular development, ovulation and luteal function. *J. Reprod. Fertil. Suppl.* 54, 367–381.

Souchaud, A., Boutillon, A., Charron, G., Asnacios, A., Noûs, C., David, N. B., et al. (2022). Live 3D imaging and mapping of shear stresses within tissues using incompressible elastic beads. *Development* 149 (4), dev199765. doi:10.1242/dev.199765

Spears, N., de Bruin, J. P., and Gosden, R. G. (1996). The establishment of follicular dominance in co-cultured mouse ovarian follicles. *J. Reprod. Fertil.* 106 (1), 1–6. doi:10.1530/jrf.0.1060001

Sridharan, R., Cavanagh, B., Cameron, A. R., Kelly, D. J., and O'Brien, F. J. (2019). Material stiffness influences the polarization state, function and migration mode of macrophages. *Acta Biomater.* 89, 47–59. doi:10.1016/j.actbio.2019.02.048

St John, M. A. R., Tao, W., Fei, X., Fukumoto, R., Carcangiu, M. L., Brownstein, D. G., et al. (1999). Mice deficient of Lats1 develop soft-tissue sarcomas, ovarian tumours and pituitary dysfunction. *Nat. Genet.* 21 (2), 182–186. doi:10.1038/5965

Stassen, O. M. J. A., Ristori, T., and Sahlgren, C. M. (2020). Notch in mechanotransduction - from molecular mechanosensitivity to tissue mechanostasis. *J. Cell Sci.* 133 (24), jcs250738. doi:10.1242/jcs.250738

Stylianopoulos, T., Martin, J. D., Chauhan, V. P., Jain, S. R., Diop-Frimpong, B., Bardeesy, N., et al. (2012). Causes, consequences, and remedies for growth-induced solid stress in murine and human tumors. *Proc. Natl. Acad. Sci. U. S. A.* 109 (38), 15101–15108. doi:10.1073/pnas.1213353109

Sugimura, K., Lenne, P. F., and Graner, F. (2016). Measuring forces and stresses *in situ* in living tissues. *Development* 143 (2), 186–196. doi:10.1242/dev.119776

Sugiura, K., Pendola, F. L., and Eppig, J. J. (2005). Oocyte control of metabolic cooperativity between oocytes and companion granulosa cells: Energy metabolism. *Dev. Biol.* 279 (1), 20–30. doi:10.1016/j.ydbio.2004.11.027

Swanson, E. A., Izatt, J. A., Lin, C. P., Fujimoto, J. G., Schuman, J. S., Hee, M. R., et al. (1993). *In vivo* retinal imaging by optical coherence tomography. *Opt. Lett.* 18 (21), 1864–1866. doi:10.1364/ol.18.001864

Takaya, R., Fukaya, T., Sasano, H., Suzuki, T., Tamura, M., and Yajima, A. (1997). Macrophages in normal cycling human ovaries; immunohistochemical localization and characterization. *Hum. Reprod.* 12 (7), 1508–1512. doi:10.1093/humrep/12.7.1508

Taubenberger, A. V., Girardo, S., Träber, N., Fischer-Friedrich, E., Kräter, M., Wagner, K., et al. (2019). 3D microenvironment stiffness regulates tumor spheroid growth and mechanics via p21 and ROCK. *Adv. Biosyst.* 3 (9), e1900128. doi:10.1002/adbi.201900128

Thomasy, S. M., Morgan, J. T., Wood, J. A., Murphy, C. J., and Russell, P. (2013). Substratum stiffness and latrunculin B modulate the gene expression of the mechanotransducers YAP and TAZ in human trabecular meshwork cells. *Exp. Eye Res.* 113, 66–73. doi:10.1016/j.exer.2013.05.014

Thuwajit, C., Ferraresi, A., Titone, R., Thuwajit, P., and Isidoro, C. (2018). The metabolic cross-talk between epithelial cancer cells and stromal fibroblasts in ovarian cancer progression: Autophagy plays a role. *Med. Res. Rev.* 38 (4), 1235–1254. doi:10.1002/med.21473

Tian, Y., Shen, W., Lai, Z., Shi, L., Yang, S., Ding, T., et al. (2015). Isolation and identification of ovarian theca-interstitial cells and granulose cells of immature female mice: Isolation of theca-interstitial cells and granulosa cells. *Cell Biol. Int.* 39 (5), 584–590. doi:10.1002/cbin.10426

Träber, N., Uhlmann, K., Girardo, S., Kesavan, G., Wagner, K., Friedrichs, J., et al. (2019). Polyacrylamide bead sensors for *in vivo* quantification of cell-scale stress in zebrafish development. *Sci. Rep.* 9 (1), 17031. doi:10.1038/s41598-019-53425-6

Trombly, D. J., Woodruff, T. K., and Mayo, K. E. (2009). Suppression of Notch signaling in the neonatal mouse ovary decreases primordial follicle formation. *Endocrinology* 150 (2), 1014–1024. doi:10.1210/en.2008-0213

Tse, J. M., Cheng, G., Tyrrell, J. A., Wilcox-Adelman, S. A., Boucher, Y., Jain, R. K., et al. (2012). Mechanical compression drives cancer cells toward invasive phenotype. *Proc. Natl. Acad. Sci. U. S. A.* 109 (3), 911–916. doi:10.1073/pnas.1118910109

Umehara, T., Winstanley, Y. E., Andreas, E., Morimoto, A., Williams, E. J., Smith, K. M., et al. (2022). Female reproductive life span is extended by targeted removal of fibrotic collagen from the mouse ovary. *Sci. Adv.* 8 (24), eabn4564. doi:10.1126/sciadv.abn4564

Vignes, H., Vagena-Pantoula, C., Prakash, M., Fukui, H., Norden, C., Mochizuki, N., et al. (2022). Extracellular mechanical forces drive endocardial cell volume decrease during zebrafish cardiac valve morphogenesis. *Dev. Cell* 57 (5), 598–609.e5. e5. doi:10.1016/j.devcel.2022.02.011

Viola, J. M., Liu, J., Prahl, L. S., Huang, A., Trevor, J., Chan, G., et al. (2022). *Tubule jamming in the developing kidney creates cyclical mechanical stresses instructive to nephron formation*. doi:10.1101/2022.06.03.494718

Voutouri, C., and Stylianopoulos, T. (2018). "Accumulation of mechanical forces in tumors is related to hyaluronan content and tissue stiffness,*PLoS One*. 13, e0193801. doi:10.1371/journal.pone.0193801

Wang, H. X., Li, T. Y., and Kidder, G. M. (2010). WNT2 regulates DNA synthesis in mouse granulosa cells through beta-catenin. *Biol. Reprod.* 82 (5), 865–875. doi:10.1095/biolreprod.109.080903

Wang, S., and Larina, I. V. (2021). *In vivo* dynamic 3D imaging of oocytes and embryos in the mouse oviduct. *Cell Rep.* 36 (2), 109382. doi:10.1016/j.celrep.2021.109382

Wang, S., and Larina, I. V. (2018). *In vivo* three-dimensional tracking of sperm behaviors in the mouse oviduct. *Development* 145, 157685. doi:10.1242/dev.157685

Wang, S., Matsumoto, K., Lish, S. R., Cartagena-Rivera, A. X., and Yamada, K. M. (2021). Budding epithelial morphogenesis driven by cell-matrix versus cell-cell adhesion. *Cell* 184 (14), 3702–3716.e30. e30. doi:10.1016/j.cell.2021.05.015

Wang, T., Brewer, M., and Zhu, Q. (2015). An overview of optical coherence tomography for ovarian tissue imaging and characterization: An overview of optical coherence tomography. *Wiley Interdiscip. Rev. Nanomed. Nanobiotechnol.* 7 (1), 1–16. doi:10.1002/wnan.1306

Watanabe, Y., Takakura, K., Kurotani, R., and Abe, H. (2015). Optical coherence tomography imaging for analysis of follicular development in ovarian tissue. *Appl. Opt.* 54 (19), 6111–6115. doi:10.1364/AO.54.006111

Watson, J. M., Rice, P. F., Marion, S. L., Brewer, M. A., Davis, J. R., Rodriguez, J. J., et al. (2012). Analysis of second-harmonic-generation microscopy in a mouse model of ovarian carcinoma. *J. Biomed. Opt.* 17 (7), 076002. doi:10.1117/1.JBO.17.7.076002

Wells, R. G. (2013). Tissue mechanics and fibrosis. *Biochim. Biophys. Acta* 1832 (7), 884–890. doi:10.1016/j.bbadis.2013.02.007

West, E., Xu, M., Woodruff, T., and Shea, L. (2007). Physical properties of alginate hydrogels and their effects on *in vitro* follicle development. *Biomaterials* 28 (30), 4439–4448. doi:10.1016/j.biomaterials.2007.07.001

West-Farrell, E. R., Xu, M., Gomberg, M. A., Chow, Y. H., Woodruff, T. K., and Shea, L. D. (2009). The mouse follicle microenvironment regulates antrum formation and steroid production: Alterations in gene expression profiles. *Biol. Reprod.* 80 (3), 432–439. doi:10.1095/biolreprod.108.071142

Wijgerde, M., Ooms, M., Hoogerbrugge, J. W., and Grootegoed, J. A. (2005). Hedgehog signaling in mouse ovary: Indian hedgehog and desert hedgehog from granulosa cells induce target gene expression in developing theca cells. *Endocrinology* 146 (8), 3558–3566. doi:10.1210/en.2005-0311

Winterhager, E., and Kidder, G. M. (2015). Gap junction connexins in female reproductive organs: Implications for women's reproductive health. *Hum. Reprod. Update* 21 (3), 340–352. doi:10.1093/humupd/dmv007

Wood, C. D., Vijayvergia, M., Miller, F. H., Carroll, T., Fasanati, C., Shea, L. D., et al. (2015). Multi-modal magnetic resonance elastography for noninvasive assessment of ovarian tissue rigidity *in vivo*. *Acta Biomater.* 13, 295–300. doi:10.1016/j.actbio.2014.11.022

Woodruff, T. K., and Shea, L. D. (2011). A new hypothesis regarding ovarian follicle development: Ovarian rigidity as a regulator of selection and health. *J. Assist. Reprod. Genet.* 28 (1), 3–6. doi:10.1007/s10815-010-9478-4

Woodruff, T. K., and Shea, L. D. (2007). The role of the extracellular matrix in ovarian follicle development. *Reprod. Sci.* 14, 6–10. doi:10.1177/1933719107309818

Wu, Z., and Guan, K. L. (2021). Hippo signaling in embryogenesis and development. *Trends biochem. Sci.* 46 (1), 51–63. doi:10.1016/j.tibs.2020.08.008

Xu, M., Kreeger, P. K., Shea, L. D., and Woodruff, T. K. (2006). Tissue-Engineered follicles produce live, fertile offspring. *Tissue Eng.* 12 (10), 2739–2746. doi:10.1089/ten.2006.12.2739

Xu, M., West, E., Shea, L. D., and Woodruff, T. K. (2006). Identification of a stage-specific permissive *in vitro* culture environment for follicle growth and oocyte development. *Biol. Reprod.* 75 (6), 916–923. doi:10.1095/biolreprod.106.054833

Yang, Y., Paivinen, P., Xie, C., Krup, A. L., Makela, T. P., Mostov, K. E., et al. (2021). Ciliary Hedgehog signaling patterns the digestive system to generate mechanical forces driving elongation. *Nat. Commun.* 12 (1), 7186. doi:10.1038/s41467-021-27319-z

Young, J. M., and McNeilly, A. S. (2010). Theca: The forgotten cell of the ovarian follicle. *Reproduction* 140 (4), 489–504. doi:10.1530/REP-10-0094

Zhang, Z., Schlamp, F., Huang, L., Clark, H., and Brayboy, L. (2020). Inflammaging is associated with shifted macrophage ontogeny and polarization in the aging mouse ovary. *Reproduction* 159 (3), 325–337. doi:10.1530/REP-19-0330

Zhao, B., Wei, X., Li, W., Udan, R. S., Yang, Q., Kim, J., et al. (2007). Inactivation of YAP oncoprotein by the Hippo pathway is involved in cell contact inhibition and tissue growth control. *Genes Dev.* 21 (21), 2747–2761. doi:10.1101/gad.1602907

Zhao, D., Liu, R., Li, G., Chen, M., Shang, P., Yang, H., et al. (2020). Connexin 43 channels in osteocytes regulate bone responses to mechanical unloading. *Front. Physiol.* 11, 299. doi:10.3389/fphys.2020.00299

Zhu, M., Zhang, K., Tao, H., Hopyan, S., and Sun, Y. (2020). Magnetic micromanipulation for *in vivo* measurement of stiffness heterogeneity and anisotropy in the mouse mandibular arch. *Res. (Wash D C)* 2020, 7914074. doi:10.34133/2020/7914074

frontiers | Frontiers in Cell and Developmental Biology

TYPE Original Research
PUBLISHED 20 March 2023
DOI 10.3389/fcell.2023.959611



OPEN ACCESS

EDITED BY
Bojana Gligorijevic,
Temple University, United States

REVIEWED BY
Stuart A. Newman,
New York Medical College, United States
Nara Guisoni,
National Scientific and Technical Research Council (CONICET), Argentina

*CORRESPONDENCE
Timothy J. Rudge,
tim.rudge@newcastle.ac.uk
Andrea Ravasio,
andrea.ravasio@uc.cl

†These authors have contributed equally to this work

SPECIALTY SECTION
This article was submitted to Cell Adhesion and Migration, a section of the journal Frontiers in Cell and Developmental Biology

RECEIVED 01 June 2022
ACCEPTED 08 February 2023
PUBLISHED 20 March 2023

CITATION
Montenegro-Rojas I, Yañez G, Skog E, Guerrero-Calvo O, Andaur-Lobos M, Dolfi L, Cellerino A, Cerda M, Concha ML, Bertocchi C, Rojas NO, Ravasio A and Rudge TJ (2023), A computational framework for testing hypotheses of the minimal mechanical requirements for cell aggregation using early annual killifish embryogenesis as a model.
*Front. Cell Dev. Biol.* 11:959611.
doi: 10.3389/fcell.2023.959611



# A computational framework for testing hypotheses of the minimal mechanical requirements for cell aggregation using early annual killifish embryogenesis as a model

Ignacio Montenegro-Rojas[1†], Guillermo Yañez[2,3†], Emily Skog[1†], Oscar Guerrero-Calvo[1], Martin Andaur-Lobos[1], Luca Dolfi[4,5], Alessandro Cellerino[6,7], Mauricio Cerda[8,9,10], Miguel L. Concha[8,9,11], Cristina Bertocchi[12,13], Nicolás O. Rojas[1], Andrea Ravasio[1]* and Timothy J. Rudge[2,3]*

[1]Laboratory for Mechanobiology of Transforming Systems, Institute for Biological and Medical Engineering, Schools of Engineering, Medicine and Biological Sciences. Pontificia Universidad Católica de Chile, Santiago, Chile, [2]Institute for Biological and Medical Engineering, Schools of Engineering, Medicine and Biological Sciences. Pontificia Universidad Católica de Chile, Santiago, Chile, [3]Interdisciplinary Computing and Complex Biosystems (ICOS) Research Group, School of Computing, Newcastle University, Newcastle upon Tyne, United Kingdom, [4]Max Planck Institute for Biology of Ageing, Cologne, Germany, [5]Center for Anatomy and Cell Biology, Medical University of Vienna, Vienna, Austria, [6]BIO@SNS, Scuola Normale Superiore, Pisa, Italy, [7]Leibniz Institute on Aging - Fritz Lipmann Institute, Jena, Germany, [8]Integrative Biology Program, Institute of Biomedical Sciences, Facultad de Medicina. Universidad de Chile, Santiago, Chile, [9]Biomedical Neuroscience Institute, Santiago, Chile, [10]Center for Medical Informatics and Telemedicine, Facultad de Medicina, Universidad de Chile, Santiago, Chile, [11]Center for Geroscience, Brain Health and Metabolism, Santiago, Chile, [12]Laboratory for Molecular Mechanics of Cell Adhesion, Department of Physiology Pontificia Universidad Católica de Chile, Santiago, Chile, [13]Graduate School of Engineering Science, Osaka University, Osaka, Japan

**Introduction:** Deciphering the biological and physical requirements for the outset of multicellularity is limited to few experimental models. The early embryonic development of annual killifish represents an almost unique opportunity to investigate *de novo* cellular aggregation in a vertebrate model. As an adaptation to seasonal drought, annual killifish employs a unique developmental pattern in which embryogenesis occurs only after undifferentiated embryonic cells have completed epiboly and dispersed in low density on the egg surface. Therefore, the first stage of embryogenesis requires the congregation of embryonic cells at one pole of the egg to form a single aggregate that later gives rise to the embryo proper. This unique process presents an opportunity to dissect the self-organizing principles involved in early organization of embryonic stem cells. Indeed, the physical and biological processes required to form the aggregate of embryonic cells are currently unknown.

**Methods:** Here, we developed an *in silico*, agent-based biophysical model that allows testing how cell-specific and environmental properties could determine the aggregation dynamics of early Killifish embryogenesis. In a forward engineering approach, we then proceeded to test two hypotheses for cell aggregation (cell-autonomous and a simple taxis model) as a proof of concept of modeling feasibility. In a first approach (cell autonomous system), we considered how intrinsic biophysical properties of the cells such as motility,

10.3389/fcell.2023.959611

polarity, density, and the interplay between cell adhesion and contact inhibition of locomotion drive cell aggregation into self-organized clusters. Second, we included guidance of cell migration through a simple taxis mechanism to resemble the activity of an organizing center found in several developmental models.

**Results:** Our numerical simulations showed that random migration combined with low cell-cell adhesion is sufficient to maintain cells in dispersion and that aggregation can indeed arise spontaneously under a limited set of conditions, but, without environmental guidance, the dynamics and resulting structures do not recapitulate *in vivo* observations.

**Discussion:** Thus, an environmental guidance cue seems to be required for correct execution of early aggregation in early killifish development. However, the nature of this cue (e.g., chemical or mechanical) can only be determined experimentally. Our model provides a predictive tool that could be used to better characterize the process and, importantly, to design informed experimental strategies.

KEYWORDS

**multicellularity, mechanics, biophysics, killifish, adhesion, modeling**

## 1 Introduction

Annual killifish have a unique early developmental pattern that differs from most teleost species. Unlike non-annual species, for whom most morphogenetic movements are concomitant, annual killifish have separated epiboly from embryo formation, resulting in an initial phase of cell dispersal that is followed by a process of cell aggregation, with embryonic cells occurring through active cell migration in the confined space between the enveloping layer (EVL) and the yolk syncytial layer (YSL) (Figure 1) (Dolfi et al., 2014; Concha and Reig, 2022). The embryonic cells remain

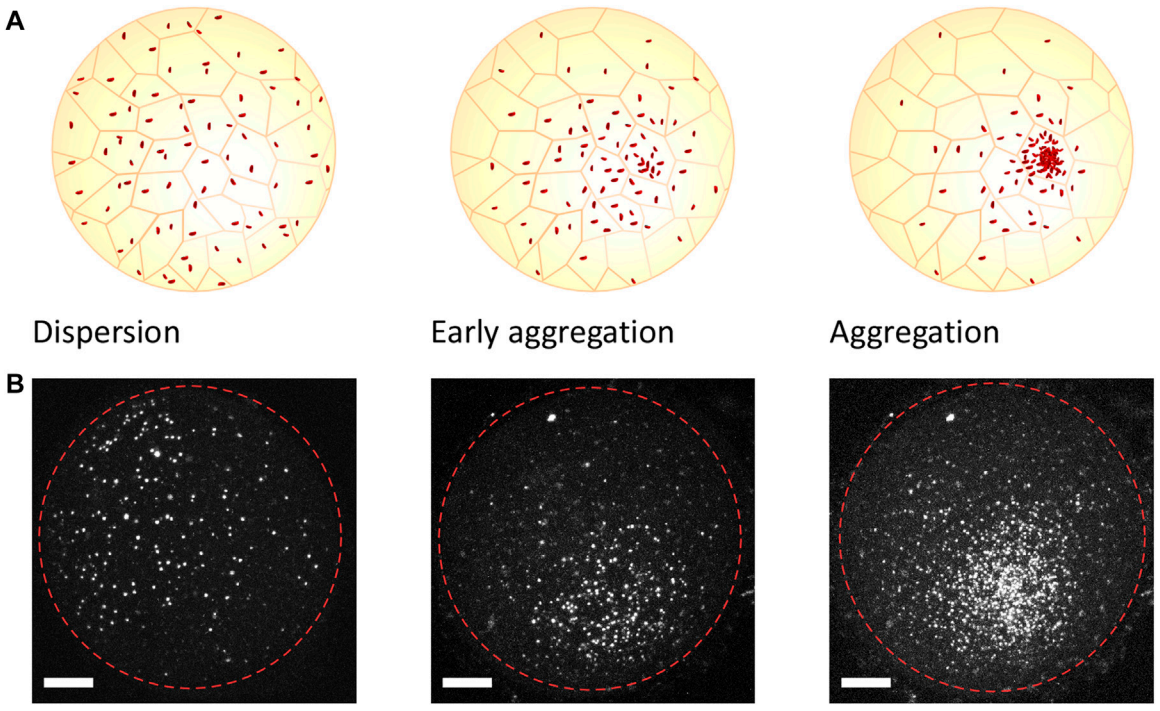


FIGURE 1
Stages of the early development of annual killifish as recorded *in vivo*. Cartoon representation **(A)** and confocal images of embryonic cell nuclei **(B)** stained using the FUCCI construct, illustrating the stages of the early development of killifish embryos. Following the dispersive state (left), the cells move directionally toward a pole of the embryo (center) and form an aggregate (right). The dashed red circles indicate the approximate outline of the embryo. The time between the stages varies between several hours to a few days, depending on the environmental condition and specific killifish species (Dolfi et al., 2014; Márquez et al., 2019). Scale bar, 200 μm.

undifferentiated, with stem-like properties during epiboly and until the end of the dispersion phase, when the cells start to aggregate at one pole of the embryo and initiate the genetic and morphogenetic processes leading to the formation of germ layers and the establishment of the embryonic axis (Wourms, 1972; Pereiro et al., 2017; Márquez et al., 2019) (Figure 1). These processes, which span between several hours and a few days depending on the specific killifish species and the environmental conditions (Dolfi et al., 2014; Márquez et al., 2019), occur in the context of a nearly spherical egg (about 1 mm diameter) and can be easily visualized in a living animal, as eggs are optically transparent and develop outside the mother (Wourms, 1972; Pereiro et al., 2017; Reig et al., 2017; Concha and Reig, 2022). The dispersion phase is characterized by a random walk of embryonic cells moving at a very low density (Márquez et al., 2019), while the cellular processes and morphogenetic mechanisms that form the aggregate are still unknown. It has been proposed that self-organizing processes may break the initial symmetry of the embryo and initiate the aggregation process (Pereiro et al., 2017; Abitua et al., 2021), since the molecular signals involved in embryo formation are apparently non-polarized during the stages prior to the aggregate formation. However, it cannot be ruled out that an organizing center, possibly located in extraembryonic structures, provides the signals that initiate the aggregate formation (Pereiro et al., 2017) as has been shown in other non-annual teleost species (Concha and Reig, 2022).

*In silico* modeling proved to be a powerful tool to accurately capture the essential features of various biological systems, such as wound healing (Ravasio et al., 2015a), tissue expansion (Ravasio et al., 2015b), cancer invasion (Stichel et al., 2017), and embryonic development (CONTE et al., 2008; Cai et al., 2016; Pereiro et al., 2017; Stepien et al., 2019). Thus, it has been proposed that they could be used as predictive tools to design informed experimental strategies (Kabla, 2012; Phillips, 2015). Here, we used an *in silico* model to understand the mechanical requirements for killifish cells to 1) remain in a dispersed state and 2) aggregate at the embryo pole to initiate embryogenesis. In our model, motile cells are represented by three-dimensional self-propelled particle spheres, which is a 3D framework commonly used to model collective cell dynamics (Belmonte et al., 2008; Henkes et al., 2011; Sepúlveda et al., 2013; Méhes and Vicsek, 2014; Tarle et al., 2015). This approach has been extended to incorporate biologically relevant interactions such as cell–substrate friction, intercellular and cell–substrate adhesions (Kanchanawong et al., 2010; Bertocchi et al., 2017), and contact inhibition of locomotion (CIL) (Abercrombie and Heaysman, 1954; Roycroft and Mayor, 2016). When generalized, this model can exhibit diverse dynamic states, such as gas phases, polar liquids, and 3D aggregates, depending on the parameter explored (Bray, 1993; Mladek et al., 2006; Moreno and Likos, 2007; Redner et al., 2013). Although these states were experimentally observed at high cell densities, it is an open question as to whether such mechanisms could account for the aggregation behavior observed at low cell densities found in the early stages of killifish development. Furthermore, to date, models have not considered the specific geometry of this process, such as the cells moving in confinement and on curved surfaces with spherical topology. Typically, these studies use periodic boundary conditions on a plane, giving a toroidal topology (Bellomo et al., 2015). Our model incorporates realistic conditions in terms of cell density, geometrical and mechanical properties of the EVL and the YSL, and their effect on the dynamics of embryonic cells. Thus, the *in silico* investigation presented aims to provide a flexible framework to model the early teleost development, which can help predict the minimal mechanical requirements for cell aggregation under the specific conditions of annual killifish early development. As the *in vivo* system is poorly understood and presents various intrinsic experimental challenges (e.g., coriaceous chorion), our forward engineering approach can provide useful information, enabling an informed experimental investigation of the biological system.

# 2 Results

During the early stages of killifish embryo development, undifferentiated stem cells move tangentially between the inner surface of the epithelial enveloping cell layer and the yolk syncytial layer (Figure 2A). The system is modeled here in two distinct ways: a cell-autonomous system that includes mechanisms that are intrinsic to the cells and the same cells that are under the influence of guidance from the environment toward an organizing center.

## 2.1 Cell-autonomous system

We present, here, a variation of the model proposed by Smeets et al. (2016) (Basan et al., 2013) for autonomous motile cells, extended to three dimensions and including the physical and geometrical constraints imposed by the EVL and the YSL, where the cells migrate tangentially to the surface of the YSL (Figure 2B).

### 2.1.1 Equations of motion

The cells have an intrinsic motile force, $F_m$, that drives them forward along their direction of polarity $\hat{\boldsymbol{p}}_i$ (Figure 2C). The cells are subject to viscous forces from the substrate with the coefficient $\gamma_s$ and from other cells $F_{ij}^{cc}$. The equation of motion is as follows:

$$F_m\hat{\boldsymbol{p}}_i = \gamma_s\dot{\boldsymbol{x}}_i + \sum_j F_{ij}^{cc}\hat{\boldsymbol{n}}_{ij} \tag{1}$$

with the left-hand term and the motile force with direction $\hat{\boldsymbol{p}}_i$, where $\gamma_s$ is the substrate viscosity and $F_{ij}^{cc}$ is the force between the cells $i$ and $j$, acting in the normal direction to their surface $\hat{\boldsymbol{n}}_{ij}$ at the point of contact. The normal direction at the point of contact in the case of the two spheres is simply the direction between their two centers so that:

$$\hat{\boldsymbol{n}}_{ij} = \frac{\left(\boldsymbol{x}_i - \boldsymbol{x}_j\right)}{d_{ij}}, \tag{2}$$

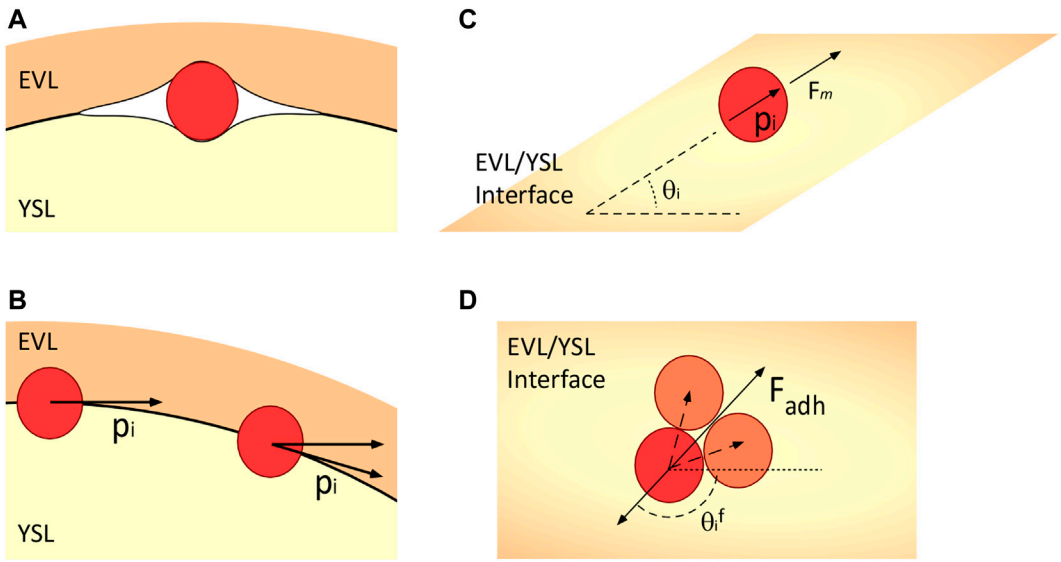


FIGURE 2
Schematic representation of the model's major components. **(A)** Embryonic cells move between the EVL and the YSL, which are roughly spherical. They are subject to forces due to the deformation of the adjacent cell layers. **(B)** Polarity of the cells is constrained to the tangential plane as they move. **(C)** Contact inhibition of locomotion repolarizes cells away from the average position of their neighbors, and adhesion forces attract them to their neighbors. **(D)** Angle with respect to the average neighbor position. The dashed vectors indicate the directions to the neighbors of the red cell, the bottom solid arrow indicates the reference direction, and $\theta_i^f$ is the angle to which the cells repolarize due to CIL. The direction of the adhesion force is shown for reference.

with $d_{ij} = |\boldsymbol{x}_i - \boldsymbol{x}_j|$ being the distance between cells. The force $F_{ij}^{cc}$ is defined in terms of $d_{ij}$.

### 2.1.2 Cell–cell adhesion and repulsion

The adhesion and repulsion between cells may play a significant role in the formation of aggregates. These forces are determined by the interaction between the cell–cell adhesion energy $W_c$ and the cell–substrate adhesion energy $W_s$, such that the intercellular force is given by (Smeets et al., 2016):

$$F_{ij}^{cc} = \frac{2}{R}\left[W_s - \frac{W_s + W_c}{R}\left(d_{ij} - R\right)\right], \tag{3}$$

for pairs of cells $i$ and $j$ in contact ($d_{ij} < 2R$) with the cell radius $R$. Here, $F_{ij}^{cc} = 0$ when $d_{ij} \geq 2R$, as the cells are not in contact. We model the EVL and the YSL as single large spherical cells of radius $R_E$ centered on the origin:

$$F_i^{YSL} = \frac{2}{R}\left[W_s - \frac{W_s + W_c}{R}\left(|\boldsymbol{x}_i| - R_E - R\right)\right],$$

which is the force applied to cell $i$ by the YSL when $|x_i| - R_E < R$ ($F_i^{YSL} = 0$ otherwise), and

$$F_i^{EVL} = \frac{2}{R}\left[W_s - \frac{W_s + W_c}{R}\left(R_E - |\boldsymbol{x}_i| - R\right)\right],$$

which is the force applied to cell $i$ by the EVL when $R_E - |\boldsymbol{x}_i| < R$ ($F_i^{EVL} = 0$ otherwise). In this way, the cells experience forces that tend to maintain them on a sphere of radius $R_E$. It should be noted that unlike in the work of Smeets et al. (2016), there is no cut-off of intercellular forces when the cells are closer than $R$, and no cells are removed from the simulation to model multiple layers. This is not necessary since our model is fully three-dimensional, and due to the spherical geometry, cells are naturally forced outward to form multilayered aggregates, which can be observed under large adhesive energies. Since the dynamics of the system depend upon the relation between cell–cell and cell–substrate energies rather than their absolute strengths, from here on, we use $W_s = 1$ and simply vary $W_c$.

### 2.1.3 Repolarization and rotational diffusion

In our model, the cell polarity vector $\hat{\boldsymbol{p}}_i$ is constrained to the tangential plane between the EVL and the YSL, and the motile force is as follows:

$$\boldsymbol{F}_m = F_m \hat{\boldsymbol{p}}_i, \tag{4}$$

where $\hat{\boldsymbol{p}}_i = (cos\,\theta_i,\ sin\,\theta_i)^T$, and $F_m$ is the magnitude of the motile force. We used the model by Smeets et al. (2016) for the repolarization of the direction vector of the cell $\hat{\boldsymbol{p}}_i$, which has angle $\theta_i$ in the tangential plane (Figure 2C):

$$\dot{\theta}_i = -f_{pol}\left(\theta_i - \theta_i^*\right) + \xi\sqrt{2D_r}, \tag{5}$$

where $\theta_i^*$ is the target or desired direction of the cell, $f_{pol}$ is the rate of repolarization, $D_r$ is the rate of angular diffusion, and $\xi$ is a Gaussian noise process. We may define any formulation for the desired direction depending on which type of repolarization process we wish to consider. This equation can be normalized by giving a single dimensionless parameter, $\psi = f_{pol}/2D_r$. In the following, we fix $D_r$ at unity.

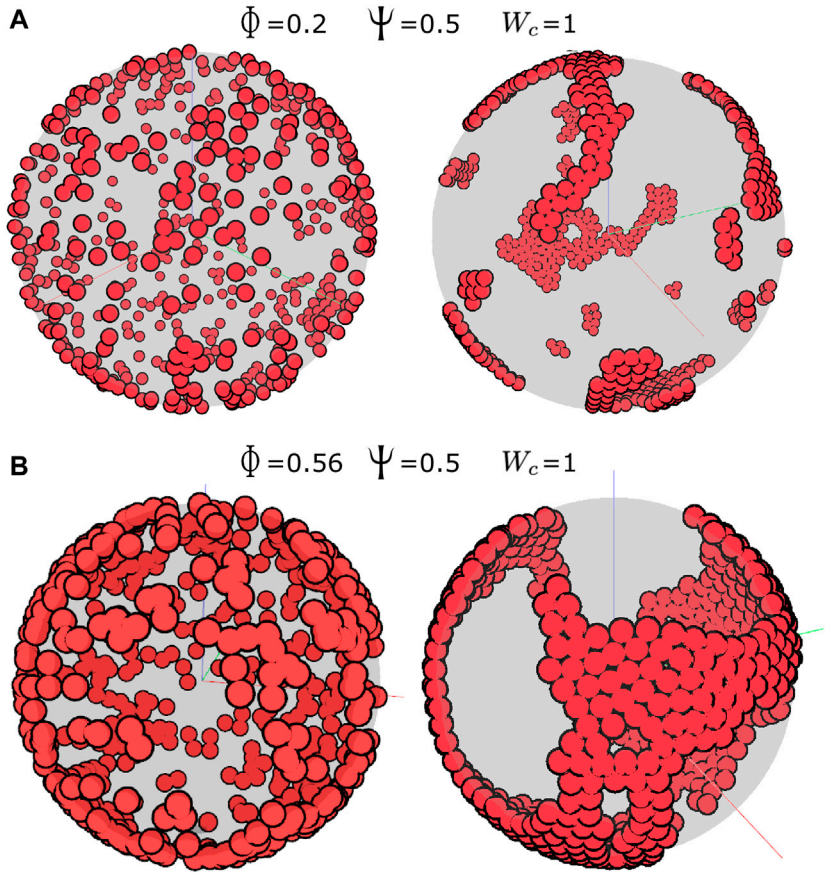


FIGURE 3
Aggregation in the cell-autonomous system. **(A)** Cell density $\phi$ = 0.2 (500 cells on a sphere of radius 25), $\psi$ = 0.5, and $W_c$ = 1. **(B)** Cell density $\phi$ = 0.56 (500 cells on a sphere of radius 15), $\psi$ = 0.5, and $W_c$ = 1. The images on the left show the initial conditions, and the images on the right show the simulations after 500 time steps. The YSL is drawn as a transparent gray sphere; hence, the cells on the far side appear darker. The three-dimensional perspective means that these cells also appear smaller.

### 2.1.4 Contact inhibition of locomotion

Contact inhibition of locomotion (CIL), which works as a repulsion interaction causing cells to steer away from each other, is another important determinant of cell migration, which we wish to test in our model. For CIL, we model the repolarization direction, $\theta_i^* = \theta_i^f$, as the direction pointing away from the average position of each cell's neighbors (contacting cells—Figure 2D), so if the average position of the neighboring cells is

$$\bar{\boldsymbol{x}}_i = \sum_j \boldsymbol{x}_j,$$

for the neighboring cells j, the desired direction vector in the tangent plane with normal $\hat{\boldsymbol{n}}_i$ is

$$\boldsymbol{v}_i^f = (\bar{\boldsymbol{x}}_i - \boldsymbol{x}_i) - [(\bar{\boldsymbol{x}}_i - \boldsymbol{x}_i) \cdot \hat{\boldsymbol{n}}_i]\hat{\boldsymbol{n}}_i.$$

Thus, the cells will turn away from contacting cells at a rate of $f_{pol} = f_{cil}$, so that

$$\dot{\theta}_i = -f_{cil} \times arccos\left(\frac{\boldsymbol{v}_i^f \cdot \hat{\boldsymbol{p}}_i}{\left|\boldsymbol{v}_i^f\right|}\right) + \sqrt{2D_r}\xi. \quad (6)$$

The system can again be normalized by the dimensionless parameter $\psi = f_{cil}/2D_r$ since $f_{pol} = f_{cil}$.

### 2.1.5 Numerical simulations

This model can be solved numerically (see Methods) for a range of parameters, providing a powerful tool to simulate developmental processes occurring in a realistic geometrical setting. Using the model described previously, we first examined the effect of the cell density on the collective behavior of cells, with other parameters for cell–cell adhesion and contact inhibition being fixed at $W_c$ = 1 and $\Psi$ = 0.5, respectively. Spherical cells of radius 1 were initialized at random positions on the surface of a sphere with a radius 25, representing the YSL, and their migration simulated 500 time steps. At a cell packing density ($\Phi = nR^2/4R_E^2$ for n cells on an embryo of radius $R_E$) similar to the annual killifish embryo (see Supplementary Material) ($\Phi$ = 0.2; 500 cells; Figure 3A and Supplementary Movie S1), the cells were able to aggregate into separated clusters and, as shown in previous studies for two-dimensional systems (Basan et al., 2013; Smeets et al., 2016), form a cohesive single aggregate at a high density ($\Phi$ = 0.56; 500 cells; in a smaller sphere of radius 15; Figure 3B and Supplementary Movie S2).

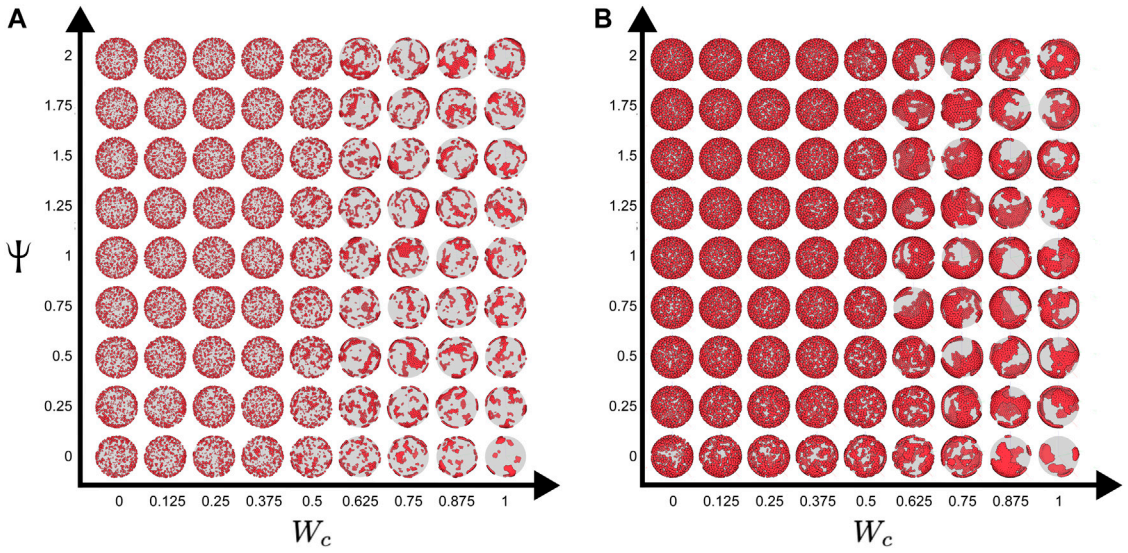


FIGURE 4
Parameter scan of the cell-autonomous system over different cell adhesion and CIL parameters. **(A)** Cell density of $\phi = 0.2$ (500 cells on a sphere of radius 25). **(B)** Cell density of $\phi = 0.56$ (500 cells on a sphere of radius 15). The dispersed states are maintained at low cell–cell adhesion, and clustering is increased by high cell–cell adhesion. High levels of CIL ($\Psi$) also increase cell clustering at moderate levels of cell–cell adhesion. The YSL is drawn as a transparent gray sphere; hence, the cells on the far side appear darker. The three-dimensional perspective means that these cells also appear smaller.

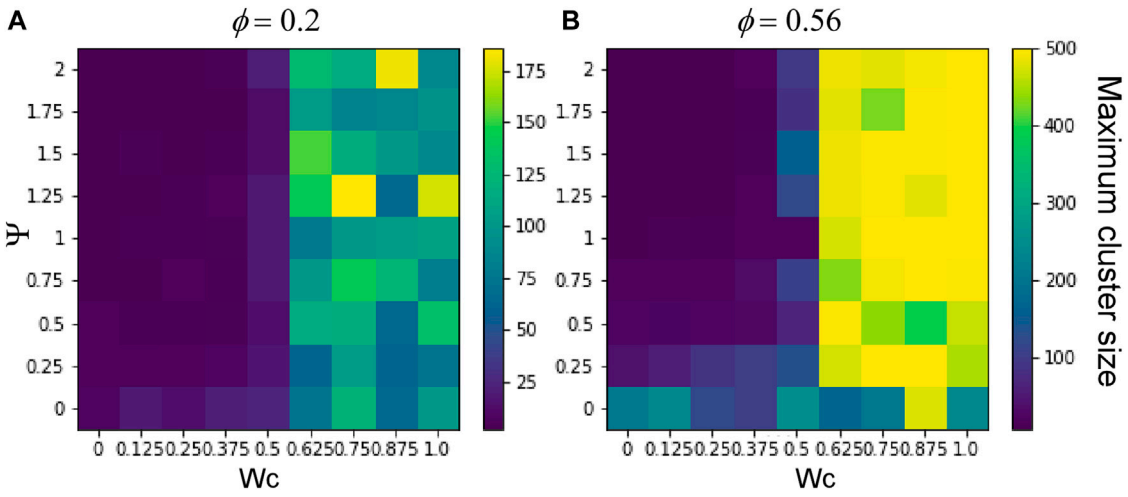


FIGURE 5
Maximum cluster size as a function of CIL and cell–cell adhesion. The maximum cluster sizes for the final states (after 500 time steps, each grid point represents the average of 25 simulations) of simulations with cell densities of **(A)** $\phi = 0.2$ (500 cells on a sphere of radius 25) and **(B)** $\phi = 0.56$ (500 cells on a sphere of radius 15). Clustering is increased by high cell–cell adhesion ($W_c$). Both high and low levels of CIL ($\Psi$) decrease cell clustering. The plots are the averages of 25 independent simulations.

To understand the effect of cell–cell adhesion and CIL on these dynamics, we scanned the parameter space, simulating the system with a range of values of $W_c$ and $\Psi$ for each density ($\Phi$ = 0.2 or 0.56). Figure 4 shows the final configurations of cells after 500 time steps for each parameter combination. A clear pattern emerges, where at low values of $W_c$, the system maintains its dispersed condition, and at high $W_c$, aggregation occurs (Figures 4A, B). Similar to what was shown previously, large single aggregates can be obtained at high densities and strong cell–cell adhesions, whereas at a first approximation, $\Psi$ appears to have only a marginal effect on the qualitative appearance of the cell aggregate. To quantify these effects, we computed the maximum cluster size at the end of simulations for each of the parameter combinations (Figure 5), and we also

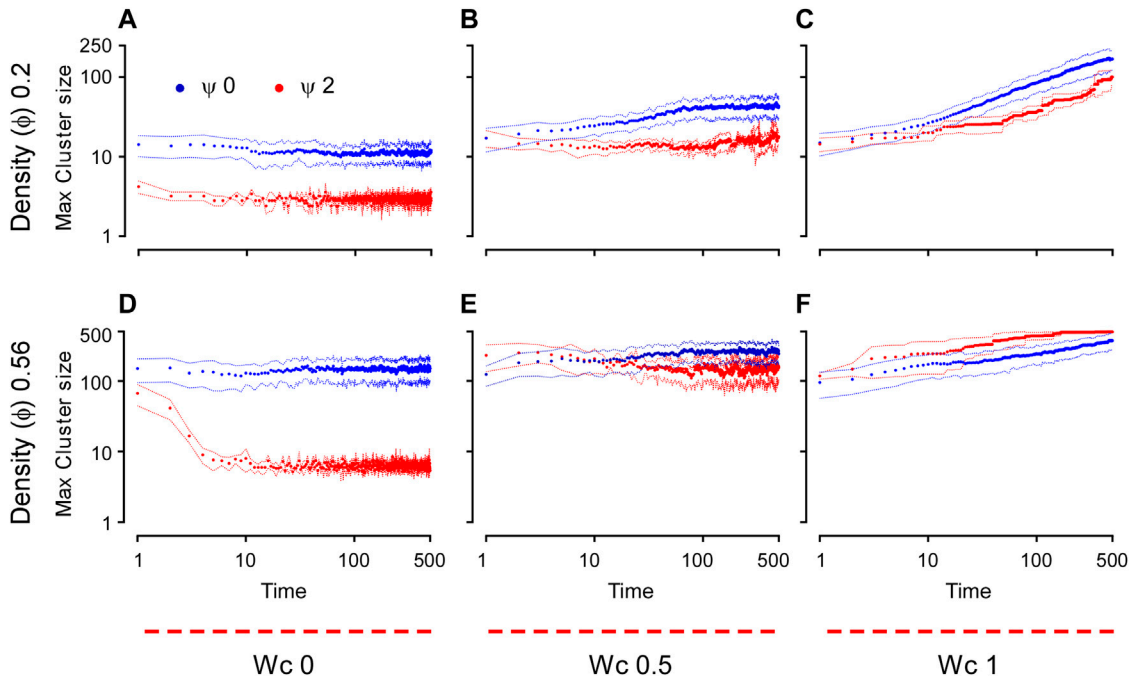


FIGURE 6
Time dynamics of the aggregation of the cell-autonomous system measured by the maximum cluster size. The cluster size is plotted here as a function of time for different cell densities, both conditions include 500 cells in each simulation ($\phi$ = 0.2, **(A–C)**; $\phi$ = 0.56, **(D–F)** for different $W_c$ (0, 0.5, and 1 for the first, second, and third column, respectively) and for two different values of $\psi$ (0 for the blue circles and 2 for the red ones). The circles are an average from 50 different simulations, and the dashed lines represent the range within the standard deviation. All plots are generated using a logarithmic scale.

analyzed its time evolution (Figure 6). This analysis clearly confirms that larger aggregates are formed at a higher $W_c$, where both cell densities are considered, and that $W_c$ has a greater influence on the formation of aggregates as compared to $\Psi$. Interestingly, it also showed a sort of weak biphasic effect of $\Psi$ on the cluster size, with larger aggregates being formed at intermediate values (between 0.75 and 1.5). However, high variations in final cluster sizes can be seen at these values, which may be due to the more pronounced stochasticity of the process.

Numerical simulations also allow us detailed insights into the dynamics of the aggregation process, which can be quantified by the time variation in the maximum cluster size (Figure 6). With no cell–cell adhesion ($W_c$ = 0), the system was largely static, with no increase in the cluster size at either density tested after 10 dimensionless time units. This is a condition that closely resembles the dynamics observed during the dispersion state. However, as $W_c$ was increased, the maximum size of the clusters tended toward the power law dynamics. On the other hand, CIL appeared to have a marginal effect on the dynamics (rate) of aggregation for intermediate and high values of $W_c$ (Figures 6B, C, E, F), whereas a marked effect of CIL can be seen when $W_c$ is absent (Figures 6A, D). In these conditions, a high CIL ($\Psi$ = 2) caused an initial decline in the size of the cluster and a generally low aggregation as compared to $\Psi$ = 0. This phenomenon, which was more pronounced at high cell densities, most likely reflects the scattering effect provided by CIL.

## 2.2 Environmental guidance

The results presented previously show that purely cell-autonomous behaviors could explain the dispersion state by keeping low cell–cell adhesion, but they were not sufficient to lead to the formation of a single aggregate at one of the embryonic poles, as seen in annual killifish early embryogenesis. It is, therefore, possible that the information provided by environmental cues is needed in the form of an organizing center that causes cells to orient toward a specific position of the embryo, where possibly a site-specific increase in $W_c$ for cells reaching the location could initiate the aggregation process. The cells might preferentially move toward the organizing center by a variety of mechanisms including chemotaxis, durotaxis, and haptotaxis (CARTER, 1967; Bellomo et al., 2015; Espina et al., 2022). A powerful feature of our model and its software implementation is that such external environmental factors can easily be included. As a proof of concept, we show, here, a simple model of repolarization that shows a bias for the cells to repolarize toward the organizing center. However, experiments support a variety of possible guidance mechanisms (Sarris and Sixt, 2015a). As a feasibility study, in the Supplementary Material, we further expand two more models (i.e., “adjustment of directional speed along gradient” and “slowing down at the source”) to demonstrate that our modeling framework provides a robust and flexible tool to model a variety of taxis models (see Supplementary Material, Figures S1, S2).

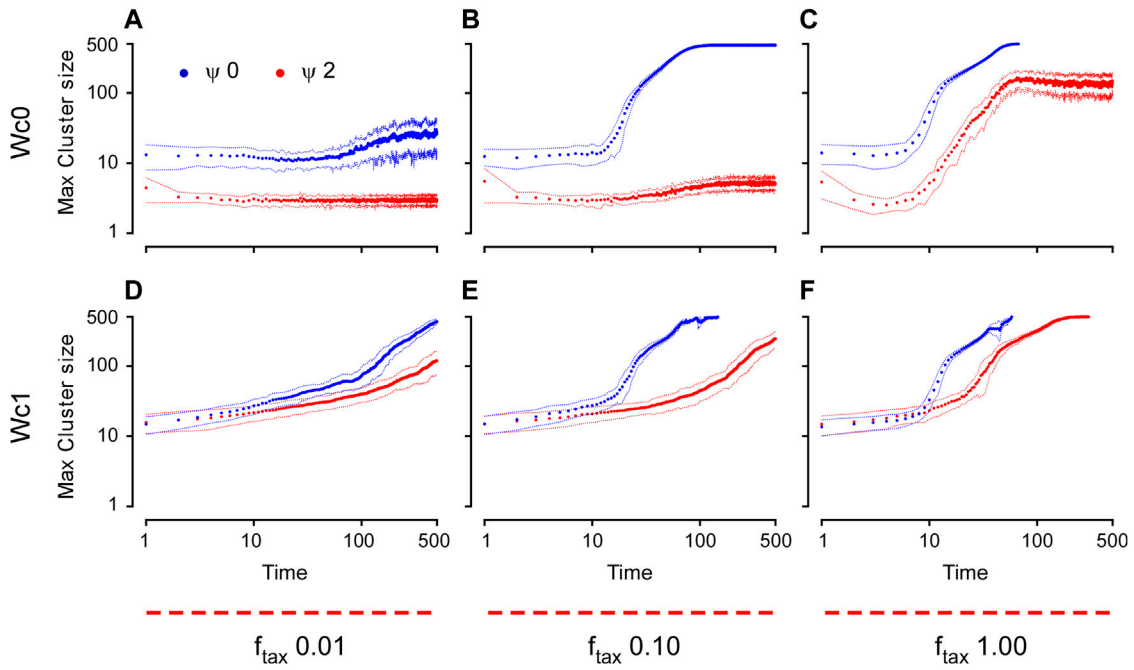


FIGURE 7
Time dynamics of aggregation for the environmental guidance model measured by the maximum cluster size. The cluster size is plotted here as a function of time for different $W_c$ [(0 for **(A–C)** and 1 for **(D–F)**], different $f_{tax}$ (0.01, 0.1, and 1 for the first, second, and third column, respectively), and for two different values of $\psi$ (0 for the blue circles, and 2 for the red ones). The data points are the average from 50 different simulations, and the dashed lines represent the standard deviation. The conditions used accurately represent the *in vivo* density of the cells ($\phi$ = 0.2, 500 cells on a sphere of radius 25). All plots are generated using a logarithmic scale. The simulations were stopped when they reached a single aggregate (maximum cluster size of exactly 500 cells). Hence, the one cluster condition is only reached in those simulations that are interrupted at an earlier time [i.e., $\psi$ = 0 in **(C, E)**; $\psi$ = 2 in **(F)**, whereas for $\psi$ = 0 in **(B)**, the curve gets very close but never reaches the single cluster condition].

### 2.2.1 External taxis

If the organizing center is at position $x_{org}$, the vector pointing from cell $i$ to the organizing center in the tangential plane is as follows:

$$\boldsymbol{v}_i^{org} = \left(\boldsymbol{x}_{org} - \boldsymbol{x}_i\right) - \left[\left(\boldsymbol{x}_{org} - \boldsymbol{x}_i\right) \cdot \hat{\boldsymbol{n}}_i\right]\hat{\boldsymbol{n}}_i. \tag{7}$$

Then, the angular equation of motion becomes

$$\dot{\theta}_i = -f_{cil} \times arccos\left(\frac{\boldsymbol{v}_i^f \cdot \hat{\boldsymbol{p}}_i}{\left|\boldsymbol{v}_i^f\right|}\right) - f_{tax} \times arccos\left(\frac{\boldsymbol{v}_i^{org} \cdot \hat{\boldsymbol{p}}_i}{\left|\boldsymbol{v}_i^{org}\right|}\right) + \sqrt{2D_r}\xi \tag{8}$$

.

In this simple model, the rate of repolarization does not depend on the distance from the organizing center, nor are there any effects on the speed of cell motion. Various mechanisms and models of taxis have been proposed (Sarris and Sixt, 2015b), which while not considered here, are straightforward to implement in our modeling framework.

### 2.2.2 Numerical simulations

To test the effect of this simple external guidance (taxis), we then performed a series of simulations using the more realistic (i.e., closest to *in vivo*) conditions with cell number = 500 and sphere radius = 25, for density $\phi$ = 0.2, while testing the effect of varying the external taxis repolarization rate ($f_{tax}$), cell adhesion ($W_c$), and CIL ($\psi$). As expected, at a low $f_{tax}$ (0.01), cells had an overall tendency to move toward the organizing center but did not form a single aggregate within the time of our simulation as the properties of the cell-autonomous system, such as rotational diffusion and CIL, prevailed (Figures 7A, D). At this low $f_{tax}$ regime, the cells mostly remained dispersed on the surface of the sphere as single cells for $W_c$ = 0 (Figure 7A) or formed small aggregates that slowly coalesced at the organizing center for $W_c$ = 1 (Figure 7D). On the other hand, intermediate and high strengths of $f_{tax}$ (0.1 and 1) showed features similar to the dynamics of aggregation principally depending on $W_c$ and CIL, while $f_{tax}$ determined the speed (rate) and the degree of the aggregation process with intermediate values of $f_{tax}$ (Figures 7B, E) being, at a first approximation and to different degrees, a slower and attenuated version of the dynamics seen for the highest $f_{tax}$ value (Figures 7C, F, 8; Supplementary Movie S3–S6). Our simulations using $f_{tax}$ = 1 showed four distinct and equally interesting phenotypes. Strong adhesion ($W_c$ = 1) combined with strong CIL ($\psi$ = 2) led the cells to the formation of small aggregates that fluctuated on the surface of the sphere and eventually coalesced into a large aggregate, only at long time scales (Figure 7F, red curve; Figure 8A; Supplementary Movie S3). This was also the case for the same conditions but using $f_{tax}$ = 0.1, where the only noticeable difference was the rate at which small aggregates moved toward the organizing center (Figure 7E, red curve). In similar conditions of CIL ($\psi$ = 2), but in the absence of adhesion ($W_c$ = 0), the cells moved toward the organizing center and remained in a form of dispersed single-cell dynamics within a small area close to the organizing center. However, due to high CIL, the cells did not form a tight

10.3389/fcell.2023.959611

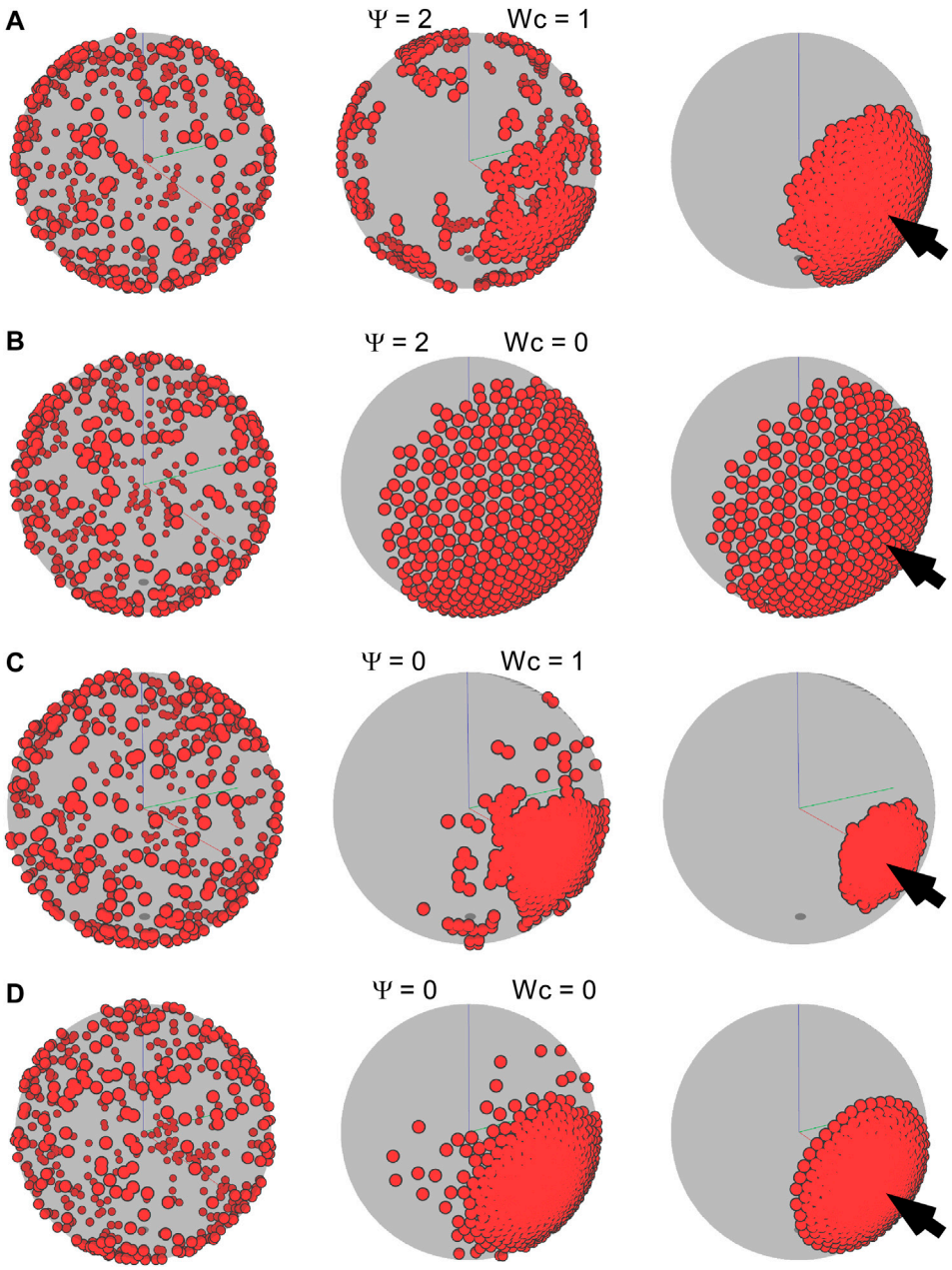


FIGURE 8
Frames of different time steps for an environmental guidance system (external taxis). For all simulations, $f_{tax}$ is 1 and $\phi = 0.2$ (500 cells on a sphere of radius 25). We varied $\psi$ and $W_c$ to explore the emerging aggregation dynamics and phenotypes. **(A)** $\psi = 2$; $W_c = 1$. **(B)** $\psi = 2$; $W_c = 0$. **(C)** $\psi = 0$; $W_c = 1$. **(D)** $\psi = 0$; $W_c = 0$. The YSL is drawn as a transparent gray sphere; hence, the cells on the far side appear darker. The three-dimensional perspective means that these cells also appear smaller. The images in the left, middle, and right columns represent the times 0, 50, and 500, respectively, except for C, where the final configuration is reached at time 72.5. The arrow indicates the position of the organizing center.

aggregate, and the maximum cluster size plateaued at about 100 cells (Figure 7C, red curve; Figure 8B; Supplementary Movie S4). This characteristic was also seen with $f_{tax} = 0.1$, where the cells randomly collided with the temporarily small clusters. However, due to the low $f_{tax}$, the cells were dispersed over a larger area as compared to $f_{tax} = 1$, thus diminishing the probability of collision (maximum cluster size stabilized at 3–5 cells). Finally, the aggregation into a single cluster at the organizing center was achieved when CIL was not present ($\psi = 0$), irrespective of the value of $W_c$ and $f_{tax}$ (Figures 7B, C, E, F, blue curves; Figures 8C, D; Supplementary Movie S5, S6). However, $W_c$ proved to play an important role in defining the mode of migration toward the organizing center, with cells at high $W_c$ moving as small aggregates (Figure 7F, blue curve; Figure 8C; Supplementary Movie S5), whereas, in the absence of adhesion ($W_c = 0$), the cells moved independently as single cells (Figure 7C, blue curve; Figure 8D; Supplementary Movie S6). Furthermore, at intermediate $f_{tax}$ and in the absence of cell–cell adhesion (Figure 7B, blue circles), the cells at the border of the

aggregate lacked the necessary pulling force from the organizing center to remain cohesively adherent to each other; thus, the aggregate approached but never reached the maximum cluster size of 500 cells. These last two conditions (Figures 7B, C, blue circles; Figure 8D; Supplementary Movie S6) seem to recapitulate the best *in vivo* observations previously reported, for example by Dolfi et al. (2014), where the cells migrate as single cells to form a loose cluster (Figure 1). However, the precise details of the migration and aggregation mechanism in annual killifish are still largely elusive. Thus, the experimental observations [as in (Dolfi et al., 2014)] need to be corroborated, expanded, and carefully analyzed before being implemented in our model.

# 3 Discussion

We have developed a computational model of cell migration and aggregation mechanisms for cells trapped between two concentric spheres, as is the case of the *in vivo* conditions of the annual killifish early embryo development. We demonstrate that numerical simulations of this model are an essential tool to test the role of physical mechanisms based on both the cell-autonomous and environmental guidance factors in driving the complex self-organizing processes during morphogenesis. Our computational model includes the full geometry of the embryo, including the spherical topology due to the constraint between the EVL and the YSL. This model was solved numerically to build phase space maps that reveal the effect of key mechanical parameters on the aggregation process.

For cell-autonomous mechanisms, the simulated aggregate phenotype was comparable to the experimental observation of the dispersed state, which could be achieved simply if the cells had low adhesion but failed to recapitulate the aggregation into a single cluster (Figures 3–6). At high adhesion, smaller clusters fused into a larger cluster, but the type of coalescence observed *in vivo* was never observed under these simple conditions. Thus, we explored the possibility that in addition to cell-autonomous factors, external cues possibly arising from a putative organizing center are also at play. The environmental taxis cues that guide cell migration could, in principle, be of many kinds, possibly chemical (i.e., diffusible or substrate-bound gradients of a chemoattractant) or physical (i.e., stiffness gradients). Using our model, we simulated a simple external cue guiding the direction of the migration of cells and showed that, under some conditions, it does indeed form single localized clusters (Figures 7, 8). In particular, our simulations determined that in order to achieve the dynamic and resulting phenotype of aggregation observed in early killifish development, an organizing center and low levels of CIL are essential. In addition, it appears that adhesive forces must remain low throughout the process and possibly increase only after the aggregate has formed.

Importantly, our strategy aims at building knowledge using a bottom-up approach by making predictions starting from the minimal condition for aggregation. Thus, at present, our model is kept to the most simplistic conditions possible in order to avoid overfitting of the system. However, more detailed models of cell motility or taxis, for example, may easily be constructed using our framework, given the relevant mechanistic details and more complete experimental evidence. Another aspect that might be considered is lateral inhibition, a mechanism that implicates the cell inhibition of adjacent cell activity. We are currently exploring all these mechanisms to simulate an aggregation process that is most like the experimental phenomena seen in annual killifish. Most importantly, despite its simplicity, our model is able to recapitulate the major features of cell aggregation in early annual killifish embryo development, a nearly unique model of cell aggregation in vertebrates.

# 4 Methods

## 4.1 Numerical simulations

The equations of motion (1) were solved using an implicit Euler method, with

$$\boldsymbol{x}_i(t+\Delta t)-\boldsymbol{x}_i(t)=\frac{\Delta t}{\gamma_s}\left(-F_m\hat{\boldsymbol{p}}_i+\sum_j F_{ij}^{cc}\frac{\left(\boldsymbol{x}_i(t+\Delta t)-\boldsymbol{x}_j(t+\Delta t)\right)}{\left|\boldsymbol{x}_i(t+\Delta t)-\boldsymbol{x}_j(t+\Delta t)\right|}\right) \quad (9)$$

so that we solve for $x_i(t+\Delta t)$ implicitly from Eq. 9. The rotational equations of motion given by Eqs 6, 8 were solved using the Euler–Maruyama scheme, such that

$$\theta_i(t+\Delta t)=\theta_i(t)+\Delta t\left[f_{pol}\left(\theta_i^*(t)-\theta_i(t)\right)\right]+\sqrt{2D_r}\xi_i, \quad (10)$$

where $\xi_i$ is the normally distributed zero mean random noise with variance $\Delta t$. In all simulations, $\Delta t$ was chosen as 0.1 for cell-autonomous and external taxis models.

For each set of parameters, 50 replicates were made for cell-autonomous and 50 for external taxis models.

## 4.2 Software implementation

All codes and models were implemented using the open-source CellModeller multicellular modeling framework (Rudge et al., 2012).

## 4.3 Embryo imaging

The *in vivo* experiments depicted in Figure 1 were performed under the license for animal housing, breeding, and manipulation that was issued by Umwelt-und Verbraucherschutzamt der Stadt Köln, with the authorization no. 576.1.36.6.G28/13 Be. All the fish used were raised in 35-L tanks at 24°C–26°C and belonged to the *N. furzeri* FUCCI transgenic strain published by Dolfi et al. (2019). They were fed two to three times a day with frozen Chironomus larvae or living nauplii of *Artemia salina*, depending

on their size. The breeders were kept in 8-L tanks with one or more boxes (9 cm × 9 cm × 4 cm) filled with 2 cm of river sand and were left to spawn eggs for 1 h. The embryos were collected by sieving the sand with a plastic net and were then embedded in 2% low melting agar. The fluorescence images shown in Figure 1 were acquired using a Leica TCS SP5-X confocal microscope and the red emission channel with 543-nm lasers. A total of 40 to 60 images per embryo were acquired at a depth distance of 6 µm. The maximum intensity projections shown have been generated using ImageJ. The contrast in the images has been adjusted, but not altered, to optimize visualization.

## Data availability statement

The raw data supporting the conclusion of this article will be made available by the authors upon request.

## Ethics statement

The animal study was reviewed and approved by Umwelt-und Verbraucherschutzamt der Stadt Köln. Authorization No. 576.1.36.6.G28/13 Be.

## Author contributions

TR wrote the simulation software; IM-R, GY, MA-L, OG-C, and ES performed all the numerical simulations; GY, AR, and TR designed and performed the analyses; IM-R and NOR contributed with theoretical formulations; LD and AC performed and supervised the animal experiments; MC, MLC, and CB contributed with critical theoretical and analytical knowledge; AR and TR designed, directed, and supervised the project; GY, IM-R, MLC, AR, and TR wrote the manuscript. All authors contributed to commenting and writing the manuscript.

## Funding

This work was funded by ANID SCIA/ACT192015, ANID FONDECYT Regular 1211598, 1210872, 1221696, 1230919, and 1190806; ANID FONDEQUIP EMQ210101, EQM210020, and EQM130051; FONDAP 15150012; ICN09_015; NCN19_170; REDES170212, and PUENTE-2022-13 from Pontificia Universidad Católica de Chile.

## Acknowledgments

AR and TR are grateful to PUC/VRI, PUC IIBM, and the graduate program at IIBM for the seed funding and support. NOR is thankful for the support received from PUC IIBM.

## Conflict of interest

The authors declare that the research was conducted in the absence of any commercial or financial relationships that could be construed as a potential conflict of interest.

## Publisher's note

All claims expressed in this article are solely those of the authors and do not necessarily represent those of their affiliated organizations, or those of the publisher, the editors, and the reviewers. Any product that may be evaluated in this article, or claim that may be made by its manufacturer, is not guaranteed or endorsed by the publisher.

## Supplementary material

The Supplementary Material for this article can be found online at: https://www.frontiersin.org/articles/10.3389/fcell.2023.959611/full#supplementary-material

## References

Abercrombie, M., and Heaysman, J. E. M. (1954). Observations on the social behaviour of cells in tissue culture. II. Monolayering of fibroblasts. *Exp. Cell Res.* 6, 293–306. doi:10.1016/0014-4827(54)90176-7

Abitua, P. B., Aksel, D. C., and Schier, A. F. (2021). Axis formation in annual killifish: Nodal coordinates morphogenesis in absence of Huluwa prepatterning. *bioRxiv*. doi:10.1101/2021.04.16.440199

Basan, M., Elgeti, J., Hannezo, E., Rappel, W. J., and Levine, H. (2013). Alignment of cellular motility forces with tissue flow as a mechanism for efficient wound healing. *Proc. Natl. Acad. Sci. U. S. A.* 110, 2452–2459. doi:10.1073/pnas.1219937110

Bellomo, N., Bellouquid, A., Tao, Y., and Winkler, M. (2015). Toward a mathematical theory of Keller–Segel models of pattern formation in biological tissues. *Math. Models Methods Appl. Sci.*25, 1663-1763. doi:10.1142/S021820251550044X

Belmonte, J. M., Thomas, G. L., Brunnet, L. G., de Almeida, R. M. C., and Chaté, H. (2008). Self-propelled particle model for cell-sorting phenomena. *Phys. Rev. Lett.* 100, 248702. doi:10.1103/PhysRevLett.100.248702

Bertocchi, C., Wang, Y., Ravasio, A., Hara, Y., Wu, Y., Sailov, T., et al. (2017). Nanoscale architecture of cadherin-based cell adhesions. *Nat. Cell Biol.* 19, 28–37. doi:10.1038/ncb3456

Bray, A. J. (1993). Theory of phase ordering kinetics. *Phys. A Stat. Mech. its Appl.* 194, 41–52. doi:10.1016/0378-4371(93)90338-5

Cai, D., Dai, W., Prasad, M., Luo, J., Gov, N. S., and Montell, D. J. (2016). Modeling and analysis of collective cell migration in an *in vivo* three-dimensional environment. *Proc. Natl. Acad. Sci.* 113. doi:10.1073/pnas.1522656113

Carter, S. B. (1967). Haptotaxis and the mechanism of cell motility. *Nature* 213, 256–260. doi:10.1038/213256a0

Concha, M. L., and Reig, G. (2022). Origin, form and function of extraembryonic structures in teleost fishes. *Philos. Trans. R. Soc. Lond B Biol. Sci.* 377, 20210264. doi:10.1098/rstb.2021.0264

Conte, V., Munoz, J., and Miodownik, M. (2008). A 3D finite element model of ventral furrow invagination in the *Drosophila melanogaster* embryo. *J. Mech. Behav. Biomed. Mater.* 1, 188–198. doi:10.1016/j.jmbbm.2007.10.002

Dolfi, L., Ripa, R., Antebi, A., Valenzano, D. R., and Cellerino, A. (2019). Cell cycle dynamics during diapause entry and exit in an annual killifish revealed by FUCCI technology. *EvoDevo* 10, 29. doi:10.1186/s13227-019-0142-5

Dolfi, L., Ripa, R., and Cellerino, A. (2014). Transition to annual life history coincides with reduction in cell cycle speed during early cleavage in three independent clades of annual killifish. *EvoDevo* 5, 32. doi:10.1186/2041-9139-5-32

Espina, J. A., Marchant, C. L., and Barriga, E. H. (2022). Durotaxis: The mechanical control of directed cell migration. *FEBS J.* 289, 2736–2754. doi:10.1111/febs.15862

Henkes, S., Fily, Y., and Marchetti, M. C. (2011). Active jamming: Self-propelled soft particles at high density. *Phys. Rev. E* 84, 040301. doi:10.1103/PhysRevE.84.040301

Kabla, A. J. (2012). Collective cell migration: Leadership, invasion and segregation. *J. R. Soc. Interface* 9, 3268–3278. doi:10.1098/rsif.2012.0448

Kanchanawong, P., Shtengel, G., Pasapera, A. M., Ramko, E. B., Davidson, M. W., Hess, H. F., et al. (2010). Nanoscale architecture of integrin-based cell adhesions. *Nature* 468, 580–584. doi:10.1038/nature09621

Márquez, S., Reig, G., Concha, M., and Soto, R. (2019). Cell migration driven by substrate deformation gradients. *Phys. Biol.* 16, 066001. doi:10.1088/1478-3975/ab39c7

Méhes, E., and Vicsek, T. (2014). Collective motion of cells: From experiments to models. *Integr. Biol.* 6, 831–854. doi:10.1039/c4ib00115j

Mladek, B. M., Gottwald, D., Kahl, G., Neumann, M., and Likos, C. N. (2006). formation of polymorphic cluster phases for a class of models of purely repulsive soft spheres. *Phys. Rev. Lett.* 96, 045701. doi:10.1103/PhysRevLett.96.045701

Moreno, A. J., and Likos, C. N. (2007). Diffusion and relaxation dynamics in cluster crystals. *Phys. Rev. Lett.* 99, 107801. doi:10.1103/PhysRevLett.99.107801

Pereiro, L., Loosli, F., Fernandez, J., Hartel, S., Wittbrodt, J., and Concha, M. L. (2017). Gastrulation in an annual killifish: Molecular and cellular events during germ layer formation in *Austrolebias*. *Dev. Dyn.* 246, 812–826. doi:10.1002/dvdy.24496

Phillips, R. (2015). Theory in biology: Figure 1 or figure 7? *Trends Cell Biol.* 25, 723–729. doi:10.1016/j.tcb.2015.10.007

Ravasio, A., Cheddadi, I., Chen, T., Pereira, T., Ong, H. T., Bertocchi, C., et al. (2015). Gap geometry dictates epithelial closure efficiency. *Nat. Commun.* 6, 7683–7713. doi:10.1038/ncomms8683

Ravasio, A., Le, A. P., Saw, T. B., Tarle, V., Ong, H. T., Bertocchi, C., et al. (2015). Regulation of epithelial cell organization by tuning cell-substrate adhesion. *Integr. Biol. (United Kingdom)* 7, 1228–1241. doi:10.1039/c5ib00196j

Redner, G. S., Baskaran, A., and Hagan, M. F. (2013). Reentrant phase behavior in active colloids with attraction. *Phys. Rev. E* 88, 012305. doi:10.1103/PhysRevE.88.012305

Reig, G., Cerda, M., Sepulveda, N., Flores, D., Castaneda, V., Tada, M., et al. (2017). Extra-embryonic tissue spreading directs early embryo morphogenesis in killifish. *Nat. Commun.* 8, 15431. doi:10.1038/ncomms15431

Roycroft, A., and Mayor, R. (2016). Molecular basis of contact inhibition of locomotion. *Cell. Mol. Life Sci.* 73, 1119–1130. doi:10.1007/s00018-015-2090-0

Rudge, T. J., Steiner, P. J., Phillips, A., and Haseloff, J. (2012). Computational modeling of synthetic microbial biofilms. *ACS Synth. Biol.* 1, 345–352. doi:10.1021/sb300031n

Sarris, M., and Sixt, M. (2015). Navigating in tissue mazes: Chemoattractant interpretation in complex environments. *Curr. Opin. Cell Biol.* 36, 93–102. doi:10.1016/j.ceb.2015.08.001

Sarris, M., and Sixt, M. (2015). Navigating in tissue mazes: Chemoattractant interpretation in complex environments. *Curr. Opin. Cell Biol.* 36, 93–102. doi:10.1016/j.ceb.2015.08.001

Sepúlveda, N., Petitjean, L., Cochet, O., Grasland-Mongrain, E., Silberzan, P., and Hakim, V. (2013). Collective cell motion in an epithelial sheet can Be quantitatively described by a stochastic interacting particle model. *PLoS Comput. Biol.* 9, e1002944. doi:10.1371/journal.pcbi.1002944

Smeets, B., Alert, R., Pešek, J., Pagonabarraga, I., Ramon, H., and Vincent, R. (2016). Emergent structures and dynamics of cell colonies by contact inhibition of locomotion. *Proc. Natl. Acad. Sci.* 113, 14621–14626. doi:10.1073/pnas.1521151113

Stepien, T. L., Lynch, H. E., Yancey, S. X., Dempsey, L., and Davidson, L. A. (2019). Using a continuum model to decipher the mechanics of embryonic tissue spreading from time-lapse image sequences: An approximate Bayesian computation approach. *PLOS ONE* 14, e0218021. doi:10.1371/journal.pone.0218021

Stichel, D., Middleton, A. M., Muller, B. F., Depner, S., Klingmuller, U., Breuhahn, K., et al. (2017). An individual-based model for collective cancer cell migration explains speed dynamics and phenotype variability in response to growth factors. *npj Syst. Biol. Appl.* 3, 5. doi:10.1038/s41540-017-0006-3

Tarle, V., Ravasio, A., Hakim, V., and Gov, N. S. (2015). Modeling the finger instability in an expanding cell monolayer. *Integr. Biol. (Camb)* 7, 1218–1227. doi:10.1039/c5ib00092k

Wourms, J. P. (1972). Developmental biology of annual fishes. I. Stages in the normal development ofAustrofundulus myersi Dahl. *J. Exp. Zoology* 182, 143–167. doi:10.1002/jez.1401820202

# Frontiers in
# Cell and Developmental Biology

**Explores the fundamental biological processes of life, covering intracellular and extracellular dynamics.**

The world's most cited developmental biology journal, advancing our understanding of the fundamental processes of life. It explores a wide spectrum of cell and developmental biology, covering intracellular and extracellular dynamics.

---

## Discover the latest Research Topics

See more →


**Frontiers**

Avenue du Tribunal-Fédéral 34
1005 Lausanne, Switzerland
frontiersin.org

**Contact us**

+41 (0)21 510 17 00
frontiersin.org/about/contact